

---

# Mechanistic Aspects of Photo-Induced Polymerization on Multiple Timescales from the Earliest Events to Product Formation

Zur Erlangung des akademischen Grades eines

DOKTORS DER NATURWISSENSCHAFTEN

(Dr. rer. nat.)

von der KIT-Fakultät für Chemie und Biowissenschaften

des Karlsruher Instituts für Technologie (KIT)

genehmigte

DISSERTATION

von

Philipp Neidinger

1. Referent: Prof. Dr. Andreas-Neil Unterreiner  
2. Referent: Prof. Dr. Patrick Théato  
Cotutelle-Referent: Prof. Dr. Christopher Barner-Kowollik

Tag der mündlichen Prüfung: 08. Februar 2024



## Danksagung

Ich möchte mich herzlichst bei allen bedanken, die mich während meines PhD und des Verfassens meiner Dissertation unterstützt haben.

An erster Stelle gilt mein Dank Prof. Dr. Andreas-Neil Unterreiner, Prof. Dr. Christopher Barner-Kowollik und Dr. Sarah Walden für die Möglichkeit an diesem faszinierenden Forschungsgebiet über die letzten Jahre teilhaben zu dürfen. Vielen Dank für den stetigen und unermüdlischen Support, womit ihr mich zu einem besseren Wissenschaftler gefördert habt.

Mein Dank gilt außerdem Prof. Dr. Matthias Olzmann, der mir auch stets bei allen Fragestellungen zur Seite stand. Herzlichen Dank an meine Arbeitsgruppe des KIT, die mich während der gesamten Zeit begleitet hat und wie eine Familie war. Ihr hattet stets ein offenes Ohr und wart stets hilfsbereit. Die lustigen Mittagspausen und Diskussionen werden mir in bester Erinnerung bleiben. Besonderen Dank gilt Dr. Nadine Michenfelder, Dr. Philipp Jöckle, Dr. Julia Leier und Pascal Rauthe als Teil der Femto-Gruppe. Danke für eure fachliche Hilfe, aufmunternden Gespräche und Hilfe, falls das Justieren mal nicht ganz klappen wollte.

Außerdem möchte ich Johannes Werner und Jisu Kim danken, die mit ihrer Arbeit für diese Thesis beigetragen haben. Vielen Dank auch an Patricia Hibomvshi und Desmond Kelly für ihre Unterstützung in technischen und IT-Fragen, sowie die lustigen Unterhaltungen. Desweiteren möchte ich mich bei Agnes Litz für die administrative Unterstützung herzlich bedanken.

Ein herzlicher Dank gilt ebenso meiner Arbeitsgruppe an der QUT, die mich während meines Aufenthalts in Australien begleitet hat. Lieben Dank für die tägliche Unterstützung in sämtlichen Fragestellungen und die unterhaltsamen Treffen in der P8 Küche. Ich werde die Zeit an der QUT immer in bester Erinnerung behalten. Besonderen Dank gilt hierbei Till Meissner, der mich auch als Mitbewohner und Freund täglich durch das Leben an der QUT und außerhalb begleitet hat.

Vielen Dank an Prof. Esa Jaatinen, Dr. Joshua Carroll, Dr. Joshua Davis, Dr. Jochen Kammerer und Dr. Dominik Voll, die in Kollaboration an den Ergebnissen für diese Thesis mitgewirkt haben. Desweiteren möchte ich mich herzlich bei Dr. Laura Delafresnaye-Broqua bedanken, die mir während meines PhD zu allen organisatorischen Fragen bzgl. der QUT zu Seite stand.

Von Herzen möchte ich mich bei meiner Familie, meiner Partnerin Leanna und meinen Freunden bedanken. Ihr seid meine größte Unterstützung und mein Rückhalt gewesen und habt immer an mich geglaubt.

## Acknowledgement

I acknowledge QUT for funding my thesis with a Tuition Fee Scholarship. Further, I acknowledge the use of Artificial Intelligence (ChatGPT 3.5) as support for English phrasing.

I would like to express my heartfelt gratitude to everyone who supported me during my PhD and the writing process of my thesis.

First and foremost, I extend my thanks to Prof. Dr. Andreas-Neil Unterreiner, Prof. Dr. Christopher Barner-Kowollik, and Dr. Sarah Walden for providing me with the opportunity to be part of this fascinating research field over the past years. Thank you for your continuous and tireless support, which has encouraged me to become a better scientist.

My thanks also go to Prof. Dr. Matthias Olzmann, who always assisted me with any questions. Heartfelt thanks to my research group at KIT, who accompanied me throughout this entire period and felt like a family. You always had an open ear and were consistently helpful. The enjoyable lunch breaks and discussions will remain cherished memories. Special thanks to Dr. Nadine Michenfelder, Dr. Philipp Jöckle, Dr. Julia Leier, and Pascal Rauthe as part of the Femto group. Thank you for your assistance, pleasant conversations, and your support whenever the adjustments were not quite working out.

I would also like to thank Johannes Werner and Jisu Kim, who contributed to this thesis with their work. Many thanks to Patricia Hibomvschi and Desmond Kelly for their support in technical and IT matters, as well as for the enjoyable conversations. Furthermore, I would like to express my sincere appreciation to Agnes Litz for the administrative support.

A warm thank you also goes to my research group at QUT, who accompanied me during my stay in Australia. Thank you for the daily support in all matters and the enjoyable meetings in the P8 Kitchen. I will always cherish the time at QUT. Special thanks to Till Meissner, who accompanied me daily as a roommate and friend both at QUT and outside.

Many thanks to Prof. Esa Jaatinen, Dr. Joshua Carroll, Dr. Joshua Davis, Dr. Jochen Kammerer and Dr. Dominik Voll, who collaborated on the results for this thesis. Furthermore, I would like to sincerely thank Dr. Laura Delafresnaye-Broqua for assisting me with all organizational questions regarding QUT during my PhD.

From the bottom of my heart, I would like to thank my family, my partner Leanna, and my friends. You were my greatest support and backbone, always believing in me.

# I Zusammenfassung

Die vorliegende Dissertation fasst die im Rahmen eines Cotutelle-Doktorats zwischen der Unterreiner-Gruppe (KIT) und der Barner-Kowollik-Gruppe (QUT) durchgeführten Forschungen zum Mechanismus der photo-induzierten Polymerisation zusammen. Photo-induzierte Polymerisationen bieten den Vorteil sowohl einer räumlich-zeitlichen Kontrolle, als auch des Potentials zur Herstellung hochgradig individualisierter Polymerketten, da man die Initiierung und Effizienz der Polymerisationen wellenlängenabhängig steuern kann. Eine präzise Steuerung photo-induzierter Polymerisationen auf gezielte Weise ist durch ein tiefgreifendes Verständnis des Polymerisationsmechanismus möglich. Ziel der vorliegenden Arbeit ist es daher, das Verständnis des Mechanismus der photo-induzierten Polymerisationen im sichtbaren Bereich (Vis) weiter zu vertiefen, angefangen bei den frühesten Ereignissen der Photonenabsorption bis hin zur Bildung des Endprodukts. Des Weiteren erforscht die vorliegende Arbeit eine Methodik zur Verschiebung der Anregungswellenlänge für die Initiation von Polymerisationen in Richtung des nahen Infrarot (NIR), da NIR-Licht gegenüber Vis-Licht entscheidende Vorteile bietet, wie beispielsweise eine geringere Schädlichkeit für Gewebe und eine tiefere Eindringtiefe.

Als Modellsystem wurde die Polymerisation von Methylmethacrylat (MMA), initiiert durch den Photoinitiator Ivocerin (*para*-methoxybisacyldiethylgerman), ausgewählt. Der Prozess der photo-induzierten Polymerisation mit Ivocerin wurde beginnend mit der Analyse der Initiatorspaltung, gefolgt vom Kettenwachstum, der Endprodukte und schließlich der Dynamik des angeregten Zustands von Ivocerin untersucht.

Wie die meisten Photoinitiatoren absorbiert Ivocerin ultraviolettes (UV) und sichtbares Licht und wurde daher resonant bei 400 nm mit einem femtosekunden (fs) gepulsten Laser angeregt, was die erste detaillierte Untersuchung der Polymerisation mit Ivocerin darstellt, die durch einen fs-Laser im Hz-Bereich ausgelöst wurde. Der erste Schritt beleuchtete den Prozess der Initiatorspaltung und der Radikalbildung. Der Initiatorabbau wurde durch stationäre UV/Vis-Spektroskopie nach Bestrahlung mit 400 nm fs-Laserpulsen unterschiedlicher Energien bestimmt. Aus den Absorptionsspektren wurde die Initiator-Konzentration (bzw. Umwandlung) mithilfe des Gesetzes von Beer-Lambert bestimmt. Ein logarithmischer Plot der Initiatorumwandlung zeigte eine lineare Beziehung zur Laserflussdichte mit einer Steigung von  $0,97 \pm 0,05$ , was auf eine lineare Abhängigkeit der Initiatorumwandlung von der Photonenanzahl hinweist, die typisch für eine resonante Ein-Photonen (1P) Anregung ist. Mittels La-

serpuls-induzierter Polymerisation (PLP) wurde der Prozess des Kettenwachstums bei variierenden Repetitionsraten der fs-Laserpulse dargestellt. Die Produktanalyse mittels Größenausschlusschromatographie (SEC) zeigte, dass die berechneten Propagationsgeschwindigkeitskoeffizienten von MMA mit den Literaturwerten der IUPAC übereinstimmten, was die Laserkontrolle über die Polymerisation bestätigte. Eine *post-mortem* Analyse der Polymerprodukte mittels Elektrospray-Ionisations-Massenspektrometrie (ESI-MS) lieferte Informationen über die Verteilung der Polymerendgruppen und ermöglichte so Einblicke in den Zerfallsmechanismus des Initiators nach gepulster fs-Laseranregung. Während acylbasierte Kombinations- und Disproportionierungsprodukte von Poly(methylmethacrylat) (PMMA) als dominante Spezies identifiziert wurden, wurden germylbasierte Spezies mit einer geringeren Häufigkeit von 30 bis 40% relativ zu den Acylprodukten zugeordnet. Schließlich wurde zeit aufgelöste fs-Absorptionsspektroskopie eingesetzt, um das elektronische Verhalten des Initiators unmittelbar nach der Photoanregung zu analysieren und Einblicke in die initialen Ereignisse nach der Photoanregung zu gewähren. Das transiente Spektrum nach Anregung bei 400 nm deutete auf breitbandige, langlebige angeregte Tripletzustände ohne Rückkehr in den Grundzustand in der beobachteten Zeit von einer Nanosekunde (ns) hin. Zusammenfassend hat sichtbares Licht, welches auf Ivocerin unter Verwendung eines gepulsten fs-Lasers im kHz-Bereich eingewirkt hat, eine 1P-Polymerisation von MMA nach einem PLP-Mechanismus initiiert, was zu Polymerprodukten führt, die sowohl acyl- als auch germylbasierte Spezies enthalten. Der Initiierungsprozess ist jedoch aufgrund langlebiger Tripletzustände von Ivocerin mit einer Radikalbildung von mehr als einer ns eher träge.

Auf der Grundlage des erlangten Wissens über gepulste fs-Laser-induzierte Polymerisation von MMA mit Ivocerin mit sichtbarem Licht, wurde die Anregungswellenlänge anschließend in den NIR-Bereich verschoben, mit dem Ziel, Ivocerin über einen Zwei-Photonen Absorptionsmechanismus (2PA) bei 800 nm anzuregen. Die Experimente wurden analog zu den 1P-Experimenten durchgeführt, beginnend mit der Analyse des Initiatorabbaus, gefolgt vom Kettenwachstums, und schließlich den Endprodukten.

Ein wesentlicher Aspekt der NIR-induzierten Polymerisation ist die energieabhängige stationäre UV/Vis-Spektroskopie, um zu bestätigen, ob der Zerfall von Ivocerin einem Zwei-Photonen (2P) Anregungsmechanismus bei 800 nm folgt. Die Photonenflussdichte abhängige Ivocerin-Umwandlung folgte auf einer doppelt logarithmischen Skala einem linearen Trend mit einer Steigung von  $2,3 \pm 0,3$ , was auf eine quadratische Abhängigkeit der Initiatorumwandlung von der Photonenzahl und einen 2P-Absorptionsprozess hinweist. Um sicherzustellen, dass

die 2P-Polymerisation (2PP) bei 800 nm ebenfalls laserkontrolliert war, wurde das Kettenwachstum der gebildeten Polymere in Abhängigkeit von der Repetitionsrate mittels PLP untersucht. Die daraus resultierenden Propagationsgeschwindigkeitskoeffizienten von MMA entsprachen erneut den anerkannten Literaturwerten des IUPAC und bestätigten somit, dass die NIR-Licht-induzierte Polymerisation bei 800 nm tatsächlich lasergesteuert war. Die Analyse der Endgruppenverteilung mittels ESI-MS zeigte eine erfolgreiche Polymerisation unter 2P-Bedingungen. Darüber hinaus wurden die Endgruppenverteilungen der Polymerisationen nach 1P- und 2P-Anregung verglichen, was auf einen identischen Zerfallsmechanismus hindeutete, jedoch eine viel geringere Häufigkeit germylbasierter Polymerspezies mit nur 10-20% im Vergleich zu den acylbasierten Spezies aufwies. Ziel war es, den Mechanismus der 2P-Anregung in seinen frühesten Stadien zu beleuchten und diese Erkenntnisse mit denen der 1P-Anregung zu vergleichen. Die 2PP von MMA mit Ivocerin führte zu identischen Produkten wie die 1P-Polymerisation (1PP), was sowohl durch acyl- als auch germylbasierte Kombinations- und Disproportionierungsprodukte belegt wurde. Im Falle der 2P-Initiierung waren jedoch die Germyl-Spezies im Vergleich zur 1P-Initiierung weniger häufig vorhanden. Übereinstimmend mit der durch sichtbares Licht ausgelösten Polymerisation erfolgte auch die durch 2P ausgelöste Polymerisation von MMA unter Verwendung von Ivocerin als Photoinitiator über einen PLP-Mechanismus.

Da 2PA-Prozesse hohe Laserintensitäten erfordern, wurden Goldnanostäbchen (AuNR) eingeführt, die als Vermittler in einer alternativen Methode fungieren, um die Polymerisation im NIR-Bereich des Lichts zu initiieren. Aufgrund plasmonischer Resonanzen im NIR-Bereich sind AuNRs bekannt dafür, absorbiertes Licht in Wärme umzuwandeln, was hier nützlich ist, um thermische Initiatoren zu zersetzen. Abhängig von ihrer molekularen Funktionalisierung können AuNRs wasserlöslich sein, was sie für Polymerisationsanwendungen in wässrigen oder biologischen Umgebungen geeignet macht.

Die AuNRs wurden mit einem wasserlöslichen Monomer, *N,N*-Dimethylacrylamid, und einem thermischen Initiator, Azobisisobutyronitril (AIBN), gemischt und mit einem fs-Laser bei 800 nm bestrahlt. ESI-MS- und SEC-Analysen bestätigten die erfolgreiche Herstellung von Polymeren und stellten fest, dass die Reaktion einem Mechanismus der freien radikalischen Polymerisation (FRP) folgte. Da frühere Studien darauf hindeuteten, dass die photochemische Reaktivität nicht immer mit der Absorptivität übereinstimmt, wurde die Monomer-zu-Polymer-Umwandlung als Funktion der Wellenlänge von 620 bis 950 nm unter Verwendung eines monochromatischen ns-Lasers untersucht. Hierbei wurde festgestellt, dass die AuNRs ausrei-

chend Wärme erzeugen, um die Polymerisation zu initiieren, selbst bei der längeren Pulsdauer eines ns-Lasers. Als entscheidende Erkenntnis zeigte der photochemische Actionplot eine Verschiebung der Reaktivität relativ zum Absorptionsspektrum der AuNRs – nach unserem besten Wissen der erste berichtete blauverschobene Actionplot. Nachdem erfolgreich demonstriert wurde, dass AuNRs Wärme aus einfallendem Licht in Zeitspannen von fs bis ns erzeugen, bestand der nächste Schritt darin, diese Experimente unter Verwendung von Leuchtdioden (LEDs) zu wiederholen. Diese Experimente weisen eine praktischere Anwendungsmöglichkeit des von AuNRs angetriebenen NIR-Polymerisationsansatzes auf und eröffnen die Möglichkeit, ihn für Bildungszwecke zu nutzen, einschließlich Experimenten in der Sekundarstufe.

## II Abstract

The presented thesis summarises the research conducted within the framework of a Cotutelle PhD between the Unterreiner (KIT) and the Barner-Kowollik group (QUT) into the mechanism of photo-induced polymerizations. Photo-induced polymerizations offer the advantage of both spatiotemporal control and the potential to produce highly customised polymer chains, as one can control the initiation and efficiency of polymerizations in a wavelength-dependent manner. Precise control over photo-induced polymerizations in a targeted fashion is accessible by a profound understanding of the polymerization mechanism. It is thus the aim of the current thesis to further deepen the understanding of the mechanism of visible (Vis) light-induced polymerisations, from the earliest events of photon absorption to end product formation. Further, the present thesis explores a methodology to shift the excitation wavelength for the initiation of polymerizations towards the near-infrared (NIR) region, as NIR light offers key advantages over Vis light, such as being more benign to tissue and penetrating deeper into it.

As a model system, the polymerization of methyl methacrylate (MMA) initiated with the photoinitiator Ivocerin (*para*-methoxybisacyldiethylgerman) was chosen. The process of photo-induced polymerization with Ivocerin was investigated beginning with the initiator decomposition, then the chain growth mechanism, the end-product analysis and finally the Ivocerin excited state dynamics.

Like most photoinitiators, Ivocerin absorbs ultraviolet (UV) and Vis light, and was thus resonantly excited at 400 nm with a femtosecond (fs) pulsed laser, constituting the first detailed study of polymerization with Ivocerin induced by a fs-laser pulsed in the Hz range. Initially, the initiator decomposition was determined from stationary UV/Vis spectroscopy after irradiation with 400 nm fs laser pulses of various energies. From the absorption spectra, the initiator concentration (or conversion) was determined using the Beer-Lambert's law. A logarithmic plot of the initiator conversion showed a linear relationship to the laser fluence with a slope of  $0.97 \pm 0.05$ , indicating a linear dependence of the initiator conversion on the photon number, typical for resonant one-photon (1P) excitation. As next step, pulsed laser-induced polymerization (PLP) was employed to monitor the process of chain growth with varying fs laser pulse repetition rates. Product analysis using Size Exclusion Chromatography (SEC) revealed that the calculated propagation rate coefficients of MMA aligned with the IUPAC literature values, confirming laser control over the polymerization. Having explored the mechanism of polymer growth, a *post-mortem* analysis of the polymer products using Electrospray

Ionization Mass Spectrometry (ESI-MS) provided information on the polymer end group distribution, thus offering insights into the decomposition mechanism of the initiator after pulsed fs laser excitation. While acyl-based combination and disproportionation poly(methylmethacrylate) (PMMA) products were identified as dominant species, germyl-based species were assigned with a lower abundance of 30 – 40% relative to the acyl-products. Finally, time-resolved fs absorption spectroscopy was employed to analyze the electronic behaviour of the initiator immediately after photoexcitation, allowing insights into the initial events following photoexcitation. The transient spectrum after excitation at 400 nm indicated broadband, long-lived excited triplet states without ground state recovery in the observed time of one nanosecond (ns). In conclusion, Vis light triggered Ivocerin using a pulsed fs laser in the kHz regime initiates 1P polymerization of MMA following a PLP mechanism, resulting in polymer products containing both acyl- and germyl-based species. The initiation process, however, is rather sluggish due to long-lived triplet states of Ivocerin with radical formation in more than one ns.

Based on the obtained knowledge regarding the Vis light pulsed fs laser-induced polymerisation of MMA with Ivocerin, the excitation wavelength was subsequently shifted to the NIR region aiming to excite Ivocerin via a two-photon absorption (2PA) mechanism at 800 nm. The experiments proceeded in an analogue fashion to the 1P experiments, beginning with the initiator decomposition, followed by the chain growth mechanism and finally the end-product analysis.

A critical aspect of NIR-induced polymerization is energy-dependent stationary UV/Vis spectroscopy, required to confirm whether the decomposition of Ivocerin follows a 2P excitation mechanism at 800 nm. The fluence dependent Ivocerin conversion followed a linear trend with a slope of  $2.3 \pm 0.3$  on a double logarithmic scale, indicating a quadratic dependency of the initiator conversion on the photon number and a 2P absorption process. To ensure that the 2P polymerisation (2PP) at 800 nm was also laser controlled, the chain growth of the formed polymers was investigated in a repetition rate dependent fashion via PLP. The resulting propagation rate coefficients of MMA were once again consistent with the IUPAC accepted literature values, confirming that the NIR light-induced polymerisation at 800 nm was indeed laser controlled. Analysing the end group distribution via ESI-MS revealed successful polymerization under two-photon (2P) conditions. In addition, the end group distributions of both the polymerisations after 1P and 2P excitation were compared, suggesting an identical decomposition mechanism, however revealing a much lower abundance of germyl-based polymer species with only 10- 20% relative to the acyl-based species. The goal was to shed light

on the mechanism of 2P excitation at its earliest stages and compare these findings with 1P excitation. The 2PP of MMA with Ivocerin led to identical products as the one-photon polymerization (1PP), evidencing both acyl- and germyl based combination and disproportionation products. In case of 2P initiation, however, the germyl-species were less abundant compared to 1P initiation. Consistent with the Vis light triggered polymerization, the 2P triggered polymerization of MMA using Ivocerin as photoinitiator was also progressing via a PLP mechanism.

As 2PA processes require high laser intensities to occur, gold nanorods (AuNR) were introduced, functioning as a mediator in an alternative method to initiate polymerization in the NIR region of light. Featuring plasmonic resonances in the NIR, AuNR are well known to convert absorbed light into heat, which herein is demonstrated useful to decompose thermal initiators. Depending on their molecular capping layer, AuNRs can be water-soluble, making them suitable for polymerization applications in aqueous or biological environments.

AuNRs were mixed with a water-soluble monomer, dimethylacrylamide, and a thermal initiator, azobisisobutyronitrile (AIBN), and irradiated with a fs laser at 800 nm. ESI-MS and SEC analysis confirmed the successful generation of polymers and established that the reaction followed a free radical polymerization (FRP) mechanism. Since previous studies indicated that photochemical reactivity is not always congruent with absorptivity, the monomer to polymer conversion was screened as a function of wavelength from 620 to 950 nm using a monochromatic ns laser. It was found that AuNRs generate sufficient heat to initiate polymerization, even with the longer pulse duration of a ns laser. Critically, a photochemical action plot displayed a blue shift in reactivity relative to the AuNR absorption spectrum – to our best knowledge the first reported blue-shifted action plot. Following the successful demonstration that AuNRs generate heat from incident light on timescales ranging from fs to ns, the next step involved replicating these experiments using Light-Emitting Diodes (LEDs). These experiments establish a more practical application of AuNR NIR driven polymerization approach, opening the possibility of using it for educational purposes, including in high-school experiments.

# Table of Contents

<b>I Zusammenfassung</b> .....	<b>I</b>
<b>II Abstract</b> .....	<b>V</b>
<b>III List of Figures</b> .....	<b>VII</b>
<b>IV List of Schemes</b> .....	<b>XIX</b>
<b>V List of Tables</b> .....	<b>XXII</b>
<b>VI List of Equations</b> .....	<b>XXIV</b>
<b>VII Abbreviations</b> .....	<b>XXVI</b>
<b>1 Motivation</b> .....	<b>1</b>
<b>2 Literature Overview</b> .....	<b>3</b>
<b>3 Theoretical Background</b> .....	<b>8</b>
3.1 Photophysical and –Chemical Processes in Molecules .....	8
3.2 Laser Principle .....	11
3.2.1 Properties of Laser Pulses .....	13
3.2.2 Q-Switch.....	14
3.2.3 Mode-locking.....	15
3.3 Nonlinear Optical Effects .....	16
3.3.1 Nonlinear Processes of Second Order.....	16
3.3.2 Nonlinear Processes of Third Order .....	20
3.4 Transient Absorption Spectroscopy.....	21
3.5 Free Radical Polymerization.....	23
3.5.1 Photoinitiators.....	29
3.5.2 Thermal initiators .....	31
3.5.3 Gold Nanorods.....	32
3.6 Size-Exclusion Chromatography .....	37
3.7 Nuclear Magnetic Resonance Spectroscopy .....	38
3.8 Electrospray Ionization Mass Spectrometry.....	41
3.8.1 C-Trap .....	42

3.8.2	Orbitrap Mass Analyzer .....	42
<b>4</b>	<b>Experimental Methods .....</b>	<b>44</b>
4.1	Materials .....	44
4.2	The fs Laser System .....	44
4.3	Frequency Variation with Optical Chopper .....	45
4.4	One-Photon PLP .....	47
4.5	Two-Photon PLP .....	48
4.6	Proof-of-Principle Polymerization with Gold Nanorods .....	49
4.7	Transient fs Absorption Spectroscopy .....	52
4.8	Tunable ns Laser .....	54
4.9	LED Polymerization .....	56
4.10	Size-Exclusion Chromatography .....	57
4.11	Nuclear Magnetic Resonance Spectrometry .....	58
4.12	Electrospray Ionization-Mass Spectrometry .....	58
<b>5</b>	<b>Visible Light-Induced Polymerization with Ivocerin .....</b>	<b>60</b>
5.1	Stationary UV/Vis/NIR Absorption Spectroscopy .....	60
5.2	Size Exclusion Chromatography .....	63
5.3	Electrospray Ionization-Mass Spectrometry .....	68
5.4	Transient Absorption Spectroscopy .....	73
5.5	Summary .....	77
<b>6</b>	<b>NIR Light-Induced Polymerization with Ivocerin .....</b>	<b>79</b>
6.1	Stationary UV/Vis/NIR Absorption Spectroscopy .....	79
6.2	Size Exclusion Chromatography .....	82
6.3	Polymerization through Tissue .....	87
6.4	Electrospray Ionization-Mass Spectrometry .....	90
6.5	Summary .....	94
<b>7</b>	<b>NIR Light-Induced Polymerization with Gold Nanorods .....</b>	<b>96</b>
7.1	Stationary Absorption Spectroscopy .....	97

7.2	<sup>1</sup> H-NMR Spectroscopy .....	98
7.3	Polymerization through Tissue .....	104
7.4	Size Exclusion Chromatography .....	105
7.5	Electrospray Ionization Mass Spectrometry .....	111
7.6	Action Plot.....	113
7.7	Polymerization with LEDs.....	122
7.8	Summary.....	126
<b>8</b>	<b>Conclusion .....</b>	<b>128</b>
<b>9</b>	<b>Outlook.....</b>	<b>131</b>
<b>10</b>	<b>Appendix .....</b>	<b>136</b>
10.1	Chapter 5 .....	136
10.2	Chapter 6 .....	142
10.3	Chapter 7 .....	143
<b>11</b>	<b>References .....</b>	<b>171</b>
<b>12</b>	<b>List of Publications .....</b>	<b>192</b>

### III List of Figures

- Figure 3.1:** Temperature vs time evolution at various distances from the AuNR boundary after excitation with a 800 nm, 35 fs laser pulse. The black dashed line indicates the temperature for decomposition of AIBN initiator (60 °C), where the initiators half-life is close to 10 h.<sup>172</sup> .....36
- Figure 3.2:** (Top) <sup>1</sup>H-NMR spectrum of pure DMA dissolved in D<sub>2</sub>O without irradiation. The resonances are assigned to the protons of DMA; (bottom) <sup>1</sup>H NMR spectrum of a solution of DMA, AIBN, AuNR and CTA dissolved in D<sub>2</sub>O after irradiation of 30 min. The resonances are assigned to the protons associated with the DMA monomer and the generated polymer after fs laser irradiation of 30 min. ....40
- Figure 5.1:** Absorption spectrum of 12 mmol L<sup>-1</sup> Ivocerin in bulk MMA with a peak absorption of about OD=1 at 408 nm in the range of 300 – 1200 nm. The small peak between 1100 nm and 1200 nm belongs to MMA. The excitation wavelength for 1P absorption experiment (400 nm) is indicated by the vertical dotted blue line....61
- Figure 5.2:** UV/Vis absorption spectra of 12 mmol L<sup>-1</sup> Ivocerin in MMA after 90 s irradiation with various energies at 400 nm (left) and plot showing the corresponding initiator concentration after each irradiation step (right). Adapted with permission from ref. 182. Copyright 2022 American Chemical Society. ....62
- Figure 5.3:** Initiator conversion after 90 s irradiation of a solution with 12 mmol L<sup>-1</sup> Ivocerin in MMA at 400 nm with various laser beam fluences, plotted on a double logarithmic scale. A linear regression was used to determine the gradient, indicating the number of photons contributing to initiator decay. Adapted with permission from ref. 182. Copyright 2022 American Chemical Society. ....63
- Figure 5.4:** SEC trace (black) and first derivative of SEC trace (red dashed) of PMMA generated by 400 nm fs laser pulse triggered Ivocerin fragmentation (*c* = 12 mmol L<sup>-1</sup> in bulk MMA) with a repetition rate of 10 Hz where the inflection points of the distribution are *M*<sub>1</sub> = 24,000 g mol<sup>-1</sup>, *M*<sub>2</sub> = 46,000 g mol<sup>-1</sup> and *M*<sub>3</sub> = 70,000 g mol<sup>-1</sup>. Adapted with permission from ref. 182. Copyright 2022 American Chemical Society.....64
- Figure 5.5:** SEC trace (black) and first derivatives of SEC trace (red dashed) of PMMA generated by 400 nm fs laser pulse triggered Ivocerin fragmentation (*c* = 12 mmol L<sup>-1</sup> in bulk MMA) with a repetition rate of 20 Hz where the inflection points of the distribution are *M*<sub>1</sub> = 13,000 g mol<sup>-1</sup>, *M*<sub>2</sub> = 25,000 g mol<sup>-1</sup> and *M*<sub>3</sub> = 38,000 g mol<sup>-1</sup>. Adapted with permission from ref. 182. Copyright 2022 American Chemical Society.....65
- Figure 5.6:** SEC trace (black) and first derivative of SEC trace of PMMA (red dashed) generated by 400 nm fs laser pulse triggered Ivocerin fragmentation (12 mmol L<sup>-1</sup> in bulk MMA) with a repetition rate of 50 Hz where the inflection points of the distribution are *M*<sub>1</sub> = 6,000 g mol<sup>-1</sup>, *M*<sub>2</sub> = 11,000 g mol<sup>-1</sup> and *M*<sub>3</sub> = 17,000 g mol<sup>-1</sup>.

- Adapted with permission from ref. 182. Copyright 2022 American Chemical Society.....66
- Figure 5.7:** SEC trace (black) and first derivative of SEC trace of PMMA (red dashed) generated by 400 nm fs laser pulse triggered Ivocerin fragmentation (12 mmol L<sup>-1</sup> in bulk MMA) with a repetition rate of 100 Hz where the inflection points of the distribution are  $M_1 = 3,200 \text{ g mol}^{-1}$ ,  $M_2 = 6,300 \text{ g mol}^{-1}$  and  $M_3 = 8,900 \text{ g mol}^{-1}$ . Adapted with permission from ref. 182. Copyright 2022 American Chemical Society.....67
- Figure 5.8:** Comparison of experimental ESI-MS spectrum (zoom into one repeat unit) of PMMA in THF/methanol (3:2) (top) with simulated isotopic pattern (bottom) in the  $m/z$  range of 1010 – 1110. The experimental mass spectrum was obtained from polymer generated after 15 min irradiation of 12 mmol L<sup>-1</sup> Ivocerin in MMA with 400 nm fs pulses with a fluence of 102  $\mu\text{J cm}^{-2}$  and a repetition rate of 100 Hz. 10  $\mu\text{L}$  of the irradiated solution were dissolved in 2 mL of a THF/methanol (3:2) solution with 100  $\mu\text{M}$  NaTFA. ....69
- Figure 5.9:** Assigned polymer species obtained from the an Xcalibur simulation of isotopic pattern corresponding to an experimental polymerization of PMMA after 15 min irradiation of 12 mmol L<sup>-1</sup> Ivocerin in MMA with 400 nm fs pulses with a fluence of 102  $\mu\text{J cm}^{-2}$  and a repetition rate of 100 Hz: **P1-P13** with Ivocerin fragment end groups; **P2, P3** and **P7-P10** are acetyl-based disproportionation products, **P4-P6** and **P11-P12** are germyl-based disproportionation products, **P1** and **P13** are combination products. ....70
- Figure 5.10:** Transient absorption spectra of 12 mmol L<sup>-1</sup> Ivocerin in MMA (OD 1) after excitation with 1  $\mu\text{J}$  fs laser pulses at 400 nm, probed at different delay times in a range of 350-720 nm. Depending on the pump-probe delay, a broadband ESA was observed with local maxima at 650 nm, 470 nm, 450 nm, as well as another ESA below 400 nm and an isosbestic point at 520 nm. The spectral region around 400 nm was greyed out as it was strongly superimposed by pump pulse scattering.73
- Figure 5.11:** Biexponential DADS of the transient spectra shown in Figure 4.9. The DADS provides three wavelength-dependent amplitudes  $A_i$  with associated time constants  $\tau_i$ .....75
- Figure 5.12:** Single transient of Ivocerin in MMA ( $c=12\text{mmol L}^{-1}$ ,  $\text{OD}=1$ ) at the probe wavelength 470 nm after excitation with 400 nm fs pulses with a pulse energy of 1  $\mu\text{J}$ . Data points were fitted with the time constants  $\tau_i$  and amplitudes  $A_i$  obtained from the global analysis. The inset shows a zoom into the first 50 ps of the fitted transient. ....76
- Figure 6.1:** Absorption spectrum of 12 mmol L<sup>-1</sup> Ivocerin in bulk MMA with a peak absorption of about OD=1 at 408 nm recorded in a 1 mm cuvette. The weak peak between

1100 nm and 1200 nm is attributed to MMA. The excitation wavelength employed for the 2PA experiment (800 nm) is indicated by the vertical dotted red line. ....80

**Figure 6.2:** UV/Vis absorption spectra of 12 mmol L<sup>-1</sup> Ivocerin in MMA after 30 min irradiation with various energies at 800 nm (left) and plot showing the corresponding initiator concentration after each irradiation step (right). Adapted with permission from ref. 182. Copyright 2022 American Chemical Society.....81

**Figure 6.3:** Initiator conversion after 30 min irradiation of solution with 12 mmol L<sup>-1</sup> Ivocerin in MMA at 800 nm with various laser beam fluences, plotted on a double logarithmic scale. A linear regression provides the gradient which in turn indicates the number of photons required for initiator decay. Adapted with permission from ref. 182. Copyright 2022 American Chemical Society. ....81

**Figure 6.4:** SEC trace (black) and first derivative of SEC trace (red dashed) of PMMA generated by 800 nm pulsed fs laser triggered Ivocerin fragmentation ( $c = 12 \text{ mmol L}^{-1}$  in bulk MMA) with a repetition rate of 10 Hz where the inflection points of the distribution are  $M_1 = 23,000 \text{ g mol}^{-1}$ ,  $M_2 = 45,000 \text{ g mol}^{-1}$  and  $M_3 = 69,000 \text{ g mol}^{-1}$ . Adapted with permission from ref. 182. Copyright 2022 American Chemical Society.....83

**Figure 6.5:** SEC trace (black) and first derivative of SEC trace of PMMA generated by 800 nm (red dashed) pulsed fs laser triggered Ivocerin fragmentation ( $c = 12 \text{ mmol L}^{-1}$  in bulk MMA) with a repetition rate of 20 Hz, where the inflection points of the distribution are close to  $M_1 = 14,000 \text{ g mol}^{-1}$ ,  $M_2 = 28,000 \text{ g mol}^{-1}$  and  $M_3 = 43,000 \text{ g mol}^{-1}$ . Adapted with permission from ref. 182. Copyright 2022 American Chemical Society.....84

**Figure 6.6:** SEC trace (black) and first derivative of SEC trace (red dashed) PMMA generated by 800 nm pulsed fs laser triggered Ivocerin fragmentation ( $c = 12 \text{ mmol L}^{-1}$  in bulk MMA) with a repetition rate of 50 Hz where the inflection points of the distribution are close to  $M_1 = 6,000 \text{ g mol}^{-1}$ ,  $M_2 = 12,000 \text{ g mol}^{-1}$  and  $M_3 = 19,000 \text{ g mol}^{-1}$ . Adapted with permission from ref. 182. Copyright 2022 American Chemical Society.....85

**Figure 6.7:** SEC trace (black) and first derivative of SEC trace (red dashed) PMMA generated by 800 nm pulsed fs laser triggered Ivocerin fragmentation ( $c = 12 \text{ mmol L}^{-1}$  in bulk MMA) with a repetition rate of 100 Hz where the inflection points of the distribution are close to  $M_1 = 3,000 \text{ g mol}^{-1}$  and  $M_2 = 6,300 \text{ g mol}^{-1}$ . Adapted with permission from ref. 182. Copyright 2022 American Chemical Society. ....86

**Figure 6.8:** SEC trace and first derivative of SEC trace PMMA generated by 800 nm pulsed fs laser triggered Ivocerin fragmentation ( $c = 12 \text{ mmol L}^{-1}$  in bulk MMA) with a repetition rate of 50 Hz after the laser beam penetrated a slice of bacon. Adapted with permission from ref. 182. Copyright 2022 American Chemical Society.....88

- Figure 6.9:** First derivative of SEC trace PMMA generated 800 nm pulsed laser triggered Ivocerin fragmentation ( $c = 12 \text{ mmol L}^{-1}$  in bulk MMA) with a repetition rate of 20 Hz after the laser beam penetrated through a slice of bacon, where the inflection points of the distribution are  $M_1 = 13,000 \text{ g mol}^{-1}$ ,  $M_2 = 24,000 \text{ g mol}^{-1}$  and  $M_3 = 36,000 \text{ g mol}^{-1}$ . .....89
- Figure 6.10:** Comparison of an experimental ESI-MS spectrum (zoom into one repeat unit) of PMMA in THF/methanol (3:2) (top) with a simulated isotopic pattern (bottom) in the  $m/z$  range of 1010 – 1110. The experimental mass spectrum was obtained from polymers generated after 30 min irradiation of 12 mmol L<sup>-1</sup> Ivocerin in MMA with 102 μJ cm<sup>-2</sup> fs laser pulses at 800 nm at a repetition rate of 100 Hz. 10 μL of the irradiated solution was dissolved in 2 mL of a THF/methanol (3:2) solution with 100 μM NaTFA. ....91
- Figure 7.1:** Extinction of the purchased solution of AuNR in water (55x15 nm, bare citrate, OD 1) in the range of 200 – 1400 nm. The stationary absorption spectrum was measured in a 1 cm cuvette. The AuNR solution shows an absorption maximum at 800 nm with an extinction of 1. Adapted with permission from ref. 183. Copyright 2022 Wiley. ....97
- Figure 7.2:** <sup>1</sup>H-NMR spectrum of pure DMA dissolved in D<sub>2</sub>O without irradiation recorded with a 400 MHz NMR spectrometer. The resonances are assigned to the protons of DMA (left); <sup>1</sup>H NMR spectrum of a solution of DMA, AIBN, AuNR and CTA dissolved in D<sub>2</sub>O after irradiation of 30 min (right). The resonances are assigned to the protons associated with the DMA monomer and the generated polymer. 99
- Figure 7.3:** Monomer conversion as a function of reaction time or number of photons; (red) conversion for the highest monomer concentration ( 6.73 mol L<sup>-1</sup> ), (black) conversion for the lowest monomer concentration (0.69 mol L<sup>-1</sup>). The lines are fits to guide the eye. Adapted with permission from ref. 183. Copyright 2022 Wiley. .... 101
- Figure 7.4:** Monomer to polymer conversion after 30 min irradiation of solutions containing 9 mmol L<sup>-1</sup> AIBN, 50 μL AuNR in water, 10<sup>-2</sup> mol L<sup>-1</sup> CTA and monomer concentrations ranging from 0.69 – 6.73 mol L<sup>-1</sup> with 800 nm fs pulses with an intensity of 25 GW cm<sup>-2</sup>; the dashed line serves to guide the eye only. Adapted with permission from ref. 183. Copyright 2022 Wiley..... 102
- Figure 7.5:** Monomer to polymer conversion after 30 min irradiation of solutions containing 6.73 mol L<sup>-1</sup> DMA, 50 μL AuNR, 10<sup>-2</sup> mol L<sup>-1</sup> CTA and varying concentration of AIBN ranging from 0.08 – 9.2 mmol L<sup>-1</sup> with 800 nm fs pulses with an intensity of 25 GW cm<sup>-2</sup>; dashed line serves to guide the eye along the data points. Adapted with permission from ref. 183. Copyright 2022 Wiley..... 103
- Figure 7.6:** Monomer to polymer conversion after 30 min irradiation of solutions containing 9 mmol L<sup>-1</sup> AIBN, 0.69 mol L<sup>-1</sup> DMA, 10<sup>-2</sup> mol L<sup>-1</sup> CTA and a varying AuNR volume

ranging from 150 – 300 $\mu\text{L}$ with 800 nm fs pulses with an intensity of 25 $\text{GW cm}^{-2}$ ; the dashed line serves to guide the eye along the data points. Adapted with permission from ref. 183. Copyright 2022 Wiley. ....	103
<b>Figure 7.7:</b> (left) Extinction measurement of 1 mm thick slice of bacon. The dashed line at 800 nm to highlight the irradiation wavelength. (right) Comparison of monomer to polymer conversion after 30 min irradiation of various monomer concentrations with AIBN and AuNR (black) and identically concentrated samples with a 1 mm thick slice of bacon placed in front of it, also irradiated for 30 min (red). Adapted with permission from ref. 183. Copyright 2022 Wiley. ....	105
<b>Figure 7.8:</b> MWD of PDMA as a function of the monomer concentration: (black) 6.73 mol $\text{L}^{-1}$ DMA, (red) 5.38 mol $\text{L}^{-1}$ , (orange) 4.04 mol $\text{L}^{-1}$ , (green) 2.69 mol $\text{L}^{-1}$ , (blue) 1.34 mol $\text{L}^{-1}$ , (violet) 0.69 mol $\text{L}^{-1}$ . Inset: Number average molecular weight, $M_n$ , after 30 min irradiation of solutions containing 9 mmol $\text{L}^{-1}$ AIBN, 50 $\mu\text{L}$ AuNR, $10^{-2}$ mol $\text{L}^{-1}$ CTA and varying monomer concentration ranging from 0.69 – 6.73 mol $\text{L}^{-1}$ with 800 nm fs pulses with an intensity of 25 $\text{GW cm}^{-2}$ . Adapted with permission from ref. 183. Copyright 2022 Wiley.....	106
<b>Figure 7.9:</b> MWD of poly(DMA) dependent on the variation of the AuNR concentration: (black) 300 $\mu\text{L}$ AuNR, (red) 250 $\mu\text{L}$ AuNR, (orange) 200 $\mu\text{L}$ AuNR, (green) 150 $\mu\text{L}$ AuNR, (blue) 100 $\mu\text{L}$ AuNR. Inset: Number average of molecular weight, $M_n$ , after 30 min irradiation of solutions containing 9 mmol $\text{L}^{-1}$ AIBN, 0.69 mol $\text{L}^{-1}$ DMA, $10^{-2}$ mol $\text{L}^{-1}$ CTA and varying AuNR volume ranging from 100 -300 $\mu\text{L}$ with 800 nm fs pulses with an intensity of 25 $\text{GW cm}^{-2}$ . Adapted with permission from ref. 183. Copyright 2022 Wiley.....	107
<b>Figure 7.10:</b> MWD of poly(DMA) as a function of the AIBN concentration; (black) 9.2 mmol $\text{L}^{-1}$ AIBN, (red) 4 mmol $\text{L}^{-1}$ AIBN, (orange) 1.56 mmol $\text{L}^{-1}$ AIBN, (green) 0.69 mmol $\text{L}^{-1}$ AIBN, (blue) 0.17 mmol $\text{L}^{-1}$ AIBN. Inset: Number average of molecular weight after 30 min irradiation of solutions containing 6.73 mol $\text{L}^{-1}$ DMA, 50 $\mu\text{L}$ AuNR, $10^{-2}$ mol $\text{L}^{-1}$ CTA and varying AIBN concentration ranging from 0.08 – 9.2 mmol $\text{L}^{-1}$ with 800 nm fs pulses with an intensity of 25 $\text{GW cm}^{-2}$ . Adapted with permission from ref. 183. Copyright 2022 Wiley.....	108
<b>Figure 7.11:</b> Comparison of the monomer concentration-dependent number average molecular weight of a solution with DMA (monomer), 50 $\mu\text{L}$ AuNR in water, $10^{-2}$ mol $\text{L}^{-1}$ CTA with 9 mmol $\text{L}^{-1}$ AIBN (blue) and without AIBN (black) after 30 min irradiation with 25 $\text{GW cm}^{-2}$ fs pulses at 800 nm.....	110
<b>Figure 7.12:</b> Zoom into the range of 1100-1210 $m/z$ of ESI-MS spectrum of PDMA in THF/methanol (3:2) after 30 min irradiation of a solution of 4.04 mol $\text{L}^{-1}$ DMA, 9 mmol $\text{L}^{-1}$ AIBN, 100 $\mu\text{L}$ AuNR and $10^{-2}$ mol $\text{L}^{-1}$ CTA with 25 $\text{GW cm}^{-2}$ fs pulses at 800 nm (top) and assigned polymer species <b>P1-P6</b> (bottom). Adapted with permission from ref. 183. Copyright 2022 Wiley.....	111

- Figure 7.13:** Assigned polymer species **P1-P6** obtained from a simulation corresponding to an experimental mass spectrum generated after 30 min irradiation of 4.04 mol L<sup>-1</sup> DMA, 9 mmol L<sup>-1</sup> AIBN, 100 μM AuNR and 10<sup>-2</sup> mol L<sup>-1</sup> CTA with 25 GW cm<sup>-2</sup> laser pulses at 800 nm. 10 μL of the irradiated solution were dissolved in 2 mL of a THF/methanol (3:2) solution with 100 μM NaTFA (left). Adapted with permission from ref. 183. Copyright 2022 Wiley..... 112
- Figure 7.14:** OD of a solution with 4.85 mol L<sup>-1</sup> DMA, 3.53 mol L<sup>-1</sup> isopropanol, 0.01 mol L<sup>-1</sup> AIBN, 75 μL AuNR in water without CTA (black) and with 10 μL (0.38 mol L<sup>-1</sup>) CTA (black dashed), corresponding to the experimental polymerization conditions, as a function of wavelength. Adapted with permission from ref. 285. Copyright 2023 Royal Society of Chemistry..... 115
- Figure 7.15:** Conversion with error bars (blue) of a solution with 4.85 mol L<sup>-1</sup> DMA, 3.53 mol L<sup>-1</sup> isopropanol, 0.01 mol L<sup>-1</sup> AIBN, 75 μL AuNR in water and with 10 μL (0.38 mol L<sup>-1</sup>) CTA, after 15 min irradiation with a ns laser at a constant number of photons (1.61·10<sup>19</sup>) and OD of this solution without CTA (black curve) and with 10 μL (0.38 mol L<sup>-1</sup>) CTA (black dashed curve), corresponding to the experimental polymerization conditions, as a function of wavelength. Adapted with permission from ref. 285. Copyright 2023 Royal Society of Chemistry..... 118
- Figure 7.16:** Absorption spectra of a solution of 4.85 mol L<sup>-1</sup> DMA, 3.53 mol L<sup>-1</sup> isopropanol, 75 μL AuNR in water. From dark to pale: Absorption spectrum of the solution immediately after preparation without irradiation, after 1 min irradiation, after 5 min irradiation, after 10 min irradiation and after 15 min irradiation with 10 ns pulses at 800 nm with 260 μJ. Adapted with permission from ref. 285. Copyright 2023 Royal Society of Chemistry..... 120
- Figure 7.17:** Absorption spectra of a solution of 4.85 mol L<sup>-1</sup> DMA, 3.53 mol L<sup>-1</sup> isopropanol, 0.01 mol L<sup>-1</sup> AIBN, 75 μL AuNR in water and 10 μL (0.38 mol L<sup>-1</sup>) 3-mercaptopropionic acid. From dark to pale: Absorption spectrum without irradiation, absorption spectrum after 1 min irradiation, absorption spectrum after 5 min irradiation, absorption spectrum after 10 min irradiation with 170 fs pulses at 800 nm with 250 μJ. The black dashed arrow indicates the blue shift of the absorption maximum during the increasing longer irradiation times. Adapted with permission from ref. 285. Copyright 2023 Royal Society of Chemistry..... 121
- Figure 7.18:** 3-mercaptopropionic acid (CTA) causes agglomeration of the AuNRs. The brightfield TEM images in the top row show the dispersion to individual AuNRs in the reaction solution without CTA. The AuNRs form agglomerates of random shape and number of NRs upon the addition of CTA (bottom row). Adapted with permission from ref. 285. Copyright 2023 Royal Society of Chemistry..... 122
- Figure 7.19:** <sup>1</sup>H-NMR spectrum of a solution of 2.4 mol L<sup>-1</sup> DMA, 4.94 mol L<sup>-1</sup> isopropanol, 0.01 mol L<sup>-1</sup> AIBN, and 350 μL AuNR in water (bottom row) and without AuNR (top

row) after 10 min irradiation with two 745 nm LEDs; recorded with a 600 MHz NMR spectrometer.....	124
<b>Figure 7.20:</b> $^1\text{H}$ -NMR spectrum of a solution of 2.4 mol L <sup>-1</sup> DMA, 4.94 mol L <sup>-1</sup> isopropanol, 0.01 mol L <sup>-1</sup> AIBN, and 350 $\mu\text{L}$ AuNR in water after 10 min irradiation with two 650 nm LEDs; recorded with a 600 MHz NMR spectrometer.....	125
<b>Figure 7.21:</b> $^1\text{H}$ -NMR spectrum of a solution of 2.4 mol L <sup>-1</sup> DMA, 4.94 mol L <sup>-1</sup> isopropanol, 0.01 mol L <sup>-1</sup> AIBN, and 350 $\mu\text{L}$ AuNR in water after 10 min irradiation with two 590 nm LEDs; recorded with a 600 MHz NMR spectrometer.....	125
<b>Figure 10.1:</b> Experimental mass spectrum of PMMA was obtained from polymer generated after 15 min irradiation of 12 mmol L <sup>-1</sup> Ivocerin in MMA with 102 $\mu\text{J cm}^{-2}$ laser pulses at 400 nm. 10 $\mu\text{L}$ of the irradiated solution were dissolved in 2 mL of a THF/methanol (3:2) solution with 100 $\mu\text{M}$ NaTFA.....	136
<b>Figure 10.2:</b> Oscilloscope showing the output of a photodiode that detects laser pulses with a dark time of 0.1 s between the pulses. This corresponds to a repetition rate of 10 Hz.....	137
<b>Figure 10.3:</b> Oscilloscope showing the output of a photodiode that detects laser pulses with a dark time of 50 ms between the pulses. This corresponds to a repetition rate of 20 Hz.....	138
<b>Figure 10.4:</b> Oscilloscope showing the output of a photodiode that detects laser pulses with a dark time of 20 ms between the pulses. This corresponds to a repetition rate of 50 Hz.....	139
<b>Figure 10.5:</b> Oscilloscope showing the output of a photodiode that detects laser pulses with a dark time of 10 ms between the pulses. This corresponds to a repetition rate of 100 Hz.....	140
<b>Figure 10.6:</b> SEC trace (black) and first derivative of SEC trace of PMMA generated by 400 nm (red dashed) pulsed laser triggered Ivocerin fragmentation ( $c = 12 \text{ mmol L}^{-1}$ in bulk MMA) with a repetition rate of 100 Hz where the inflection points of the distribution are close to $M_1 = 13963 \text{ g mol}^{-1}$ , $M_2 = 28379 \text{ g mol}^{-1}$ and $M_3 = 42756 \text{ g mol}^{-1}$ .....	141
<b>Figure 10.7:</b> Incident power on the z-scan photodiode vs. output voltage generated by the incident 775 nm photons. ....	142
<b>Figure 10.8:</b> Normalized transmission curve of an open aperture z-scan measurement of a $10^{-3} \text{ M}$ Rhodamine in ethanol solution (black data point) with nonlinear fit-function (red).....	143
<b>Figure 10.9:</b> Photo of a cuvette containing precipitated PDMA forming a white solid after 30 min irradiation of a solution of 9 mmol L <sup>-1</sup> AIBN, 2.69 mol L <sup>-1</sup> DMA, and 150 $\mu\text{L}$ of AuNR with 800 nm fs pulses with an intensity of 25 GW cm <sup>-2</sup> .....	143

- Figure 10.10:** Full ESI-MS spectrum of PDMA in THF/methanol (3:2) after 30 min irradiation of a solution of 4.04 mol L<sup>-1</sup> DMA, 9 mmol L<sup>-1</sup> AIBN, 100 μL AuNR and 10<sup>-2</sup> mol L<sup>-1</sup> CTA with 25 GW cm<sup>-2</sup> fs pulses at 800 nm in the range of 1000 – 2000 *m/z*..... 144
- Figure 10.11:** Superimposed <sup>1</sup>H-NMR spectra of solutions with 4.04 mol L<sup>-1</sup> DMA, 9 mmol L<sup>-1</sup> AIBN, 50 μL AuNR and 10<sup>-2</sup> mol L<sup>-1</sup> CTA, dissolved in D<sub>2</sub>O, irradiated with 25 GW cm<sup>-2</sup> at 800 nm for various times: (black) without irradiation – 0 min, (violet) 1 min, (blue) 2 min, (dark green) 3 min, (pale green) 4 min, (yellow) 5 min, (pale orange) 10 min, (orange) 15 min, (red) 30 min, (dark red) 45 min..... 144
- Figure 10.12:** Superimposed <sup>1</sup>H NMR spectra of solutions with 4.04 mmol L<sup>-1</sup> DMA, 9 mmol L<sup>-1</sup> AIBN, 50 μL AuNR and 10<sup>-2</sup> mol L<sup>-1</sup> CTA, dissolved in D<sub>2</sub>O, irradiated with 25 GW cm<sup>-2</sup> at 800 nm for various times, zoomed into the regions of resonance associated with the polymer between 1 – 2 ppm: (black) without irradiation – 0 min, (violet) 1 min, (blue) 2 min, (dark green) 3 min, (pale green) 4 min, (yellow) 5 min, (pale orange) 10 min, (orange) 15 min, (red) 30 min, (dark red) 45 min. .... 145
- Figure 10.13:** Superimposed <sup>1</sup>H-NMR spectra of solutions with 50 μL AuNR, 9 mmol L<sup>-1</sup> AIBN, 10<sup>-2</sup> mol L<sup>-1</sup> CTA and various monomer concentrations, irradiated with 25 GW cm<sup>-2</sup> at 800 nm for 30 min, dissolved in D<sub>2</sub>O: (black) 6.73 mol L<sup>-1</sup> DMA, (blue) 5.38 mol L<sup>-1</sup> DMA, (green) 4.04 mol L<sup>-1</sup> DMA, (yellow) 2.69 mol L<sup>-1</sup> DMA, (red) 1.34 mol L<sup>-1</sup> DMA. .... 145
- Figure 10.14:** Superimposed <sup>1</sup>H-NMR spectra of solutions with 50 μL AuNR, 9 mmol L<sup>-1</sup> AIBN, 10<sup>-2</sup> mol L<sup>-1</sup> CTA and various monomer concentrations, irradiated with 25 GW cm<sup>-2</sup> at 800 nm for 30 min, dissolved in D<sub>2</sub>O, zoomed into polymer peak between 1 – 2 ppm: (black) 6.73 mol L<sup>-1</sup> DMA, (blue) 5.38 mol L<sup>-1</sup> DMA, (green) 4.04 mol L<sup>-1</sup> DMA, (yellow) 2.69 mol L<sup>-1</sup> DMA, (red) 1.34 mol L<sup>-1</sup> DMA. .... 146
- Figure 10.15:** Superimposed <sup>1</sup>H-NMR spectra of solutions with 50 μL AuNR, 6.73 mol L<sup>-1</sup> DMA, 10<sup>-2</sup> mol L<sup>-1</sup> CTA and various AIBN concentrations, irradiated with 25 GW cm<sup>-2</sup> at 800 nm for 30 min, dissolved in D<sub>2</sub>O: (black) 0.08 mol L<sup>-1</sup> AIBN, (violet) 0.17 mol L<sup>-1</sup> AIBN, (blue) 0.35 mol L<sup>-1</sup> AIBN, (dark green) 0.69 mol L<sup>-1</sup> AIBN, (yellow) 1.56 mol L<sup>-1</sup> AIBN, (orange) 4 mol L<sup>-1</sup> AIBN, (red) 9.2 mol L<sup>-1</sup> AIBN. .... 146
- Figure 10.16:** Superimposed <sup>1</sup>H-NMR spectra of solutions with 50 μL AuNR, 6.73 mol L<sup>-1</sup> DMA, 10<sup>-2</sup> mol L<sup>-1</sup> CTA and various AIBN concentrations, irradiated with 25 GW cm<sup>-2</sup> at 800 nm for 30 min dissolved in D<sub>2</sub>O, zoomed into polymer peak between 1 – 2 ppm: (black) 0.08 mol L<sup>-1</sup> AIBN, (violet) 0.17 mol L<sup>-1</sup> AIBN, (blue) 0.35 mol L<sup>-1</sup> AIBN, (dark green) 0.69 mol L<sup>-1</sup> AIBN, (yellow) 1.56 mol L<sup>-1</sup> AIBN, (orange) 4 mol L<sup>-1</sup> AIBN, (red) 9.2 mol L<sup>-1</sup> AIBN. .... 147

- Figure 10.17:** Superimposed  $^1\text{H-NMR}$  spectra of solutions with  $0.69 \text{ mol L}^{-1}$  DMA,  $9 \text{ mmol L}^{-1}$  AIBN  $10^{-2} \text{ mol L}^{-1}$  CTA and various AuNR concentrations, irradiated with  $25 \text{ GW cm}^{-2}$  at  $800 \text{ nm}$  for  $30 \text{ min}$ , dissolved in  $\text{D}_2\text{O}$ : (black)  $300 \text{ }\mu\text{L}$  AuNR, (blue)  $250 \text{ }\mu\text{L}$  AuNR, (yellow)  $200 \text{ }\mu\text{L}$  AuNR, (red)  $150 \text{ }\mu\text{L}$  AuNR. .... 147
- Figure 10.18:** Superimposed  $^1\text{H-NMR}$  spectra of solutions with  $0.69 \text{ mol L}^{-1}$  DMA,  $9 \text{ mmol L}^{-1}$  AIBN  $10^{-2} \text{ mol L}^{-1}$  CTA and various AuNR concentrations, irradiated with  $25 \text{ GW cm}^{-2}$  at  $800 \text{ nm}$  for  $30 \text{ min}$ , dissolved in  $\text{D}_2\text{O}$ , zoomed into polymer peak between  $1 - 2 \text{ ppm}$ : (black)  $300 \text{ }\mu\text{L}$  AuNR, (blue)  $250 \text{ }\mu\text{L}$  AuNR, (yellow)  $200 \text{ }\mu\text{L}$  AuNR, (red)  $150 \text{ }\mu\text{L}$  AuNR. .... 148
- Figure 10.19:** : Stacked  $^1\text{H-NMR}$  spectra of solution with  $4.85 \text{ mol L}^{-1}$  DMA,  $0.01 \text{ mol L}^{-1}$  AIBN,  $3.53 \text{ mol L}^{-1}$  isopropanol,  $75 \text{ }\mu\text{L}$  AuNR and  $10 \text{ }\mu\text{L}$  ( $0.38 \text{ mol L}^{-1}$ ) CTA, irradiated with  $10 \text{ ns}$  pulses for  $15 \text{ min}$ , with (from dark to pale):  $335 \text{ }\mu\text{J}$  at  $620 \text{ nm}$ ,  $325 \text{ }\mu\text{J}$  at  $640 \text{ nm}$ ,  $315 \text{ }\mu\text{J}$  at  $660 \text{ nm}$ ,  $306 \text{ }\mu\text{J}$  at  $680 \text{ nm}$ ,  $297 \text{ }\mu\text{J}$  at  $700 \text{ nm}$ ,  $289 \text{ }\mu\text{J}$  at  $720 \text{ nm}$ ,  $281 \text{ }\mu\text{J}$  at  $740 \text{ nm}$ ,  $274 \text{ }\mu\text{J}$  at  $760 \text{ nm}$ ,  $267 \text{ }\mu\text{J}$  at  $780 \text{ nm}$ ,  $260 \text{ }\mu\text{J}$  at  $800 \text{ nm}$ ,  $254 \text{ }\mu\text{J}$  at  $820 \text{ nm}$  and  $248 \text{ }\mu\text{J}$  at  $840 \text{ nm}$ . .... 148
- Figure 10.20:** Stacked  $^1\text{H-NMR}$  spectra of solution with  $4.85 \text{ mol L}^{-1}$  DMA,  $0.01 \text{ mol L}^{-1}$  AIBN,  $3.53 \text{ mol L}^{-1}$  isopropanol,  $75 \text{ }\mu\text{L}$  AuNR and  $10 \text{ }\mu\text{L}$  ( $0.38 \text{ mol L}^{-1}$ ) CTA, irradiated with  $10 \text{ ns}$  pulses for  $15 \text{ min}$ , with (from dark to pale):  $335 \text{ }\mu\text{J}$  at  $620 \text{ nm}$ ,  $325 \text{ }\mu\text{J}$  at  $640 \text{ nm}$ ,  $315 \text{ }\mu\text{J}$  at  $660 \text{ nm}$ ,  $306 \text{ }\mu\text{J}$  at  $680 \text{ nm}$ ,  $297 \text{ }\mu\text{J}$  at  $700 \text{ nm}$ ,  $289 \text{ }\mu\text{J}$  at  $720 \text{ nm}$ ,  $281 \text{ }\mu\text{J}$  at  $740 \text{ nm}$ ,  $274 \text{ }\mu\text{J}$  at  $760 \text{ nm}$ ,  $267 \text{ }\mu\text{J}$  at  $780 \text{ nm}$ ,  $260 \text{ }\mu\text{J}$  at  $800 \text{ nm}$ ,  $254 \text{ }\mu\text{J}$  at  $820 \text{ nm}$  and  $248 \text{ }\mu\text{J}$  at  $840 \text{ nm}$ . Zoom into region  $0\text{-}3.5 \text{ ppm}$ . .... 149
- Figure 10.21:**  $^1\text{H-NMR}$  spectra of solutions with  $4.85 \text{ mol L}^{-1}$  DMA,  $0.01 \text{ mol L}^{-1}$  AIBN,  $3.53 \text{ mol L}^{-1}$  isopropanol,  $75 \text{ }\mu\text{L}$  AuNR and  $10 \text{ }\mu\text{L}$  CTA, dissolved in  $\text{D}_2\text{O}$ , irradiated with  $620 \text{ nm}$  ns laser pulses with  $0.87 \text{ J cm}^{-2}$  at a repetition rate of  $20 \text{ Hz}$  for  $15 \text{ min}$ . .... 149
- Figure 10.22:**  $^1\text{H-NMR}$  spectra of solutions with  $4.85 \text{ mol L}^{-1}$  DMA,  $0.01 \text{ mol L}^{-1}$  AIBN,  $3.53 \text{ mol L}^{-1}$  isopropanol,  $75 \text{ }\mu\text{L}$  AuNR and  $10 \text{ }\mu\text{L}$  CTA, dissolved in  $\text{D}_2\text{O}$ , irradiated with  $640 \text{ nm}$  ns laser pulses with  $0.84 \text{ J cm}^{-2}$  at a repetition rate of  $20 \text{ Hz}$  for  $15 \text{ min}$ . .... 150
- Figure 10.23:**  $^1\text{H-NMR}$  spectra of solutions with  $4.85 \text{ mol L}^{-1}$  DMA,  $0.01 \text{ mol L}^{-1}$  AIBN,  $3.53 \text{ mol L}^{-1}$  isopropanol,  $75 \text{ }\mu\text{L}$  AuNR and  $10 \text{ }\mu\text{L}$  CTA, dissolved in  $\text{D}_2\text{O}$ , irradiated with  $640 \text{ nm}$  ns pulses with  $0.84 \text{ J cm}^{-2}$  at a repetition rate of  $20 \text{ Hz}$  for  $15 \text{ min}$ . .... 150
- Figure 10.24:**  $^1\text{H-NMR}$  spectra of solutions with  $4.85 \text{ mol L}^{-1}$  DMA,  $0.01 \text{ mol L}^{-1}$  AIBN,  $3.53 \text{ mol L}^{-1}$  isopropanol,  $75 \text{ }\mu\text{L}$  AuNR and  $10 \text{ }\mu\text{L}$  CTA, dissolved in  $\text{D}_2\text{O}$ , irradiated with  $660 \text{ nm}$  ns pulses with  $0.81 \text{ J cm}^{-2}$  at a repetition rate of  $20 \text{ Hz}$  for  $15 \text{ min}$ . .... 151
- Figure 10.25:**  $^1\text{H-NMR}$  spectra of solutions with  $4.85 \text{ mol L}^{-1}$  DMA,  $0.01 \text{ mol L}^{-1}$  AIBN,  $3.53 \text{ mol L}^{-1}$  isopropanol,  $75 \text{ }\mu\text{L}$  AuNR and  $10 \text{ }\mu\text{L}$  CTA, dissolved in  $\text{D}_2\text{O}$ , irradiated with  $660 \text{ nm}$  ns pulses with  $0.81 \text{ J cm}^{-2}$  at a repetition rate of  $20 \text{ Hz}$  for  $15 \text{ min}$ . .... 151



- Figure 10.39:**  $^1\text{H-NMR}$  spectra of solutions with 4.85 mol L $^{-1}$  DMA, 0.01 mol L $^{-1}$  AIBN, 3.53 mol L $^{-1}$  isopropanol, 75  $\mu\text{L}$  AuNR and 10  $\mu\text{L}$  CTA, dissolved in D $_2\text{O}$ , irradiated with 780 nm ns pulses with 0.69 J cm $^{-2}$  at a repetition rate of 20 Hz for 15 min. .... 158
- Figure 10.40:**  $^1\text{H-NMR}$  spectra of solutions with 4.85 mol L $^{-1}$  DMA, 0.01 mol L $^{-1}$  AIBN, 3.53 mol L $^{-1}$  isopropanol, 75  $\mu\text{L}$  AuNR and 10  $\mu\text{L}$  CTA, dissolved in D $_2\text{O}$ , irradiated with 780 nm ns pulses with 0.69 J cm $^{-2}$  at a repetition rate of 20 Hz for 15 min. .... 159
- Figure 10.41:**  $^1\text{H-NMR}$  spectra of solutions with 4.85 mol L $^{-1}$  DMA, 0.01 mol L $^{-1}$  AIBN, 3.53 mol L $^{-1}$  isopropanol, 75  $\mu\text{L}$  AuNR and 10  $\mu\text{L}$  CTA, dissolved in D $_2\text{O}$ , irradiated with 780 nm ns pulses with 0.69 J cm $^{-2}$  at a repetition rate of 20 Hz for 15 min. .... 159
- Figure 10.42:**  $^1\text{H-NMR}$  spectra of solutions with 4.85 mol L $^{-1}$  DMA, 0.01 mol L $^{-1}$  AIBN, 3.53 mol L $^{-1}$  isopropanol, 75  $\mu\text{L}$  AuNR and 10  $\mu\text{L}$  CTA, dissolved in D $_2\text{O}$ , irradiated with 800 nm ns pulses with 0.67 J cm $^{-2}$  at a repetition rate of 20 Hz for 15 min. .... 160
- Figure 10.43:**  $^1\text{H-NMR}$  spectra of solutions with 4.85 mol L $^{-1}$  DMA, 0.01 mol L $^{-1}$  AIBN, 3.53 mol L $^{-1}$  isopropanol, 75  $\mu\text{L}$  AuNR and 10  $\mu\text{L}$  CTA, dissolved in D $_2\text{O}$ , irradiated with 800 nm ns pulses with 0.67 J cm $^{-2}$  at a repetition rate of 20 Hz for 15 min. .... 160
- Figure 10.44:**  $^1\text{H-NMR}$  spectra of solutions with 4.85 mol L $^{-1}$  DMA, 0.01 mol L $^{-1}$  AIBN, 3.53 mol L $^{-1}$  isopropanol, 75  $\mu\text{L}$  AuNR and 10  $\mu\text{L}$  CTA, dissolved in D $_2\text{O}$ , irradiated with 800 nm ns pulses with 0.67 J cm $^{-2}$  at a repetition rate of 20 Hz for 15 min. .... 161
- Figure 10.45:**  $^1\text{H-NMR}$  spectra of solutions with 4.85 mol L $^{-1}$  DMA, 0.01 mol L $^{-1}$  AIBN, 3.53 mol L $^{-1}$  isopropanol, 75  $\mu\text{L}$  AuNR and 10  $\mu\text{L}$  CTA, dissolved in D $_2\text{O}$ , irradiated with 820 nm ns pulses with 0.65 J cm $^{-2}$  at a repetition rate of 20 Hz for 15 min. .... 161
- Figure 10.46:**  $^1\text{H-NMR}$  spectra of solutions with 4.85 mol L $^{-1}$  DMA, 0.01 mol L $^{-1}$  AIBN, 3.53 mol L $^{-1}$  isopropanol, 75  $\mu\text{L}$  AuNR and 10  $\mu\text{L}$  CTA, dissolved in D $_2\text{O}$ , irradiated with 820 nm ns pulses with 0.65 J cm $^{-2}$  at a repetition rate of 20 Hz for 15 min. .... 162
- Figure 10.47:**  $^1\text{H-NMR}$  spectra of solutions with 4.85 mol L $^{-1}$  DMA, 0.01 mol L $^{-1}$  AIBN, 3.53 mol L $^{-1}$  isopropanol, 75  $\mu\text{L}$  AuNR and 10  $\mu\text{L}$  CTA, dissolved in D $_2\text{O}$ , irradiated with 820 nm ns pulses with 0.65 J cm $^{-2}$  at repetition rate of 20 Hz for 15 min. .... 162
- Figure 10.48:**  $^1\text{H-NMR}$  spectra of solutions with 4.85 mol L $^{-1}$  DMA, 0.01 mol L $^{-1}$  AIBN, 3.53 mol L $^{-1}$  isopropanol, 75  $\mu\text{L}$  AuNR and 10  $\mu\text{L}$  CTA, dissolved in D $_2\text{O}$ , irradiated with 840 nm ns pulses with 0.63 J cm $^{-2}$  at a repetition rate of 20 Hz for 15 min. .... 163
- Figure 10.49:**  $^1\text{H-NMR}$  spectra of solutions with 4.85 mol L $^{-1}$  DMA, 0.01 mol L $^{-1}$  AIBN, 3.53 mol L $^{-1}$  isopropanol, 75  $\mu\text{L}$  AuNR and 10  $\mu\text{L}$  CTA, dissolved in D $_2\text{O}$ , irradiated with 840 nm ns pulses with 0.63 J cm $^{-2}$  at a repetition rate of 20 Hz for 15 min. .... 163
- Figure 10.50:**  $^1\text{H-NMR}$  spectra of solutions with 4.85 mol L $^{-1}$  DMA, 0.01 mol L $^{-1}$  AIBN, 3.53 mol L $^{-1}$  isopropanol, 75  $\mu\text{L}$  AuNR and 10  $\mu\text{L}$  CTA, dissolved in D $_2\text{O}$ , irradiated with 840 nm ns pulses with 0.63 J cm $^{-2}$  at a repetition rate of 20 Hz for 15 min. .... 164
- Figure 10.51:** Stacked SEC traces of PDMA and DMA after 15 min irradiation of a solution with 4.85 mol L $^{-1}$  DMA, 3.53 mol L $^{-1}$  isopropanol, 0.01 mol L $^{-1}$  AIBN, 75  $\mu\text{L}$  AuNR solution and 10  $\mu\text{L}$  3-mercaptopropionic acid with a 10 ns laser with (from dark

to pale) 335 $\mu\text{J}$ at 620 nm, 325 $\mu\text{J}$ at 640 nm, 315 $\mu\text{J}$ at 660 nm, 306 $\mu\text{J}$ at 680 nm, 297 $\mu\text{J}$ at 700 nm, 289 $\mu\text{J}$ at 720 nm, 281 $\mu\text{J}$ at 740 nm, 274 $\mu\text{J}$ at 760 nm, 267 $\mu\text{J}$ at 780 nm, 260 $\mu\text{J}$ at 800 nm, 254 $\mu\text{J}$ at 820 nm and 248 $\mu\text{J}$ at 840 nm. ....	164
<b>Figure 10.52:</b> SEC trace of PDMA and DMA after 15 min irradiation of a solution with 4.85 mol L <sup>-1</sup> DMA, 3.53 mol L <sup>-1</sup> isopropanol, 0.01 mol L <sup>-1</sup> AIBN, 75 $\mu\text{L}$ AuNR solution and 10 $\mu\text{L}$ 3-mercaptopropionic acid with a ns laser at 620 nm. ....	165
<b>Figure 10.53:</b> SEC trace of PDMA and DMA after 15 min irradiation of a solution with 4.85 mol L <sup>-1</sup> DMA, 3.53 mol L <sup>-1</sup> isopropanol, 0.01 mol L <sup>-1</sup> AIBN, 75 $\mu\text{L}$ AuNR solution and 10 $\mu\text{L}$ 3-mercaptopropionic acid with a ns laser at 640 nm. ....	165
<b>Figure 10.54:</b> SEC trace of PDMA and DMA after 15 min irradiation of a solution with 4.85 mol L <sup>-1</sup> DMA, 3.53 mol L <sup>-1</sup> isopropanol, 0.01 mol L <sup>-1</sup> AIBN, 75 $\mu\text{L}$ AuNR solution and 10 $\mu\text{L}$ 3-mercaptopropionic acid with a ns laser at 660 nm. ....	166
<b>Figure 10.55:</b> SEC trace of PDMA and DMA after 15 min irradiation of a solution with 4.85 mol L <sup>-1</sup> DMA, 3.53 mol L <sup>-1</sup> isopropanol, 0.01 mol L <sup>-1</sup> AIBN, 75 $\mu\text{L}$ AuNR solution and 10 $\mu\text{L}$ 3-mercaptopropionic acid with a ns laser at 680 nm. ....	166
<b>Figure 10.56:</b> SEC trace of PDMA and DMA after 15 min irradiation of a solution with 4.85 mol L <sup>-1</sup> DMA, 3.53 mol L <sup>-1</sup> isopropanol, 0.01 mol L <sup>-1</sup> AIBN, 75 $\mu\text{L}$ AuNR solution and 10 $\mu\text{L}$ 3-mercaptopropionic acid with a ns laser at 700 nm. ....	167
<b>Figure 10.57:</b> SEC trace of PDMA and DMA after 15 min irradiation of a solution with 4.85 mol L <sup>-1</sup> DMA, 3.53 mol L <sup>-1</sup> isopropanol, 0.01 mol L <sup>-1</sup> AIBN, 75 $\mu\text{L}$ AuNR solution and 10 $\mu\text{L}$ 3-mercaptopropionic acid with a ns laser at 720 nm. ....	167
<b>Figure 10.58:</b> SEC trace of PDMA and DMA after 15 min irradiation of a solution with 4.85 mol L <sup>-1</sup> DMA, 3.53 mol L <sup>-1</sup> isopropanol, 0.01 mol L <sup>-1</sup> AIBN, 75 $\mu\text{L}$ AuNR solution and 10 $\mu\text{L}$ 3-mercaptopropionic acid with a ns laser at 740 nm. ....	168
<b>Figure 10.59:</b> SEC trace of PDMA and DMA after 15 min irradiation of a solution with 4.85 mol L <sup>-1</sup> DMA, 3.53 mol L <sup>-1</sup> isopropanol, 0.01 mol L <sup>-1</sup> AIBN, 75 $\mu\text{L}$ AuNR solution and 10 $\mu\text{L}$ 3-mercaptopropionic acid with a ns laser at 760 nm. ....	168
<b>Figure 10.60;</b> SEC trace of PDMA and DMA after 15 min irradiation of a solution with 4.85 mol L <sup>-1</sup> DMA, 3.53 mol L <sup>-1</sup> isopropanol, 0.01 mol L <sup>-1</sup> AIBN, 75 $\mu\text{L}$ AuNR solution and 10 $\mu\text{L}$ 3-mercaptopropionic acid with a ns laser at 780 nm. ....	169
<b>Figure 10.61:</b> SEC trace of PDMA and DMA after 15 min irradiation of a solution with 4.85 mol L <sup>-1</sup> DMA, 3.53 mol L <sup>-1</sup> isopropanol, 0.01 mol L <sup>-1</sup> AIBN, 75 $\mu\text{L}$ AuNR solution and 10 $\mu\text{L}$ 3-mercaptopropionic acid with a ns laser at 800 nm. ....	169
<b>Figure 10.62:</b> SEC trace of PDMA and DMA after 15 min irradiation of a solution with 4.85 mol L <sup>-1</sup> DMA, 3.53 mol L <sup>-1</sup> isopropanol, 0.01 mol L <sup>-1</sup> AIBN, 75 $\mu\text{L}$ AuNR solution and 10 $\mu\text{L}$ 3-mercaptopropionic acid with a ns laser at 820 nm. ....	170
<b>Figure 10.63:</b> SEC trace of PDMA and DMA after 15 min irradiation of a solution with 4.85 mol L <sup>-1</sup> DMA, 3.53 mol L <sup>-1</sup> isopropanol, 0.01 mol L <sup>-1</sup> AIBN, 75 $\mu\text{L}$ AuNR solution and 10 $\mu\text{L}$ 3-mercaptopropionic acid with a ns laser at 840 nm. ....	170

## IV List of Schemes

- Scheme 3.1:** Scheme of possible photophysical and photochemical processes after photoexcitation, shown as Jablonski diagram. Absorption into excited electronic states (orange) can result in either non-radiative relaxation processes, such as vibrational relaxation (VR), intramolecular vibrational redistribution (IVR), internal conversion (IC) and intersystem crossing (ISC) or radiative processes, fluorescence (green) and phosphorescence (red). Additionally, chemical reaction or charge transfer (CT) can occur from the excited states. The thick horizontal lines depict electronic states, e.g. the ground state  $S_0$  first excited singlet  $S_1$  and triplet  $T_1$  states, as well as higher excited singlet  $S_n$  and triplet  $T_n$  states. The thin lines represent vibrational levels of the electronic states. ....10
- Scheme 3.2:** Schematic illustration of a three-level laser system. Electrons are excited into the pump-level (2) and subsequently relax into laser level (1). The population of level 1 leads to population inversion. Radiation is amplified by stimulated emission from the laser level to the lower laser level (ground state). ....13
- Scheme 3.3:** Scheme of sum frequency generation in a nonlinear crystal of second order with two incident frequencies  $\omega_1$  and  $\omega_2$  and the additional output frequency  $\omega_3$  (left). Scheme of an energy diagram showing the summation of the energy of both frequencies  $\omega_1$  and  $\omega_2$  equal to the energy of the output frequency  $\omega_3$  (right). 17
- Scheme 3.4:** Scheme of SHG in a nonlinear crystal of second order with incident photons of identical frequency  $\omega$  and the additional frequency-doubled output  $2\omega$  (left). Scheme of an energy diagram showing the summation of the energy of two photons with frequencies  $\omega$  equal to the energy of one photon with the output frequency  $2\omega$  (right).....18
- Scheme 3.5:** Scheme of difference frequency generation in a nonlinear crystal of second order with incident photons of the frequencies  $\omega_1$  and  $\omega_2$  and the generated photons with the output frequency  $\omega_3$  as difference of  $\omega_1$  and  $\omega_2$  enhancing the field of  $\omega_2$  (left). Scheme of an energy diagram showing the difference of the energy of two photons with frequencies  $\omega_1$  and  $\omega_2$  into a third photon with the output frequency  $\omega_3$  (right).....18
- Scheme 3.6:** Scheme showing the principle of difference frequency generation in an optical parametric oscillator (OPO). Photons of the incident frequencies  $\omega_1$  and  $\omega_2$  oscillate in a resonator with a nonlinear crystal of second order, generating photons of  $\omega_2$  and a third frequency  $\omega_3$ , thus enhancing the optical field of  $\omega_2$ . Due to the oscillation this process repeats and further enhances  $\omega_2$  and  $\omega_3$ . ....19
- Scheme 3.7:** Principle of two photon absorption; two photons of the frequency  $\omega$  are simultaneously absorbed via a virtual state, thus exciting electrons into an excited electronic state, as an excitation with photons of  $2\omega$ .....20

<b>Scheme 3.8:</b> Possible contributions to the spectrum $\Delta A$ of the transient response after photo excitation, presented in a simplified Jablonski diagram. The electronic ground state $S_0$ and excited electronic states $S_n$ are shown as thick lines, vibrational states as thin lines, transitions are implicated as vertical arrows. The possible photophysical processes are ESA with $\Delta A > 0$ , stimulated emission (SE) with $\Delta A < 0$ , ground state bleaching (GSB) with $\Delta A < 0$ (from left to right).....	22
<b>Scheme 3.9:</b> Mechanism of FRP. After thermally or photochemically induced fragmentation of the initiator molecule $I$ into free radicals $R$ ., chain growth $P_1$ . is initiated by the reaction of radicals with a monomer unit $M$ (chain initiation). The chains grow $P_i + 1$ . (chain propagation) until terminated (chain termination) by either disproportionation $P_i + P_j$ or combination $P_i + j$ of polymer chains. When an additional chain transfer agent $S$ is present, the radical character can also be transferred from one chain to another $R_1$ ., leading to termination of the initial chain $P_i$ .....	24
<b>Scheme 3.10:</b> Scheme of chain transfer and chain termination via chain combination and disproportionation. ....	27
<b>Scheme 3.11:</b> Scheme of three-step termination of polymer chains with the center-of-mass diffusion as the first, the segmental diffusion as the second and the chemical reaction as the third step. ....	28
<b>Scheme 3.12:</b> Principle of photo-induced radical generation of photoinitiators.....	29
<b>Scheme 3.13:</b> Simplified Jablonski diagram of photochemically induced initiator decomposition, showing the quantum yield $\phi$ of each step of primary free radical production and the possible competitive channels. After photoexcitation from $S_0$ into $S_1$ , the initiator can change its multiplicity from singlet ( $S_1$ ) into triplet ( $T_1$ ) via ISC. From here, the initiator can either form a radical $R$ or be deactivated, for example by quenching processes. A step prior to polymer chain growth, radicals need to initially react with a monomer unit to induce polymerization. Alternatively, deactivation processes can stop the reaction. ....	30
<b>Scheme 3.14:</b> Schematic representation of the structure of azo- and peroxy compound usable as thermal initiators.....	31
<b>Scheme 3.15:</b> The timescale of the fundamental processes of $47 \times 14 \text{ nm}^2$ gold nanoparticles after heating with fs laser pulses with $0.47 \text{ mJ cm}^{-2}$ , as a result of a heating simulation Ben-Yakar and colleagues. <sup>39</sup> Reproduced with permission from [39]. ....	34
<b>Scheme 3.16:</b> Scheme of SEC column with porous material (grey) and polymers of different hydrodynamic size, large polymers in black, middle-sized polymers in red and small polymers in blue, elute through the column. ....	38
<b>Scheme 3.17:</b> Principle of charged molecule generation in the vacuum chamber of an electrospray ionization apparatus. ....	41

- Scheme 4.1:** Scheme of the setup of the optical chopper to vary the repetition rate for the fs PLP experiments: The chopper (white) control is either directly triggered by the repetition rate of the laser via the DG535 or by the frequency halver (grey), which is connected to various output channels of the DG535. Setting multiple options, the chopper control triggers the optical chopper, achieving several possible repetition rate using the inner or outer slits as input reference.....46
- Scheme 4.2:** Simplified scheme of the setup for PLP experiments; the laser beam is redirected from the tabletop to the upside via a 45° mirror and penetrates the sample, which is placed in a sample holder, from below. The beam energy can be recorded using a detector.....47
- Scheme 4.3:** Setup of the SHG and THG generation. SHG (blue) from the laser fundamental wavelength (red) takes place in a BBO crystal. The generation of the THG (pale blue) takes place in a second BBO by overlapping the fundamental wavelength and the second harmonic. To do so, the fundamental part is turned in its polarisation by 90° to achieve a type-1 process in the nonlinear crystal. A dielectric mirror separates the fundamental and the second harmonic. ....48
- Scheme 4.4:** Scheme of the experimental setup of a transient spectrometer. The generated pulses are split into an excitation and a probe pulse. The excitation pulse can be tuned to a range of various wavelengths via nonlinear optics, such as SHG, THG or NOPA. Every second excitation pulse is blocked by an optical chopper and subsequently turned in its polarization by a  $\lambda/2$  plate to achieve the magic angle relative to the probe pulse. The probe pulses are aligned along a computer-controlled stage to generate a temporal delay relative to the pump pulses. Both the excitation and the probe pulses are overlapped in the sample in space and time. A white-light continuum generated in a CaF<sub>2</sub> crystal and focused via a focusing lens (FL) is used for broadband probing. After passing the sample, this WL is separated in its single spectral parts by a prism to be detected by a CCD camera. ....54
- Scheme 5.1:** Proposed decomposition pathway of Ivocerin after photoexcitation. In a first step, Ivocerin cleaves into an acylgermyl and an acyl radical. In a potential second step, the acylgermyl radical further cleaves into an acyl radical and a germyl biradical. ....72
- Scheme 6.1:** Schematic picture of the through tissue irradiation set-up; the incident 800 nm laser beam (1) (40 fs, 1 kHz, 25 GW cm<sup>-2</sup>) propagates through a 1 mm thick slice of bacon (2), which decreases the laser intensity to 10 GW cm<sup>-2</sup>. Subsequently the laser beam penetrates a 1 mm cuvette (3). The bacon closely adhered to the sample holder. The distance between the bacon and the cuvette in the picture only portrays the weaker laser beam after tissue penetration. ....87

## V List of Tables

<b>Table 4.1:</b> Overview of sample preparation for the monomer variation experiment. ....	51
<b>Table 4.2:</b> Overview of sample preparation for the AuNR variation experiment.....	51
<b>Table 4.3:</b> Overview of sample preparation for the AIBN variation experiment.....	52
<b>Table 5.1:</b> Overview of molecular weight of the polymer chains $M_i$ at the inflection points in the first derivative of the SEC trace generated by 400 nm fs laser pulse triggered Ivocerin fragmentation ( $c = 12 \text{ mmol L}^{-1}$ in bulk MMA) with various repetition rates. ....	67
<b>Table 5.2:</b> Overview of the propagation rate coefficients ( <b>Eq. 3.33</b> ) of MMA calculated for polymer chains with the assigned molecular weight $M_i$ generated by 400 nm fs laser pulse triggered Ivocerin fragmentation ( $c = 12 \text{ mmol L}^{-1}$ in bulk MMA) with a repetition rate of 50 Hz and compared to the IUPAC literature <sup>275</sup> propagation rate coefficient of MMA ( $267 \text{ L mol}^{-1} \text{ s}^{-1}$ ). ....	68
<b>Table 5.3:</b> Overview of the exact mass, resolution and relative abundance $X$ of the assigned species in the recorded and simulated spectrum of the PMMA after PLP of MMA with Ivocerin triggered by 400 nm fs pulses with a fluence $102 \mu\text{J cm}^{-2}$ and a repetition rate of 100 Hz. ....	71
<b>Table 6.1:</b> Overview of molecular weight of the polymer chains $M_i$ at the inflection points in the first derivative of the SEC trace generated by 800 nm pulsed fs laser triggered Ivocerin fragmentation ( $c = 12 \text{ mmol L}^{-1}$ in bulk MMA) with various repetition rates. ....	86
<b>Table 6.2:</b> Overview of the propagation rate coefficients ( <b>Eq. 3.33</b> ) of MMA calculated for polymer chains with the assigned molecular weight $M_i$ generated by 800 nm pulsed fs laser triggered Ivocerin fragmentation ( $c = 12 \text{ mmol L}^{-1}$ in bulk MMA) with a repetition rate of 50 Hz and compared to the IUPAC literature <sup>275</sup> propagation rate coefficient of MMA ( $267 \text{ L mol}^{-1} \text{ s}^{-1}$ ). ....	87
<b>Table 6.3:</b> Overview of molecular weight of the polymer chains $M_i$ at the inflection points in the first derivative of the SEC generated trace at 800 nm with a repetition rate of 20 Hz, after the penetration of thin tissue and without tissue. ....	89
<b>Table 6.4:</b> Overview of the propagation rate coefficients ( <b>Eq. 3.33</b> ) of MMA calculated for polymer chains with the assigned molecular weight $M_i$ generated by 800 nm (red dashed) pulsed fs laser triggered Ivocerin fragmentation ( $c = 12 \text{ mmol L}^{-1}$ in bulk MMA) with a repetition rate of 20 Hz after penetration through tissue and compared to the IUPAC literature <sup>275</sup> propagation rate coefficient of MMA. ....	89
<b>Table 6.5</b> Overview of the exact mass, resolution and relative abundance of the assigned species in the recorded and simulated spectrum of the PMMA after PLP of MMA with Ivocerin triggered by 800 nm fs pulses with a fluence of $5.5 \text{ mJ cm}^{-2}$ and a repetition rate of 100 Hz. ....	92

<b>Table 6.6:</b> Comparison of the relative abundances $X$ of the assigned polymer species $P_i$ in the mass spectra after irradiation of $12 \text{ mmol L}^{-1}$ Ivocerin in MMA with $800 \text{ nm fs}$ laser pulses under 1P conditions ( $5.5 \text{ mJ cm}^{-2}$ ) and with $400 \text{ nm fs}$ pulses under 2P conditions ( $102 \text{ }\mu\text{J cm}^{-2}$ ).....	93
<b>Table 7.1:</b> Overview of the $M_n$ values, dispersity, after 30 min irradiation of solutions containing various monomer concentrations and $50 \text{ }\mu\text{L AuNR}$ , $9 \text{ mmol L}^{-1}$ AIBN and $10^{-2} \text{ mol L}^{-1}$ CTA with $800 \text{ nm fs}$ pulses with an intensity of $25 \text{ GW cm}^{-2}$ ..	106
<b>Table 7.2:</b> Overview of the $M_n$ values, dispersities and monomer conversion after 30 min irradiation of a solution with various AuNR concentrations and $9 \text{ mmol L}^{-1}$ AIBN, $6.73 \text{ mol L}^{-1}$ DMA and $10^{-2} \text{ mol L}^{-1}$ CTA with $800 \text{ nm fs}$ pulses with an intensity of $25 \text{ GW cm}^{-2}$ .....	108
<b>Table 7.3:</b> Overview of the $M_n$ values, dispersities, and monomer conversion after 30 irradiation of a solution with various AIBN concentrations and $50 \text{ }\mu\text{L AuNR}$ , $6.73 \text{ mol L}^{-1}$ DMA and $10^{-2} \text{ mol L}^{-1}$ CTA with $800 \text{ nm fs}$ pulses with an intensity of $25 \text{ GW cm}^{-2}$ .....	109
<b>Table 7.4:</b> Overview of monomer concentration-dependent $M_n$ of a solution with DMA, $50 \text{ }\mu\text{L AuNR}$ in water, $10^{-2} \text{ mol L}^{-1}$ CTA with $9 \text{ mmol L}^{-1}$ AIBN and without AIBN after 30 min irradiation with $25 \text{ GW cm}^{-2}$ fs pulses at $800 \text{ nm}$ .....	110
<b>Table 7.5:</b> Overview of the exact mass, resolution and relative abundance of the assigned species in the recorded and simulated mass spectrum of PDMA 30 min irradiation of $4.04 \text{ mol L}^{-1}$ DMA, $9 \text{ mmol L}^{-1}$ AIBN, $100 \text{ }\mu\text{L AuNR}$ and $10^{-2} \text{ mol L}^{-1}$ CTA with $25 \text{ GW cm}^{-2}$ laser pulses at $800 \text{ nm}$ .....	113
<b>Table 7.6:</b> Overview of wavelength-dependent energy for the action plot.....	116
<b>Table 7.7:</b> Overview of the wavelength-dependent triplicate conversions and average conversion as well as the error determined by standard deviation of the action plot.....	118

## VI List of Equations

Eq. 3.1	8
Eq. 3.2	8
Eq. 3.3	9
Eq. 3.4	9
Eq. 3.5	12
Eq. 3.6	13
Eq. 3.7	14
Eq. 3.8	14
Eq. 3.9	14
Eq. 3.10	15
Eq. 3.11	15
Eq. 3.12	15
Eq. 3.13	16
Eq. 3.14	16
Eq. 3.15	16
Eq. 3.16	16
Eq. 3.17	17
Eq. 3.18	17
Eq. 3.19	17
Eq. 3.20	18
Eq. 3.21	20
Eq. 3.22	20
Eq. 3.23	22
Eq. 3.24	23
Eq. 3.25	24
Eq. 3.26	25
Eq. 3.27	25
Eq. 3.28	25
Eq. 3.29	25
Eq. 3.30	26
Eq. 3.31	26
Eq. 3.32	28
Eq. 3.33	29
Eq. 3.34	30
Eq. 3.35	31
Eq. 3.36	31
Eq. 3.37	31
Eq. 3.38	32

<b>Eq. 3.39</b>	.....	32
<b>Eq. 3.40</b>	.....	33
<b>Eq. 3.41</b>	.....	33
<b>Eq. 3.42</b>	.....	34
<b>Eq. 3.43</b>	.....	34
<b>Eq. 3.44</b>	.....	35
<b>Eq. 3.45</b>	.....	35
<b>Eq. 3.46</b>	.....	35
<b>Eq. 3.47</b>	.....	39
<b>Eq. 3.48</b>	.....	39
<b>Eq. 3.49</b>	.....	40
<b>Eq. 3.50</b>	.....	42
<b>Eq. 3.51</b>	.....	43
<b>Eq. 3.52</b>	.....	43
<b>Eq. 4.1</b>	.....	55
<b>Eq. 4.2</b>	.....	55
<b>Eq. 4.3</b>	.....	55

## VII Abbreviations

AIBN	Azobisisobutyronitrile
AR	Antireflective
ATRAP	Atom transfer radical polymerization
AuNR	Gold nanorod
BBO	Beta Barium Borate
CCD	Charge-Coupled Device
COB	Chip-on-board
CT	Charge transfer
CTA	Chain transfer agent
CTAB	Cetyl trimethylammonium bromide
DADS	Decay Associated Difference Spectrum
DG	Delay generator
DI	Direct injection
DMA	N,N-dimethylacrylamide
DMAc	Dimethylacetamide
DLW	Direct laser writing
EPR	Electron Paramagnetic Resonance
ESA	Excited state absorption
ESI	Electrospray ionization
ESI-MS	Electrospray Ionization Mass Spectrometry
FRP	Free Radical Polymerization
fs	Femtosecond
GSB	Ground state bleaching

GVM	Group velocity mismatch
IC	Internal conversion
IR	Infrared
ISC	Intersystem crossing
IUPAC	International Union of Pure and Applied Chemistry
IVR	Intramolecular Vibrational Redistribution
KIT	Karlsruhe Institute of Technology
LBO	Lithiumtriborate
LED	Light-Emitting Diode
LSPR	Localized surface plasmon resonance
LTS	Long travel stage
MEHQ	Monomethyl ether hydroquinone
MHz	Megahertz
MMA	Methyl-methacrylate
ms	Millisecond
MWD	Molecular weight distribution
NaTFA	Sodium trifluoroacetate
ND	Neutral density
NIR	Near-infrared
NLT	Nonlinear Transmission
NMP	Nitrogen-mediated polymerization
NMR	Nuclear Magnetic Resonance
NOPA	Nonlinear optical parametric amplifier
ns	Nanosecond

OD	Optical density
OPO	Optical parametric oscillator
PEG	Polyethylene glycol
PhD	Doctor of Philosophy
PLP	Pulsed laser-induced polymerization
PMMA	Poly(methyl-methacrylate)
ppm	Parts per million
ps	Picosecond
PTFE	Polytetrafluorethylen
Q-switch	Quality-switch
QUT	Queensland University of Technology
RAFT	Reversible addition-fragmentation chain transfer
SE	Stimulated emission
SEC	Size Exclusion Chromatography
SHG	Second harmonic generation
S	Singlet State
TEM	Transmission Electron Microscopy
Ti:Sapphir	Titanium-Sapphire
THF	Tetrahydrofuran
THG	Third Harmonic Generation
TMS	Tetramethylsilane
T	Triplet state
UV	Ultraviolet
Vis	Visible

VR	Vibrational Relaxation
WL	White light
1P	One-photon
1PA	One-photon absorption
1PP	One-photon polymerization
2P	Two-photon
2PA	Two-photon absorption
2PIF	2P-induced fluorescence
2PP	Two-photon polymerization
3D	3-dimensional

# 1 Motivation

Photo-induced chemical reactions, including polymerization reactions, have been gaining increasing emphasis in recent years. With advancements in the control of spatiotemporal aspects of reactions,<sup>1</sup> the development of light sources emitting narrow wavelengths,<sup>2,3</sup> such as lasers, and the evolution of polymerization techniques,<sup>4-16</sup> it is now possible to generate highly customized polymers. To design specific polymer products, a deep understanding of the polymerization mechanism is essential. Numerous experiments have been conducted to gain insight into various aspects of polymerization processes, ranging from *post-mortem* analysis of final polymer products via soft ionization mass spectrometry, Electron Paramagnetic Resonance (EPR) Spectroscopy, Nuclear Magnetic Resonance (NMR) Spectroscopy to Size Exclusion Chromatography (SEC). To examine initial events on ultrashort time scales, femtosecond (fs) transient absorption spectroscopy has been employed.<sup>17-21</sup>

Traditionally, ultraviolet (UV) or visible (Vis) light has been exploited to induce polymerization, as most known photoinitiators can be excited within this region of the electromagnetic spectrum, leading to the formation of radicals.<sup>18-25</sup> The current thesis aims to advance the understanding of the underlying mechanism during Vis light-induced free-radical polymerization using fs pulsed laser irradiation in the Hz and kHz regime, with subsequent exploration of the earliest events of radical formation via fs transient spectroscopy as well as ultimately product formation using SEC and <sup>1</sup>H-NMR spectroscopy.

In recent decades, near-infrared (NIR) light has gained increasing attention for polymerization induction. Prominent examples of NIR light utilization include two-photon polymerization (2PP) and direct laser writing (DLW).<sup>26-32</sup> In addition to the in-depth investigation of Vis light-induced polymerization, a further significant part of the current thesis will evidence that pulsed laser-induced polymerization (PLP) in the Hz and kHz regime is also accessible via two-photon absorption (2PA) using the advantageous properties of NIR light, which was hitherto mainly used for polymerization in the MHz regime.<sup>33-36</sup> A detailed analysis of 2PP, in an identical manner as the Vis light-induced polymerization, aims to better understand NIR-induced 2PP, revealing possible mechanistic differences on the path to polymer formation. NIR light is known for its ability to penetrate deeply into materials, a phenomenon familiar from the heating effect of red-light heat lamps. Moreover, red light is less harmful to biological tissues and can penetrate deeper, making red-light-induced chemical reactions highly promising for applications in biology and medicine.<sup>37,38</sup> These properties are intended to be exploited

inserting a tissue, here a thin slice of bacon, between the laser beam and the polymerization sample to highlight that 2PP is even initiated after the light penetrated through tissue.

As mentioned above, NIR light offers several advantages due to its benign nature and penetration depth into biological tissue. In addition to advancing the mechanistic understanding of photoinitiator-mediated polymerizations, a novel method for NIR light-initiated polymerization was explored. Instead of relying on the direct excitation and decay of a photoinitiator, this approach will involve the use of gold nanorods (AuNR). Depending on their dimension, these nanorods can convert light across the Vis or NIR spectrum into heat,<sup>39</sup> which in turn can trigger the decomposition of a thermal initiator, thus initiating free radical polymerization (FRP). An initial proof-of-principle experiment using AuNR with a maximum absorptivity at 800 nm, exposed to fs laser irradiation, confirmed that the approach allows the initiation of NIR light-triggered polymerization as an alternative approach. Subsequently, mapping the wavelength dependent reaction progress provided insights into the efficiency of the process at different wavelengths. As previous publications have reported, the reactivity spectrum is often not identical to the absorption spectrum.<sup>11,40-44</sup> Therefore, it is mandatory to record the wavelength-dependent monomer conversion of AuNR using a monochromatic tuneable nanosecond (ns) laser and compare it with the absorptivity. Given their low cytotoxicity, AuNR are highly promising for *in vivo* NIR-induced polymerization.<sup>45</sup> Analogue to the 2PP experiments, a slice of bacon is inserted between the laser beam and the AuNR containing polymerization sample, simulating biological tissue to underpin the strong potential of AuNR-mediated NIR polymerization. The process of plasmonic heat production via AuNR does not require as much light intensity as 2PP. Therefore, Light Emitting Diodes (LEDs), a more practical light source than lasers, will be tested to determine whether AuNR still produce sufficient heat for the decomposition of thermal initiators. Employing LEDs may enable a broader application of AuNR for polymerizations in biological environments and a potential setup for a high school experiment to visualize cutting-edge academic science.

## 2 Literature Overview

During the last decades, photo-induced chemical reactions – in particular polymerization – have gained increasing focus, due to their spatiotemporal control.<sup>1,46–49</sup> In the early days of photo-induced polymerization, sunlight,<sup>50–53</sup> or broadly emitting lamps<sup>54–62</sup> were used as light sources. Later, these broadly emitting light source were widely replaced by light-emitting diodes (LED),<sup>63–71</sup> with a narrow spectral width as one major advantage,<sup>72</sup> allowing a more targeted excitation of photosensitive molecules. LEDs also offer the advantage of high energy efficiency, defined by a high luminous flux emitted compared to the electrical power converted.<sup>72</sup> Moreover, low purchasing costs, low energy consumption and a high durability of 100.000 h or more,<sup>73</sup> make LEDs a very economical light source. Due to their cost-efficiency and benign nature, LEDs are perfectly suitable for sensitive practical application, such as photopolymerization of oral biomaterials.<sup>74–77</sup> However, the light divergence and distinct emission wavelength limit the practicability of LEDs.

The development of light sources with an even more narrow spectral bandwidth and coherent emission, such as lasers, enabled highly precise photochemical reactions, as well as advanced applications including wavelength-orthogonal, antagonistic and synergistic polymerizations.<sup>41,78–86</sup> Several polymerization techniques, such as reversible addition-fragmentation chain transfer (RAFT), atom transfer radical polymerization (ATRP) and nitrogen-mediated polymerization (NMP) have been performed with photoinitiators, seeking milder reaction conditions and – importantly – fine control over the chain length and dispersity of the generated polymers.<sup>4–16</sup> Light, as trigger for the initiation of polymerization, was also used for pulsed laser-induced polymerization (PLP); a powerful technique to precisely determine propagation rate coefficients, first introduced by Olaj and colleagues.<sup>87</sup> PLP can also be employed to customize the chain length of polymers, specifically for mass spectrometric analysis.<sup>20,88,89</sup> While an initial pulse stimulates the generation of radicals to initiate polymer chain growth, subsequent pulses generate new radicals leading to termination of the propagating polymer chains. PLP has, in many cases, been performed using ultraviolet (UV), nanosecond (ns) laser pulses,<sup>18,19,22–25</sup> as the majority of photoinitiators absorb in this region of the electromagnetic (EM) spectrum. ns laser pulses, however, act on molecules on a timescale that is much longer than ultrashort processes (e.g. intersystem crossing (ISC)). Thus, excess energy can be transferred to vibrational states, potentially inducing competitive channels to ISC, which can decrease the efficiency of triplet state population and thus radical formation. Femtosecond (fs) laser pulses are characterized by a remarkably shorter duration, potentially

leading to higher ISC efficiency. Therefore, it is highly interesting to examine fs pulse triggered PLP.

Radical formation, prior to initiation, is perhaps the most critical step of a polymerization process as it dictates the reaction conditions and progress of free radical polymerizations (FRP). In the course of photo-induced polymerization, photoinitiators, such as carbonyl compounds,<sup>1,90</sup> are increasingly employed as a viable alternative to thermal initiators, typically peroxy<sup>91,92</sup> and nitrogen-based<sup>93</sup> compounds. Pump-probe spectroscopy is a powerful technique to examine excited electronic state dynamics after photoexcitation. Eigen, Norrish and Porter were awarded the Nobel Prize for the first pump-probe measurements in 1949.<sup>94</sup> These authors used the discharge of a large condenser in a quartz tube filled with rare gas, resulting in a pulse duration of 4 ns. However, for the evaluation of chemical reactions it is necessary to use ultrashort laser pulses. The improvement of laser systems, and the development of pulsed lasers, enabled time resolutions that were sufficiently short, such as ns, picoseconds (ps)<sup>2</sup> and even fs.<sup>3</sup> Pump-probe measurements have become an essential tool in probing electron dynamics, so much so that in 1999 Zewail was awarded the Nobel Prize for applying fs spectroscopy to observe chemical reactions in real time. The commercial availability of fs lasers has enabled chemists to probe the earliest events of photoexcited molecules. The technique of fs spectroscopy comprises a higher energy pump pulse followed by a weaker probe pulse. The pump pulse is used to excite the ground state electrons of the investigated molecule into an excited singlet state. The probe pulse subsequently probes the excited molecule at various time intervals after excitation to elucidate the processes and transitions between the excited states of the molecule. In the past, a plethora of fs spectroscopy experiments have been performed on photoinitiators, for example on benzoin-,<sup>20,21</sup> dione-,<sup>21</sup> acylgermane-,<sup>17,19,89</sup> and coumarin-based<sup>95</sup> compounds. While the carbonyl-based<sup>19-21</sup> compounds preferably form triplet states and cleave into radicals, coumarin-based<sup>95</sup> molecules form excited singlet states and relax to the electronic ground state by fluorescence. As germyl-based photoinitiators are applied more widely, more research is required to understand how they can be modified to extend their applicability.

Photochemistry is a critically important process for photolithography,<sup>96-103</sup> adhesives materials,<sup>104-108</sup> dentistry,<sup>109-113</sup> tissue engineering<sup>114-117</sup> and biological applications.<sup>48,118-122</sup> However, due to the low penetration depth and possible harmful consequences of UV light, short wavelengths – as mostly required to excite photoinitiators – are often not suitable for sensitive applications. Shifting the excitation wavelength to the NIR region of the light broadens the range of photochemistry, for example enabling spatiotemporal control of biology.<sup>48</sup> Catalysts,

such as metals,<sup>123</sup> bacteriochlorophyll,<sup>124</sup> or upconverting nanoparticles,<sup>125,126</sup> make NIR sensitized photo-induced polymerization accessible. Two-photon polymerization (2PP) offers a powerful alternative technique to directly excite photoinitiators using near-infrared (NIR) light.<sup>127</sup> First theorized by Maria Goeppert-Mayer,<sup>128</sup> a two-photon absorption (2PA) process is based on the simultaneous absorption of two low energy photons, which collectively deliver sufficient energy to elevate electrons into excited states. 2PP is a technique enabling direct laser writing (DLW)<sup>26-32</sup> and microfabrication by 3-dimensional (3D) printing,<sup>129-134</sup> typically with repetition rates in the MHz regime.<sup>32-36</sup> In particular, photopolymerization in 3D printing realizes high product customization, smooth object surfaces and high precision.<sup>135,136</sup> While 3D printing is widely applicable, the high precision, however, is often accompanied by a limitation of the size of products.<sup>137</sup> Therefore, 3D printing is mainly used for manufacturing small objects for jewelry,<sup>138</sup> dentistry,<sup>139-142</sup> but also for aerospace<sup>143-146</sup> and automotive.<sup>147</sup> However, to date there has been no report detailing how fs 2PP with low repetition rates controls polymer molecular weight distributions (MWD).

Given that 2PA is statistically significantly less likely to occur than 1P absorption, as it is a third order nonlinear process, high light intensities are required to observe 2PA events. Such high intensities tend to be harmful for sensitive environments, such as biological tissue. Therefore, new techniques are required, which offer high penetration depth and are benign to biomaterials, such as tissue. Several approaches have been described using organic molecules,<sup>148-152</sup> borate dyes<sup>153,154</sup> and cyanines,<sup>155</sup> absorbing NIR light and transforming it into heat, which ultimately induces radical polymerization via the decay of a thermally activated initiator. However, these approaches are not ideal for aqueous systems. An alternate mechanism that has been employed for NIR photothermal conversion is the use of plasmonic nanoparticles, such as gold nanorods (AuNR). Amongst a plethora of unique electronic and optical properties,<sup>156-162</sup> metal nanoparticles are capable of converting light into heat.<sup>39,163-165</sup> This photothermal effect is based on the collective oscillation of free electrons in solids, so-called surface plasmons, first described for spherical nanoparticles by Gustav Mie<sup>166</sup> and extended for non-spherical particle by Rayleigh and Gans.<sup>167,168</sup> The heat generation and transfer to the surrounding medium was theoretically predicted by Ekici *et al.*<sup>39</sup> presenting a strongly localized source of heat in the direct vicinity of the AuNR. The heating effect of nanoparticles was not only calculated, but also experimentally probed.<sup>163-165,169,170</sup> Kinetic studies by Alivisatos and coworkers<sup>163</sup> revealed that the produced heat dissipates on ultrafast timescales, using time-resolved fs spectroscopy. Depending on the surface coating, AuNR can be functionalized lipophilic, hydrophilic and biocompatible.<sup>171-175</sup> In recent years, water-soluble AuNR have

gained increasing popularity, and have been used in biomedical application, such as cancer cell imaging and treatment via local heat,<sup>176-178</sup> or drug delivery.<sup>179-181</sup>

Previous studies<sup>11,41-44</sup> on photo-reactive molecules in the Barner-Kowollik group have revealed that absorptivity is no predictor for photochemical reactivity using the so-called action plot technique.<sup>41</sup> Interestingly, the vast majority of experiments, including photoATRP complexes,<sup>11</sup> photo cycloadditions of styrylpyrene<sup>41</sup> or poly(ethyleneglycol)-styrylquinoxaline<sup>43</sup> as well as methylarylketones<sup>42</sup> and thioethers,<sup>44</sup> unveil a red-shifted reactivity. The action plot technique relies on a tunable ns laser capable of emitting nearly monochromatic wavelengths.

Aiming to close the above mentioned literature gaps, the current thesis describes, for the first time, in-depth Vis light triggered fs PLP experiments<sup>182</sup> with Ivocerin. The polymerization mechanism was investigated by *post-mortem* analysis via Size Exclusion Chromatography (SEC) and Electrospray Ionization Mass Spectrometry (ESI-MS). To deepen the understanding of the polymerization mechanism from the earliest events to product formation, the current thesis introduces the first detailed time-resolved fs spectroscopy analysis of Ivocerin to combine the obtained knowledge of the product formation and the behaviour immediately after photoexcitation. The shorter pulse duration and higher peak intensity of fs laser pulses may lead to an increased probability of ultrashort photophysical processes, e.g. ISC into triplet states and to a higher probability of absorbing photons, compared to longer ns laser pulses.

Shifting focus from the UV/Vis region of the EM spectrum towards the NIR region, the current thesis introduces chain lengths controlled NIR 2PP using fs PLP techniques, closing a critical literature gap, following the formation of polymer by means of <sup>1</sup>H-NMR spectroscopy and the PLP generated molecular weight distribution (MWD) via SEC.<sup>182</sup> Further, it demonstrates that the high penetration depth of NIR light is able to induce polymerization even after penetration through biological tissue.<sup>182</sup>

Further, the current thesis introduces citrate-functionalized gold nanorods (AuNR) as photo-thermal converters operating in water, revealing the unique ability of AuNR to mediate NIR-induced polymerizations in water under mild conditions using a water-soluble monomer and thermal initiator, with successful polymerization evidenced via <sup>1</sup>H-NMR spectroscopy and SEC.<sup>183</sup>

The current thesis also introduces the first action plot analysis exploiting AuNR as a photo-sensitive species during FRP elucidating the optimum wavelength for heat generation. Moreover, LEDs are introduced as a more practical light source for inducing heat through photo-

excitation of AuNR, thereby initiating polymerization. Utilizing LEDs facilitates the establishment of an educational connection between advanced academic research and potential high school experiments, offering a means to teach the conversion of light energy into heat by means of a cutting-edge scientific experiment.

The experiments presented in the current thesis rely on various physical and chemical processes. The following chapters explain the fundamental background of these processes to assist the reader with a better understanding of the described experiments.

## 3 Theoretical Background

### 3.1 Photophysical and -Chemical Processes in Molecules

Photo-induced chemical reactions and spectroscopic methods for the analysis of electronic behaviour of excited molecules are based on the interaction of matter with light. Whenever molecules experience photoexcitation, electrons undergo vibronic transitions, a simultaneous transition between electronic and vibrational states.<sup>184</sup> Vibronic transitions are based on the Franck-Condon principle,<sup>185,186</sup> which postulates that the position of the nuclei is constant during an electronic transition, due to the much higher mass of the nuclei compared to the electrons.

Transitions are only possible for a non-zero transition dipole moment and the statistical likelihood of transitions occurring is given by the square value of the transition dipole moment  $|\mu|^2$ , known as the Franck-Condon-factor.<sup>184</sup> The transition dipole moment operator  $\hat{\mu}$  contains information on both electronic and nuclear transitions (**Eq. 3.1**), describing the behaviour of the electrons ( $e$ ) and nucleus ( $N$ ), respectively. However, since electronic transitions are considered to be adiabatic, and the mass of an electron is significantly smaller than that of the nucleus, the nucleus can be regarded as quasi-stationary. According to the Born-Oppenheimer-approximation, this allows the separation of contributions from the nuclear and electronic dipole moments:<sup>187</sup>

$$\hat{\mu} = \hat{\mu}_e + \hat{\mu}_N . \quad \text{Eq. 3.1}$$

It has to be considered that transitions are also dependent on the temperature ( $T$ ) and the population ( $N_j$ ) of electronic states with the energy ( $E_j$ ), as well as the Boltzmann constant:<sup>188</sup>

$$N_j \propto N \cdot \exp\left(\frac{-E_j}{k_B T}\right) . \quad \text{Eq. 3.2}$$

At ambient temperature, electrons often populate vibrational levels of the electronic ground state. Depending on the overlap integral, transitions can occur that elevate electrons into higher vibrational levels within the excited electronic state. Thus, such transitions are called vibronic transitions.<sup>184</sup> According to the Franck-Condon-principle<sup>185,186</sup> a transition is more likely, the more the initial and the final wavefunctions overlap corresponding to the highest value for the transition dipole moment. The absorbance ( $A$ ) depends on the Franck-Condon-factors.<sup>184</sup> As the absorbance can also be described via the integration of the molar extinction coefficient  $\epsilon$ , **Eq. 3.3** correlates the transition dipole moment with an experimental determinable measure:<sup>184,188</sup>

$$A = \left( \frac{3\pi \cdot \omega}{3 \cdot \epsilon_0 \cdot h \cdot v_{\text{Light}}} \right) \cdot N_A \cdot |\mu_e|^2 = \int \epsilon(\omega) d\omega . \quad \text{Eq. 3.3}$$

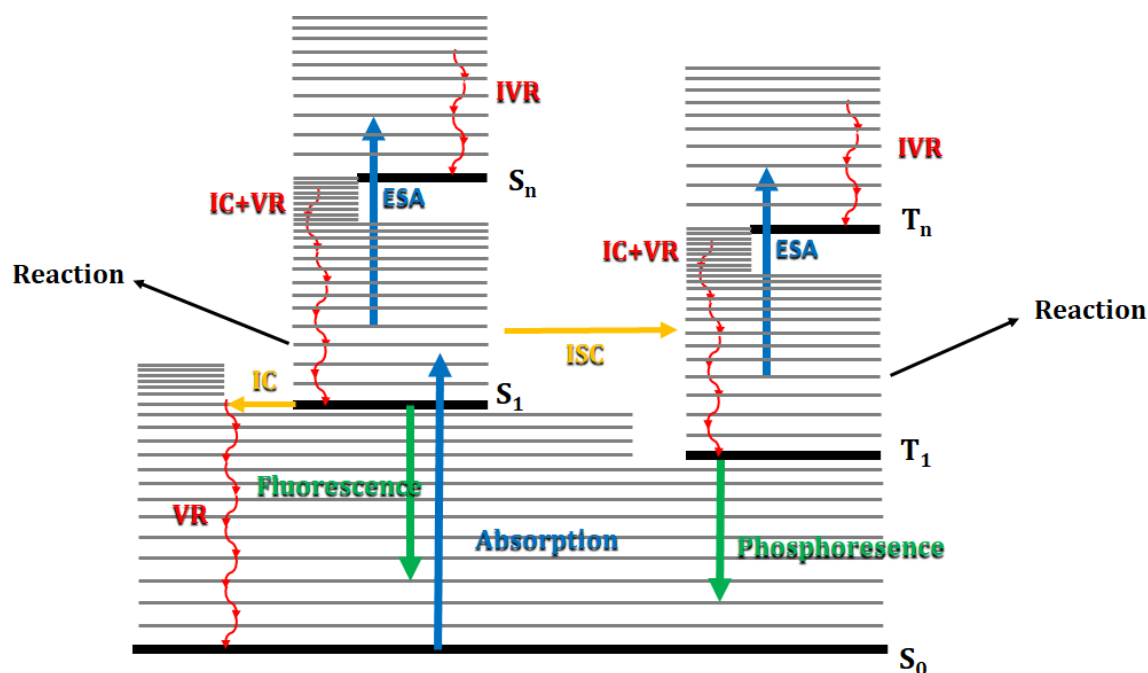
In this equation  $\omega$  describes the frequency of the absorbed light,  $\epsilon_0$  is the dielectric constant of vacuum,  $v_{\text{Light}}$  the velocity of light,  $\mu_e$  defines the electronic dipole moment and  $N_A$  the Avogadro constant. On the macroscopic scale, the absorbance is given by the Beer-Lambert law, which describes the optical density (OD), defined by the decadic logarithm of the ratio of incident light ( $I_0$ ) and transmitted light ( $I$ ). The intensity of the transmitted light depends on the molar decadic extinction coefficient  $\epsilon$ , which can be described as the macroscopic equivalent to the transition dipole moment, as well as the concentration ( $c$ ) of the molecule of interest and the optical path length ( $d$ ):<sup>189</sup>

$$OD = A = \log\left(\frac{I_0}{I}\right) = c \cdot \epsilon \cdot d . \quad \text{Eq. 3.4}$$

Molecules that experience photoexcitation can undergo vibronic transitions, populating excited electronic states. From these states several processes can occur, either the molecule can undergo a chemical reaction, it can be heated by non-radiative energy dissipation or the electrons relax to the electronic ground state by radiative energy dissipation producing photoluminescence. The likelihood of each of these processes occurring depends on several factors, including the lifetime of excited states.

According to the transition state theory,<sup>190,191</sup> the possible pathways of energy distribution follow a multi-dimensional energy hypersurface. Due to the complexity of potential hypersurfaces, a simplified 2-dimensional diagram, known as a Jablonski diagram,<sup>192</sup> is often used to describe the photophysical and photochemical relaxation pathways. A typical diagram is depicted in **Scheme 3.1**.

Originating from an excited electronic state, a molecule can relax via various physical processes. Due to the previously discussed Franck-Condon factors,<sup>184</sup> electrons often populate higher vibrational levels of the excited electronic state after photoexcitation. The energy can subsequently be distributed via the vibrational degrees of freedom (Intramolecular Vibrational Redistribution, IVR), heating the molecule on a typical ultrashort time scale of  $10^{-11}$ - $10^{-13}$  s.<sup>193</sup> Besides intramolecular redistribution of energy, molecules can dissipate heat to the surrounding medium via interactions with the various degrees of freedom of the solvent molecules (Vibrational Relaxation, VR), which occurs in timescales of  $10^{-9}$ - $10^{-11}$  s.<sup>187</sup>



**Scheme 3.1:** Scheme of possible photophysical and photochemical processes after photoexcitation, shown as Jablonski diagram. Absorption into excited electronic states (orange) can result in either non-radiative relaxation processes, such as vibrational relaxation (VR), intramolecular vibrational redistribution (IVR), internal conversion (IC) and intersystem crossing (ISC) or radiative processes, fluorescence (green) and phosphorescence (red). Additionally, chemical reaction or charge transfer (CT) can occur from the excited states. The thick horizontal lines depict electronic states, e.g. the ground state  $S_0$  first excited singlet  $S_1$  and triplet  $T_1$  states, as well as higher excited singlet  $S_n$  and triplet  $T_n$  states. The thin lines represent vibrational levels of the electronic states.

VR often occurs after a rapid non-radiative transition, given by ultrafast internal conversion (IC). IC describes non-radiative transitions from higher electronic states to lower electronic states of the same spin multiplicity, such as transitions from  $S_{n+1} \rightarrow S_n$  or  $T_{n+1} \rightarrow T_n$ .<sup>187</sup> Considering that the energy gaps between higher excited states are smaller compared to the energy gap between an excited state and the ground state, IC transitions are usually faster between higher excited states.<sup>193</sup> Nonetheless, ultrafast transitions between excited states and the electronic ground state potentially occur via so-called conical intersections.

A conical intersection is given by a crossing of two or more potential hypersurfaces of electronic states due to non-adiabatic effects.<sup>194–196</sup> Since the energy levels are degenerate at this point, a highly efficient pathway is formed whereby the excited molecule can relax.

Transitions between electronic states of different spin multiplicity are forbidden due to the selection rules of quantum mechanics. However, spin-orbit coupling can enable such an intersystem crossing (ISC).<sup>187</sup> According to the El-Sayed rules,<sup>197</sup> ISC transitions are expected to last on a long time scale ( $10^{-9}$ - $10^{-6}$  s) because of the required change in the spin multiplicity of

the electrons.<sup>197</sup> However, there are literature-known ISC processes that occur within a few ps.<sup>198,198,199</sup>

Besides the non-radiative relaxation pathways, molecules can also distribute energy by the emission of light. Light can either be emitted from singlet states via fluorescence or from a triplet state by phosphorescence following ISC. According to Kasha's rule,<sup>200</sup> emission processes typically occur from the lowest vibrational level of either  $S_1$  or  $T_1$ . The typical lifetime of fluorescent emission is  $10^{-9}$ - $10^{-6}$  s and sometimes as fast as  $10^{-12}$  s.<sup>187</sup> Phosphorescence is considered to occur on longer time scales ( $10^{-6}$ - $10^3$  s) because of the changed spin multiplicity from  $T_1 \rightarrow S_0$ .<sup>187</sup>

Molecules can not only undergo photophysical processes, but also cleave bonds as an initial step for subsequent chemical reactions. Most photo-sensitive molecules that are used as initiators for photo-induced chemical reactions, such as photopolymerization, initiate bond cleavage from excited triplet states. These molecules must first undergo an ISC before reaching a triplet state. However, often there is not one definitive pathway that the electrons can traverse, but competitive relaxation processes resulting in complex channel branching. The ultrashort lifetime of many relaxation processes immediately after photoexcitation requires experimental techniques that are capable of resolving these processes, such as ultrafast spectroscopy. Even with these techniques, in case of high channel branching several different experiments are often required to resolve all fundamental processes.

Photoexcitation as well as subsequent physical and chemical relaxation processes, for example ISC or bond cleavage, are fundamental for the characterization of photoinitiators, such as Ivocerin, which was used in the present thesis.

## 3.2 Laser Principle

Experimental techniques that are capable of resolving ultrafast or higher order absorption processes require ultrafast excitation source emitting highly intense light, such as that produced from lasers. In the most basic form, a laser consists of three parts: an active medium, a light source that pumps the active medium and a cavity resonator.<sup>201</sup> As the name suggests, a laser functions by light amplification of stimulated emission produced as the photons oscillate within the cavity resonator.

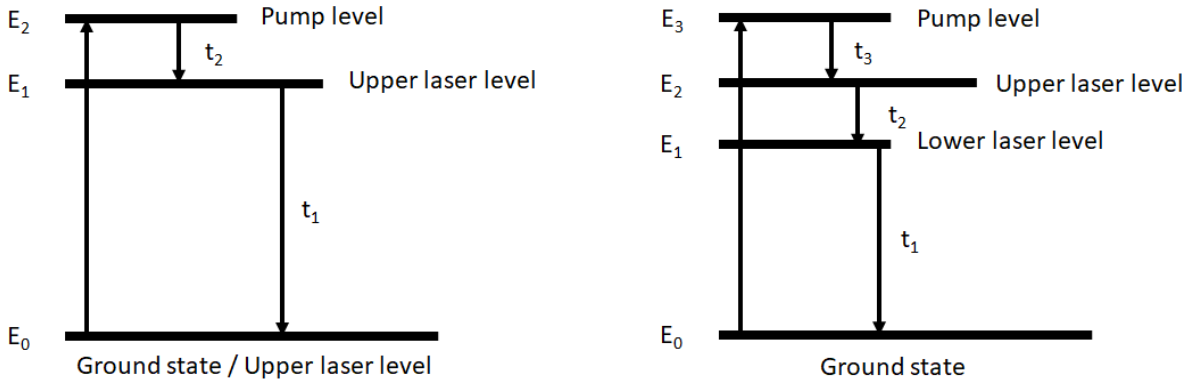
Pumped by an external light source, there are two radiative processes that occur in the active medium. While most lasers operate on a four-level system, for simplicity a two-level system is considered here. Initially, a photon with the energy  $h\omega = E_2 - E_1$ , where  $h$  represents the

Planck constant and  $\omega$  the frequency of the incident light, is absorbed to excite electrons from state  $E_1$  into state  $E_2$ . The energy level can either be depopulated by spontaneous emission or, the preferred process, stimulated emission. Stimulated emission occurs when a photon with energy equivalent to the electronic transition is incident on an excited medium, leading to the de-excitation of an excited electron and emission of a second photon, possessing identical properties to the first.<sup>202,203</sup>

For stimulated emission to occur, the active medium must first undergo population inversion. In order to reach equilibrium the rate of change of population of both states  $E_1$  and  $E_2$  should be identical. More importantly, to achieve a population inversion the following condition has to be satisfied:

$$\frac{N_2}{N_1} > 1 . \quad \text{Eq. 3.5}$$

In practice, this is not possible to achieve for a two-level system in thermal equilibrium, since each of the transition processes are dependent on the population of the state, the likelihood of transition becomes lower as the population decreases. To achieve population inversion, three-level (**Scheme 3.2**) or four-level systems are required.<sup>203</sup> In these systems, electrons are excited into the so-called pump level, which is, however, short-lived and thus quickly depopulated into the upper laser level. Since the upper laser level is a long-lived state, a population inversion can be produced. While in the case of a three-level system, the lower laser level is identical to the ground state, in a four-level system the lower laser level can be further depopulated into the ground state  $E_0$ . Therefore, a three-level system requires much stronger pumping power to achieve efficient population inversion than a four-level system, which makes a four-level system advantageous over a three-level system. Regarding the photons as stationary waves between the end mirrors, the resonator serves as an amplifier. Each photon within the amplifier travelling through the active medium can stimulate the emission of a second photon with the same temporal and spatial phase, thus amplifying the coherent laser light. One of the end mirrors is semitransparent enabling the coherent light to be decoupled.



**Scheme 3.2:** Schematic illustration of a three-level laser system. Electrons are excited into the pump-level (2) and subsequently relax into laser level (1). The population of level 1 leads to population inversion. Radiation is amplified by stimulated emission from the laser level to the lower laser level (ground state).

### 3.2.1 Properties of Laser Pulses

Laser pulses are considered to be high intensity wave packets that are identical in spatial and temporal properties, resulting from the superposition of laser modes.<sup>204</sup> Depending on the technique of generation, for example Q-switch or mode-locking, laser pulses have a specific pulse duration  $\tau_p$  (refer to **Section 3.2.2** and **3.2.3** for more details), which forms a Fourier pair together with the spectral width  $\Delta\nu$  of the pulses analogue to Heisenberg's uncertainty principle of energy and time:<sup>204</sup>

$$\tau_p \Delta\nu \geq K . \quad \text{Eq. 3.6}$$

This equation is often called time-bandwidth product with Fourier limit  $K$ . In many cases, laser pulses can be considered as Gaussian shape. For Gaussian-shaped pulses the Fourier limit is  $K = 0.441$ .<sup>204</sup> This has a significant impact on the magnitude of the spectral properties of laser pulses in case of different pulse durations. Thus, the Fourier limit defines the minimum achievable spectral width of laser pulses. For example, fs laser pulses have minimum spectral width in the range of 10 nm. A laser producing ns pulses, has a minimum spectral width in the range of  $10^{-5}$  nm, which is essentially monochromatic. Therefore, ns lasers are ideal for probing wavelength dependent processes, such as action plots. Ultrashort pulsed lasers, such as fs lasers, are more prone to temporal broadening by dispersion while propagating through optical media.

Since the refractive index  $n(\omega)$  is dependent on the frequency  $\omega$ , the frequency modes within an ultrashort wave packet possess various phase velocity  $v_{\text{ph}}$  leading to dispersion, described in the dispersion relation<sup>189,204</sup>

$$v_{\text{ph}} = \frac{\omega}{k} = \frac{v_{\text{Light}}}{n(\omega)}, \quad \text{Eq. 3.7}$$

where  $v_{\text{Light}}$  is the speed of light,  $k$  the wave vector and  $n$  the frequency-dependent refractive index. The velocity of the entire wave packet consisting of many modes with corresponding phase velocities is described by the group velocity. Due to the wavelength dependency of the phase velocity, the group velocity of a wave packet is described as the phase velocity and an additional contribution, the wavelength-dependent derivation of the phase velocity  $dv_{\text{ph}}/d\lambda$ .<sup>189,204</sup>

$$v_{\text{gr}} = v_{\text{ph}} - \lambda \frac{dv_{\text{ph}}}{d\lambda}. \quad \text{Eq. 3.8}$$

Propagating through vacuum, the derivation of the phase velocity is zero resulting in equality of group velocity and phase velocity. However, when propagating through media the group velocity must be considered. This is particularly important for pump-probe experiments, where two pulses containing different frequencies will experience a group velocity mismatch (GVM) given by:<sup>205</sup>

$$\text{GVM} = \left| \frac{1}{v_{\text{gr},1}} - \frac{1}{v_{\text{gr},2}} \right|, \quad \text{Eq. 3.9}$$

which must be accounted for in the experimental design.

### 3.2.2 Q-Switch

ns laser pulses can be generated by placing a Q-switch in the laser resonator. A Q-switch consists, for example, of an electro-optical crystal, known as a Pockels cell, combined with a polarizer. The application of an electric potential to the Pockels cell changes the polarity in the anisotropic crystal, and hence controlling the transmission through the laser cavity. Initially, the Q-switch blocks transmission, so that the resonator remains below the oscillation threshold, until a population inversion is achieved in the active medium. At a defined time  $t_0$  the Q-switch is activated by a change of the applied potential, enabling the electromagnetic waves to propagate through the resonator and trigger lasing. Thus oscillation is enabled in an abrupt manner, strongly amplifying the waves in the resonator due to stimulated emission from the highly populated excited laser level.<sup>206</sup> The ns pulses emitted by the Coherent Opolette laser system used for the action plot experiments were generated by a Q-switch.

### 3.2.3 Mode-locking

Ultrashort laser pulses can be generated via mode-locking, where numerous modes constructively interfere with each other.<sup>207</sup> Every mode  $i$  is characterized by an amplitude  $E_i$ , frequency  $\omega_i$  and phase shift  $\varphi_i$ :

$$E = E_i \cos(\omega_i t + \varphi_i(t)). \quad \text{Eq. 3.10}$$

Constructive interference occurs when modes initially oscillate in phase. However, due to their different frequencies, they eventually dephase over time and interfere destructively. Once their phase align again after a certain time, constructive interference is re-established, leading to the generation of periodic pulses with a repetition rate  $\eta$ , as given by:<sup>208</sup>

$$\eta = \frac{c}{2nL}. \quad \text{Eq. 3.11}$$

Here,  $n$  is the refractive index,  $L$  the length of the resonator and  $c$  the speed of light. The more modes interfere with each other, the shorter the pulses become, which can be explained by equation:<sup>204,207</sup>

$$\tau_p = \frac{1}{N\Omega}. \quad \text{Eq. 3.12}$$

In this equation,  $\tau_p$  represents the pulse duration,  $N$  is the number of modes and  $\Omega$  is the modulation frequency. There are two primary forms of mode-locking, active and passive. Active mode-locking involves the use of optical modulators, such as Pockels cells or Kerr cells, within the laser resonator.<sup>209</sup> This modulates the intensity of the light wave, generating sidebands with the frequency  $\omega$  in addition to the carrier frequency  $\omega_0$ . To ensure the sidebands participate in oscillations and are modulated, their frequencies must align with the equation  $\omega = \frac{v_{\text{Light}}}{2d}$ . This approach amplifies the laser pulses effectively.<sup>207</sup> In passive mode-locking, a saturable absorber is placed in front of one of the resonator end mirrors. The active medium emits photon avalanches for a brief duration once the pumping power exceeds a certain threshold. Nonlinear saturation of the absorber results in higher light intensities being absorbed less and, consequently, experiencing greater net gain, resulting in stronger amplification.<sup>207</sup> Both the Coherent Astrella laser and the Clark-MXR CPA-2210 laser used in this thesis employ passive mode-locking.

### 3.3 Nonlinear Optical Effects

Nonlinear optical effects are fundamental for the generation of high intensity laser light and the tunability of lasers. They occur by the modification of the optical properties of nonlinear materials interacting with light of different intensities. This phenomenon is called nonlinear, because the way the material responds to the light does not depend linearly on the strength of the applied optical field. The light-induced polarization  $P(t)$  inside an optical medium with the linear susceptibility  $\chi^{(1)}$  can be described mathematically as:<sup>189,210</sup>

$$P(t) = \varepsilon_0 \chi^{(1)} E(t). \quad \text{Eq. 3.13}$$

Which is adequate to describe the behaviour under low intensity light. However, when high intensity fields  $E(t)$  are applied, Taylor series expansion of **Eq. 3.14** is required to describe higher-order contributions to the polarization:<sup>210</sup>

$$P_i(t) = \varepsilon_0 \left[ \sum_j \chi_{ij}^{(1)} E_j(t) + \chi_{ijk}^{(2)} E_j E_k(t) + \chi_{ijkl}^{(3)} E_j E_k E_l(t) + \dots \right]. \quad \text{Eq. 3.14}$$

The contribution of  $\chi^{(2)}$  describes the second-order and  $\chi^{(3)}$  the third-order nonlinear optical susceptibilities. The indices in **Eq. 3.14** define the components in the Cartesian coordinate system. Second and third order nonlinear processes are considered to be the most important nonlinear processes for laser pulse generation and wavelength tunability of lasers.

#### 3.3.1 Nonlinear Processes of Second Order

If two optical fields with different frequencies superimpose in a second order nonlinear crystal, such as  $\beta$ -bariumborate (BBO) or lithiumtriborate (LBO), the electrical field can be described as:<sup>210,211</sup>

$$E(t) = E_1 e^{-i\omega_1 t} + E_2 e^{-i\omega_2 t} + c. c. . \quad \text{Eq. 3.15}$$

Substituting this expression into **Eq. 3.14** leads to a second order polarization of:<sup>210,211</sup>

$$P^{(2)}(t) = \varepsilon_0 \chi^{(2)} \left[ E_1^2 e^{-2i\omega_1 t} + E_2^2 e^{-2i\omega_2 t} + 2E_1 E_2 e^{-i(\omega_1 + \omega_2)t} + 2E_1 E_2^* e^{-i(\omega_1 - \omega_2)t} + c. c. \right] + 2\varepsilon_0 \chi^{(2)} [E_1 E_1^* + E_2 E_2^*]. \quad \text{Eq. 3.16}$$

Separating **Eq. 3.16**, there are several terms contributing to the polarization, expressed by **Eq. 3.17**. The first and second term are attributed to frequency-doubling  $2\omega$ , called second harmonic generation (SHG), the third term describes the summation of two frequencies  $\omega_1$  and  $\omega_2$ , known as sum-frequency generation (SFG), and the fourth term difference-frequency

generation (DFG), a subtraction of  $\omega_1$  and  $\omega_2$ . The last term, which is independent of frequencies belongs to an effect leading to a static field across the nonlinear crystal, known as optical rectification:<sup>210,211</sup>

$$\begin{aligned}
 SHG: P(2\omega_1) &= \varepsilon_0 \chi^{(2)} E_1^2, \\
 SHG: P(2\omega_2) &= \varepsilon_0 \chi^{(2)} E_2^2, \\
 SFG: P(\omega_1 + \omega_2) &= 2\varepsilon_0 \chi^{(2)} E_1 E_2, \\
 DFG: P(\omega_1 - \omega_2) &= 2\varepsilon_0 \chi^{(2)} E_1 E_2^*, \\
 OR: P(0) &= 2\varepsilon_0 \chi^{(2)} (E_1 E_1^* + E_2 E_2^*).
 \end{aligned}
 \tag{Eq. 3.17}$$

The amplitude of the optical fields of each frequency can be expressed in terms of the wave vectors  $\vec{k}_i$ . The intensity variation of the resulting field with the wave vector  $\vec{k}_3$  is then governed by the wave vector mismatch  $\Delta\vec{k}$ :<sup>189,201</sup>

$$\Delta\vec{k} = \vec{k}_1 + \vec{k}_2 - \vec{k}_3.
 \tag{Eq. 3.18}$$

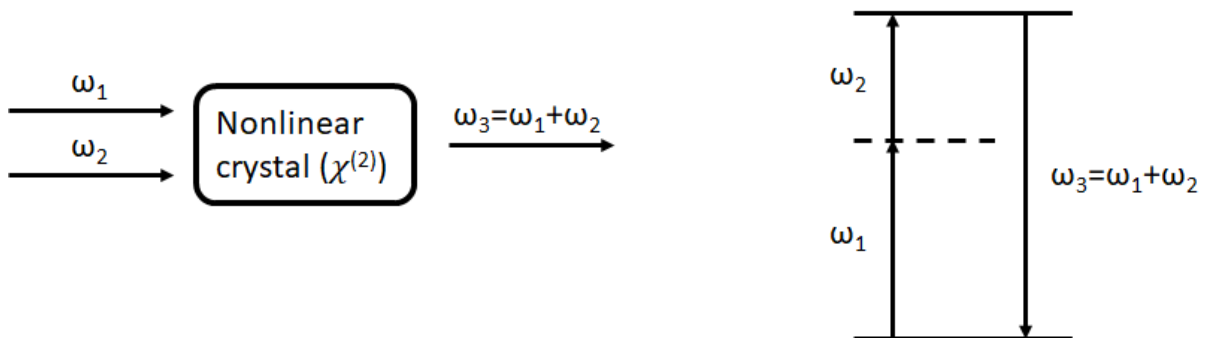
When  $\Delta\vec{k} = 0$ , the phase matching condition is met and the maximum amplitude is produced.

### Sum Frequency Generation

As depicted in **Eq. 3.17** the nonlinear polarization of SFG processes is given by:<sup>210,211</sup>

$$P(\omega_1 + \omega_2) = 2\varepsilon_0 \chi^{(2)} E_1 E_2.
 \tag{Eq. 3.19}$$

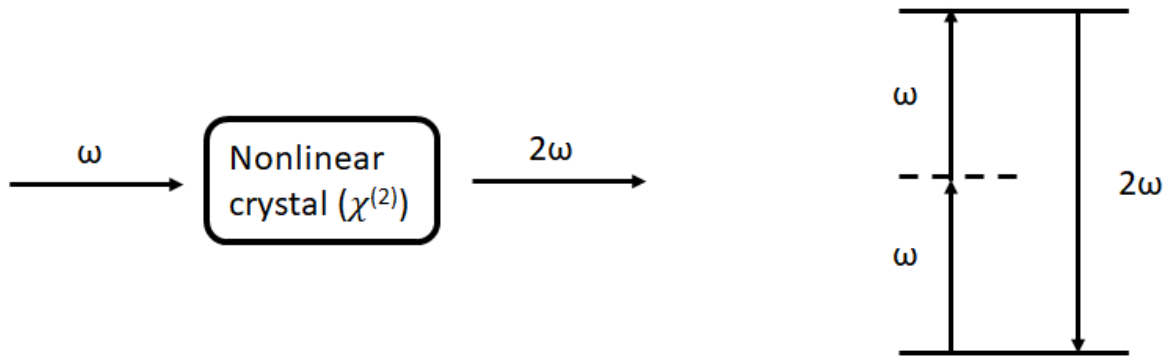
In case of SFG, photons with two different frequencies  $\omega_1$  and  $\omega_2$  are superimposed in the nonlinear crystal, generating photons with the frequency  $\omega_3 = \omega_1 + \omega_2$ . This second order nonlinear process is schematically shown in **Scheme 3.3**. Tunable lasers make use of SFG, for example using two Vis light frequencies to produce radiation in the UV region.



**Scheme 3.3:** Scheme of sum frequency generation in a nonlinear crystal of second order with two incident frequencies  $\omega_1$  and  $\omega_2$  and the additional output frequency  $\omega_3$  (left). Scheme of an energy diagram showing the summation of the energy of both frequencies  $\omega_1$  and  $\omega_2$  equal to the energy of the output frequency  $\omega_3$  (right).

## Second Harmonic Generation

SHG describes a special kind of SFG transforming two photons with the same frequency  $\omega$  into one photon of frequency  $2\omega$ ,<sup>210,211</sup> as displayed in **Scheme 3.4**.



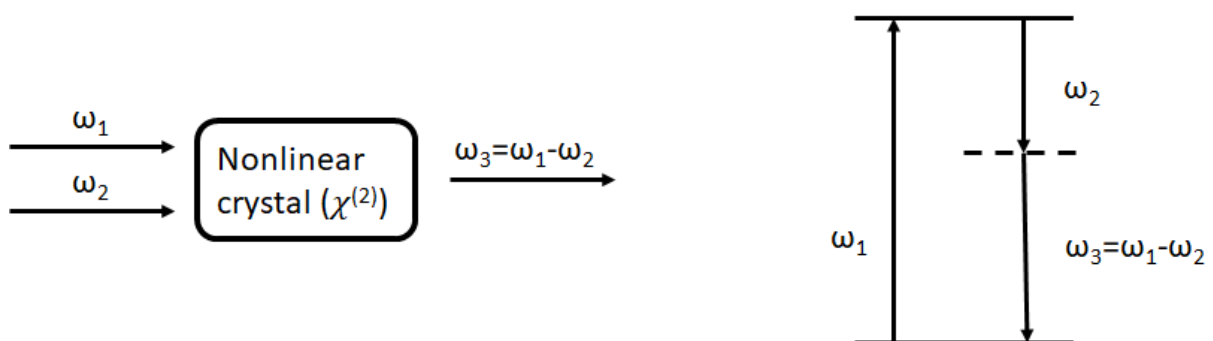
**Scheme 3.4:** Scheme of SHG in a nonlinear crystal of second order with incident photons of identical frequency  $\omega$  and the additional frequency-doubled output  $2\omega$  (left). Scheme of an energy diagram showing the summation of the energy of two photons with frequencies  $\omega$  equal to the energy of one photon with the output frequency  $2\omega$  (right).

In the present thesis SHG was applied for the excitation of Ivocerin in the Vis light-induced fs PLP experiments.

## Difference Frequency Generation

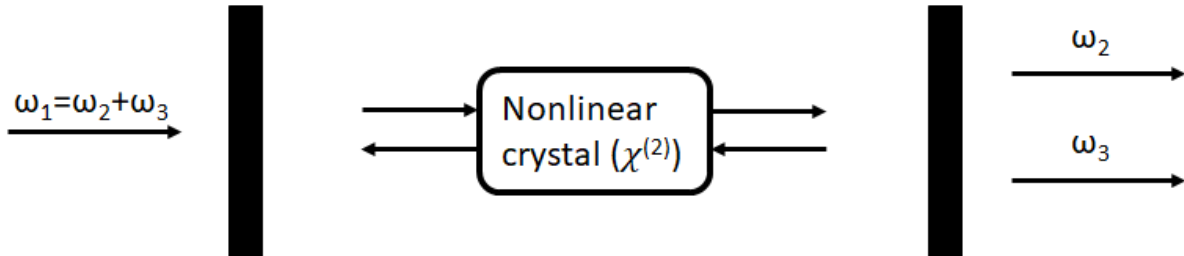
DFG (**Scheme 3.5**) can be described by the fourth term of nonlinear polarization:<sup>210,211</sup>

$$P(\omega_1 - \omega_2) = 2\varepsilon_0\chi^{(2)}E_1E_2^* . \quad \text{Eq. 3.20}$$



**Scheme 3.5:** Scheme of difference frequency generation in a nonlinear crystal of second order with incident photons of the frequencies  $\omega_1$  and  $\omega_2$  and the generated photons with the output frequency  $\omega_3$  as difference of  $\omega_1$  and  $\omega_2$  enhancing the field of  $\omega_2$  (left). Scheme of an energy diagram showing the difference of the energy of two photons with frequencies  $\omega_1$  and  $\omega_2$  into a third photon with the output frequency  $\omega_3$  (right).

Due to energy conservation, the generation of photons  $\omega_3 = \omega_1 - \omega_2$  as depicted in **Scheme 3.5** requires the destruction of input photons of higher frequency  $\omega_1$  and the creation of further photons of the lower input frequency  $\omega_2$  at the same time. This process is initiated when the higher input frequency photon  $\omega_1$  excites an electron to a virtual level within the crystal band gap, followed by the production of two photons of lower frequencies  $\omega_2$  and  $\omega_3$ . If desired, one of the frequencies can be enhanced by seeding the crystal with a weak optical field, known as the signal at lower input frequency  $\omega_2$ . The second frequency  $\omega_3$ , known as the idler, is also produced, but it is much weaker. This amplified process is known as optical parametric amplification. The emission process can occur in the absence of the optical field of  $\omega_2$ . However, since the resulting fields are much weaker, this process is known as parametric fluorescence. If a nonlinear crystal is placed in an optical resonator (**Scheme 3.6**), the waves with the frequencies  $\omega_1$  and  $\omega_2$  oscillate within the resonator, leading to a strong amplification of the optical field of  $\omega_2$  and  $\omega_3$ . Such a setup is called optical parametric oscillator (OPO).<sup>210</sup> OPOs are often used in tunable lasers, in particular for the generation of Vis and IR wavelengths. Theoretically, any frequency satisfying the equation  $\omega_1 = \omega_2 + \omega_3$ , can be produced in an OPO, however practical limitations arise in finding suitable nonlinear crystals with strong  $\chi^{(2)}$  in the desired wavelength range.

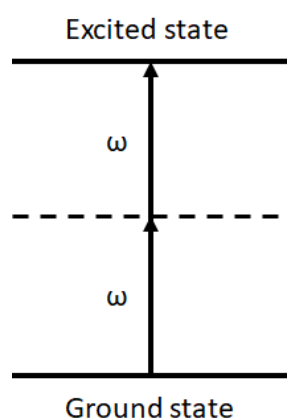


**Scheme 3.6:** Scheme showing the principle of difference frequency generation in an optical parametric oscillator (OPO). Photons of the incident frequencies  $\omega_1$  and  $\omega_2$  oscillate in a resonator with a nonlinear crystal of second order, generating photons of  $\omega_2$  and a third frequency  $\omega_3$ , thus enhancing the optical field of  $\omega_2$ . Due to the oscillation this process repeats and further enhances  $\omega_2$  and  $\omega_3$ .

### 3.3.2 Nonlinear Processes of Third Order

#### Two Photon Absorption

2PA is an intensity-dependent, third order nonlinear process, which describes atoms making transitions from the electronic ground state to an excited electronic state via a virtual state by simultaneous absorption of two photons of the same wavelength (**Scheme 3.7**). This process was first discovered by Kaiser and Garrett<sup>212</sup> and described by Maria Goeppert Mayer<sup>128</sup> in 1931. The absorption cross-section shows a linear dependency on the laser intensity with the coefficient as proportionality constant.



**Scheme 3.7:** Principle of two photon absorption; two photons of the frequency  $\omega$  are simultaneously absorbed via a virtual state, thus exciting electrons into an excited electronic state, as an excitation with photons of  $2\omega$ .

The nonlinearity of 2PA is expressed by the transition rate  $R$ , that scales quadratically with the intensity  $I$ :<sup>210</sup>

$$R = \frac{\sigma^{(2)} I^2}{\hbar \omega}. \quad \text{Eq. 3.21}$$

In this equation,  $\omega$  describes the frequency of the incident light,  $\hbar$  the Planck constant  $h$  divided by  $2\pi$  and  $\sigma^{(2)}$  the 2PA coefficient. Vis light photoinitiators, such as Ivocerin, can potentially be excited with high intensity NIR light based on a 2PA process as applied in the NIR-light fs 2P PLP experiment.

#### The Optical Kerr Effect

The optical Kerr-Effect is a refractive nonlinear process of third order that enables ultrashort laser pulses of less than 100 fs. It is based on self-focussing of the laser beam during the propagation through the laser crystal due to the intensity-dependent refraction index:<sup>207</sup>

$$n(I) = n_0(\omega) + n_2(\omega) \cdot I. \quad \text{Eq. 3.22}$$

The radial variation of intensity inherent in a Gaussian-shaped laser beam causes a stronger focussing effect in the centre of the beam, where the intensity is much higher, and weaker focussing effect in the lower intensity regions. The result of this is known as self-focussing and results in an increase in the pulse intensity as light propagates through the nonlinear medium. Additionally, self-phase-modulation,<sup>207</sup> also known as temporal Kerr effect,<sup>210</sup> is a further phenomenon causing pulse compression but in the temporal domain instead of the spatial domain. At high intensities the nonlinear third-order susceptibility in the refractive index  $n_2$  of **Eq. 3.22** causes dispersion of the pulse maximum propagating through the medium. Hence, the spectral broadening causes a compression of the pulse duration. Almost every modern Ti:Sapphire fs laser system, as the one that was used for the current thesis, makes use of self-phase modulation and the Kerr-Lens-effect in the nonlinear crystal for mode-locking as a powerful technique for the generation of ultrashort, highly intense laser pulses.

As self-phase modulation leads to a spectral broadening of highly intense laser pulses, thin nonlinear crystals with third order susceptibility can be used for the generation of a white light (WL) continuum focussing laser pulses. Such crystals, for example  $\text{CaF}_2$ , are used in transient fs absorption spectroscopy experiments for the generation of broadband probe pulses.

### 3.4 Transient Absorption Spectroscopy

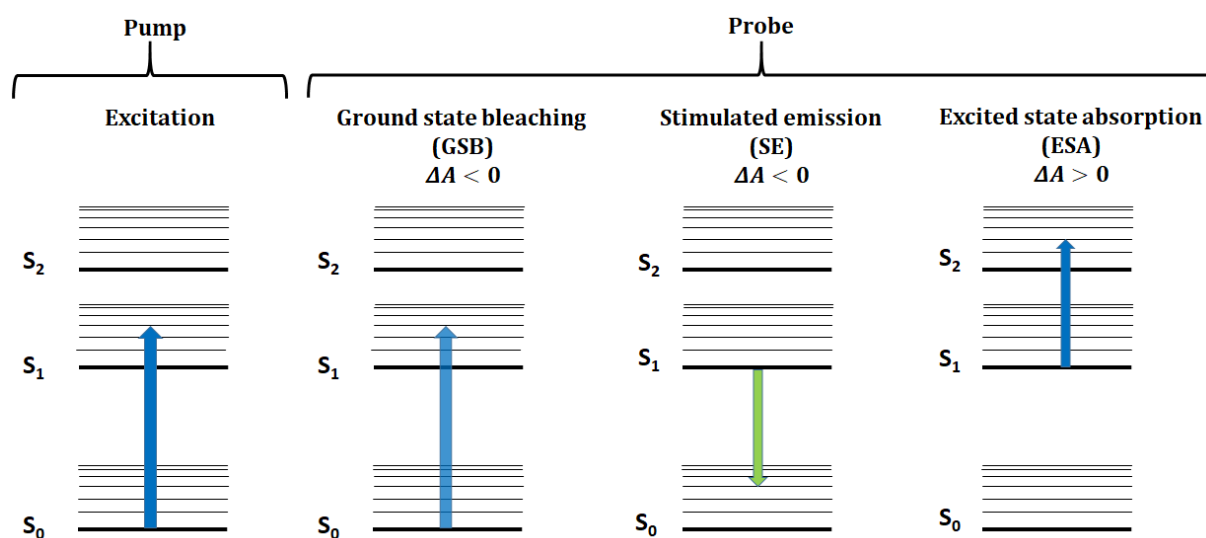
In order to characterize and understand relaxation processes after photoexcitation, carefully designed experiments are necessary to allow a thorough interpretation. Spectroscopic methods are effective techniques to observe electronic transitions within photoexcited molecules and immediate electronic processes after excitation. Time-resolved pump-probe experiments can provide information about the occurring relaxation processes in a photo-excited molecule and about the channel branching of relaxation pathways.

Transient absorption spectroscopy is a commonly employed method to measure the time-resolved change in the absorbance of a system. The laser pulse is divided into two pulses, the excitation pulse and the probe pulse. The excitation pulse is used for photophysical excitation of the sample with desired wavelengths, for example using a nonlinear optical parametric amplifier (NOPA), SHG or Third Harmonic Generation (THG). The probe pulse detects the transient absorption spectrum after excitation of the sample at defined times  $t = t_d - t_0$ , passing a delay stage. Here  $t_d$  is the delay time and  $t_0$  is the time at which the sample is excited. With the aid of a translation stage,  $t_d$  can be varied and both pulses are brought to overlap in space

and time at the location of the sample. This allows the observation and analysis of the relaxation dynamics of excited molecules.<sup>213,214</sup> Finally, subtracting the ground state absorption spectrum of the sample without excitation  $A_{\omega,t_0}$  from the transient absorption spectrum  $A_{\omega}(t)$  results in a differential absorption  $\Delta A(t, \lambda)$  according to equation:

$$\Delta A(t, \lambda) = A_{\omega}(t, \lambda) - A_{\omega,t_0}(\lambda). \quad \text{Eq. 3.23}$$

In principle, different processes can be observed in transient absorption spectroscopy (**Scheme 3.8**). Ground state bleaching (GSB) describes a depletion of the ground state after photoexcitation ( $\Delta A < 0$ ). In stimulated emission (SE,  $\Delta A < 0$ ) the probe pulse triggers relaxation of excited electrons into the ground state by emitting photons. Excited state absorption (ESA) with  $\Delta A > 0$  is a process where an already excited electron enters a higher electronically excited state by absorbing a second photon.



**Scheme 3.8:** Possible contributions to the spectrum  $\Delta A$  of the transient response after photo excitation, presented in a simplified Jablonski diagram. The electronic ground state  $S_0$  and excited electronic states  $S_n$  are shown as thick lines, vibrational states as thin lines, transitions are implicated as vertical arrows. The possible photophysical processes are ESA with  $\Delta A > 0$ , stimulated emission (SE) with  $\Delta A < 0$ , ground state bleaching (GSB) with  $\Delta A < 0$  (from left to right).

Transient spectra can be analysed by means of a decay associated difference spectrum (DADS), also known as global analysis. Herein, a parametric model provides a decomposition basis set of time constants for all probed wavelengths without *a priori* knowledge of the excited state processes. Such a model involves one exponential or stretched exponential function to simultaneously fit all of the recorded transient absorption data, with the corresponding amplitudes resulting in a DADS spectrum. The size of the basis set for the data description model can be tested for with any desired complexity. However, it is not trivial to find a suitable

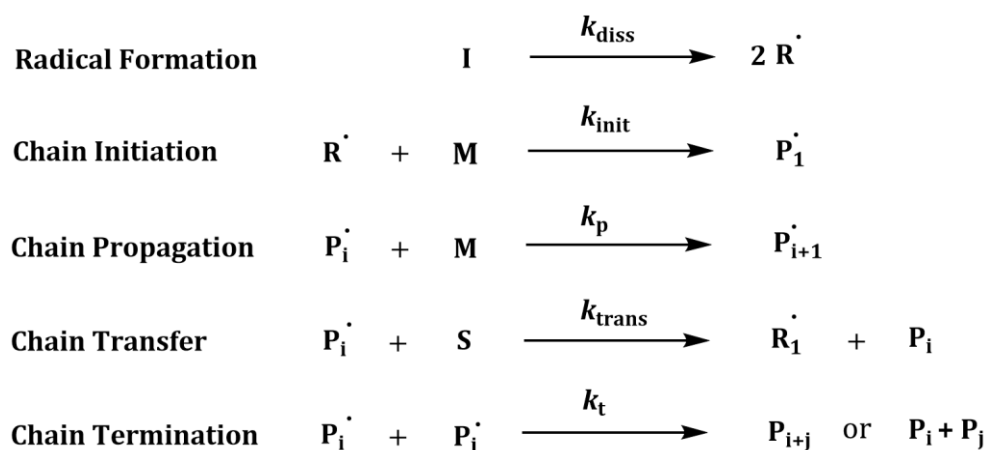
number of parameters for proper fitting. A high number of selected parameters potentially exceed the actual number of physical processes occurring. Also, the recovery of ultrashort lifetimes may be limited by instantaneous response functions and coherent artifacts.<sup>215,216</sup> Further, multiexponential functions are known to cause problems due to their sensitivity of initial values, as noise-induced local minima potentially interfere the sum-of-error surface optimization.<sup>217,218</sup> Therefore, to find the best quality fit, it is often better to choose a minimal descriptive model instead of risking over parameterization using too complex functions.<sup>219</sup>

In the current thesis, a common set of parameters is obtained, including the rise time  $\tau_0$ , time constants  $\tau_i$  and amplitudes  $A_i$  for photo-physical and photo-reactive process  $i$  using the program Matlab with a previously developed algorithm at KIT.<sup>220</sup> During analysis, every probed wavelength is analyzed with a multiexponential function using the parameters from the script. While a positive amplitude describes a decreasing transient response, a negative amplitude describes a rising transient response. Subsequently, fitting the probed wavelengths with a multi-exponential function as expressed in **Eq. 3.24** using the obtained time constants  $\tau_i$  and amplitudes  $A_i$  serves to validate the quality of the parameters:

$$\frac{1}{2} \left( 1 + \operatorname{erf} \left( \sqrt{(4 \ln(2))} \cdot (t - t_0) / \tau_0 \right) \right) \cdot \sum_i \left( A_i \exp \left( - \frac{(t - t_0)}{\tau_i} \right) \right). \quad \text{Eq. 3.24}$$

### 3.5 Free Radical Polymerization

FRP entails a mechanism based on the generation of primary radicals  $R^\cdot$  by either thermal or photo-induced decomposition of a thermal or photoinitiator  $I$  (**Scheme 3.9**). These primary radicals subsequently initiate polymer chain growth  $P_1$  by reaction with the (activated) double bond of a monomer  $M$ , subsequently leading to chain propagation  $P_{i+1}$ . In the presence of transfer agent reactants  $S$ , polymer chain growth can be terminated by transferring the radical position to another polymer chain  $R_1$ . A recombination of either two radical polymer chains or polymer chains with free initiator radical ( $P_{i+j}$ ) as well as disproportionation reaction of radical polymer chains ( $P_i + P_j$ ) finally causes termination of polymer chain growth.<sup>221</sup>



**Scheme 3.9:** Mechanism of FRP. After thermally or photochemically induced fragmentation of the initiator molecule  $I$  into free radicals  $R^{\cdot}$ , chain growth  $P_1^{\cdot}$  is initiated by the reaction of radicals with a monomer unit  $M$  (chain initiation). The chains grow  $P_{i+1}^{\cdot}$  (chain propagation) until terminated (chain termination) by either disproportionation  $P_i^{\cdot} + P_j^{\cdot}$  or combination  $P_{i+j}^{\cdot}$  of polymer chains. When an additional chain transfer agent  $S$  is present, the radical character can also be transferred from one chain to another  $R_1^{\cdot}$ , leading to termination of the initial chain  $P_i^{\cdot}$ .

In order to execute radical polymerization processes efficiently, it is essential to fundamentally understand the kinetics of each individual polymerization step. However, the determination of polymerization kinetics can be highly challenging, due to the often complex nature of polymerization reactions. Each FRP commences with either the thermal or photo-induced decomposition of an initiator into radicals as schematically shown in **Scheme 3.9**. The kinetics of the initiator decay are crucial as they define the rate and efficiency of the entire polymerization. The time dependent decay of the initiator concentration  $\frac{d[I]}{dt}$  is given by:<sup>221</sup>

$$-\frac{d[I]}{dt} = k_{\text{diss}}[I]. \quad \text{Eq. 3.25}$$

Note that – keeping in line with the convention in literature –  $k$  is used to indicate rate coefficients in this subchapter, different to the photon wavenumber in previous chapters. In **Eq. 3.25**,  $k_{\text{diss}}$  represents the rate coefficient of the dissociation reaction. However, not every initiator radical automatically reacts with a monomer molecule. It has to be considered that the radicals are enclosed in a solvent cage, which they must escape before they can react. Moreover, radicals can not only react with the monomer, but there are also alternative reaction routes, for example recombination with other initiator radicals. Therefore, a further quantity, the initiator efficiency  $\gamma$ , is introduced, which plays an important role in the initiation reaction and enables determination of the polymerization rate  $R_d$ :<sup>221</sup>

$$R_d = \frac{d[I]}{dt} = -2\gamma \frac{d[I]}{dt} = 2\gamma k_{\text{diss}}[I]. \quad \text{Eq. 3.26}$$

Regarding the initiation reaction of an initiator radical with a monomer, the addition rates of symmetric and asymmetric radicals may differ, resulting in different rate coefficients  $k_1$  and  $k_2$  for each individual addition step. The initiation rate is given by the following rate law:<sup>221</sup>

$$R_i = k_i[M][I], \quad \text{Eq. 3.27}$$

where  $[M]$  represents the monomer concentration,  $[I]$  is the concentration of both types of radicals  $I_1$  and  $I_2$  and  $k_i$  is the composite of both rate coefficients  $k_1$  and  $k_2$ :

$$k_i = \frac{k_i^{(1)} + k_i^{(2)}}{2}. \quad \text{Eq. 3.28}$$

Once the rate coefficients of the different steps are known, it is possible to predict the outcome of polymerizations. To gain knowledge of the kinetics, accurate experiments are the first critical step, followed by precise analysis of the obtained data.

Following the kinetics of the initiation, the next critical step is to understand the kinetics of the chain propagation. The propagation rate with the coefficient  $k_p^i$  is given by:<sup>221</sup>

$$-\frac{d[M]}{dt} = \sum_i k_p^i [R_i][M]. \quad \text{Eq. 3.29}$$

Investigation of liquids have shown that molecules collide with a rate of about  $10^{12} \text{ s}^{-1}$ , while  $10^9$  collisions of propagating chain radicals with monomer units are required to successfully continue propagation reactions. Thus, the propagation reaction in FRP is chemically controlled. This observation is valid up to very high monomer conversions of >80%. At such high conversions the viscosity of the liquid remarkably increases, decreasing the ability of small monomer units to move freely. As noted via the index  $i$ ,  $k_p^i$  is also – mildly – dependent on the chain length of the propagating macroradical. Some studies have suggested that there is a significant difference in addition rate between the early steps of chain propagation with only a few monomer units and long radical chains.<sup>222</sup> Steric effects of the chemical structure of the monomers and the resulting radical chains also affect the rate of chain growth. Conceptually, it is important to note the antagonistic reactivity of the propagating radical and its corresponding monomer unit – a reactive monomer generates a relatively sluggishly propagating radical (for example styrene). In any case it is critical that a radical chain needs to live sufficiently long to survive the  $10^9$  collisions before it successfully reacts with a further monomer unit. A practical method to determine the propagation rate coefficient  $k_p$  is the PLP-SEC method,<sup>87</sup> which is explained in more details in **Section 3.6**.

If chain transfer reactants  $S$  are present in the polymerization mixture – either inherently or deliberately added - the propagating chain can abstract a weakly bonded atom, such as hydrogen, to generate a more stable radical species. As a consequence, the generated small radical initiate a new macromolecular growth process, limiting the overall achievable molecular weight. Kinetically, the transfer rate coefficient is often ratioed with the propagation rate coefficient, affording the transfer constant  $C$ :<sup>221</sup>

$$C = \frac{k_{\text{trans}}}{k_p}. \quad \text{Eq. 3.30}$$

The effect of chain transfer on the polymerization depends on the propagation rate coefficient  $k_p$ , the reinitiation rate coefficient  $k_{re}$  and the transfer rate coefficient  $k_{\text{trans}}$ , which can be rationalized in four scenarios. In the first case  $k_p > k_{\text{trans}}$  and  $k_{re} = k_p$ , resulting in a decrease of the number average molecular weight  $M_n$  with almost no effect on the polymerization rate  $R$ . In the second case,  $k_p < k_{\text{trans}}$  and  $k_{re} = k_p$ , leading to a significant decrease of  $M_n$  with no measurable effect on  $R$ , called telomerization. In the third case,  $k_p > k_{\text{trans}}$  and  $k_{re} < k_p$ . Here,  $M_n$  and  $R$  decrease at the same time, an effect known as rate retardation. Finally, in the fourth case  $k_p < k_{\text{trans}}$  and  $k_{re} < k_p$ ,  $M_n$  as well as  $R$  decrease strongly, termed degenerative chain transfer. In summary, the use of a chain transfer agent (CTA) can cause a reduction in the average molecular weight of polymer chains, yet also lead to a concomitant reduction in the rate of polymerization, depending on the characteristics of the CTA and monomer(s). Further, the concentration of the used CTA  $[S]$  significantly affects the degree of polymerization  $\bar{D}_p$ , introduced by the Mayo equation:<sup>223,224</sup>

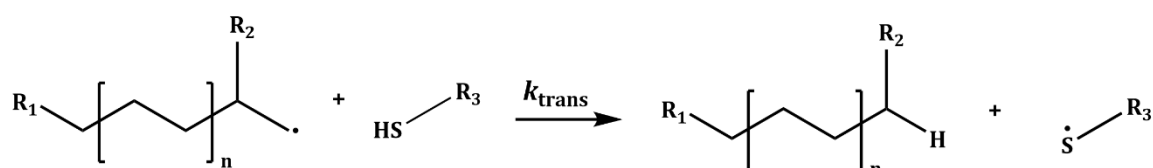
$$\frac{1}{\bar{D}_p} = C \frac{[S]}{[M]} + \frac{1}{\bar{D}_{p_0}}, \quad \text{Eq. 3.31}$$

where  $\bar{D}_{p_0}$  describes the degree of polymerization in the absence of a solvent. As alluded to above, it is important to note that some chain transfer events cannot be avoided, such as inherent transfer to monomer (i.e. the monomer acts as the CTA). Equally, transfer to solvent can be prevalent as the solvent concentration in solution is usually high. At elevated monomer to polymer conversions, transfer to polymer can become relevant, resulting in long- and short-chain branching. Interestingly, transfer to polymer constants are higher than the corresponding transfer to monomer constants.<sup>221</sup>

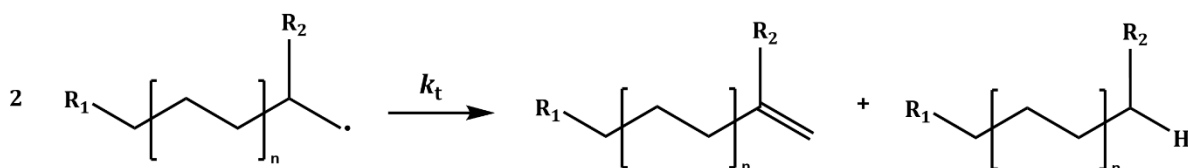
Chain termination is considered as the most complex step in the mechanism of FRP.<sup>225</sup> A termination reaction can either occur via the combination of two propagating chains or via disproportionation, characterized by the abstraction of a hydrogen atom from one chain, forming

a double bond at the terminus of the corresponding polymer chain, as depicted in **Scheme 3.10**. In principle both termination reactions are possible, while their relative propensity depends on the structure of the monomer unit. In addition, higher temperatures slightly favour disproportionation reactions. Generally, the termination kinetics are not affected by the two termination modes. However, the MWD is affected by the termination modes. Most importantly, the termination rate coefficient critically depends on the viscosity of the system, the chain length of the terminated polymer, the temperature and pressure and – as a corollary of its dependence on viscosity – on the monomer to polymer conversion.

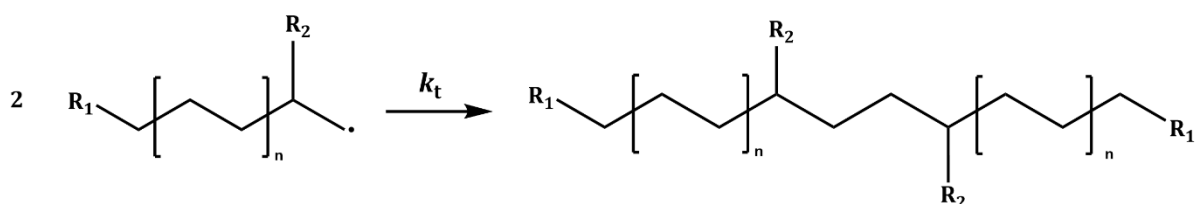
#### Chain Transfer



#### Chain Combination



#### Chain Disproportionation

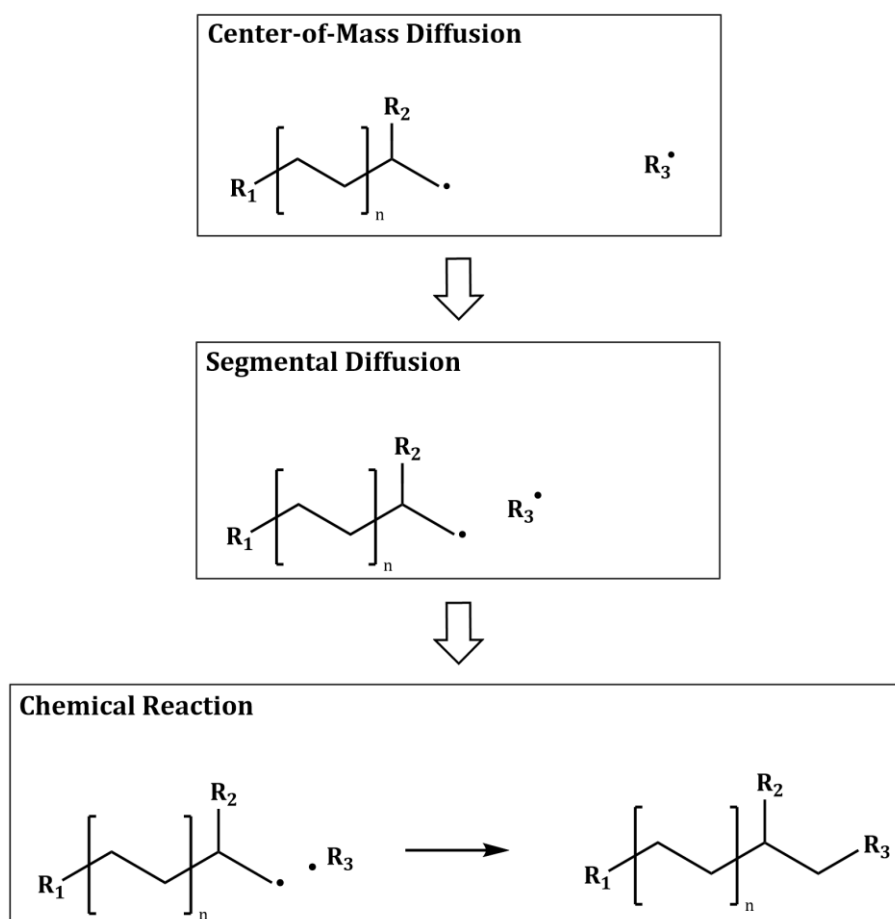


**Scheme 3.10:** Scheme of chain transfer and chain termination via chain combination and disproportionation.

Termination reactions can generally be described as a three-step process, as shown in **Scheme 3.11**: the first step is called center-of-mass diffusion of the polymer chain through the liquid, the second step is so-called segmental diffusion of the chain ends towards each other and the third step is the actual chemical reaction. The overall termination reaction is governed by the slowest step, which is either step 1 or 2. As a diffusion controlled reaction, the termination rate coefficient ranges between  $10^8$  and  $10^6 \text{ L mol}^{-1} \text{ s}^{-1}$ . Determining termination rate coefficients – including average ones – is highly challenging due to the above noted

dependencies. Thus, the termination rate coefficient is often reported as an average quantity  $\langle k_t \rangle$  involving two individual radical species  $R_i$  and  $R_j$  as illustrated by **Eq. 3.32**:

$$\langle k_t \rangle = \frac{\sum_i \sum_j k_t^{ij} [R_i][R_j]}{(\sum_i [R_i])^2}. \quad \text{Eq. 3.32}$$



**Scheme 3.11:** Scheme of three-step termination of polymer chains with the center-of-mass diffusion as the first, the segmental diffusion as the second and the chemical reaction as the third step.

Pulse-induced laser polymerization (PLP) is a specific type of FRP making use of pulsed laser systems. The technique was first introduced by Olaj<sup>87</sup> in 1987, who reported a laser-based method to precisely determine the propagation rate coefficient of polymer reactions. A first initial laser pulse generates radicals through the decomposition of photoinitiator molecules. These radicals initiate polymer chain growth by reaction with monomer units. Subsequent pulses generate new radicals, which – in addition to initiating further polymer chains growth – terminate radical chains that were able to grow in the dark time between consecutive pulses. Thus, the PLP technique does not only allow determination of propagation rate coefficients, but also enables a defined length of polymer chains depending on the applied pulse frequency,

enabling chain length control. The defined chain length ( $M_i$ ) of PLP generated polymers can be read out from SEC traces. The molecular weights of the polymer chains are multiples of each other and can be assigned to the inflection points of the SEC traces, which are represented by the peaks of the first derivative.

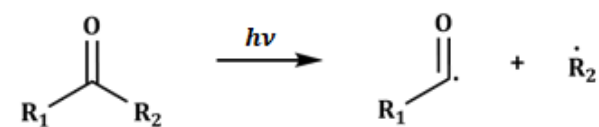
Reading out the multiple molecular weight of the polymer chains allows the determination of the propagation rate coefficient, using the following equation:<sup>87</sup>

$$M_i = k_p c_M i \nu^{-1} . \quad \text{Eq. 3.33}$$

The multiple molecular weights  $M_i$  of the polymer chains are given by the product of the propagation rate coefficient  $k_p$ , the initial concentration of the monomer  $c_M$  and the dark time between the laser pulses  $\nu^{-1}$ .

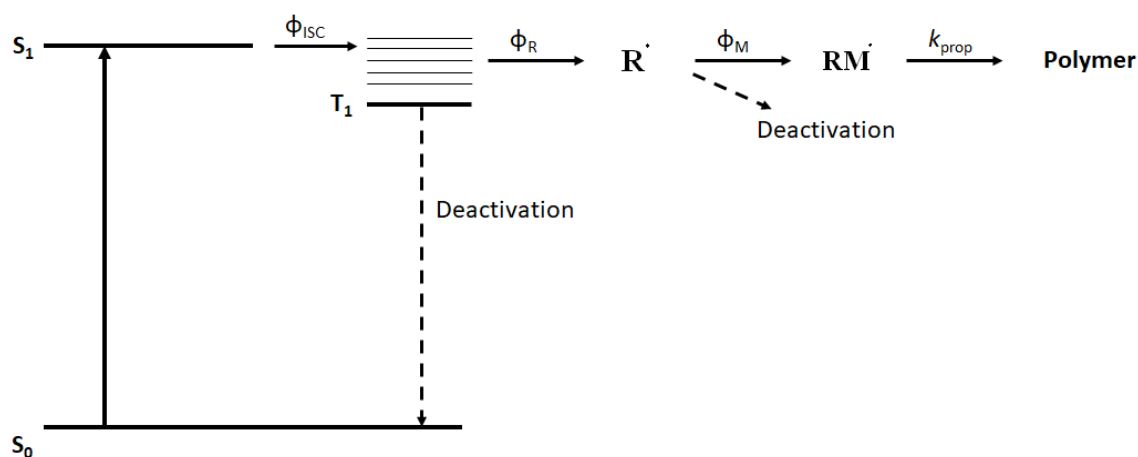
### 3.5.1 Photoinitiators

Photoinitiators are photo-sensitive molecules, which often absorb UV or Vis light, followed by decomposition into radicals. The main advantage of photo-induced reactions is the temporal control over the start and end point of decomposition via the on-off mechanism of light. In contrast to thermally activated processes, the rate of polymerization is independent of the system temperature, but is instead dependent on the light intensity. The decomposition of photoinitiators is schematically shown in **Scheme 3.12**.



**Scheme 3.12:** Principle of photo-induced radical generation of photoinitiators.

Typically, photoinitiators can be defined in two types. Type 1 initiators undergo unimolecular bond breakage, whereas type 2 initiators react with a second molecule to generate radicals. When choosing an initiator for a reaction there are some critical criteria that need to be taken into account. The most important aspect to consider is the spectral region where the initiator absorbs light. In order to optimize polymerization efficiency, it is critical to choose an initiator that absorbs light at the incident wavelength, whereas the monomer must not absorb. However, it is not only the ability to absorb, but the initiator should also be characterized by a high efficiency of forming radicals. As an illustration, a simplified scheme of the Jablonski (**Scheme 3.13**) serves to better explain the efficiency of an initiator.



**Scheme 3.13:** Simplified Jablonski diagram of photochemically induced initiator decomposition, showing the quantum yield  $\phi$  of each step of primary free radical production and the possible competitive channels. After photoexcitation from  $S_0$  into  $S_1$ , the initiator can change its multiplicity from singlet ( $S_1$ ) into triplet ( $T_1$ ) via ISC. From here, the initiator can either form a radical  $R$  or be deactivated, for example by quenching processes. A step prior to polymer chain growth, radicals need to initially react with a monomer unit to induce polymerization. Alternatively, deactivation processes can stop the reaction.

As described in **Section 3.1**, a molecule needs to be excited by a suitable light source prior to reaction with a monomer. Most radicals are formed from triplet states, so the spin multiplicity has to be changed from singlet to triplet via ISC. Due to the affinity of  $n\pi^*$  transitions, ketones are prone to very high ISC quantum yields  $\Phi_{ISC}$  of close to 1.<sup>226</sup> Besides generating radicals with the quantum yield  $\Phi_R$ , which can subsequently lead to chemical reactions, there are multiple competitive processes that can occur, for example quenching of the excited triplet state by oxygen. This is why samples are usually purged with nitrogen prior to irradiation. Even if radical generation has been successful, the radical still has to overcome solvent effects that can lead to deactivation. The quantum yield of the final reaction of a radical with a monomer is expressed by  $\Phi_M$ . All these single steps have associated efficiencies. The overall quantum yield  $\Phi$  can be calculated by:

$$\Phi = \Phi_{ISC} \cdot \Phi_R \cdot \Phi_M \leq 1. \quad \text{Eq. 3.34}$$

Considering that the mechanism of initiator decomposition is often more complex, accompanied by the generation of more than one radical species, the kinetics are much more complicated. Even some thermal initiators can serve as UV absorbing, type 1 photoinitiators, undergoing a *cis* to *trans* isomerization before bond cleavage. This additional step plays a further role in the efficiency and kinetics, since it requires more time.

The available concentration of radicals  $\rho$  induced by the application of light can be calculated via

$$\rho = 2\Phi \frac{n_{\text{abs}}}{V}, \quad \text{Eq. 3.35}$$

with illuminated volume  $V$  and the absorbed number of photons<sup>221</sup>

$$n_{\text{abs}} = \frac{E_p}{E_\lambda} \cdot (1 - 10^{-\varepsilon \cdot c \cdot d}). \quad \text{Eq. 3.36}$$

In **Eq. 3.36**  $E_p$  represents the deposited energy and  $E_\lambda$  the energy of one mole of photons at the irradiation wavelength  $\lambda$ . Further  $\varepsilon$  describes the molar extinction coefficient of the initiator molecule as a function of  $\lambda$ ,  $c$  is the initiator concentration and  $d$  the optical pathlength of the irradiated sample.

### 3.5.2 Thermal initiators

Thermal initiators are compounds that decompose under the application of heat. Mostly, thermal initiators can be classified as azo- or peroxy compounds (**Scheme 3.14**).



**Scheme 3.14:** Schematic representation of the structure of azo- and peroxy compound usable as thermal initiators.

The half time ( $t_{1/2}$ ), which describes the period that is necessary to decompose the half of the initial initiator molecules is defined by:

$$t_{1/2} = \frac{\ln(2)}{k_d}. \quad \text{Eq. 3.37}$$

Decomposition temperature of thermal initiators can have a broad range from ambient temperature up to more than 100 °C. Depending on the solvent and the desired reaction conditions, there is a broad range of possible initiators. In **Chapter 7** of this thesis a thermally activated polymerization experiment in aqueous solution was performed. Therefore, a water-soluble azo-compound, azobisisobutyronitrile (AIBN), was chosen.

### 3.5.3 Gold Nanorods

Gold, one of the most common precious metals, possesses a range of intriguing properties. When gold is confined to the size of  $10^{-9}$  m, known as nanostructures, the electronic, optical, and catalytic characteristics differ significantly from bulk gold.<sup>227,228</sup> This phenomenon arises due to the substantial increase in the surface area-to-volume ratio, resulting in a higher number of surface electrons and the spatial confinement of electrons. This confinement leads to highly interesting properties, including shifts in energy levels, nonlocal dielectric responses, and enhanced optical transitions. The shape of the nanoparticles plays a crucial role in determining the optical properties. Gold nanoparticles have experienced a surge in research interest due to their numerous advantageous properties, making them promising candidates for applications in photonics, electronics, catalysis, and biology.<sup>227,229</sup> One of the most fascinating aspects of metallic nanoparticles is their localized surface plasmon resonance (LSPR), which are electromagnetic modes related to the collective oscillation of free electrons. When exposed to resonant excitation, metallic nanoparticles exhibit a unique ability to concentrate free-space optical fields within subwavelength regions, enabling an extreme enhancement of the electric field. This phenomenon has paved the way for new mechanisms, including plasmon-enhanced spectroscopy,<sup>230</sup> high harmonic generation,<sup>231</sup> optical antenna effects,<sup>232</sup> and photothermal conversion.<sup>39,163–165,169,170,233</sup>

#### Local Surface Plasmon Resonance

Plasmonic resonances are the collective oscillation of free conduction electrons in solids, first described by Mie.<sup>166</sup>

The extinction efficiency of a nanoparticle exposed to an EM field can be expressed by the following equation:<sup>234</sup>

$$Q_{\text{ext}} = \frac{C_{\text{ext}}}{G}, \quad \text{Eq. 3.38}$$

where the extinction cross-section  $C_{\text{ext}}$  is defined as the sum of the absorption cross-section  $C_{\text{abs}}$  and scattering cross-section  $C_{\text{sca}}$ .<sup>234</sup>

$$C_{\text{ext}} = C_{\text{sca}} + C_{\text{abs}}, \quad \text{Eq. 3.39}$$

and  $G = \pi a^2$  is the cross-sectional area of a particle with radius  $a$ .

In the case of nanoparticles smaller than the incident wavelength, plasmonic properties can be described by a quasistatic approximation of Mie,<sup>161,235–237</sup> treating the electromagnetic field as uniform throughout the particle:

$$C_{\text{ext}} = \frac{9V\epsilon_m^{3/2}}{c} \cdot \frac{\omega\epsilon_2(\omega)}{[\epsilon_1(\omega) + 2\epsilon_m]^2 + \epsilon_2(\omega)^2}, \quad \text{Eq. 3.40}$$

where  $V$  is the volume of the particle,  $v_{\text{Light}}$  the speed of light,  $\omega$  the angular frequency of the incident light,  $\epsilon_m$  the dielectric constant of the medium and  $\epsilon_1$  and  $\epsilon_2$  the real and imaginary part of the dielectric function of the material of the particle. In case of non-spherical nanoparticles, such as AuNR, the absorption cross-section can be described according to the approximation of Rayleigh and Gans:<sup>167,168,234</sup>

$$C_{\text{abs}} = \alpha V, \quad \text{Eq. 3.41}$$

with the absorption coefficient  $\alpha = (4\pi n_i)/\lambda$ . In this equation  $n_i$  represents the imaginary part of the refractive index of the particle.

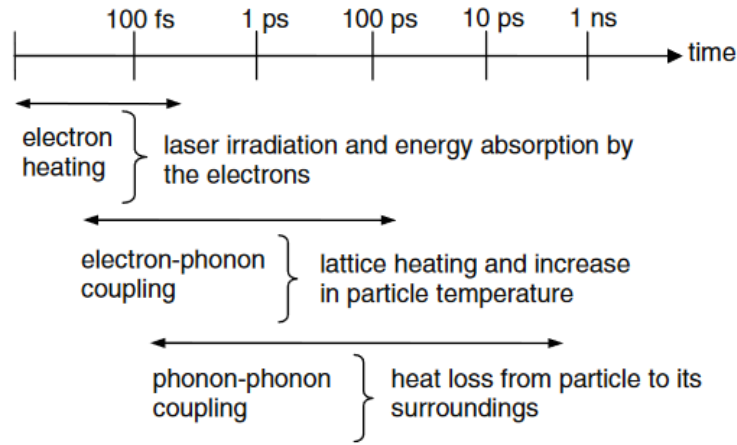
Although the Mie theory<sup>166</sup> for small nanoparticles is size independent, the quantum mechanical theory of Persson<sup>238</sup> predicts a diameter-dependence of the plasmon bandwidth for non-spherical nanoparticles, underpinned by experiments by Kreibig and Frangstein<sup>239</sup> as well as Link and El-Sayed.<sup>240</sup> For small particles the diameter becomes smaller than the mean free path of the conduction electrons resulting in a  $1/r$  dependence of the plasmon bandwidth. Moreover, the extinction of small nanoparticles increases with increasing diameter.<sup>167,241</sup> While the absorption dominates over scattering for small diameter, scattering increases more than absorption for increasing diameters. An increase in the aspect ratio leads to an enlargement of the extinction cross-section for both the longitudinal and transverse plasmon modes, resulting in a shift in the plasmon resonance wavelength.<sup>242,243</sup> However, these shifts differ significantly, with only a few nm for the transverse mode, but up to a hundred nm for the longitudinal mode. As the diameter also affects the aspect ratio; a variation of the diameter shifts the plasmonic resonance wavelength. Notably, as LSPR properties are highly sensitive to the size and shape of metallic nanostructures, including AuNRs, they offer significant opportunities to tailor their properties to specific applications.

The excitation of plasmonic modes can generate electron-hole pairs, thermally heat the lattice due to Joule heating, or be damped by the emission of photons. Sönnichsen *et al.*<sup>244</sup> reported that the relaxation pathway of plasmons is strongly influenced by the aspect ratio. As the aspect ratio increases, the full width at half maximum of the longitudinal plasmon resonance quadratically expands, leading to enhanced radiation damping.<sup>245</sup> In contrast, nanorods with

dimensions in the order of the mean free path of electrons are characterized by electron scattering on the surface.<sup>245</sup> Furthermore, Mulvaney and Hartland<sup>246</sup> found that small diameters of about 20 nm of gold nanorods result in relaxation governed by electron surface scattering, while large diameters tend to lead to photon absorption.

### Local Heating of AuNR

One of the most intriguing properties of AuNRs is the plasmonic heating. Ben-Yakar and colleagues<sup>39</sup> simulated the heating process of 47 x 14 nm<sup>2</sup> AuNR in aqueous solution after excitation with 250 fs laser pulses with an average fluence of 0.47 mJ cm<sup>-2</sup>, providing a timeline of the single steps of heat dissipation, shown in **Scheme 3.15**.



**Scheme 3.15:** The timescale of the fundamental processes of 47 x 14 nm<sup>2</sup> gold nanoparticles after heating with fs laser pulses with 0.47 mJ cm<sup>-2</sup>, as a result of a heating simulation Ben-Yakar and colleagues.<sup>39</sup> Reproduced with permission from [39].

They describe the heating process with a two temperature model for the particles including a temperature for the electron gas  $T_e$  and a temperature for the lattice  $T_l$ . Depending on the absorption cross-section  $C_{abs}$ , the electrons of the nanoparticles absorb photons with the energy  $E_{abs}$  when exposed to laser light with the fluence  $F_{pulse}$ . The relationship can be described mathematically by **Eq. 3.42**:<sup>39</sup>

$$E_{abs} = C_{abs} \cdot F_{pulse} \cdot \quad \text{Eq. 3.42}$$

Thus, the kinetic energy of the electrons is increased due to increasing temperature. As the conductive electrons absorb the laser energy and subsequently thermalize the lattice, the initial heating of gold electrons with the heat capacity  $C_e$ :<sup>247</sup>

$$C_e \frac{dT_e}{dt} = g(T_l - T_e) + \frac{E_{abs}}{V_p \cdot \tau_{pulse}} \cdot \quad \text{Eq. 3.43}$$

Here the particle volume is given by  $V_p$ ,  $\tau_{\text{pulse}}$  is the pulse duration,  $T_e$  and  $T_l$  the temperature of the electrons and the lattice, respectively. Further,  $g$  describes a coupling factor,<sup>39,247,248</sup> which is critical to calculate the heat transfer between electrons and the lattice. Collisions between the electrons distribute the photonic energy, reaching equilibrium after 10-50 fs.<sup>39</sup> During this ultrashort time scale, there is no energy exchange between the electron and the lattice of the particle. Subsequently, the hot electrons dissipate their energy to the lattice by electron-phonon coupling, heating the lattice with the heat capacity  $C_l$  according to **Eq. 3.44**.<sup>39,247</sup>

$$C_l \frac{dT_l}{dt} = g(T_e - T_l) - \frac{\dot{Q}_w}{V_p}. \quad \text{Eq. 3.44}$$

$\dot{Q}_w$  describes the rate of heat loss to the surrounding medium via the surface of the particles  $A_{\text{surface}}$ , which is given by:<sup>39</sup>

$$\dot{Q}_w = A_{\text{surface}} \cdot G \cdot (T_l - T_{w,s}). \quad \text{Eq. 3.45}$$

$\dot{Q}_w$  is dependent on the conductance of the particle-medium interface ( $G$ ) and the water temperature at the surface of the particles ( $T_{w,s}$ ). Usually, the lattice heating process occurs on a time scale of 10-50 ps. The energy is subsequently distributed from the particle to the surrounding medium by phonon-phonon coupling. Equilibrium between the particle and the solvent is reached in 100 ps up to 1 ns, ceasing the temperature increase of the gold nanoparticles. The heat distribution in the surrounding water, featuring the specific heat capacity  $c_{p,w}$  and density  $\rho_w$  can be described with cylindrical coordinates, due to the cylindrical geometry of the AuNRs with the thermal conductivity  $k$ :<sup>39</sup>

$$\rho_w c_{p,w} \frac{\partial T_w}{\partial t} = \frac{\partial}{\partial z} \left( k \frac{\partial T_w}{\partial z} \right) + \frac{1}{r} \frac{\partial}{\partial r} \left( kr \frac{\partial T_w}{\partial r} \right). \quad \text{Eq. 3.46}$$

Following the simulations by Ben-Yakar and colleagues,<sup>39</sup> as a precursor to this work, collaborators at the Queensland University of Technology (QUT)<sup>183</sup> theoretically calculated the heat transfer of AuNR with dimensions of 55 x 15 nm<sup>2</sup> under theoretical exposure of 40 fs laser pulses. Initially, the absorption cross section of the AuNR was quantified by means of finite element model simulations in COMSOL Multiphysics®.<sup>249</sup> These served as the foundation for the calculation of the temperature increase in the AuNR and the surrounding medium after excitation with 800 nm fs laser pulses. Due to the ultrashort pulse duration and the fact that the electron gas thermalises on a shorter time scale than external heat diffusion, the simulation used a one-temperature model, ignoring the electron gas temperature, in contrast to the two-temperature model used by Ben-Yakar and colleagues.<sup>39</sup> Instead, this simulation considered the optical power absorbed by the electron gas and transferred to the lattice increasing

the temperature of the particle. The particles cool by dissipating the heat to the surrounding medium. In the heat dissipation process, the thermal interface resistance, also known as Kapitza resistance,<sup>169</sup> between the AuNR and the medium causes a temperature discontinuity. The simulated thermal evolution of the temperature of the AuNR and the surrounding water is shown in **Figure 3.1**. As indicated by the black curve, the initial AuNR temperature is more than 1100 K, but it cools on an ultrafast timescale, indicating that the heat transfer occurs on a timescale of hundreds of ps. The medium in the direct vicinity of the AuNR significantly rises in temperature, reaching just over 60 °C at a distance of 10 nm from the AuNR. However, as demonstrated by Ben-Yakar and coworkers,<sup>39</sup> the bulk medium is not significantly affected by the temperature increase, but only the region within a few nm of the AuNR. Thus the produced heat is strongly localized.

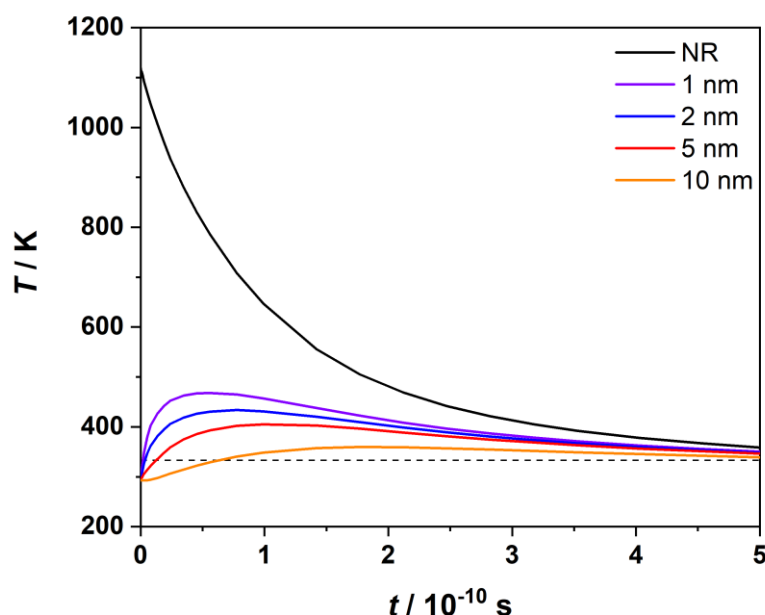


**Figure 3.1:** Temperature vs time evolution at various distances from the AuNR boundary after excitation with a 800 nm, 35 fs laser pulse. The black dashed line indicates the temperature for decomposition of AIBN initiator (60 °C), where the initiators half-life is close to 10 h.<sup>172</sup>

The heat transfer of AuNR is not only probed with theoretical calculations, but also experimentally. Alivisatos and colleagues<sup>163</sup> have recorded NIR excited time-resolved IR spectra of AuNR. Since heat can be detected as radiation in the IR region, their experiment tracked the heat production and distribution of AuNR. The transient spectrum shows a negative response in the IR region with a minimum at 2150  $\text{cm}^{-1}$  (4650 nm) after a few hundred ps, which can be assigned to the emission of heat due to heat transfer from the AuNR to the surrounding medium. Further, Alivisatos and coworkers<sup>163</sup> conducted kinetic studies on the AuNR heat

transfer at various excitation energies to determine the heat transfer time. These authors varied the intensity in a range of 0.3 – 3 GW cm<sup>-2</sup>, showing that the heat is distributed faster in case of higher intensities, due to the higher temperature difference of AuNR and medium. Consequently, their experiments highlight that the rate of heat transfer can be tuned via the incident light intensity. For each intensity, however, the heat is fully distributed within 2 ns.

The choice of surface coating for AuNRs depends on the intended application and the polarity of the solvent. AuNRs can be synthesized with a diverse range of functionalized groups to enhance their stability. The most common form of functionalization involves cetyl trimethylammonium bromide (CTAB)-capped AuNRs, which are suitable for use with organic solvents. In this configuration, ammonium groups bind to the gold surface,<sup>250,251</sup> while the carbon chain is hydrophobic, rendering the particles insoluble in water. However, the double-layered structure of CTAB makes it hydrophilic, as the second carbon chain points toward the gold surface, resulting in a positive charge on the outside. Alternatively, AuNRs can be functionalized using polyethylene glycol (PEG) that offers advantages in terms of high stability and biocompatibility. PEG-functionalized AuNRs can be dispersed in water and polar organic solvents. For applications requiring excellent biocompatibility and low cytotoxicity, PEG- or citrate-based functionalization is recommended.<sup>45,252,253</sup>

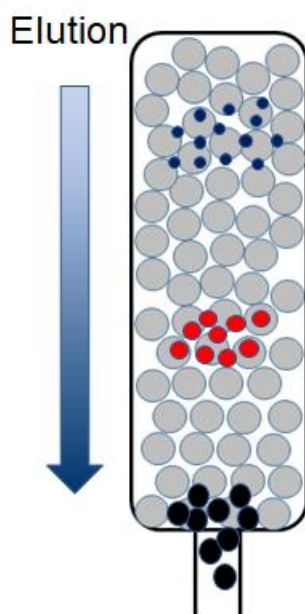
Exploring the strongly localized heat and ultrafast heat dissipation to the surrounding medium, as well as the tunability of plasmonic wavelength, the current subchapter highlights why AuNR are ideal for use in NIR light-induced polymerization. The AuNR-mediated heat production can be used for the decomposition of thermal initiators, thus initiating polymer chain growth. The potential solubility in aqueous environment makes AuNR an exciting prospect for polymerization in biomedical application.

### 3.6 Size-Exclusion Chromatography

SEC is a method used for the determination of the average molecular weight and MWD of polymers. It was originally developed by Porath and Flodin,<sup>254,255</sup> in 1959, which required several hours to a full day for operation. However, modern SEC systems can measure MWD and all statistical moments of polymer distribution within just half an hour.

The operating principle of SEC relies on the separation of particles based on their hydrodynamic size when dissolved in a suitable solvent. The essential components of an SEC setup include columns packed with porous material of defined pore size. In this setup, the polymer, typically dissolved in a solvent identical to the mobile phase within the column, flows through the system (as schematically shown in **Scheme 3.16**).

Larger polymers cannot pass through the pores and thus elute quicker through the column. In contrast, polymers with smaller sizes and lower molecular weights can penetrate the pores, leading to longer elution times. Consequently, the elution time is directly proportional to the polymer size. This results in the larger polymers being detected first, followed by the smaller polymers.<sup>256</sup>



**Scheme 3.16:** Scheme of SEC column with porous material (grey) and polymers of different hydrodynamic size, large polymers in black, middle-sized polymers in red and small polymers in blue, elute through the column.

### 3.7 Nuclear Magnetic Resonance Spectroscopy

NMR spectroscopy is based on the interaction between the magnetic moments of nuclei and magnetic fields. This effect was first discovered by Purcell and Bloch.<sup>257,258</sup> In this context, the magnetic moment is associated with the spin of the nucleus. Nuclei with an even number of protons and neutrons possess no spin, while those with an odd number of protons and neutrons have a half-integer spin. Magnetic moments arise exclusively from nuclei with non-zero spins. Certain nuclei, such as  $^1\text{H}$ ,  $^{13}\text{C}$ ,  $^{15}\text{N}$ , and  $^{31}\text{P}$ , exhibit a spin of  $\frac{1}{2}$ . When exposed to a magnetic field, the magnetic moments of nuclei tend to align with the direction of the magnetic field to minimize their energy. However, this alignment is disturbed by the thermal energy of the nuclei, resulting in random deviations from the perfect alignment of the magnetic moment. The application of a static magnetic field causes the summation of all magnetic moments, resulting in a magnetization vector  $\vec{B}_M$ . As the magnetic moments reach equilibrium, the magnetization aligns itself with the direction of the applied magnetic field. The interaction

between the applied magnetic field  $\vec{B}$  and the magnetization can be expressed by the following equation:<sup>259</sup>

$$\frac{dM}{dt} = -\gamma \vec{B}_M \times \vec{B} = -\vec{M} \times \vec{\omega}. \quad \text{Eq. 3.47}$$

In this equation,  $\gamma$  represents the gyromagnetic constant, describing the ratio of the nuclear magnetic moment to the angular momentum, and  $\omega$  is the angular frequency. When  $\vec{B}_M$  aligns with the magnetic field of the induction  $\vec{B}_0$  (in equilibrium), the vector product becomes zero. However, if  $\vec{B}_M$  and  $\vec{B}_0$  are not parallel,  $\vec{B}_M$  precesses with a frequency  $\omega$ , known as the Larmor frequency. The detection of magnetization for spectroscopic purposes is only possible when  $\vec{B}_M$  is precessing and not static. According to Faraday's law, a non-static magnetization induces an electromotive force in a coil, which is proportional to the rate of change of  $\vec{B}_M$  with respect to time.<sup>259</sup> Therefore, the magnetization must be tilted away from equilibrium, often achieved through an external force, in order to be detectable. An electric current passing through a coil around the sample can induce a radiofrequency magnetic field  $\vec{B}_1$  perpendicular to  $\vec{B}_0$  momentarily disturbing the equilibrium and causing  $\vec{B}_M$  to precess. This results in a decaying electromotive force that can be detected as an NMR signal.<sup>259</sup>

Interestingly, nuclei of the same species may exhibit different resonance frequencies due to their local electron environments. Depending on the specific electron surroundings, the applied magnetic field induces a counter magnetic field caused by the motion of electrons, which weakens the field experienced by the nuclei. This shielding effect is dependent on the chemical structure and is therefore characteristic of specific chemical fragments. Since this shield effect is proportional to  $\vec{B}_0$ , a new field-independent parameter, known as the chemical shift  $\delta$ , was introduced to account for these variations in resonance frequency:<sup>259</sup>

$$\delta = \frac{(\omega - \omega_{\text{ref}})}{\omega_{\text{ref}}}. \quad \text{Eq. 3.48}$$

In this equation,  $\omega$  represents the resonance frequency of the measured component, and  $\omega_{\text{ref}}$  is the resonance frequency of a reference component, measured under the same magnetic field conditions. In most cases, the reference component used is tetramethylsilane (TMS). In this thesis, <sup>1</sup>H-NMR spectroscopy was employed to determine the monomer conversion in a polymerization reaction. As the chemical shift is unique to the local chemical environment, <sup>1</sup>H-NMR spectroscopy serves as a method to quantitatively identify molecules. Thus, the monomer conversion can be determined via the ratio of detected monomer and polymer protons. Typically, gravimetry is a more commonly used technique for this purpose. However, in the

case of the monomer DMA, it evaporates extremely slowly due to its low vapor pressure. Consequently, gravimetry is not effective in this context, making  $^1\text{H}$ -NMR spectroscopy the preferred technique. Monomer conversion can be calculated by comparing the ratio of the integral of the peak assigned to the polymer protons to the sum of the integrals assigned to both the polymer and the monomer protons.

**Figure 3.2** illustrates an example of  $^1\text{H}$ -NMR spectra obtained from the AuNR experiments (see **Chapter 7**) both without polymer (top) and with polymer (bottom). In the graph without polymer, all peaks, except of the water peak at 4.87 ppm, can be distinctly attributed to the monomer protons. The peaks 'a' and 'b' with a chemical shift around 5.7 ppm and 6.2 ppm, and 'c' at 6.75 ppm, represent the protons of the double bond. The peaks 'd' and 'e' at 3 ppm are associated with the 3 protons of each methyl group. However, in the  $^1\text{H}$ -NMR spectrum containing polymer, two additional peaks arise labelled as 'g' at 1.5 ppm and 'f' at 2.5-3 ppm, which can be assigned to the protons of the polymer backbone repeating unit. It is worth noting that the monomer conversion cannot be accurately calculated using the polymer resonances close to 2.5-3 ppm, as they overlap with the monomer peaks at 3 ppm. In contrast, the polymer peak at 1.5 ppm is well-separated from the monomer peaks and is therefore suitable for calculating the monomer conversion. Since the resonances labelled as 'a' and 'b' in the monomer spectrum correspond to analogous protons to those in resonance 'g' of the polymer spectrum, the monomer conversion can be calculated by taking the ratio of the resonance 'g' and the sum of resonances 'a', 'b' and 'g'.

$$\text{Conversion} = \frac{\int(g)}{\int(a) + \int(b) + \int(g)} \cdot 100\% \quad \text{Eq. 3.49}$$

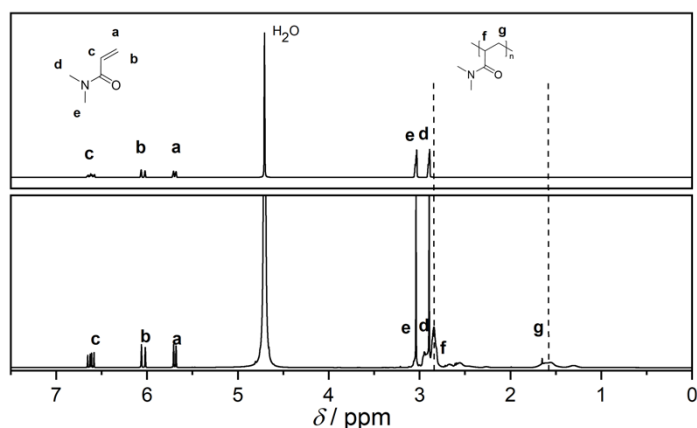
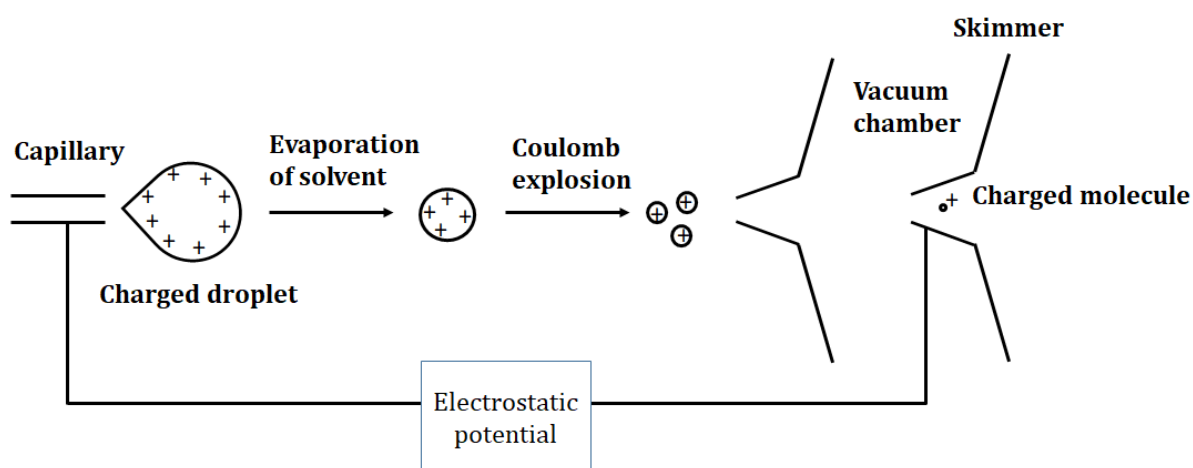


**Figure 3.2:** (Top)  $^1\text{H}$ -NMR spectrum of pure DMA dissolved in  $\text{D}_2\text{O}$  without irradiation. The resonances are assigned to the protons of DMA; (bottom)  $^1\text{H}$  NMR spectrum of a solution of DMA, AIBN, AuNR and CTA dissolved in  $\text{D}_2\text{O}$  after irradiation of 30 min. The resonances are assigned to the protons associated with the DMA monomer and the generated polymer after fs laser irradiation of 30 min.

### 3.8 Electrospray Ionization Mass Spectrometry

Amongst a plethora of ionization techniques, electrospray ionization (ESI), as schematically shown in **Scheme 3.17**, stands out as a gentle method employed to transfer molecules from a solution into the gas phase. ESI operates on a principle that does not require a vacuum, but instead accomplishes the transformation of molecules into the gas phase under atmospheric pressure conditions.



**Scheme 3.17:** Principle of charged molecule generation in the vacuum chamber of an electrospray ionization apparatus.

The primary advantage of ESI, when compared to other more aggressive ionization methods, lies in its ability to generate intact, undamaged analytes. Consequently, ESI is suitable for a wide variety of samples, including large molecules. In ESI, samples are injected into a first chamber at a relatively low flow rate, typically around 1 to 20  $\mu\text{L}/\text{min}$ , through a fine hypodermic needle.<sup>260</sup> An applied voltage of a few kilovolts to the liquid generates an electric field on the surface of the solution, leading to the dispersion of the sample into a spray composed of charged droplets. These charges result from Coulomb forces acting on the charged surface. An applied potential of 3-4 kV<sup>261</sup> on the chamber wall creates an electric field that accelerates the charged droplets. Within the chamber, a flow of bath gas at a temperature of 350 K and a pressure of 800 torr initiates the evaporation of the solvent, reducing the size of the droplets.<sup>260</sup> Thus, this process enhances the charge density on the surface of the droplets. As the droplets traverse the chamber, this evaporation process iterates, causing the droplets to shrink until they reach the Rayleigh limit.<sup>260,262</sup> At this point, the Coulomb forces outweigh the surface tension, leading to the rupture of the droplets into smaller ones. This effect, known as Coulomb explosion, occurs sequentially, resulting in a significant increase in the electric field strength in the droplets. Eventually, this extreme charge density leads to the desorption of small ions from the tiny droplets.<sup>260</sup> This phenomenon was first described by Iribane and

Thomson.<sup>263</sup> The ions are subsequently propelled towards the end of the chamber wall through the applied electric field. The following zone constitutes the first vacuum region, serving to remove any residual solvent from the ions. Additionally, it acts as a lens, focusing the ion beam, by the use of an electric gradient.<sup>264</sup>

### 3.8.1 C-Trap

Orbitrap mass analyzers are immensely powerful instruments known for their high-performance mass-to-charge ratio ( $m/z$ ) analysis capabilities. However, they are extremely sensitive to precise ion injection and require a high vacuum environment to ensure the longevity of transients. Achieving high-quality results hinges on the correct positioning of ions concerning the electrodes and their angle during injection. In addition to ion position, factors such as injection velocity, timing, and the duration of ions in the analyzer are crucial considerations. The c-trap, driven by a quadrupole, plays a pivotal role in preparing and controlling ions before their final injection into the Orbitrap. This trap is filled with low-pressure nitrogen, where collision with the bath gas dampens the kinetic energy of ions. This kinetic damping is necessary to maintain ion stability within the instrument. In the last stage, ions are ejected by short, high-voltage electric pulses in a meticulously controlled manner to meet the stringent requirements of the Orbitrap. Due to the c-shaped geometry of the c-trap, all ions exit along converging paths, ensuring they are precisely centered at the entrance of the Orbitrap analyzer.<sup>265</sup>

### 3.8.2 Orbitrap Mass Analyzer

An Orbitrap mass analyzer comprises a spindle-like central electrode and a cylindrical outer coating with a radius that gradually decreases toward the outer edges. Ions are injected into the mass analyzer tangentially to the central electrode of the spindle, with an applied electrostatic potential. The trajectories of these ions are governed by the complex interaction of forces, including the centrifugal force generated by the central wire and the electrostatic forces arising from the field between the cylinder and the wire.<sup>265</sup> Such an electric field,  $U(r, z)$ , necessary for trapping and storing ions in the mass analyzer can be expressed as follows:<sup>266</sup>

$$U(r, z) = \frac{\kappa}{2} \left( z^2 - \frac{x^2}{2} \right) + \frac{\kappa}{2} (r_m)^2 \ln \left[ \frac{x}{r_m} \right] + Z. \quad \text{Eq. 3.50}$$

Here,  $x$  and  $z$  represent cylindrical coordinates,  $\kappa$  is the field curvature,  $r_m$  is the radius, and  $Z$  is a constant.

This electric field compels ions to follow trajectories with harmonic axial oscillations with a frequency  $\omega$  that depends on their charge  $q$  and mass  $m$ :<sup>266</sup>

$$\omega = \left(\frac{\kappa q}{m}\right)^{1/2}. \quad \text{Eq. 3.51}$$

Due to the preceding ion injection method, all ions possess the same amplitude, but differ in their oscillation frequencies. As these propagating ions induce an image current, the harmonic axial oscillation can be detected by the outer electrodes, generating a sine wave for each  $m/z$  ratio via Fourier transformation. The image current  $I(t, r)$  is defined as:<sup>267</sup>

$$I(t, r) = -qN\omega \frac{\Delta z}{\Omega(r)} \sin(\omega t), \quad \text{Eq. 3.52}$$

where  $N$  is the number of trapped ions,  $\Delta z$  the axial amplitude and  $\Omega(r)$  a monotonically decrease function, which depends on the geometry.

## 4 Experimental Methods

This chapter will explore the materials and experimental methods utilized throughout this thesis to gain a comprehensive understanding of how the experiments were conducted. At the beginning, the fs laser setup will be introduced, which played a pivotal role in conducting both one-photon (1P) and 2P PLP experiments. Following this, the initial proof-of-principle experiments that showcased the feasibility of AuNR-mediated fs polymerization and the fs transient spectrometer will be presented. Subsequently, the ns laser experiment that was used for the action plot measurements will be introduced. This will be followed by an exploration of how the AuNR experiments were carried out using LEDs as irradiation source. To complete the understanding of the experimental framework, an overview of the instruments SEC, <sup>1</sup>H-NMR spectrometry and ESI-MS used for the thorough analysis of the polymer samples generated in these experiments will be provided.

### 4.1 Materials

Methyl-methacrylate (MMA, 99%, contains  $\leq 30$  ppm monomethyl ether hydroquinone (MEHQ) as inhibitor), Ivocerin<sup>®</sup> (Kindly provided by Ivoclar Vivadent) *N,N*-dimethylacrylamide (DMA, 99%, contains 500 ppm MEHQ as inhibitor, Sigma-Aldrich), azoisobutyronitrile (AIBN, 98%, Sigma-Aldrich), 3-mercaptopropionic acid (99%, Sigma-Aldrich), gold nanorods (AuNRs, 800 nm, OD=1, bare citrate, Nanocomposix), basic aluminium oxide 90 (Activision grade 1, Carl Roth), Deuterium oxide (Carl Roth).

### 4.2 The fs Laser System

The laser system is composed of various components designed to generate and amplify laser pulses. It all begins with the Verdi-G CW-Solid State Laser, which serves as the pump source for the Vitara-S Ti:Sapphire oscillator. This laser system is capable of producing an output power of 3.2 W at a central wavelength of 532 nm.

Employing mode-locking techniques, the Vitara-S Ti:Sapphire oscillator generates 800 nm pulses. These pulses have a power output of approximately 460 mW and pulses are produced at a high repetition rate of 80 MHz. To ensure the safety of the optics and minimize the risk of damage caused by the high pulse intensity, the generated pulses are then subjected to a pulse stretching unit, involving the use of two optical gratings.

Subsequently, the stretched pulses are directed into the regenerative amplifier collinear with the pump pulse generated by the Revolution pump laser. The Revolution pump laser is a diode-pumped Nd:YLF laser that incorporates a Q-switch and intra-cavity frequency-doubling.

As a result, this laser system is capable of producing 131 ns pulses with an energy output of approximately 40 mJ. These ns pulses have a wavelength of 527 nm and are generated at a repetition rate of 1 kHz.

To effectively control the pulse amplification and trigger the polarization angle, two Pockels cells are integrated into the amplifier setup. These Pockels cells play a crucial role in achieving the desired pulse characteristics and enable the decoupling of the laser pulses.

In the final stage of the laser system, the pulses are compressed into ultrashort output pulses featuring a pulse duration of 35 fs, a repetition rate of 1 kHz, and an energy output of 7 mJ at 800 nm. To mitigate the impact of their high intensity, the pulses are divided into multiple laser beams, three of which with a maximum energy of 1 mJ. This division is crucial to prevent nonlinear effects within the experimental optics.

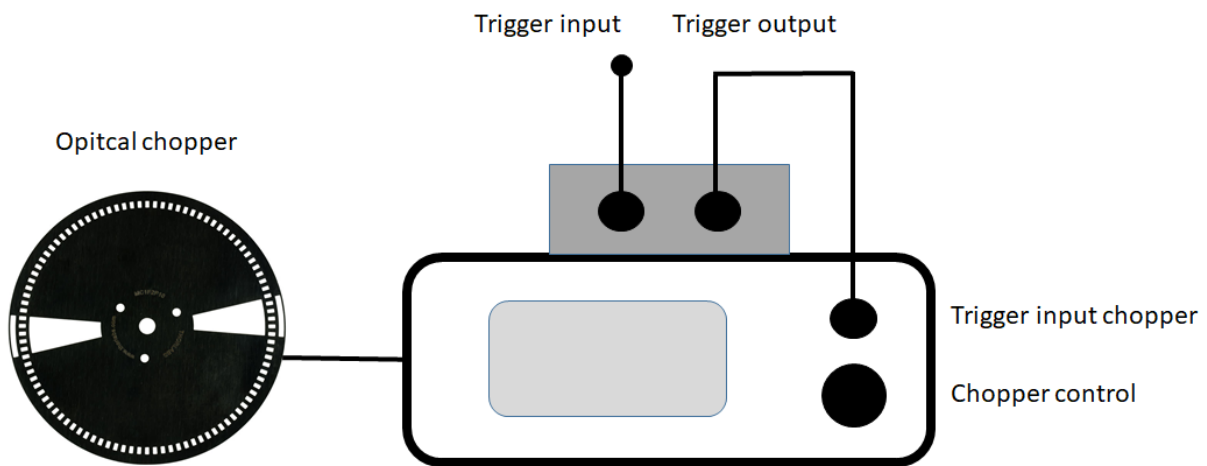
### 4.3 Frequency Variation with Optical Chopper

The laser pulse frequency played a pivotal role in all experiments conducted in this study. In the context of transient spectroscopy experiments, it is essential to divide the pulse repetition rate of the excitation beam by a factor of two relative to the pulse frequency of the probe beam. This adjustment is necessary to satisfy the requirements of the **Eq. 3.23** and thereby generate a transient spectrum. Furthermore, in the case of PLP experiments, the length of the polymer chains is contingent on the pulse repetition rate.

Given that the laser system emits pulses at a fixed repetition rate of 1 kHz, the experiments require a method to manipulate the pulse frequency. An optical chopper is a practical device for externally modulating the pulse frequency by selectively blocking and transmitting pulses based on the configuration of the chopper blade. Chopper blades are circular metal components equipped with periodic slits, as illustrated in **Scheme 4.1**. By applying an external frequency, the blade rotates, causing an alternation between pulse-transmitting slits and pulse-blocking metal sections. The chopper is synchronized using an external frequency delay generator (DG) (Stanford Research Systems DG535). Additionally, a frequency divider can be interposed between the DG and the chopper to reduce the applied repetition rate by a factor of two. **Scheme 4.1** provides a visual representation of the chopper setup.

Depending on the desired repetition rate, each experiment requires a specific chopper blade in conjunction with the appropriate DG settings. For the transient spectroscopy experiment, a MC1F10 blade (Thorlabs) with alternating equal sized slits and metal parts was triggered

by a 500 Hz signal. To obtain a 500 Hz trigger signal, the 1 kHz output of the DG535 was connected to the frequency divider.

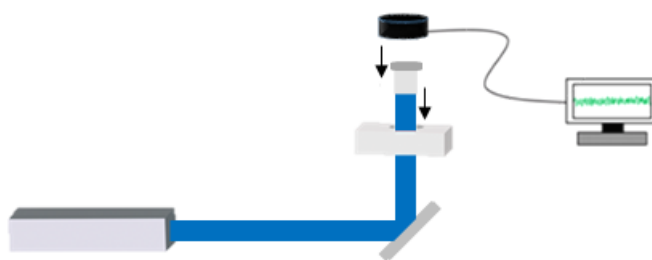


**Scheme 4.1:** Scheme of the setup of the optical chopper to vary the repetition rate for the fs PLP experiments: The chopper (white) control is either directly triggered by the repetition rate of the laser via the DG535 or by the frequency halver (grey), which is connected to various output channels of the DG535. Setting multiple options, the chopper control triggers the optical chopper, achieving several possible repetition rate using the inner or outer slits as input reference.

For the PLP experiments, the MC1F10 chopper blade was replaced with one featuring two distinct frequency input sensors: an inner reference circle and an outer reference circle with a frequency 50 times higher than that of the inner circle (blade Thorlabs MC1F2P10). When combined with the programmable delay generator, utilizing either the outer slits or the inner slits as references, a diverse array of repetition rates became accessible. In the context of the PLP experiments, both 1000 Hz (standard) and 100 Hz were employed. To achieve a 100 Hz pulse frequency, which was the highest frequency required for the PLP experiments, the 100 Hz output from the DG is directly applied to the inner reference of the chopper blade. Consequently, a pulse frequency of 50 Hz is generated by connecting the 100 Hz DG output to a frequency divider, which was then linked to the inner reference of the chopper. When using the 1000 Hz output in combination with the outer reference, the chopper applies a repetition rate of 20 Hz to the inner reference circle due to the 50-fold increase in frequency between the outer and inner circles. Finally, the lowest applied repetition rate of 10 Hz was set by utilizing a 500 Hz signal generated by the frequency divider, which is then applied to the outer reference circle of the chopper, resulting in an inner reference frequency of 10 Hz. **Figure 10.2 - Figure 10.5** in the appendix show an oscilloscope display confirming the pulse frequency for each setting of the chopper.

## 4.4 One-Photon PLP

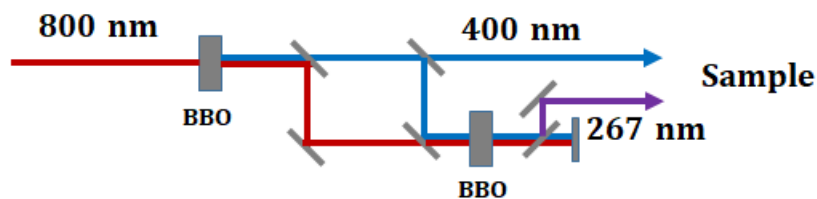
For the 1P PLP experiments a custom-built sample holder consisting of an elevated metal block with a central hole, which was adjustable parallel to the table plane, functioned to enable a sample to be irradiated from below to ensure maximum illumination (**Scheme 4.2**). A 45° dichroic 400 nm mirror redirected the laser beam from the tabletop up into the vial. Each sample, containing 12 mmol L<sup>-1</sup> of the photoinitiator Ivocerin dissolved in the monomer MMA, was taken from a bulk solution and transferred to a capped laser vial with a transparent base. Each sample was flushed with nitrogen to avoid quenching by oxygen, and placed in the hole of the metal block. As described in more detail in **Section 5.1** the samples were triggered with 400 nm fs laser pulses, which closely matched the absorption maximum of Ivocerin. To achieve this, the fundamental wavelength of 800 nm emitted by the laser system described in **Section 4.2** was divided into multiple segments using beam splitters, as shown in **Scheme 4.3**. The portion of the beam designated for 1P PLP experiments was frequency doubled via a second-order nonlinear Beta Barium Borate (BBO) crystal, resulting in the generation of 400 nm photons with a maximum average energy of 56 μJ (250 μJ cm<sup>-2</sup>). Given that the polymer chain length was expected to be frequency-dependent via the PLP mechanism, various repetition rates (10 Hz, 20 Hz, 50 Hz, and 100 Hz) were applied. To do so, an optical chopper (refer to **Section 4.3** for details) was positioned between the incident laser beam and the 400 nm mirror.



**Scheme 4.2:** Simplified scheme of the setup for PLP experiments; the laser beam is redirected from the tabletop to the upside via a 45° mirror and penetrates the sample, which is placed in a sample holder, from below. The beam energy can be recorded using a detector.

For each repetition rate, the irradiation time was adjusted to maintain an identical number of incident photons for each experiment. As a result, the irradiation time decreased with higher frequencies, with the sample solution being irradiated for 900 s at 10 Hz, 450 s at 20 Hz, 180 s

at 50 Hz, and 90 s at 100 Hz. The same setup and beam path were also employed for the fluence-dependent UV/Vis/NIR spectroscopy easily adjusting the incident energy in a range of 5 – 20  $\mu\text{J}$  by varying the vertical position of the BBO crystal.



**Scheme 4.3:** Setup of the SHG and THG generation. SHG (blue) from the laser fundamental wavelength (red) takes place in a BBO crystal. The generation of the THG (pale blue) takes place in a second BBO by overlapping the fundamental wavelength and the second harmonic. To do so, the fundamental part is turned in its polarisation by  $90^\circ$  to achieve a type-1 process in the nonlinear crystal. A dielectric mirror separates the fundamental and the second harmonic.

### Sample preparation

For each experiment, an aliquot of 500  $\mu\text{L}$  was taken from a stock solution containing 12  $\text{mmol L}^{-1}$  Ivocerin (kindly provided by Ivoclar Vivadent) in bulk MMA (Sigma-Aldrich) and transferred into a capped glass vial with a diameter of 7 mm. The purchased MMA was inhibited with monomethyl ether hydroquinone (MEHQ) as protective group to prevent undesired polymerization. This protective group was removed, and the monomer was activated by filtering it in a plastic syringe with a polytetrafluoroethylene (PTFE) filter filled with basic aluminium oxide. The samples were flushed with nitrogen to avoid oxygen quenching during the reaction. To do so, two needles were inserted into the rubber-capped vial, one was immersed in the solution, while the other remained in the atmosphere between the solution and the cap for reasons of pressure compensation. The needle in the solution was then connected to a Schlenk line allowing to adjust the nitrogen pressure such that the volatile monomer did not evaporate excessively. Each sample was flushed for a duration of 5 min.

### 4.5 Two-Photon PLP

The setup for 2P PLP experiments shares fundamental similarities with the 1P PLP experiments (see **Scheme 4.2**); irradiating the sample from below using the elevated metal block. However, the 400 nm dichroic mirror was replaced by an 800 nm dichroic mirror to redirect the beam into the sample and an 800 nm beam path was employed for these experiments. As described in detail in **Section 3.3.2**, 2PA is a nonlinear 3<sup>rd</sup> order process, and the likelihood of absorption is directly proportional to the square of the laser intensity. There are two primary ways to modulate laser intensity: by varying the beam diameter and by adjusting the

beam energy. In this particular experiment, the beam energy was controlled using a Glan-Taylor polarizer. This approach was chosen because decreasing the beam diameter was accompanied of two significant challenges. If the beam had been focused into the sample, it would have significantly increased the volume fraction of the solution, which did not match the 2PA conditions, resulting in non-uniform excitation within the solution and an extremely low polymer yield. By using a high-energy beam, both illumination homogeneity and a sufficiently high polymer yield were ensured. For the NIR 2P PLP experiments, a beam energy of  $650 \mu\text{J}$  ( $5.5 \text{ mJ cm}^{-2}$ ) was employed. To maintain comparability with the 1P PLP experiments, the same repetition frequencies (10 Hz, 20 Hz, 50 Hz, and 100 Hz) were applied. A Glan-Taylor polarizer was utilized to adjust the beam energy in a range of  $25 - 70 \mu\text{J}$  ( $1.6$  to  $4 \text{ mJ cm}^{-2}$ ), allowing for the verification of the quadratic dependency of 2PP via energy-dependent UV/Vis spectroscopy.

### **Sample Preparation**

The samples for 2P PLP were prepared identically to the 1P PLP samples. For each experiment, an aliquot of  $500 \mu\text{L}$  was taken of a stock solution containing  $12 \text{ mmol L}^{-1}$  Ivocerin (kindly provided by Ivoclar Vivadent) in bulk MMA (Sigma-Aldrich) and transferred into a capped glass vial with a diameter of 7 mm. The purchased MMA was inhibited with a protective group to prevent undesired polymerization. This protective group was removed, and the monomer was activated by filtering it in a plastic syringe with a PTFE filter filled with basic aluminium oxide. The samples were flushed with nitrogen to avoid oxygen quenching during the reaction. To do so, two needles were inserted into the rubber-capped vial, one was immersed in the solution, while the other remained in the atmosphere between the solution and the cap for reasons of pressure compensation. The needle in the solution was then connected to a Schlenk line allowing to adjust the nitrogen pressure such that the volatile monomer did not evaporate excessively. Each sample was flushed for a duration of 5 min.

## **4.6 Proof-of-Principle Polymerization with Gold Nanorods**

The citrate-functionalized AuNR in water (55x15 nm, OD 1) exhibit resonant plasmonic absorption in the NIR region, peaking at 800 nm. Given that electron heating occurs within fs, the fs laser system operating at 800 nm (as detailed in **Section 4.2**) was exceptionally well-suited for conducting proof-of-principle experiments on thermally induced polymerization mediated by AuNR. In this experiment, a  $250 \mu\text{J}$  laser pulse with a diameter of 5 mm, resulting in a laser intensity of approximately  $25 \text{ GW cm}^{-2}$ , was employed to excite the AuNR. The reaction solution was placed in a 1 mm cuvette and inserted into a sample holder for an irradiation

period of 30 min. Subsequently, the product was transferred to an NMR tube and diluted with 250  $\mu\text{L}$  of  $\text{D}_2\text{O}$  for  $^1\text{H}$ -NMR spectroscopy analysis to determine the monomer-to-polymer conversion.

### Sample Preparation

The monomer used in this study, DMA, was initially purchased with MEHQ as an inhibitor. To enable the initiation of the polymerization reaction, it was necessary to remove the inhibitor from DMA. This protective group was removed, and the monomer was activated by filtering it in a plastic syringe with a PTFE filter filled with basic aluminium oxide.

For the initial proof-of principle experiment, a solution containing 9  $\text{mmol L}^{-1}$  AIBN, 2.69  $\text{mol L}^{-1}$  DMA, 150  $\mu\text{L}$  of AuNR and  $10^{-2}$   $\text{mol L}^{-1}$  3-mercaptopropionic acid as CTA was prepared and transferred to a 1mm glass cuvette.

For the systematic variation of parameters in the experiments, bulk solutions were prepared, allowing the preparation of individual samples a variable concentration of one component while keeping the concentrations of all other components constant (refer to **Table 4.1**). A defined volume of the bulk solution was transferred into a 1 mm cuvette and filled up with the variable chemical or water to achieve the desired parameter concentration. All concentrations were calculated for a cuvette volume of 350  $\mu\text{L}$  and then scaled up based on the number of samples required for the variation experiment. **Table 4.1** provides a summary of the preparation procedure for the series of monomer variation experiments.

Every bulk solution was prepared for seven samples, one more than required to account for any potential issues. For the monomer variation experiment, the bulk solution consisted of 3.5 mg AIBN dissolved in 350  $\mu\text{L}$  solution of an AuNR and DMA. From this bulk solution, 100  $\mu\text{L}$  was extracted for each sample and topped up with precise amounts of DMA and distilled water. This process ensured that each sample had an identical concentration of AIBN and AuNR, but varying concentrations of DMA. As shown in the **Table 4.1**, the proportion of additional DMA was systematically increased by 50  $\mu\text{L}$ , while the amount of added water was decreased step by step by 50  $\mu\text{L}$ . This resulted in a gradual increase in DMA concentration across the sample sequence, starting from an initial concentration of 0.69  $\text{mol L}^{-1}$  DMA and reaching 6.73  $\text{mol L}^{-1}$  DMA in the final sample, where no water was added.

**Table 4.1:** Overview of sample preparation for the monomer variation experiment.

<i>Bulk solution</i>	<i>0.69 mol L<sup>-1</sup></i>	<i>1.34 mol L<sup>-1</sup></i>	<i>2.38 mol L<sup>-1</sup></i>	<i>4.04 mol L<sup>-1</sup></i>	<i>5.38 mol L<sup>-1</sup></i>	<i>6.73 mol L<sup>-1</sup></i>
	<i>DMA</i>	<i>DMA</i>	<i>DMA</i>	<i>DMA</i>	<i>DMA</i>	<i>DMA</i>
350 $\mu$ L AuNR in water, 350 $\mu$ L DMA, 3.5 mg AIBN	100 $\mu$ L bulk + 250 $\mu$ L wa- ter	100 $\mu$ L bulk + 50 $\mu$ L DMA + 200 $\mu$ L wa- ter	100 $\mu$ L bulk + 100 $\mu$ L DMA + 150 $\mu$ L wa- ter	100 $\mu$ L bulk + 150 $\mu$ L DMA + 100 $\mu$ L wa- ter	100 $\mu$ L bulk + 200 $\mu$ L DMA + 50 $\mu$ L water	100 $\mu$ L bulk + 250 $\mu$ L DMA

In the case of the AuNR variation experiments, the initial bulk solution was prepared following the same procedure as the DMA variation sequence. However, in this case, the DMA concentration remained constant, and the 100  $\mu$ L bulk solutions were filled up with AuNR and distilled water to vary the AuNR concentration (refer to **Table 4.2**). For the first sample, 250  $\mu$ L of water were added to 100  $\mu$ L of the bulk solution to achieve a final volume of 350  $\mu$ L of AuNR in a 350  $\mu$ L solution. Subsequently, the additional water volume was reduced by 50  $\mu$ L, while the additional AuNR volume was increased by 50  $\mu$ L for each concentration step. Finally, the 100  $\mu$ L bulk solution was adjusted with 250  $\mu$ L of AuNR solution to achieve a final volume of 300  $\mu$ L of AuNR in a 350  $\mu$ L solution.

**Table 4.2:** Overview of sample preparation for the AuNR variation experiment.

<i>Bulk solution</i>	<i>50 <math>\mu</math>L AuNR</i>	<i>100 <math>\mu</math>L AuNR</i>	<i>150 <math>\mu</math>L AuNR</i>	<i>200 <math>\mu</math>L AuNR</i>	<i>250 <math>\mu</math>L AuNR</i>	<i>300 <math>\mu</math>L AuNR</i>
350 $\mu$ L AuNR in water, 350 $\mu$ L DMA, 3.5 mg AIBN	100 $\mu$ L bulk + 250 $\mu$ L wa- ter	100 $\mu$ L bulk + 50 $\mu$ L AuNR + 200 $\mu$ L wa- ter	100 $\mu$ L bulk + 100 $\mu$ L AuNR + 150 $\mu$ L wa- ter	100 $\mu$ L bulk + 150 $\mu$ L AuNR + 100 $\mu$ L wa- ter	100 $\mu$ L bulk + 200 $\mu$ L AuNR + 50 $\mu$ L water	100 $\mu$ L bulk + 250 $\mu$ L AuNR

The preparation of the samples for the AIBN variation experiments faced some challenges. It was difficult and not sufficiently precise to directly dispense the required amount of AIBN for each concentration step into the cuvette. Consequently, an initial bulk solution (containing 0.014 mg of AIBN in 350  $\mu$ L of DMA) was prepared. However, since the total solution volume was always 350  $\mu$ L for each sample, simply adding an identical volume of the initial bulk solution to each sample would have resulted in the same AIBN concentration throughout. To achieve varying AIBN concentrations, while keeping other parameters constant, it was necessary to withdraw different volumes from the stock solution and supplement them with AuNR and water. Notably, as DMA served as the solvent for the bulk solution, altering the volume of DMA also affected its concentration. Consequently, different specific amounts of DMA had to

be added to the various sample volumes to decrease the AIBN concentration while maintaining all other parameters unchanged. The details of this procedure are provided in **Table 4.3**.

**Table 4.3:** Overview of sample preparation for the AIBN variation experiment.

<i>Bulk solution</i>	<i>0.69 mol L<sup>-1</sup></i> <i>AIBN</i>	<i>0.35 mol L<sup>-1</sup></i> <i>AIBN</i>	<i>0.17 mol L<sup>-1</sup></i> <i>AIBN</i>	<i>0.08 mol L<sup>-1</sup></i> <i>AIBN</i>
0.014 mg AIBN, 350 $\mu$ L DMA,	100 $\mu$ L bulk + 50 $\mu$ L AuNR + 200 $\mu$ L water	50 $\mu$ L bulk + 50 $\mu$ L DMA + 50 $\mu$ L AuNR + 200 $\mu$ L water	25 $\mu$ L bulk + 75 $\mu$ L DMA + 50 $\mu$ L AuNR + 200 $\mu$ L water	12.5 $\mu$ L bulk + 87.5 $\mu$ L DMA + 50 $\mu$ L AuNR + 200 $\mu$ L water

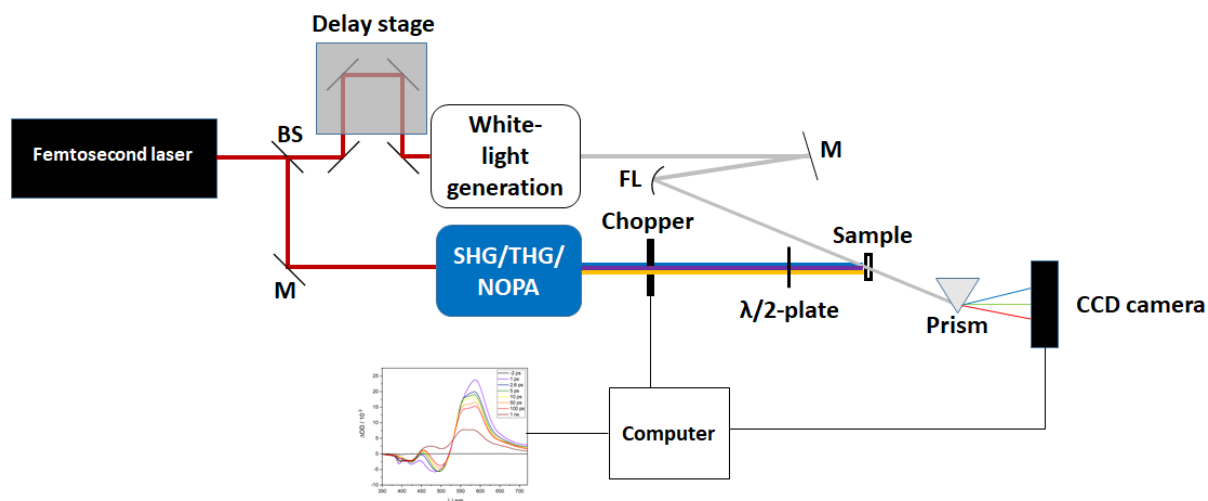
## 4.7 Transient fs Absorption Spectroscopy

Transient absorption Spectroscopy (**Scheme 4.4**) makes use of two laser pulses, a pump and a probe pulse, that are overlapped in a sample in space and time. The fundamental laser pulses (800 nm) for this experiment were generated using the laser system described in **Section 4.2** and split into four different beam lines to avoid damaging of the optics due to high intensities. One beamline was further split into two pulses, one for excitation and the other for probing of the sample. A charge-coupled device (CCD) camera detected a sequence of probe pulses. Finally, a self-written LabView program from former PhD students of the Unterreiner group recorded the data for subsequent analysis.

The excitation pulse wavelength was tuned using experimental setups with the functionality based on nonlinear effects, such as SHG, THG and NOPA. An optical chopper with alternating equal sized slits and metal parts (MCB2000EC with MC1F10 blade, Thorlabs) operated at 500 Hz blocking every second pump pulse to match the **Eq. 3.23** allowing the generation of a transient spectrum (as described in **Section 3.4**). The chopper was triggered by the frequency divider, which received the repetition rate of the laser as input signal aiming for the chopper to be synchronized with the laser frequency at 1 kHz. Prior to the excitation of the sample, the pump pulse passed through a  $\lambda/2$  waveplate (Alphas) modulating the polarization by a degree of 54.7, referred to as magic angle, aiming to mitigate pump-induced anisotropic effect in the sample. The  $\lambda/2$  plate featured a spectral range of 150-6000 nm, a diameter of 24 mm, and a thickness of 2.5 mm.

For WL generation used as the probe pulse, a portion of the laser pulse (2-3  $\mu$ J) was temporally delayed using an automated 300 mm long travel stage (Thorlabs LTS 300) with an accuracy of 2  $\mu$ m (equivalent to 13.3 fs) for each step. By delaying the probe pulses it was possible to study the sample at various time intervals after excitation. After the delay stage, the probe

pulse was focused into a nonlinear CaF<sub>2</sub> crystal (1", Nortus Optic) to generate a WL continuum. The incident energy on the crystal could be controlled using a neutral density (ND) filter and an aperture. To maintain the correct intensity, an achromatic antireflective (AR, 50-1150 nm) double lens was used to focus the beam into the 2 mm thin CaF<sub>2</sub> crystal. WL generation relies on self-phase modulation and is strongly intensity-dependent. Therefore, the lens was positioned on a manually adjustable stage to control the intensity. To prevent damage due to high intensity, the crystal was secured in a motor-driven mount with 20 rotations per minute. This technique ensured uniform motion of the crystal without prolonged exposure to one point. A concave mirror positioned behind the crystal was installed to collimate the converging beam. A further mirror redirected the WL to a UV-enhanced Al mirror, focusing the beam onto the sample, reaching a diameter of approximately 50 μm in the sample. While the excitation pulse was blocked after passing through the sample, the probe pulse was dispersed into its spectral components by a prism (SF10-lead glass, Brewster, Newport) before being detected by a CCD camera (Linescan Series2000, 512 pixels, Si-detector, Stresing). A filter (BG18, 1 mm, Schott) in front of the camera sorted out the fundamental wavelength of the laser. Both the camera and the optical chopper were externally triggered using a frequency delay generator DG535 (Stanford Research Systems) to synchronize with the laser pulses. Control of the translation stage and the camera was facilitated through an inhouse written LabView program, which recorded the data for subsequent analysis. Each spectrum was recorded moving the stage in steps of 19 x 0.2 ps, 135 x 0.02 ps, 50 x 0.2 ps, 50 x 5 ps and 14 x 60 ps. In pursuit of enhancing the signal-to-noise ratio, the data points were subjected to an averaging process, typically 1000 spectra were recorded and averaged at a given delay position. Due to different GVM of the single wavelengths of the WL continuum caused by the glass cuvette containing the sample, the transient spectra were corrected via a Sellmeier plot prior to data analysis.



**Scheme 4.4:** Scheme of the experimental setup of a transient spectrometer. The generated pulses are split into an excitation and a probe pulse. The excitation pulse can be tuned to a range of various wavelengths via nonlinear optics, such as SHG, THG or NOPA. Every second excitation pulse is blocked by an optical chopper and subsequently turned in its polarization by a  $\lambda/2$  plate to achieve the magic angle relative to the probe pulse. The probe pulses are aligned along a computer-controlled stage to generate a temporal delay relative to the pump pulses. Both the excitation and the probe pulses are overlapped in the sample in space and time. A white-light continuum generated in a  $\text{CaF}_2$  crystal and focused via a focusing lens (FL) is used for broadband probing. After passing the sample, this WL is separated in its single spectral parts by a prism to be detected by a CCD camera.

## Sample preparation

A solution of  $12 \text{ mmol L}^{-1}$  Ivocerin in MMA was filled in a 1 mm glass cuvette. As the purchased MMA was inhibited with a protective group to prevent undesired polymerization. This protective group was removed first by filtering the monomer in a plastic syringe with a PTFE filter filled with basic aluminium oxide. The sample was flushed with nitrogen using the aforementioned method to avoid oxygen quenching during the reaction. The sample was flushed for a duration of 5 min.

## 4.8 Tunable ns Laser

Previous publications<sup>11,41–44</sup> have demonstrated that the absorptivity of photoinitiators and their reactivity do not necessarily align. The experimental technique, a so-called action plot, precisely determines the wavelength-dependent conversion making use of a light source with a narrow spectral width. Tunable ns lasers are ideal for such experiments due to their quasi-monochromatic properties (refer to **Section 3.2.1**), allowing for the assessment of monomer conversions at specific wavelengths.

The action plot was conducted using a Coherent Opolette 355 tunable OPO laser that operates within a wavelength range of 210 nm to 2400 nm. This laser emits pulses with a duration of 7 ns at a repetition rate of 20 Hz. The output beam from the laser was expanded using a telescope comprising two lenses. A manual stage allowed for adjusting the telescope to tailor the beam diameter, which, for this thesis, was approximately 6 mm. Subsequently, a right angle-prism redirected the beam upward through a cylindrical hole in a custom-built sample holder, within which a glass vial containing the samples was placed. Since the refractive index of dispersive media varies with wavelength, the transmission angle of the prism differed slightly for each applied wavelength. As a result, the horizontal and vertical angles of the prism relative to the incident beam had to be aligned via screws for each experiment involving various wavelengths. To ensure comparability of the absorption efficiency, the incident number of photons into the sample remained constant across all experiments. The number of photons was controlled using a calculated pulse energy specific to each wavelength and a shutter positioned between the telescope and the prism, allowing for precise control of the irradiation time. The number of photons, represented as  $n_p$ , for a monochromatic light source is determined by the Planck-Einstein equation:<sup>268</sup>

$$n_p = \frac{E_{\text{pulse}} \lambda}{h \cdot c \cdot N_A}. \quad \text{Eq. 4.1}$$

In this equation,  $E_{\text{pulse}}$  represents the energy of the laser pulses,  $\lambda$  denotes the wavelength,  $h$  is known as Planck constant,  $c$  stands for the speed of light, and  $N_A$  represents the Avogadro constant. Using this equation, the required energy for each wavelength can be calculated to achieve a defined number of photons. This approach ensures a consistent number of photons entering the sample for each experiment at varying wavelengths. However, it is important to note that the energy was measured before inserting the sample vial. As glass vials can attenuate the light, meaning the beam energy may decrease as it penetrates the samples. The "effective" energy within the sample is then given by:

$$E_0 = \frac{n_p \cdot N_A \cdot h \cdot c}{k \cdot T_\lambda \cdot \lambda}, \quad \text{Eq. 4.2}$$

introducing the transmittance  $T_\lambda$

$$T_\lambda = \frac{E_n}{E_0}, \quad \text{Eq. 4.3}$$

with  $E_n$  as energy per pulse with calibration vial in the sample holder.

The transmittance was calibrated prior to the measurements by using several empty glass vials. This calibration involved measuring the energy on top of the sample holder both with and without the empty vials in place using a pyroelectric energy sensor in combination with a digital energy meter. Typically, one would need to consider the absorption of the solution at a specific wavelength when performing such measurements. However, in the case of the action plot experiments involving AuNRs, the OD was relatively low (0.25 OD), and the solution height in the vial with a diameter of 7 mm was only 7.8 mm. Consequently, the effect of the absorption of the solution on the transmittance was approximately negligible as the entire solution was illuminated sufficiently.

### **Sample preparation**

Prior to preparing bulk solutions of 1.5 mg AIBN dissolved in 450  $\mu\text{L}$  DMA for each triplicate recorded data point, the monomer containing MEHQ as inhibitor was activated by filtering through a syringe with basic aluminium oxide. 150  $\mu\text{L}$  aliquots were taken from this bulk solution and transferred to a laser vial with 7 mm diameter and filled up with 75  $\mu\text{L}$  AuNR solution, 75  $\mu\text{L}$  isopropanol and 10  $\mu\text{L}$  CTA, such that each sample featured a concentration of 0.01 mol L<sup>-1</sup> AIBN, 4.85 mol L<sup>-1</sup> DMA, 3.53 mol L<sup>-1</sup> isopropanol, 0.38 mol L<sup>-1</sup> CTA and 75  $\mu\text{L}$  of AuNR.

## **4.9 LED Polymerization**

To set up the LED experiment for irradiating the solution, a vertical row of three clamps was positioned on a tripod. The central clamp was used to secure two 10 W chip-on-board (COB) LEDs with identical emission wavelengths, maintaining a distance of 1 cm between them. This arrangement allowed for the placement of a 1 cm glass cuvette, held by the upper clamp, between the two LEDs without any gaps, ensuring that the solution would be uniformly illuminated by the LEDs.

The LEDs were connected to a power supply to regulate the applied voltage and current, providing control over the LED operation. To prevent excessive heating and minimize any potential impact on the thermal initiator, a fan was attached to the lower clamp, facilitating ventilation from below. Additionally, the entire setup was enclosed within an opaque box to protect the eyes of the operator from scattered light, given the high intensity of the LEDs. Importantly, the power supply was positioned outside the box, allowing for continuous control over the applied voltage as needed (1V, 5.14 A).

## Sample Preparation and Experimental Procedure

In the LED polymerization experiment, DMA was activated by a thermal initiator in the presence of AuNR in a water solution, leading to the conversion of the incident radiation from the LEDs into heat. Isopropanol was also included in the reaction mixture to reduce thermal conductivity. The purchased DMA monomer was inhibited with the protective group MEHQ to prevent undesired reactivity. The first step involved removing this protective group to enable polymerization. To achieve this, the monomer was filtered through a syringe containing activated basic aluminium oxide and a PTFE filter. For each experiment, a new syringe with fresh aluminium oxide was used to ensure proper activation of the monomer.

In the first experiment, 1.5 mg of the thermal initiator (AIBN) was accurately weighed and placed in a 1 cm glass cuvette. The AIBN was then dissolved in 250  $\mu\text{L}$  of activated DMA through careful shaking followed by the addition of 350  $\mu\text{L}$  of isopropanol and 350  $\mu\text{L}$  of distilled water. Once the solution was prepared, the cuvette was sealed with a suitable PTFE cap. Two 745 nm LEDs were secured in the experimental setup, with the cuvette placed in between them. After closing the protective enclosure, both LEDs were set to 1 V and 5.14 A, and the solution was illuminated for 10 min.

The second experiment followed the same procedure as the first, but instead of distilled water, AuNR solution was added to the mixture (consisting of 1.5 mg AIBN, 250  $\mu\text{L}$  DMA, 350  $\mu\text{L}$  isopropanol, and 350  $\mu\text{L}$  AuNR solution).

For the third experiment, the solution composition was identical to the second experiment, but the 745 nm LEDs were replaced with 590 nm LEDs (1 V, 5.14 A), and the solution was irradiated for 10 min.

### 4.10 Size-Exclusion Chromatography

At the KIT, SEC measurements were conducted using polymers generated by PLP. These measurements were carried out on a SECurity2-GPC-System 1260 Infinity II, which included an autosampler, two PL HFIPgel columns (7.5 x 300 mm), an UV detector, and a differential refractive index detector. The eluent used was tetrahydrofuran (THF), and the measurements were performed at 40  $^{\circ}\text{C}$  with a flow rate of 1  $\text{mL min}^{-1}$ . The SEC system was calibrated using linear poly(methyl-methacrylate) standards with molecular weights ranging from 800 to 2,200,000 Da. It is important to note that the reported molecular weights in the manuscript and the Supplementary Information were provided by the SEC software. However, the overall accuracy of directly calibrated SEC may have an error of about 20%.

For the polymers generated by thermal initiation with AuNR, SEC measurements were conducted on the same SECurity2-GPC-System 1260 Infinity II. This system included an autosampler, a GRAM Lux 5  $\mu\text{m}$  column (8 x 50 mm), a GRAM Lux 1000A 5  $\mu\text{m}$  column (8 x 300 mm), and a GRAM Lux 100,000A 5  $\mu\text{m}$  column (8 x 300 mm). It also featured a UV detector and a differential refractive index detector. Dimethylacetamide (DMAc) was used as the eluent, and the measurements were performed at 70  $^{\circ}\text{C}$  with a flow rate of 1  $\text{mL min}^{-1}$ . The SEC system was calibrated using linear poly(methyl methacrylate) standards with molecular weights ranging from 800 to 2,200,000 Da.

At the QUT, SEC measurements for the AuNR-induced action plot experiments were conducted using a PSS SECurity2 system. This system comprised a PSS SECurity Degasser, a PSS SECurity TCC6000 Column Oven, and a PSS GRAM Column Set with 8 x 150 mm 10  $\mu\text{m}$  Pre-column and 8 x 300 mm 10  $\mu\text{m}$  Analytical Columns. Additionally, it included an Agilent 1260 Infinity Isocratic Pump, an Agilent 1260 Infinity Standard Autosampler, an Agilent 1260 Infinity Diode Array detector, and a refractive index detector. The solvent used was HPLC-grade DMAc with 0.01 M LiBr, and the flow rate was set at 1  $\text{mL min}^{-1}$ . A poly(methyl methacrylate) standard was employed for calibration.

#### **4.11 Nuclear Magnetic Resonance Spectrometry**

At the KIT,  $^1\text{H}$ -NMR experiments were carried out using a Bruker Ascend 400 MHz instrument. Deuterium oxide ( $\text{D}_2\text{O}$ ) was used as the solvent, and it served as the reference for the calibration of delta shifts. The detected resonances were reported in parts per million (ppm) relative to TMS.

At the QUT,  $^1\text{H}$ -NMR spectra were recorded using a Bruker Ascend 600 MHz instrument. Deuterium oxide ( $\text{D}_2\text{O}$ ) was used as the solvent, similar to the setup at KIT. Additionally, deuterated methanol ( $\text{CD}_3\text{OD}$ ) was used for these experiments. Resonances in the spectra were also reported relative to TMS.

#### **4.12 Electrospray Ionization-Mass Spectrometry**

ESI-MS spectra were acquired using an LTQ mass spectrometer manufactured by Thermo Fisher Scientific, based in San Jose, CA, USA. The instrument underwent calibration within the mass-to-charge ratio ( $m/z$ ) range of 195 to 1822. This calibration utilized a solution containing SDS, sodium taurocholate, and Ultramark 1621 dissolved in an acetonitrile-methanol-acetic acid mixture.

During the measurements, a constant spray voltage of 3.8 kV was applied, and nitrogen was utilized as the sheath gas with a dimensionless sheath gas flow rate set to 5. The capillary temperature was maintained at 320°C. For direct infusion ESI-MS experiments, a solution of THF/methanol in a 3:2 volume-to-volume ratio was employed. This solution also contained 100  $\mu\text{M}$  of sodium trifluoroacetate (NaTFA). The polymer concentration utilized in these measurements was 0.03  $\text{mg mL}^{-1}$ .

## 5 Visible Light-Induced Polymerization with Ivocerin

In the following chapter, Ivocerin-initiated polymerization of MMA, from photon absorption to end-product formation, is comprehensively analyzed. Free-radical polymerization was triggered by fs laser pulses operating at a repetition rate in the Hz range using an optical chopper, as described in more detail in **Section 4.3**. Stationary absorption spectroscopy was initially used to study the absorption behaviour of Ivocerin, thus providing information on the spectral region where electronic transitions occur. Initiator conversion was monitored by recording absorption spectra of Ivocerin after laser fluence-dependent exposure at a suitable wavelength with the fs laser. By varying the repetition rate of the pulsed laser, the frequency-dependent chain growth of MMA was analyzed using SEC. This method was employed to confirm the underlying PLP mechanism via the propagation rate coefficients of MMA, thus evidencing laser control over the polymerization reaction. Having explored the mechanism of chain growth, the next step included a *post-mortem* analysis of the polymerization products of MMA using ESI-MS. The analysis of the polymer mass spectrum provided insights into the distribution of initiator fragment end groups, elucidating the decomposition mechanism of the photoinitiator. Finally, time-resolved fs absorption spectroscopy was employed to examine the electronic behaviour and potential radical formation of Ivocerin immediately after photoexcitation, which is directly linked to the observed end groups in the mass spectrum, for the first time.

### 5.1 Stationary UV/Vis/NIR Absorption Spectroscopy

Initially, the absorption spectrum of Ivocerin, dissolved in MMA, was measured in a 1 mm quartz glass cuvette within the wavelength range of 300 nm to 1200 nm, as illustrated in **Figure 5.1**, using a Varian Cary 500 spectrometer. The spectrum exhibits a broad absorption peak around 400 nm, consisting of two transitions, a HOMO-LUMO at 425 nm and a HOMO-LUMO+1 at 410 nm.<sup>269</sup> Both correspond to an  $n-\pi^* S_1 \leftarrow S_0$  transition, typical for carboxyl compounds.<sup>270,271</sup> A further small peak was observed between 1100 and 1200 nm, which is literature-known as the third harmonic stretching vibration of the C-H bond ( $\nu_{3,CH}$ ) of MMA.<sup>272</sup> For this particular experiment, Ivocerin was dispersed in MMA to a concentration of 12 mmol L<sup>-1</sup>, resulting in an OD of approximately 1 at 400 nm.

Given that MMA absorbs light in the spectral region below 300 nm, excitation of the solution in this wavelength region can potentially lead to direct excitation of the monomer and undesired, self-initiated polymerization.<sup>273,274</sup> To ensure that the polymerization is induced by the

radical formation of Ivocerin, and not self-initiation of MMA, 400 nm was chosen as the excitation wavelength (represented by the blue dotted line in **Figure 5.1**). This wavelength falls within the absorption band of Ivocerin, readily accessible through frequency-doubling the fundamental wavelength of the Ti-Sapphire laser at 800 nm and is far removed from the absorption of MMA.

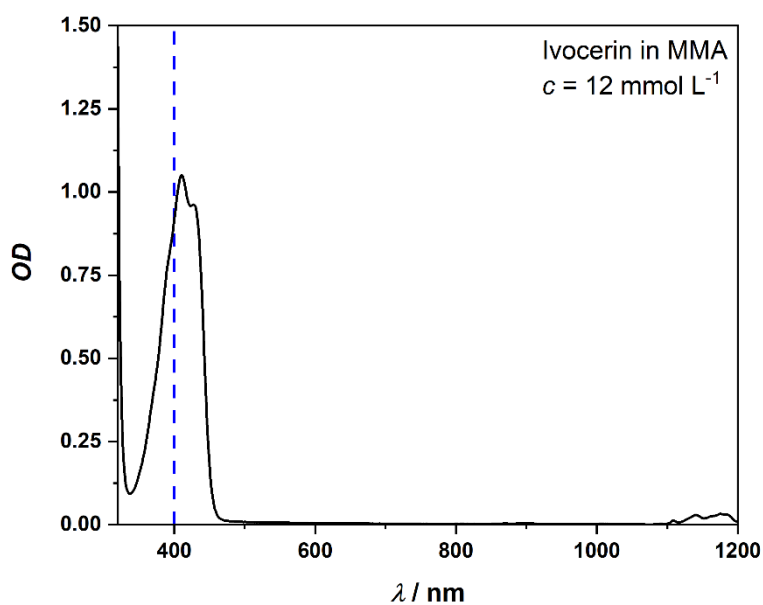


**Figure 5.1:** Absorption spectrum of 12 mmol L<sup>-1</sup> Ivocerin in bulk MMA with a peak absorption of about OD=1 at 408 nm in the range of 300 – 1200 nm. The small peak between 1100 nm and 1200 nm belongs to MMA. The excitation wavelength for 1P absorption experiment (400 nm) is indicated by the vertical dotted blue line.

In the following step, UV/Vis spectroscopy was employed to analyze the Vis light-induced decomposition of the photoinitiator Ivocerin. Thus, the OD of Ivocerin was measured as a function of the incident beam fluence. Since 400 nm photons excite Ivocerin in its resonant, one-photon absorption (1PA) band, one would anticipate a linear dependence of the initiator decomposition on the variation of the laser pulse energy.

For these measurements, a stock solution containing 12 mmol L<sup>-1</sup> Ivocerin in MMA was prepared. 250 μL aliquots were taken from the stock solution and filled into a vial to be irradiated from below using a metal block with a hole in the center for the vials, as described in the experimental **Section 4.4**. Each sample was irradiated for 90 s with various pulse energies (5-20 μJ) at 400 nm (35 fs, 100 Hz). After irradiation, the solutions were transferred from the vial into a 1 mm cuvette in order to record stationary absorption measurements. The concen-

tration of Ivocerin remaining in each sample after irradiation was determined from the absorption spectra using the molar decadic extinction coefficient and Beer-Lambert law, as introduced in **Eq. 3.4**. Since both the initiator concentration and the pathlength of the cuvette are known, the concentration for each wavelength can be calculated by **Eq. 3.4** utilizing the OD given by the absorption spectrum (**Figure 5.2**, left). The final concentration was determined by averaging the concentration (**Figure 5.2**, right) over the range from 380 - 440 nm after each step of irradiation. As expected, the concentration of Ivocerin remaining in the sample decreased with increasing pulse fluence.

Finally, the conversion of the Ivocerin concentration, relative to the reference measurement without irradiation, was graphed as a function of pulse fluence (**Figure 5.3**). The gradient was extracted using regression analysis and indicates the number of contributing photons to Ivocerin photocleavage. Plotting these data points on a double-logarithmic scale, a linear trend with  $m = 0.97 \pm 0.05$  was obtained, confirming a dominant 1P absorption process.

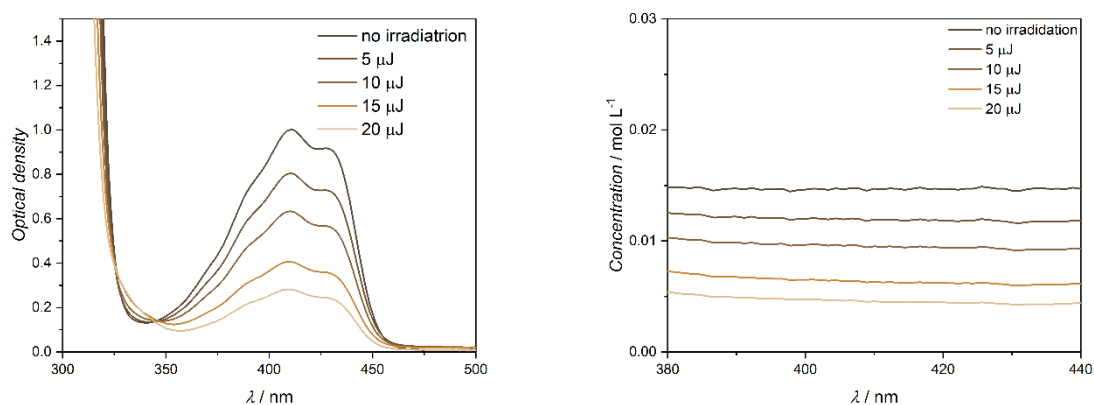


**Figure 5.2:** UV/Vis absorption spectra of 12 mmol L<sup>-1</sup> Ivocerin in MMA after 90 s irradiation with various energies at 400 nm (left) and plot showing the corresponding initiator concentration after each irradiation step (right). Adapted with permission from ref. 182. Copyright 2022 American Chemical Society.

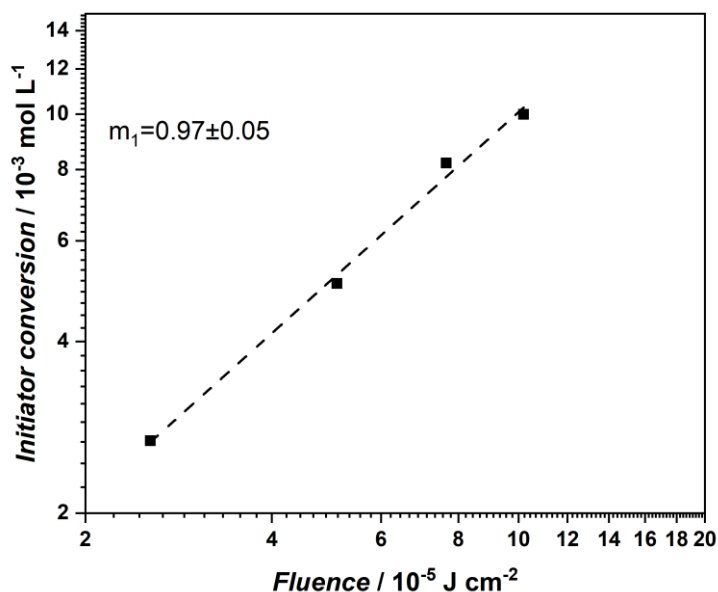


**Figure 5.3:** Initiator conversion after 90 s irradiation of a solution with 12 mmol L<sup>-1</sup> Ivocerin in MMA at 400 nm with various laser beam fluences, plotted on a double logarithmic scale. A linear regression was used to determine the gradient, indicating the number of photons contributing to initiator decay. Adapted with permission from ref. 182. Copyright 2022 American Chemical Society.

## 5.2 Size Exclusion Chromatography

Having presented the decomposition of the photoinitiator Ivocerin as critical process prior to the initiation reaction of a polymer chain growth initiation, the following section aims to demonstrate laser control over the polymer chain growth in the Vis light region via PLP mechanism. To do so, 500  $\mu$ L aliquots were taken from a 12 mmol L<sup>-1</sup> stock solution of Ivocerin in MMA and filled in a capped laser vial. Each sample was flushed with nitrogen to avoid oxygen quenching of the excited electronic states of the initiator. The vial was subsequently placed in an elevated metal block containing a central hole, enabling exposure of the sample from below. The solutions were irradiated with 400 nm fs laser pulses with a pulse energy of 56  $\mu$ J varying the pulse repetition rates (10 Hz, 20 Hz, 50 Hz, and 100 Hz) using a chopper at the laser repetition rate of 1 kHz prior to analysis via SEC (for detailed experimental procedure refer to **Section 4.4**). According to Olaj *et al.*,<sup>87</sup> a reliable indicator of the PLP structure and, consequently, the laser-controlled reaction, can be elucidated from the MWD of the polymer. Using this analytical approach, which ultimately provides the first derivatives of the SEC distributions, the laser pulse frequency can be correlated with the molecular weight  $M_i$  of the polymer chains. This correlation enables the determination of the propagation rate coefficient

(refer to **Section 3.5**). **Figure 5.4 - Figure 5.7** depict the MWD and their first derivatives for PMMA synthesized with laser pulse frequencies of 10 Hz, 20 Hz, 50 Hz and 100 Hz. These plots are displayed on a logarithmic scale ranging from 3.5 (5,000 g mol<sup>-1</sup>) to 6 (1,000,000 g mol<sup>-1</sup>).

The SEC trace shown **Figure 5.4** (10 Hz) exhibits multiple peaks between 10,000 g mol<sup>-1</sup> and 100,000 g mol<sup>-1</sup>, indicating the formation of polymer chains with distinct molecular weights, characteristic of PLP behaviour. To further support this observation, it is critical to analyze the first derivative of the SEC trace, according to the theory outlined in **Section 3.5**. The peaks in the first derivative trace, corresponding to the inflection points of the SEC trace, can be directly associated with the molecular weights of polymer chains that have grown between laser pulses. The assigned molecular weights  $M_1 = 24,000$  g mol<sup>-1</sup>,  $M_2 = 46,000$  g mol<sup>-1</sup>, and  $M_3 = 70,000$  g mol<sup>-1</sup> are approximately multiples of each other, which is a typical feature of PLP behaviour. **Table 5.1** provides an overview of the molecular weights  $M_i$  of the polymer chains. Notably, the calculated propagation rate coefficients (**Eq. 3.33**) are within 10% deviation from the literature-accepted value for MMA<sup>275</sup> (267 L mol<sup>-1</sup> s<sup>-1</sup>), as shown in **Table 5.2**. This deviation falls within the SEC instrument error of approximately 20%, providing clear evidence that the polymer chain growth of PMMA at a pulse frequency of 10 Hz follows the PLP mechanism.

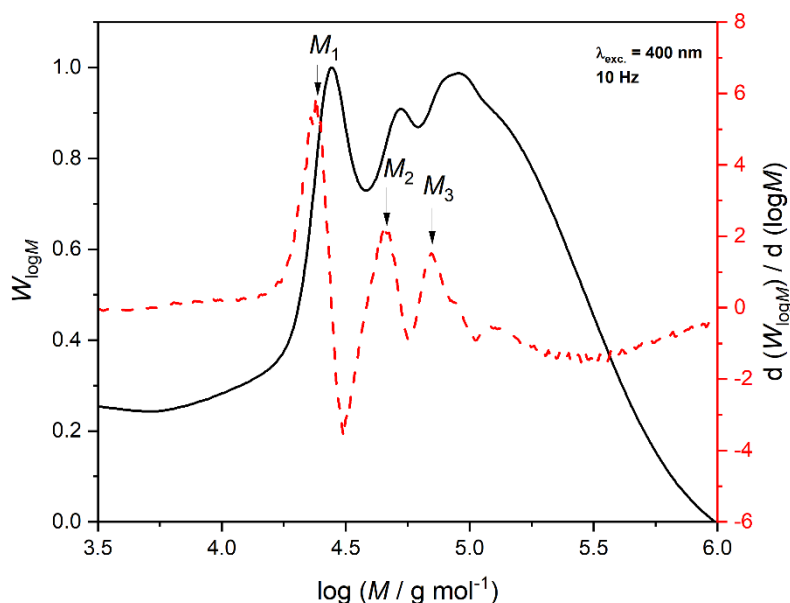


**Figure 5.4:** SEC trace (black) and first derivative of SEC trace (red dashed) of PMMA generated by 400 nm fs laser pulse triggered Ivocerin fragmentation ( $c = 12$  mmol L<sup>-1</sup> in bulk MMA) with a repetition rate of 10 Hz where the inflection points of the distribution are  $M_1 = 24,000$  g mol<sup>-1</sup>,  $M_2 = 46,000$  g mol<sup>-1</sup> and  $M_3 = 70,000$  g mol<sup>-1</sup>. Adapted with permission from ref. 182. Copyright 2022 American Chemical Society.

Furthermore, the SEC traces following polymerization at 20 Hz and 50 Hz were subjected to detailed analysis to confirm that the polymerization is indeed fully laser-controlled according to the PLP mechanism. **Figure 5.5** displays the SEC trace and first derivative of the 20 Hz experiment. Similar to the SEC trace at 10 Hz (**Figure 5.4**), the SEC trace at 20 Hz also exhibits multiple peaks of well-defined molecular weights. It was anticipated that changing the repetition rate from 10 Hz to 20 Hz (as described in the theory **Section 4.3**) would result in polymer chains with approximately half the molecular weight. This prediction is confirmed by the molecular weights  $M_i$  (**Table 5.1**) assigned to the peaks in the first derivative (**Figure 5.5**). Once again, the molecular weights  $M_1 = 13,000 \text{ g mol}^{-1}$ ,  $M_2 = 25,000 \text{ g mol}^{-1}$  and  $M_3 = 38,000 \text{ g mol}^{-1}$  are approximately multiples of each other, and as expected, are approximately half the molecular weight of the corresponding polymer chains formed at 10 Hz. The propagation rate coefficients (refer to **Table 6.2**) align with the value documented in the IUPAC literature,<sup>275</sup> with a maximum deviation of 16.9%. As the  $k_p$  deviations are within the instrument error limit of 20%, this validates the quality of the experiments. These findings emphasize that altering the laser repetition rate yields the anticipated outcomes in line with the PLP mechanism.

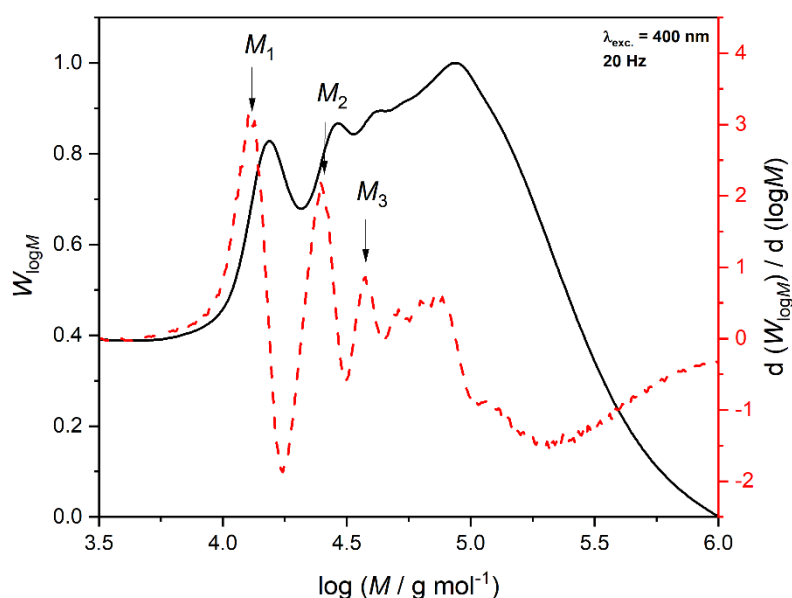


**Figure 5.5:** SEC trace (black) and first derivatives of SEC trace (red dashed) of PMMA generated by 400 nm fs laser pulse triggered Ivocerin fragmentation ( $c = 12 \text{ mmol L}^{-1}$  in bulk MMA) with a repetition rate of 20 Hz where the inflection points of the distribution are  $M_1 = 13,000 \text{ g mol}^{-1}$ ,  $M_2 = 25,000 \text{ g mol}^{-1}$  and  $M_3 = 38,000 \text{ g mol}^{-1}$ . Adapted with permission from ref. 182. Copyright 2022 American Chemical Society.

To further ensure that the current polymerization experiment is laser-controlled, a third experiment at 50 Hz (**Figure 5.6**) was performed. In line with the previously presented PLP experiments (**Figure 5.4** and **Figure 5.5**), **Figure 5.6** depicts the SEC trace of PMMA generated at 50 Hz with multiple peaks. The peaks of the first derivative can be assigned to polymers with the assigned molecular weight  $M_1 = 6,000 \text{ g mol}^{-1}$ ,  $M_2 = 11,000 \text{ g mol}^{-1}$ , and  $M_3 = 17,000 \text{ g mol}^{-1}$  (**Table 5.1**). Considering the deviation of only 4.9%, the calculated  $k_p$  values related to the  $M_i$  at 50 Hz show the highest consistency with the literature value compared to the other frequencies. The higher deviation of  $k_p$  at 10 Hz and 20 Hz likely arises from a systematic error of the SEC instrument up to 20%.

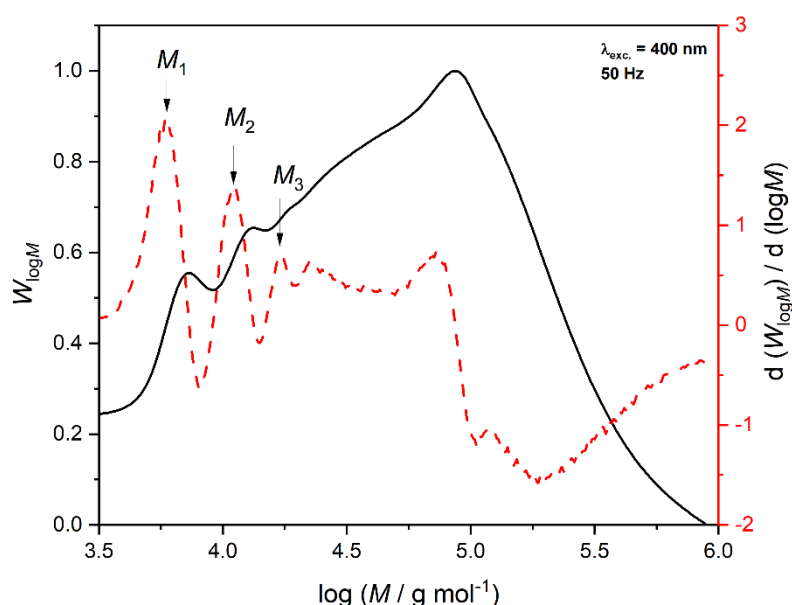


**Figure 5.6:** SEC trace (black) and first derivative of SEC trace of PMMA (red dashed) generated by 400 nm fs laser pulse triggered Ivocerin fragmentation ( $12 \text{ mmol L}^{-1}$  in bulk MMA) with a repetition rate of 50 Hz where the inflection points of the distribution are  $M_1 = 6,000 \text{ g mol}^{-1}$ ,  $M_2 = 11,000 \text{ g mol}^{-1}$  and  $M_3 = 17,000 \text{ g mol}^{-1}$ . Adapted with permission from ref. 182. Copyright 2022 American Chemical Society.

The analysis of the SEC trace obtained for a laser pulse frequency of 100 Hz (**Figure 5.7**) served to complete the series of repetition rate variation experiments, revealing laser control over the polymerization reaction. The peaks of the first derivative were associated to polymer chains with the molecular weight of  $M_1 = 3,200 \text{ g mol}^{-1}$ ,  $M_2 = 6,300 \text{ g mol}^{-1}$  and  $M_3 = 8,900 \text{ g mol}^{-1}$ . With a deviation of only 0.7 – 8%, the calculated  $k_p$  values for 100 Hz are well-consistent with the IUPAC literature<sup>275</sup> value of  $267 \text{ L mol}^{-1} \text{ s}^{-1}$  (see **Table 6.2**). Given the

certainty that Ivocerin, triggered with 400 nm fs laser pulses in the Hz regime, is able to initiate laser controlled polymerization, the final product formation was examined in the next subchapter using ESI-MS.

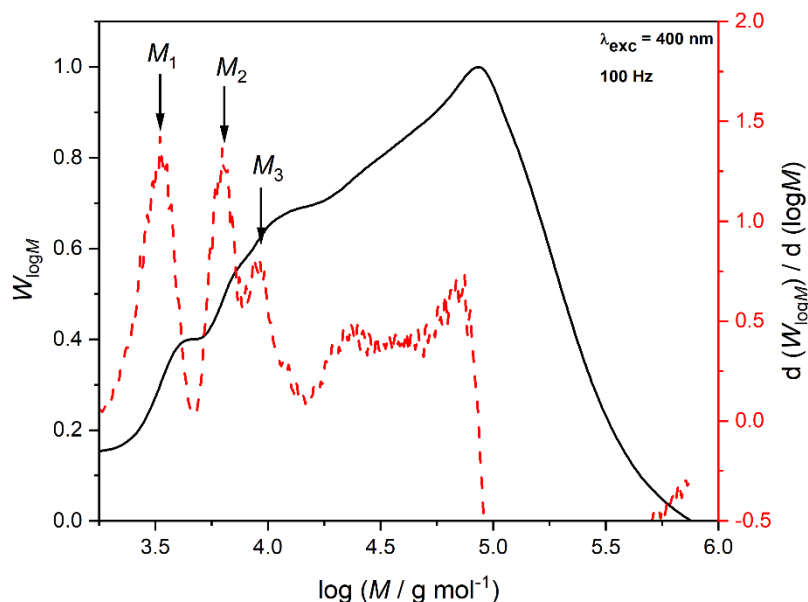


**Figure 5.7:** SEC trace (black) and first derivative of SEC trace of PMMA (red dashed) generated by 400 nm fs laser pulse triggered Ivocerin fragmentation (12 mmol L<sup>-1</sup> in bulk MMA) with a repetition rate of 100 Hz where the inflection points of the distribution are  $M_1 = 3,200$  g mol<sup>-1</sup>,  $M_2 = 6,300$  g mol<sup>-1</sup> and  $M_3 = 8,900$  g mol<sup>-1</sup>. Adapted with permission from ref. 182. Copyright 2022 American Chemical Society.

**Table 5.1:** Overview of molecular weight of the polymer chains  $M_i$  at the inflection points in the first derivative of the SEC trace generated by 400 nm fs laser pulse triggered Ivocerin fragmentation ( $c = 12$  mmol L<sup>-1</sup> in bulk MMA) with various repetition rates.

$f / \text{Hz}$	$M_1 / \text{g mol}^{-1}$	$M_2 / \text{g mol}^{-1}$	$M_3 / \text{g mol}^{-1}$
10	24,000	46,000	70,000
20	13,000	25,000	38,000
50	6,000	11,000	17,000
100	3,200	6,300	8,900

**Table 5.2:** Overview of the propagation rate coefficients (**Eq. 3.33**) of MMA calculated for polymer chains with the assigned molecular weight  $M_i$  generated by 400 nm fs laser pulse triggered Ivocerin fragmentation ( $c = 12 \text{ mmol L}^{-1}$  in bulk MMA) with a repetition rate of 50 Hz and compared to the IUPAC literature<sup>275</sup> propagation rate coefficient of MMA ( $267 \text{ L mol}^{-1} \text{ s}^{-1}$ ).

Repetition rate / Hz	$k_p (M_1) / \text{L mol}^{-1} \text{ s}^{-1}$	$k_p (M_2) / \text{L mol}^{-1} \text{ s}^{-1}$	$k_p (M_3) / \text{L mol}^{-1} \text{ s}^{-1}$
10	242	247	244
20	239	222	224
50	267	254	257
100	290	283	269

### 5.3 Electrospray Ionization-Mass Spectrometry

In the previous **Chapters 5.1** and **5.2** the Vis light fs pulse-induced polymerization was step-wise explored, beginning with the initiator decomposition, followed by the laser controlled chain growth of the polymers. The next sub-chapter will take the final step towards the analysis of the polymer products. Prior to the examination of the polymerization product formation via end group distribution analysis, a solution containing  $12 \text{ mmol L}^{-1}$  Ivocerin in MMA was prepared and subsequently transferred to a capped vial to flush the sample with nitrogen. Analogue to **Section 4.2**, the sample was exposed from below with 400 nm pulses with an energy of  $56 \mu\text{J}$  per pulse from below (for detailed description of the experiment refer to **Section 4.5**). Applying a frequency of 100 Hz for a total irradiation time of 15 min, resulted in a cumulative incident pulse count of 90,000 and an overall energy input of 5.04 J. Under these reaction conditions, the polymer chain growth relies on the PLP mechanism, as highlighted in detail in the previous **Section 5.2**, resulting in polymer chains with 10 - 30 monomer units and molecular weights ranging from  $1000$  to  $3000 \text{ g mol}^{-1}$ , synthesized as predicted by **Eq. 3.33**, making them suitable for analysis via ESI-MS. After irradiation, each sample was transferred from the laser vial into a small aluminium pan for the monomer to evaporate and the dissolved polymer to precipitate. The synthesized polymer was subsequently dissolved in a 3:2 v/v mixture of THF and methanol to a molarity of  $0.03 \text{ mg mL}^{-1}$ , adding  $30 \mu\text{L}$  of a  $100 \mu\text{M}$  NaTFA and then injected into the direct injection (DI)-ESI-MS instrument for analysis. The complete acquired mass spectrum, spanning the range of  $1000$  to  $2000 m/z$ , is depicted in the **Appendix Section 10.1, Figure 10.1**. For clarity, only one repeating unit, from  $1010$  to  $1110 m/z$ , is presented here to enable a more detailed assessment of the polymer species dis-

tribution (**Figure 5.8**). To analyze the isotopic patterns of the generated polymers, the spectrum was simulated using Xcalibur (Thermo Fisher), assuming Gaussian-shaped peaks with a resolution (mass resolving power) of 60,000. This simulation method facilitated the identification of individual polymer species within the recorded repeating pattern.

Using the simulation, a total of 13 distinct polymer species were identified (**Figure 5.9**). These species predominantly consisted of combination or disproportionation products associated with sodium or potassium counter ions. The polymer species were identified based on their mass-to-charge ratios ( $m/z$ ), as depicted in **Figure 5.8**, and each exhibit distinct characteristics, which are outlined below.

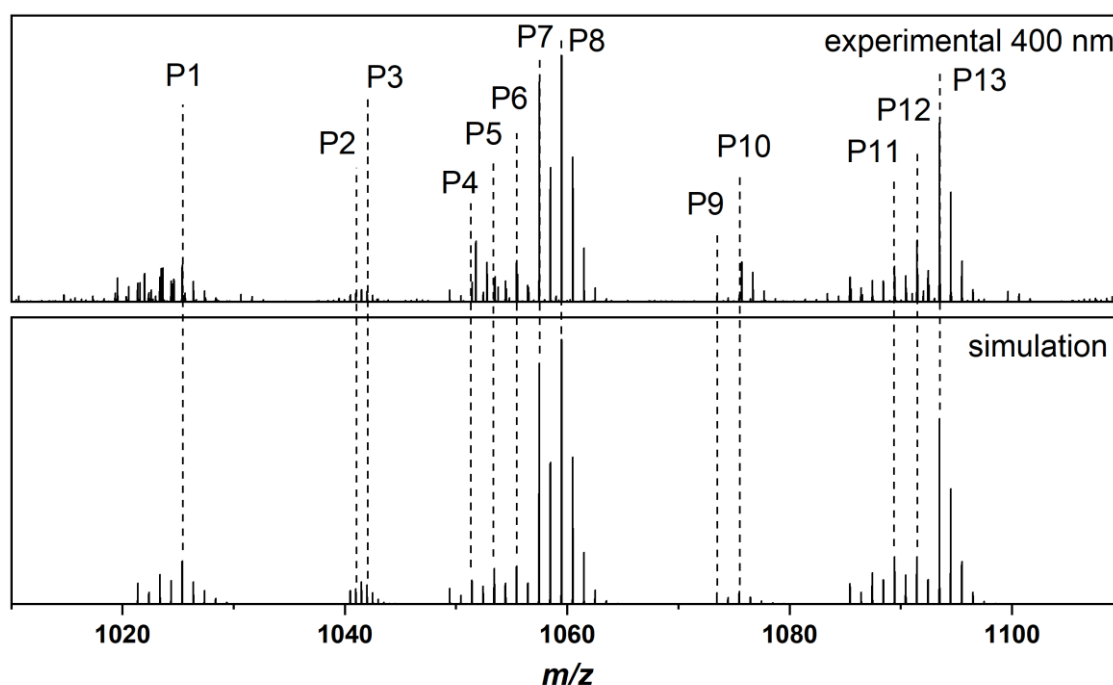


**Figure 5.8:** Comparison of experimental ESI-MS spectrum (zoom into one repeat unit) of PMMA in THF/methanol (3:2) (top) with simulated isotopic pattern (bottom) in the  $m/z$  range of 1010 – 1110. The experimental mass spectrum was obtained from polymer generated after 15 min irradiation of 12 mmol L<sup>-1</sup> Ivocerin in MMA with 400 nm fs pulses with a fluence of 102  $\mu\text{J cm}^{-2}$  and a repetition rate of 100 Hz. 10  $\mu\text{L}$  of the irradiated solution were dissolved in 2 mL of a THF/methanol (3:2) solution with 100  $\mu\text{M}$  NaTFA.

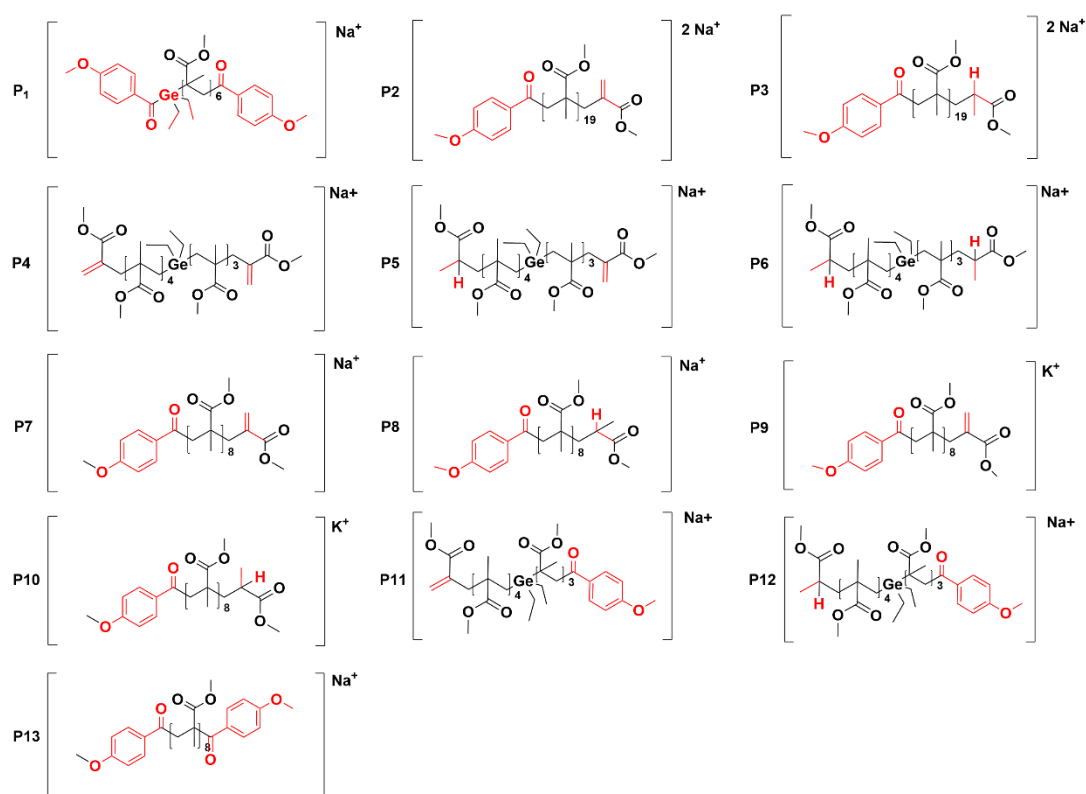


**Figure 5.9:** Assigned polymer species obtained from the an Xcalibur simulation of isotopic pattern corresponding to an experimental polymerization of PMMA after 15 min irradiation of 12 mmol L<sup>-1</sup> Ivocerin in MMA with 400 nm fs pulses with a fluence of 102 μJ cm<sup>-2</sup> and a repetition rate of 100 Hz: **P1-P13** with Ivocerin fragment end groups; **P2, P3** and **P7-P10** are acetyl-based disproportionation products, **P4-P6** and **P11-P12** are germyl-based disproportionation products, **P1** and **P13** are combination products.

**P1** (1025 *m/z*) corresponds to a PMMA polymer with an acylgermyl end group in the  $\alpha$ -position and an acyl end group in the  $\omega$ -position. **P13** (1093 *m/z*) is identical to **P1**, except the acylgermyl end group is replaced with an acyl end group. **P7** (1057 *m/z*) and **P8** (1059 *m/z*) represent disproportionation products. In **P7**, an acyl end group is located at the  $\alpha$ -position, while an MMA unit with a double bond is at the  $\omega$ -position. On the other hand, **P8** features a MMA unit with a hydrogen atom at the  $\omega$ -position. **P2** (1041 *m/z*) and **P3** (1042 *m/z*) are MMA chains with an acyl group, as well as a double bond, at the  $\alpha$ -position (**P2**) and a hydrogen atom at the  $\omega$ -position (**P3**), respectively, both bound to two sodium counter ions. **P4** (1053 *m/z*), **P5** (1055 *m/z*) and **P6** (1057 *m/z*) can be described as germyl-centered disproportionation products. While **P4** is characterized by terminal MMA units with double bonds at each end, **P5** and **P6** are characterized by both an MMA unit with a double bond terminus and one with a hydrogen terminus as well as an MMA unit with added hydrogen at both terminal MMA units. **P11** (1089 *m/z*) and **P12** (1091 *m/z*) are disproportionation species with an additional acyl fragment terminus on one side of the polymer chain. **P9** (1073 *m/z*) and

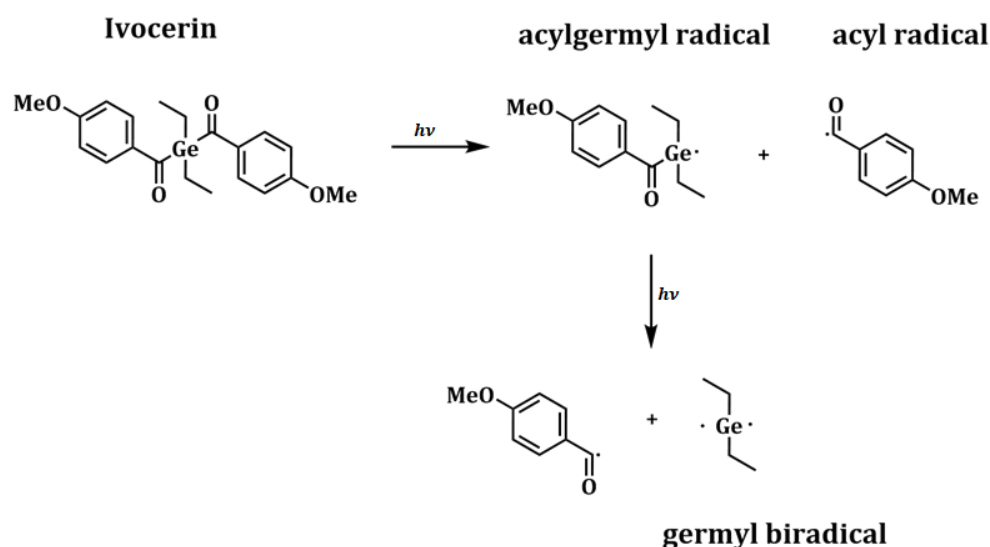
**P10** (1075  $m/z$ ) represent polymer products identical to **P7** and **P8**, however, bound to potassium counter ions instead of sodium. Among these species, three were notably prevalent, specifically **P7** and **P8**, disproportionation species with an acyl fragment terminus as well as **P13**, identified as combination product with two acyl end groups.

**Table 5.3:** Overview of the exact mass, resolution and relative abundance  $X$  of the assigned species in the recorded and simulated spectrum of the PMMA after PLP of MMA with Ivocerin triggered by 400 nm fs pulses with a fluence 102  $\mu\text{J cm}^{-2}$  and a repetition rate of 100 Hz.

<i>Species</i>	<i>Ionization</i>	<i>(m/z)<sup>exp</sup> (Da)</i>	<i>(m/z)<sup>sim</sup> (Da)</i>	$\Delta(m/z)$	$X$
<b>P1</b>	Na <sup>+</sup>	1025.395	1025.394	0.001	0.4
<b>P2</b>	2 Na <sup>+</sup>	1041.009	1041.007	0.002	0.05
	2 Na <sup>+</sup>	1091.035	1091.034	0.001	0.05
<b>P3</b>	2 Na <sup>+</sup>	1042.016	1042.014	0.002	0.05
	2 Na <sup>+</sup>	1092.041	1042.040	0.001	0.05
<b>P4</b>	Na <sup>+</sup>	1053.465	1053.458	0.007	0.3
<b>P5</b>	Na <sup>+</sup>	1055.461	1055.465	0.004	0.3
<b>P6</b>	Na <sup>+</sup>	-	1135.677		0.3
<b>P7</b>	Na <sup>+</sup>	1057.500	1057.494	0.006	1
<b>P8</b>	Na <sup>+</sup>	1059.515	1059.512	0.003	1
<b>P9</b>	K <sup>+</sup>	1073.474	1073.472	0.002	0.05
<b>P10</b>	K <sup>+</sup>	1075.488	1075.487	0.001	0.05
<b>P11</b>	Na <sup>+</sup>	1089.447	1089.453	0.006	0.4
<b>P12</b>	Na <sup>+</sup>	1091.464	1091.459	0.005	0.4
<b>P13</b>	Na <sup>+</sup>	1093.499	1093.498	0.001	0.8

The significant difference in the abundance of acyl- and germyl-based polymer species suggests a difference in the channel branching of the initiation mechanisms, while the fundamental cleavage mechanism remains unchanged. **Scheme 6.1** depicts the proposed photo-induced decomposition of Ivocerin. In an initial step, the incident 400 nm laser pulses cause cleavage of at least one C-Ge bond in Ivocerin generating an acyl and an acylgermyl radical. Further, the cleavage of the acylgermyl radical into another acyl and a germyl radical is presumably caused by either thermally or photo-induced fragmentation. A thermally driven fragmentation would require a sufficient amount of excess energy in vibrationally hot states. However, due to the short duration of fs laser pulses, a high excess energy input seems to be rather unlikely. As mono-*para*-methoxybenzoyldiethylgermyl has a chemical structure similar to

that of mono-*para*-methoxyacyldiethylgermane, both featuring a  $\pi\pi^*$  band,<sup>276</sup> which absorbs in the Vis light region, the formation of a germyl species as a secondary radical is rather likely via the absorption of a second photon. Neshchadin *et al.*<sup>277</sup> reported the formation of radicals from bisacylgermane, slightly shifting towards the red-edge of the absorption maximum of bisacylgermane. Considering Ivocerin as a *para*-substituted bisacylgermane, it is plausible that a radical originating from Ivocerin may also appear red-shifted to the absorption peak of Ivocerin at 410 nm. Presuming that acylgermyl can still be excited at the fringe of the absorption band using 400 fs laser pulses, conceivable pathways for generating secondary germyl fragments include direct cleavage of the C-Ge bond of primary acylgermyl radicals via 2PA or the consecutive cleavage of an acyl radical subsequent to the reaction of the acylgermyl radical with a monomer unit. However, the germyl fragments may be deactivated by quenching before they can participate in the diffusion-controlled initiation reaction with the monomer, resulting in a short lifetime of the biradicals formed. Instead, a different mechanism channel is proposed. The stabilized acylgermyl radical initiates macromolecular growth with a subsequent C-Ge bond cleavage triggered by a second photon, forming a germyl-centered two-armed polymer chain.



**Scheme 5.1:** Proposed decomposition pathway of Ivocerin after photoexcitation. In a first step, Ivocerin cleaves into an acylgermyl and an acyl radical. In a potential second step, the acylgermyl radical further cleaves into an acyl radical and a germyl biradical.

Since ESI-MS analysis is not sufficient to provide a final explanation for the channel branching during radical formation. The following section will explore the electronic behaviour of the excited states of Ivocerin after photoexcitation via fs transient absorption spectroscopy. Using this powerful technique, potentially enables a comprehensive understanding of the relaxation channels on short time scales prior to radical formation.

## 5.4 Transient Absorption Spectroscopy

Previous studies have highlighted that the progress of polymerization can be predicted by understanding the process of initiator cleavage, as this initial reaction strongly contributes to the reaction conditions for the overall polymerization.<sup>21</sup> It is therefore critical to deepen the understanding of the earliest steps after photoexcitation. A pump-probe transient absorption spectrometer was employed to investigate the electronic dynamics of a 12 mmol L<sup>-1</sup> sample of Ivocerin in MMA ( $\lambda_{max} = 408 \text{ nm}$ ,  $OD = 1$ ) in a 1 mm cuvette. A 400 nm beam served as the pump to resonantly excite the  $n\pi^*$  band of Ivocerin with an energy of 1  $\mu\text{J}$ . A second beam probed the pump-induced absorption changes at regular intervals using a CaF<sub>2</sub>-generated WL continuum in the range of 350-720 nm.

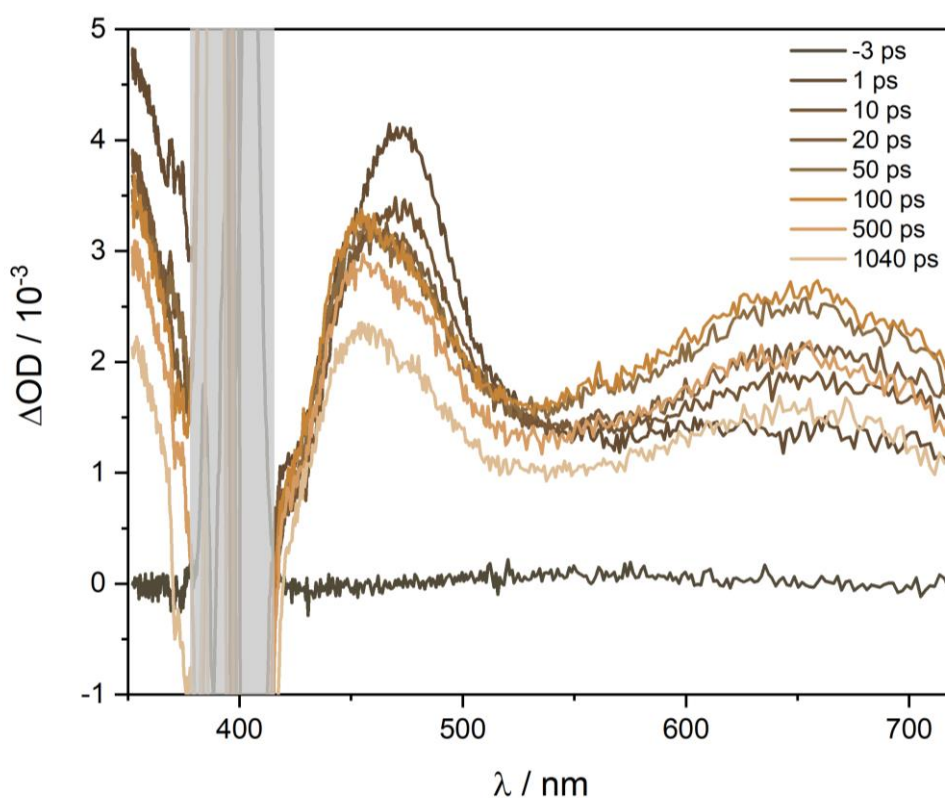


**Figure 5.10:** Transient absorption spectra of 12 mmol L<sup>-1</sup> Ivocerin in MMA (OD 1) after excitation with 1  $\mu\text{J}$  fs laser pulses at 400 nm, probed at different delay times in a range of 350-720 nm. Depending on the pump-probe delay, a broadband ESA was observed with local maxima at 650 nm, 470 nm, 450 nm, as well as another ESA below 400 nm and an isosbestic point at 520 nm. The spectral region around 400 nm was greyed out as it was strongly superimposed by pump pulse scattering.

The transient spectrum presented in **Figure 5.10** depicts a dominant broadband ESA over the entire observed wavelength range with local maxima around 650 nm, 470 nm, 450 nm and in the UV range below 400 nm. In addition, an isosbestic point was observed at  $\sim 525 \text{ nm}$  from 10 – 50 ps. An isosbestic point usually implies no change of the stoichiometry and notably, no

secondary processes (see IUPAC Gold Book<sup>278</sup> for references). An isosbestic point between singlet ESA and stimulated emission is usually characterized by a crossing at zero  $\Delta OD$ . However, the isosbestic point at a positive  $\Delta OD$  at  $\sim 525$  nm between two local maxima of a broadband ESA was assigned to a transition into different higher excited states at 450 nm and 650 nm. The spectral region around 400 nm has been greyed out as it is superimposed by strong scattering from the 400 nm pump pulse. The transient response below 400 nm reaches its maximum within one ps, followed by a long-lived component, similar to that at 470 nm and 450 nm, respectively. However, being at the edge of the WL spectrum, it was not properly resolved and was not further analyzed. The transient response around the local maximum at 650 nm rises within tens of ps with subsequent long-lived behaviour, which does not relax to zero in the observed time of 1 ns.

The transient spectra were analysed using a Matlab algorithm written by a colleague<sup>220</sup> at KIT to generate a decay-associated difference spectra (DADS, **Figure 5.11**). DADS results from multi-exponential fitting of all probed wavelengths with one set of parameters (for more details, refer to **Section 3.4**). Such an analysis provides information about the time constants and associated amplitudes over a wide range of probed wavelengths. A negative amplitude  $A_1$  in the DADS spectrum is related to an increase in the transient spectra, a positive amplitude to a decrease, an amplitude crossing zero  $\Delta OD$  indicates an isosbestic point. The calculated time constants and amplitudes fitted the probed wavelength well, as exemplarily shown in **Figure 5.12** using a biexponential fit function. Given  $\tau_0 \ll 1$  ps, the transients were interpreted rising ultrafast into an excited singlet state. The amplitude  $A_1$  switches the sign from positive to negative, representing a decrease in the transient spectrum from 430 – 530 nm with a local maximum at 470 nm as well as a rising transient response in the spectral range from 530 nm beyond 700 nm showing a local maximum at 650 nm.  $A_2$  exhibits a broadband positive amplitude with local maxima at 450 nm and 650 nm, which was associated with the decrease of a long-lived ESA with a time constant of more than the maximum delay time of 1 ns, with an estimated value of  $\tau_2 > 3$  ns.

Further, the amplitude spectrum indicates a blue-shift from the local maximum of  $A_1$  at 470 nm to the local maximum of  $A_2$  at 450 nm within  $\tau_1 = 9.2$  ps, likely indicating either an IVR, the transition from a singlet to a triplet state via ISC or a radical formation. Since the blue-shift in the transient spectrum in **Figure 5.10** is not gradual, but rather abrupt, an IVR was practically ruled out. Ultrafast radical formation within a few ps is feasible, as known from benzoin.<sup>21</sup> However, Neshchadin<sup>277</sup> reported a radical formation in the transient spectra of

bisacylgermane at 500 nm, thus red-shifted to the ESA at 470 nm. Given that Ivocerin is structurally similar to bisacylgermane, it was assumed that any potential radical formation would also be red-shifted to the ESA at 470 nm in the transient spectrum of Ivocerin. As no such new bathochromic band was observed, the blue-shift was attributed to ISC from an excited singlet state to a triplet state. The isosbestic point of  $A_1$  at  $\sim 525$  nm confirms the assumption that 450 nm and 650 nm are related to the same excited state. Therefore, the positive part of  $A_1$  was interpreted as a depopulation of the excited singlet state, while the negative part of  $A_1$  described the rise of a triplet state after ISC with a lifetime of  $\tau_1 = 9.2$  ps. Consequently,  $A_2$  was attributed to broadband triplet ESA with local maxima at 450 nm and 650 nm in the transient absorption spectrum, consistent with the literature.<sup>277</sup>

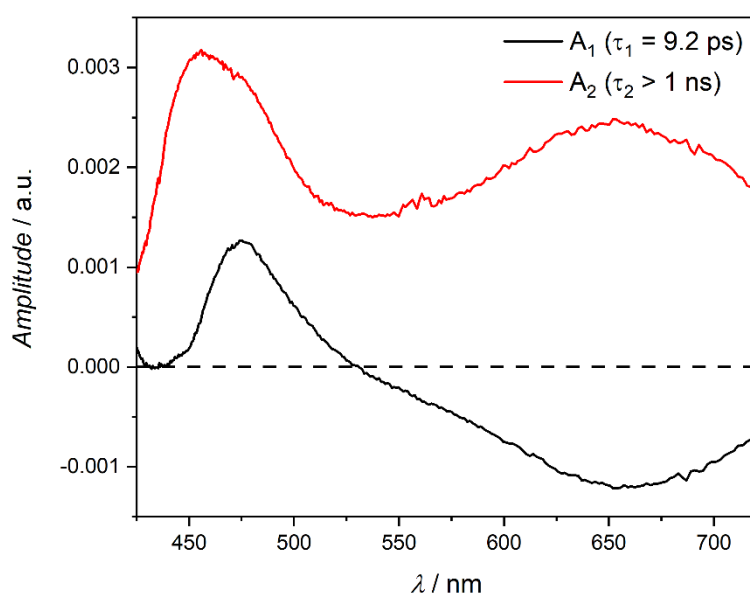


**Figure 5.11:** Biexponential DADS of the transient spectra shown in Figure 4.9. The DADS provides three wavelength-dependent amplitudes  $A_i$  with associated time constants  $\tau_i$ .

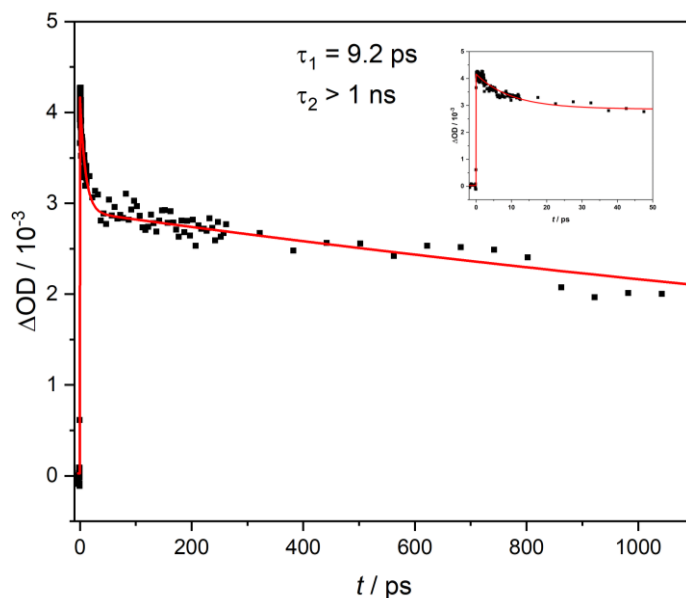


**Figure 5.12:** Single transient of Ivocerin in MMA ( $c=12\text{mmol L}^{-1}$ ,  $\text{OD}=1$ ) at the probe wavelength 470 nm after excitation with 400 nm fs pulses with a pulse energy of 1  $\mu\text{J}$ . Data points were fitted with the time constants  $\tau_i$  and amplitudes  $A_i$  obtained from the global analysis. The inset shows a zoom into the first 50 ps of the fitted transient.

While the global fit of Ivocerin in MMA provides an ISC time of  $\tau_1 = 9.2$  ps, Neshchadin *et al.*<sup>277</sup> measured a time of 30 ps for the ISC of bisacylgermane in toluene and 50 ps in acetonitrile. Remarkably, the ISC lifetime of Ivocerin is  $\sim 3 - 5$  times lower compared to bisacylgermane. As a result, the triplet states appear to be populated between three and five times faster in the case of Ivocerin compared to the unsubstituted bisacylgermanes. In accordance with this relationship, the lifetime of the triplet states of Ivocerin decreases by a factor of about 5. Reportedly,<sup>277</sup> the triplet state lifetime of bisacylgermane is approximately 14 - 16 ns, depending on the solvent. In correlation with the previous findings of the current chapter, these results underpin the hypothesis that Ivocerin is a high potential photoinitiator with efficient triplet state formation. This hypothesis is further supported by a photobleaching study of Ivocerin by Fröhvirt *et al.*,<sup>279</sup> who reported a quantum yield of 0.86 indicating that the population of triplet states with subsequent radical formation represents the main photophysical channel of photoexcited Ivocerin. However, since initiation reactions are governed by various parameters, such as radical formation, reaction conditions, diffusion and solvents, as described in **Section 3.5**, further systematic in-depth studies on the initiation efficiency of Ivocerin will be required (refer to **Section 9**).

The current sub-chapter on fs time-resolved absorption spectroscopy with Ivocerin expanded the investigation of photo-induced polymerization with Ivocerin from the product formation,

followed by polymer chain growth towards the earliest events after photoexcitation. This thesis, in particular, revealed the earliest events in the photo-induced decomposition of Ivocerin prior to radical formation for the first time.

## 5.5 Summary

In this chapter, the mechanism of the photopolymerization of MMA using Ivocerin as photoinitiator was mapped from the earliest events through to polymer formation. Initially, stationary absorption spectroscopy served to study the absorption behaviour of Ivocerin prior to monitoring the fs laser beam fluence-dependent initiator conversion recording absorption spectra. Employing SEC analysis after fs PLP experiments at 400 nm in the Hz regime confirmed the generation of polymers and demonstrated laser control over the polymerization reaction via the underlying PLP mechanism by varying the repetition rate of the incident fs laser pulses was varied. The next step included a *post-mortem* analysis of the polymerization products using ESI-MS. Analyzing the end group distribution in the mass spectrum allowed for drawing conclusions on the initiator fragmentation and thus the decomposition mechanism of the initiator. Finally, to expand the time scale from product formation to the earliest events, time-resolved fs absorption spectroscopy experiment served to examine the electronic behaviour of Ivocerin immediately after photoexcitation.

In the realm of recording energy-dependent absorption spectra, initially one non-irradiated sample was analyzed, followed by several samples irradiated in the range between  $25 \mu\text{J cm}^{-2}$  and  $102 \mu\text{J cm}^{-2}$  at 400 nm. The initiator concentration after each experiment was determined from the absorption spectra and plotted on a double-logarithmic scale dependent on the laser beam fluence. The data points of the experiment at 400 nm excitation followed a linear function with a slope of  $0.97 \pm 0.05$ , underpinning a linear initiator decay at resonant absorption, as expected for photoexcitation of Ivocerin in this spectral region.

The fs PLP experiments were excited at 400 nm with various repetition rates, 10 Hz, 20 Hz, 50 Hz and 100 Hz and the generated polymers were subsequently analyzed using SEC. By means of a method developed by Olaj *et al.*<sup>87</sup> (refer to **Section 3.5**), multiples of the polymer molecular weight were assigned to the inflection point of the SEC traces, or the repeating peaks of the first derivatives, respectively. **Eq. 3.33** served to calculate the propagation rate coefficient  $k_p$  of the propagating polymer chains  $M_i$  at each repetition rate, which was consistent with the IUPAC accepted literature value ( $267 \text{ mol L}^{-1} \text{ s}^{-1}$ ),<sup>275</sup> unambiguously evidencing that polymerization at 400 nm in the Hz regime followed the PLP mechanism.

The end group distribution of the isotopic pattern recorded via ESI-MS revealed a total amount of 13 acyl-based and germyl-based combination and disproportionation products, being part of a pool of expected polymer products. In general, it was evident that the acyl-based species are more abundant compared to the germyl-based species, with the germyl-based products only occurring with a relative abundance of about 30 - 40% of the acyl-based products. Based on the observed end group distribution a two-step initiator cleavage was proposed generating both an acyl and an acylgermyl radical with cleavage of the biradical germyl species in a second step.

The transient spectrum of Ivocerin was dominated by a broadband ESA over the entire observed wavelength range from 350 - 720 nm. The electronic behaviour was likely characterized by ultrafast absorption into excited singlet states with subsequent ISC within 9.2 ps into broadband long-lived triplet states ( $\tau > 1$  ns) with local maxima at 450 nm and 650 nm in the probed range. From these triplet states, radicals can be potentially generated by initiator bond cleavage. The ultrafast ISC was in line with reported ISC lifetime of 2 - 4 ps for other acylgermanes.<sup>17</sup> However, the extrapolated triplet state lifetime of  $\sim 3$  ns indicated a comparably fast radical formation, a conclusion that is supported by the theoretical rate coefficient for radical formation of  $k_{rad} = 7 \cdot 10^7$  s<sup>-1</sup> and triplet lifetime of 14 - 16 ps of the unsubstituted bisacylgermane.<sup>277</sup> Ivocerin proved to be an efficient photoinitiator, which was further underlined by the reported photobleaching quantum yield of 0.86.<sup>279</sup>

## 6 NIR Light-Induced Polymerization with Ivocerin

The following chapter reports the first detailed study of the polymerization of MMA initiated by the 2PA induced decomposition of Ivocerin into radicals using fs NIR laser pulses. The 2PP is investigated using an identical analytical procedure as that outlined in **Section 5**. Initially, stationary absorption spectroscopy is employed to determine the dependence of initiator decay on photon flux. This is followed by a study of the generation of polymers via SEC. This method also allows the verification of the underlying PLP mechanism – and thus laser-control of the polymer chain growth – by employing various repetition rates. Taking advantage of the well-known penetration depth of NIR light and its benign nature to tissue,<sup>37,38</sup> 2PP through tissue will be demonstrated. The generation of polymers is again highlighted using SEC analysis. Subsequently, *post-mortem* end group analysis of the generated polymer products evidences the initiator fragment distribution, which informs the decomposition mechanism of the initiator.

### 6.1 Stationary UV/Vis/NIR Absorption Spectroscopy

The NIR fs PLP experiments were conducted with a solution of 12 mmol L<sup>-1</sup> Ivocerin in MMA, identically concentrated as in the Vis light fs PLP experiments. The absorbance was measured in a 1 mm cuvette in the range from 200 to 1200 nm with a Varian Cary 500 spectrometer and is shown in **Figure 6.1**. The spectrum shows an n- $\pi^*$  transition of Ivocerin around 400 nm with a HOMO-LUMO transition at 425 nm and a HOMO-LUMO+1 transition at 410 nm, as well as a stretching vibration of a C-H bond of MMA at 1100-1200 nm (for more details refer to **Chapter 5.1**). The solution was prepared at a concentration (12 mmol L<sup>-1</sup>) to achieve an OD of 1 at 400 nm. Since Ivocerin was intended to be excited in the NIR range via 2PA, 800 nm was employed as the excitation wavelength. This wavelength is far from the n- $\pi^*$  band, thus not enabling resonant absorption. In addition, this wavelength was readily accessible, as 800 nm is the fundamental emission wavelength of the Ti-Sapphire laser.

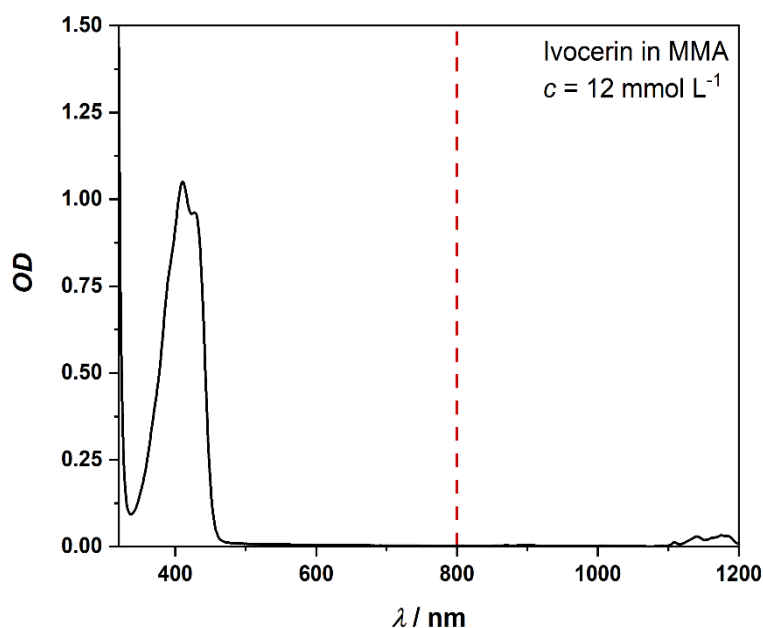


**Figure 6.1:** Absorption spectrum of 12 mmol L<sup>-1</sup> Ivocerin in bulk MMA with a peak absorption of about OD=1 at 408 nm recorded in a 1 mm cuvette. The weak peak between 1100 nm and 1200 nm is attributed to MMA. The excitation wavelength employed for the 2PA experiment (800 nm) is indicated by the vertical dotted red line.

The NIR-induced decomposition of Ivocerin was subsequently examined using UV/Vis spectroscopy. For this, the absorbance of Ivocerin was recorded as a function of the incident fs laser beam fluence at 800 nm. As 2PA processes depend quadratically on the light intensity, a quadratic dependence of the initiator conversion on the variation of the laser pulse energy is expected. To ascertain 2P-induced cleavage of Ivocerin, identical samples (12 mmol L<sup>-1</sup> in MMA) were irradiated for 30 min with various pulse energies (25-70 μJ) at 800 nm and a repetition rate of 100 Hz. Similar to the experiments conducted at 400 nm (refer to **Section 5.1**), 250 μL aliquots were taken from a 12 mmol L<sup>-1</sup> stock solution, placed in transparent vials and irradiated from below, as described in the experimental section. **Figure 6.3** presents the fluence-dependent stationary absorption spectrum. The bulk solution initially featured an OD of close to 1 at the absorption maximum, which decreased with increasing incident energy. The recorded spectra were used to determine the concentration of Ivocerin in each sample utilizing the wavelength-dependent extinction coefficient calculated from the OD of the bulk solution and Beer-Lambert's law. The final concentration was determined by averaging the concentration (**Figure 6.3**, right) over the range from 380-440 nm after each step of irradiation as in **Section 5.1**. These results are plotted in **Figure 6.3**. Finally, the concentration of Ivocerin was analyzed as a function of pulse fluence on a double-logarithmic scale, with the data points showing a quadratic trend with a gradient of  $m = 2.3 \pm 0.3$  (**Figure 6.2**). This gradient indicates that on average, 2.3 photons contribute to the photo-induced decay of Ivocerin

at 800 nm, meaning the decay can predominantly be attributed to a 2P process. This result aligns with a previous publication by Batchelor *et al.*,<sup>280</sup> who reported using Ivocerin as a suitable 2P NIR-triggered photoinitiator in three-dimensional laser lithography, demonstrating its ability to fragment after NIR light exposure. In the current thesis, however, the NIR light-induced decomposition of Ivocerin was examined in detail for the first time, evidencing 2PA.

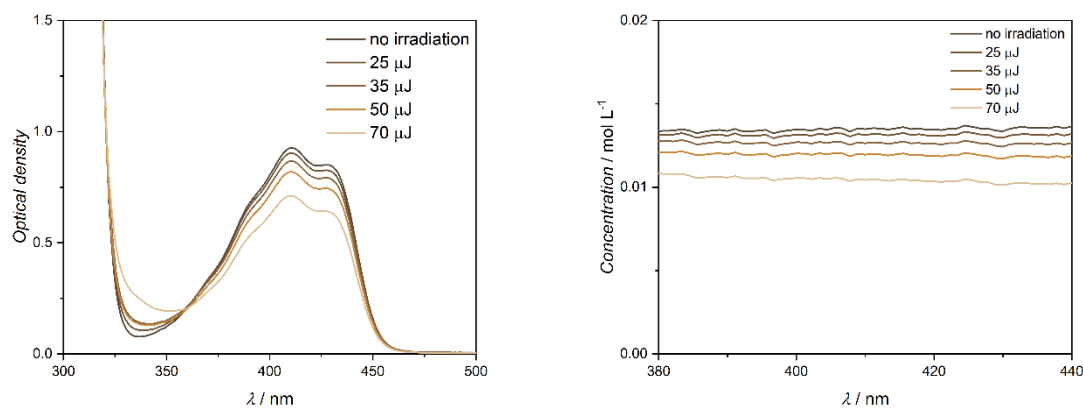


**Figure 6.3:** UV/Vis absorption spectra of 12 mmol L<sup>-1</sup> Ivocerin in MMA after 30 min irradiation with various energies at 800 nm (left) and plot showing the corresponding initiator concentration after each irradiation step (right). Adapted with permission from ref. 182. Copyright 2022 American Chemical Society.

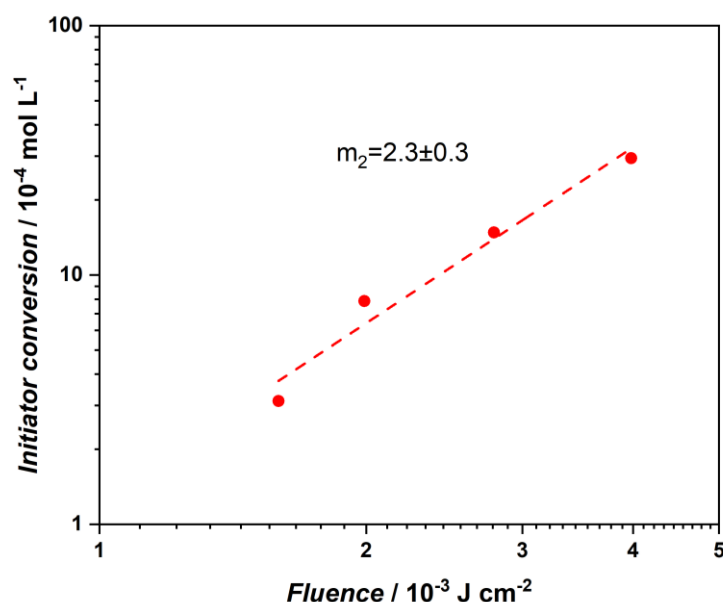


**Figure 6.2:** Initiator conversion after 30 min irradiation of solution with 12 mmol L<sup>-1</sup> Ivocerin in MMA at 800 nm with various laser beam fluences, plotted on a double logarithmic scale. A linear regression provides the gradient which in turn indicates the number of photons required for initiator decay. Adapted with permission from ref. 182. Copyright 2022 American Chemical Society.

## 6.2 Size Exclusion Chromatography

The following subchapter demonstrates that the 2P excitation of Ivocerin, when exposed to NIR light in bulk MMA, both initiates polymer chain growth and that the polymerization is laser controlled following a PLP mechanism. Analogous to **Section 5.2**, the experimental method for the determination of propagation rate coefficients of monomers by means of the repetition rate of a pulsed laser developed by Olaj *et al.*<sup>87</sup> was employed. Aliquots of 500  $\mu\text{L}$  were taken from a bulk solution of Ivocerin ( $12 \text{ mmol L}^{-1}$ ) in MMA and placed in transparent laser vials and purged of oxygen by nitrogen percolation. The samples were irradiated from below with fs laser pulses at 800 nm ( $5.5 \text{ mJ cm}^{-2}$ ), varying the pulse repetition rate (10 Hz, 20 Hz, 50 Hz, and 100 Hz) in an identical manner as described in **Section 5.2** using an optical chopper. **Figure 6.4** to **Figure 6.7** depict the MWD obtained from SEC traces, and first derivatives, for the generated PMMA at 10 Hz, 20 Hz, and 50 Hz, plotted on a logarithmic scale ranging from 3.5 ( $5,000 \text{ g mol}^{-1}$ ) to 6 ( $1,000,000 \text{ g mol}^{-1}$ ).

The SEC trace in **Figure 6.4** (10 Hz) reveals multiple peaks between  $10^4 \text{ g mol}^{-1}$  and  $10^5 \text{ g mol}^{-1}$  indicating the formation of polymer chains with discrete molecular weights, a characteristic feature of PLP behaviour. To substantiate this observation, the first derivative was analyzed in accordance with the procedure described in the theoretical **Section 3.5**. The peaks in the first derivative, corresponding to the inflection points of the SEC trace, can be directly associated with the kinetic chain length during macromolecular growth. The molecular weights  $M_1 = 23,000 \text{ g mol}^{-1}$ ,  $M_2 = 45,000 \text{ g mol}^{-1}$ , and  $M_3 = 69,000 \text{ g mol}^{-1}$  are approximately multiples of each other, which is typical of PLP behaviour. An overview of the molecular weights  $M_i$  of the polymer chains is provided in **Table 6.1**. Notably, the calculated propagation rate coefficient (**Eq. 3.33**) for these  $M_i$  values at 10 Hz, reported in **Table 6.2**, aligns with the IUPAC-accepted literature value for MMA ( $267 \text{ L mol}^{-1} \text{ s}^{-1}$ ),<sup>275</sup> with a deviation of 7-10%. This result provides clear evidence that the polymer chain growth of PMMA at a pulse frequency of 10 Hz follows a PLP mechanism.

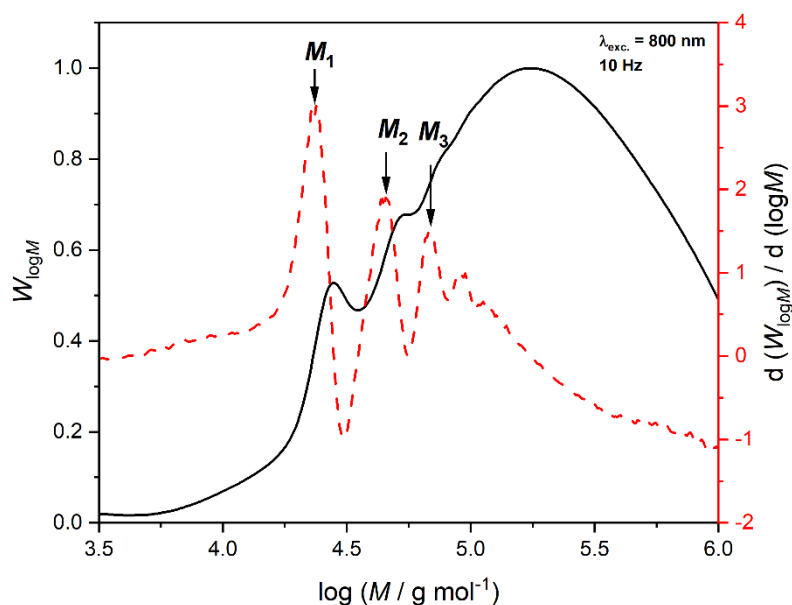


**Figure 6.4:** SEC trace (black) and first derivative of SEC trace (red dashed) of PMMA generated by 800 nm pulsed fs laser triggered Ivocerin fragmentation ( $c = 12 \text{ mmol L}^{-1}$  in bulk MMA) with a repetition rate of 10 Hz where the inflection points of the distribution are  $M_1 = 23,000 \text{ g mol}^{-1}$ ,  $M_2 = 45,000 \text{ g mol}^{-1}$  and  $M_3 = 69,000 \text{ g mol}^{-1}$ . Adapted with permission from ref. 182. Copyright 2022 American Chemical Society.

In addition, the SEC traces obtained after polymerization at 20 Hz and 50 Hz were subjected to an identical detailed analysis to ensure that the polymerization process is indeed fully controlled by the laser and follows the PLP mechanism. **Figure 6.5** presents the SEC trace and the first derivative of polymer generated during the 20 Hz experiment. Similar to the SEC trace of polymer generated at 10 Hz (**Figure 6.4**), the SEC trace at 20 Hz also exhibits a multiple peak distribution with well-defined molecular weights. As expected, changing the repetition rate from 10 Hz to 20 Hz using the chopper (refer to experimental **Section 4.3**) results in polymer chains with approximately half the molecular weight, which is confirmed by the molecular weights  $M_i$  (refer to **Table 6.1**) assigned to the peaks via its first derivative (**Figure 6.5**). Once again, the molecular weights  $M_1 = 14,000 \text{ g mol}^{-1}$ ,  $M_2 = 28,000 \text{ g mol}^{-1}$ , and  $M_3 = 43,000 \text{ g mol}^{-1}$  are approximately multiples of each other and align with the predicted values. The calculated propagation rate coefficient (**Eq. 3.33**) for these  $M_i$  at 20 Hz closely matches the IUPAC literature value<sup>275</sup> with a deviation of 3 -5%, further confirming that the molecular weights  $M_i$  (**Table 6.2**) correspond to the growth of PMMA chains via the PLP mechanism. These results evidence that changing the laser repetition rate indeed leads to the expected outcomes consistent with the PLP mechanism.

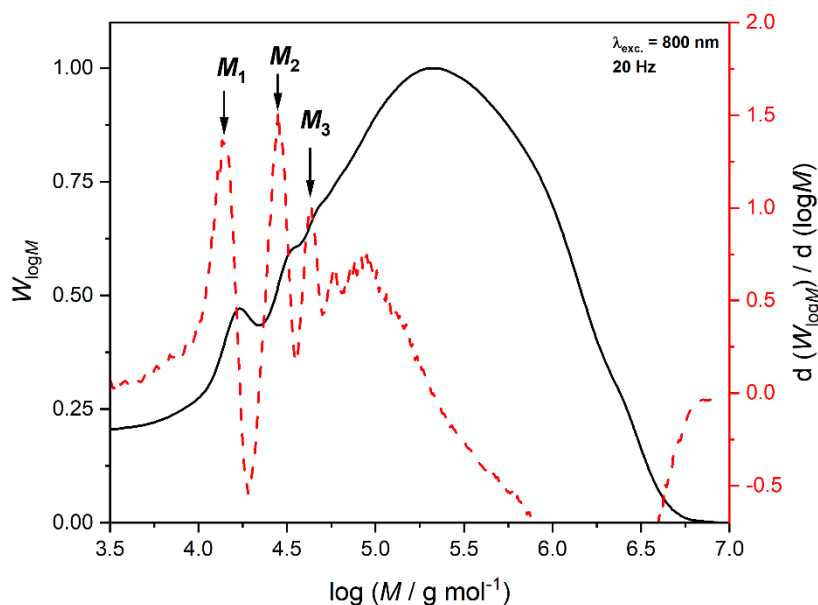


**Figure 6.5:** SEC trace (black) and first derivative of SEC trace of PMMA generated by 800 nm (red dashed) pulsed fs laser triggered Ivocerin fragmentation ( $c = 12 \text{ mmol L}^{-1}$  in bulk MMA) with a repetition rate of 20 Hz, where the inflection points of the distribution are close to  $M_1 = 14,000 \text{ g mol}^{-1}$ ,  $M_2 = 28,000 \text{ g mol}^{-1}$  and  $M_3 = 43,000 \text{ g mol}^{-1}$ . Adapted with permission from ref. 182. Copyright 2022 American Chemical Society.

To ensure that the current polymerization experiment is indeed laser-controlled, a third experiment at 50 Hz (**Figure 6.6**) was conducted. Similar to the previously presented PLP experiments (**Figure 6.4** and **Figure 6.5**), **Figure 6.6** illustrates the SEC trace of PMMA generated at 50 Hz, displaying multiple peaks similar to the SEC traces at 10 Hz and 20 Hz. The peaks in the first derivative can be associated with polymers possessing molecular weights of  $M_1 = 6,000 \text{ g mol}^{-1}$ ,  $M_2 = 12,000 \text{ g mol}^{-1}$ , and  $M_3 = 19,000 \text{ g mol}^{-1}$ . With regard to the calculated propagation rate coefficient, the 50 Hz experiment closely aligns with the literature<sup>275</sup> value of  $267 \text{ L mol}^{-1} \text{ s}^{-1}$  with a deviation of only 1-7% (refer to **Table 6.2**). Given that all three experiments at various repetition rates follow the PLP mechanism, and the propagation rate coefficients remain consistent with the literature<sup>275</sup> (see **Table 6.2**), providing clear evidence of laser control in Vis light fs polymerization using Ivocerin as the photoinitiator.

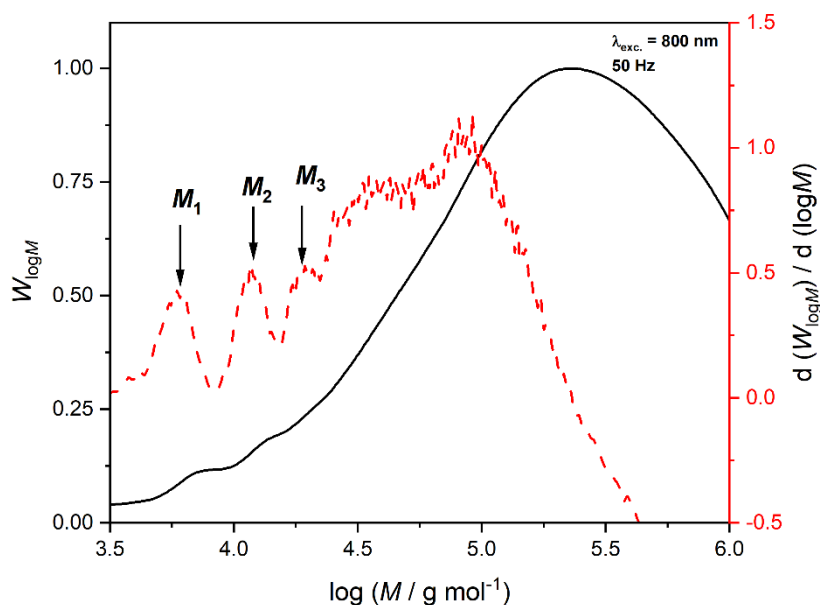


**Figure 6.6:** SEC trace (black) and first derivative of SEC trace (red dashed) PMMA generated by 800 nm pulsed fs laser triggered Ivocerin fragmentation ( $c = 12 \text{ mmol L}^{-1}$  in bulk MMA) with a repetition rate of 50 Hz where the inflection points of the distribution are close to  $M_1 = 6,000 \text{ g mol}^{-1}$ ,  $M_2 = 12,000 \text{ g mol}^{-1}$  and  $M_3 = 19,000 \text{ g mol}^{-1}$ . Adapted with permission from ref. 182. Copyright 2022 American Chemical Society.

Finally, the 100 Hz SEC experiment completed the repetition rate variation series. Although the SEC trace in **Figure 6.7** only displays a weak PLP structure, its first derivative trace was used to assign the molecular weight  $M_1 = 3,000 \text{ g mol}^{-1}$  and  $M_2 = 6,300 \text{ g mol}^{-1}$  to the propagating polymer chains. In contrast to the previous frequencies  $M_3$  was not resolved with sufficient quality to be analyzed. Nonetheless, the presence of  $M_1$  and  $M_2$ , as well as the minor deviation of the calculated  $k_p$  values the IUPAC literature by only 1.8 – 5.9%, were considered sufficient evidence to verify laser control over the 100 Hz polymerization. Consequently, the 800 nm 2PP of MMA using Ivocerin as photoinitiator is fs laser pulse controlled for all applied frequencies. In a following step, the final product formation was explored in the next subchapter using ESI-MS.

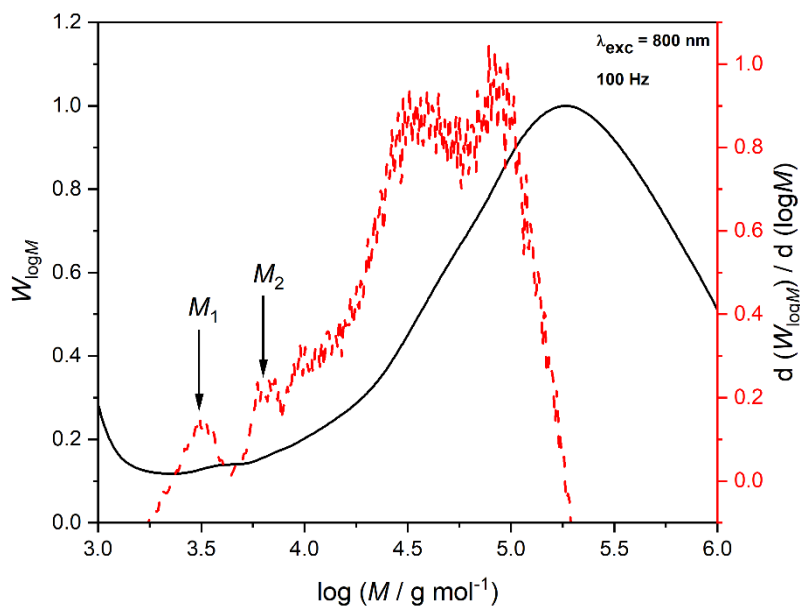


**Figure 6.7:** SEC trace (black) and first derivative of SEC trace (red dashed) PMMA generated by 800 nm pulsed fs laser triggered Ivocerin fragmentation ( $c = 12 \text{ mmol L}^{-1}$  in bulk MMA) with a repetition rate of 100 Hz where the inflection points of the distribution are close to  $M_1 = 3,000 \text{ g mol}^{-1}$  and  $M_2 = 6,300 \text{ g mol}^{-1}$ . Adapted with permission from ref. 182. Copyright 2022 American Chemical Society.

**Table 6.1:** Overview of molecular weight of the polymer chains  $M_i$  at the inflection points in the first derivative of the SEC trace generated by 800 nm pulsed fs laser triggered Ivocerin fragmentation ( $c = 12 \text{ mmol L}^{-1}$  in bulk MMA) with various repetition rates.

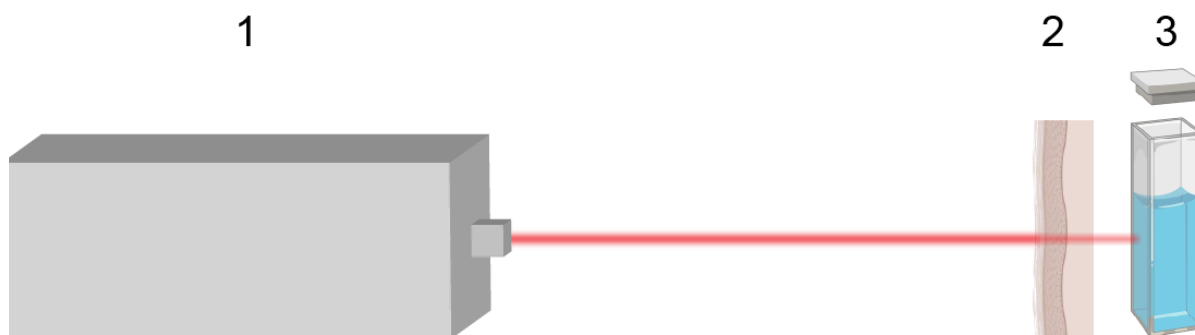
$f / \text{Hz}$	$M_1 / \text{g mol}^{-1}$	$M_2 / \text{g mol}^{-1}$	$M_3 / \text{g mol}^{-1}$
10	23,000	45,000	69,000
20	14,000	28,000	43,000
50	6,000	12,000	19,000
100	3,000	6,300	-

**Table 6.2:** Overview of the propagation rate coefficients (**Eq. 3.33**) of MMA calculated for polymer chains with the assigned molecular weight  $M_i$  generated by 800 nm pulsed fs laser triggered Ivocerin fragmentation ( $c = 12 \text{ mmol L}^{-1}$  in bulk MMA) with a repetition rate of 50 Hz and compared to the IUPAC literature<sup>275</sup> propagation rate coefficient of MMA ( $267 \text{ L mol}^{-1} \text{ s}^{-1}$ ).

Repetition rate / Hz	$k_p (M_1) / \text{L mol}^{-1} \text{ s}^{-1}$	$k_p (M_2) / \text{L mol}^{-1} \text{ s}^{-1}$	$k_p (M_3) / \text{L mol}^{-1} \text{ s}^{-1}$	$k_p(\text{Lit.}) / \text{L mol}^{-1} \text{ s}^{-1}$
10	242	247	248	267
20	256	255	258	267
50	267	266	288	267
100	272	283	-	267

### 6.3 Polymerization through Tissue

NIR light features advantageous properties, such as deep penetration depth and benign nature to tissue. This is especially significant when comparing to UV and Vis light, which are typically used in most conventional photo-induced initiation mechanisms of polymerization. Therefore, the current thesis aimed to illustrate the ability of NIR light to trigger 2PP after propagation through biological tissue using fs laser pulses. Subsequent SEC analysis confirmed polymer generation and laser control of the polymerization. To conduct this experiment, a thin slice (1 mm) of bacon was positioned in the path of the laser beam just in front of the sample. Bacon, due to its natural structure, scatters the laser beam as it penetrates the tissue. Placing the bacon slice directly in front of a 1 mm cuvette helped minimize the scattering effects, and better mimic *in vivo* conditions.



**Scheme 6.1:** Schematic picture of the through tissue irradiation set-up; the incident 800 nm laser beam (1) (40 fs, 1 kHz,  $25 \text{ GW cm}^{-2}$ ) propagates through a 1 mm thick slice of bacon (2), which decreases the laser intensity to  $10 \text{ GW cm}^{-2}$ . Subsequently the laser beam penetrates a 1 mm cuvette (3). The bacon closely adhered to the sample holder. The distance between the bacon and the cuvette in the picture only portrays the weaker laser beam after tissue penetration.

Using the above setup (**Scheme 6.1**), the generation of polymer was investigated after irradiating a solution of Ivocerin in MMA ( $12 \text{ mmol L}^{-1}$ ) with a fluence of  $10 \text{ GW cm}^{-2}$  (which was reduced to close to  $10 \text{ GW cm}^{-2}$  by passing through the tissue) at a repetition rate of 20 Hz. The SEC trace (**Figure 6.8**, black curve) suggests a PLP structure, which is further confirmed by the first derivative trace (**Figure 6.8**, red curve) and peak assignments (**Figure 6.9**). The molecular weights of the polymer chains, specifically  $M_1 = 13,000 \text{ g mol}^{-1}$ ,  $M_2 = 24,000 \text{ g mol}^{-1}$  and  $M_3 = 36,000 \text{ g mol}^{-1}$ , deviate 8-17% from the molecular weights of the polymer chains  $M_i$  generated without the presence of tissue (**Table 6.3**). Calculating the propagation rate coefficient  $k_p$  with **Eq. 3.33** results in propagation rate coefficients with a deviation of 12-19% from the IUPAC literature value,<sup>275</sup> presented in **Table 7.4**. As the  $k_p$  values are within the limit accuracy ( $\sim 20\%$ ) of the SEC instrument, the experiment was considered as laser controlled through biological tissue.

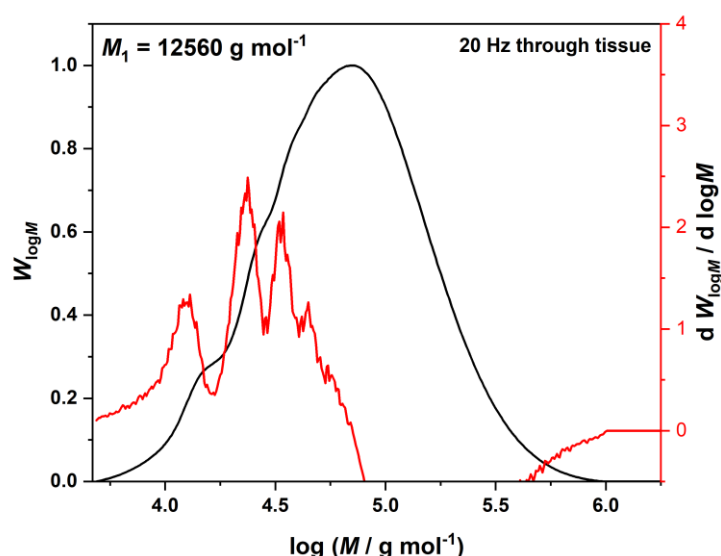


**Figure 6.8:** SEC trace and first derivative of SEC trace PMMA generated by 800 nm pulsed fs laser triggered Ivocerin fragmentation ( $c = 12 \text{ mmol L}^{-1}$  in bulk MMA) with a repetition rate of 50 Hz after the laser beam penetrated a slice of bacon. Adapted with permission from ref. 182. Copyright 2022 American Chemical Society.

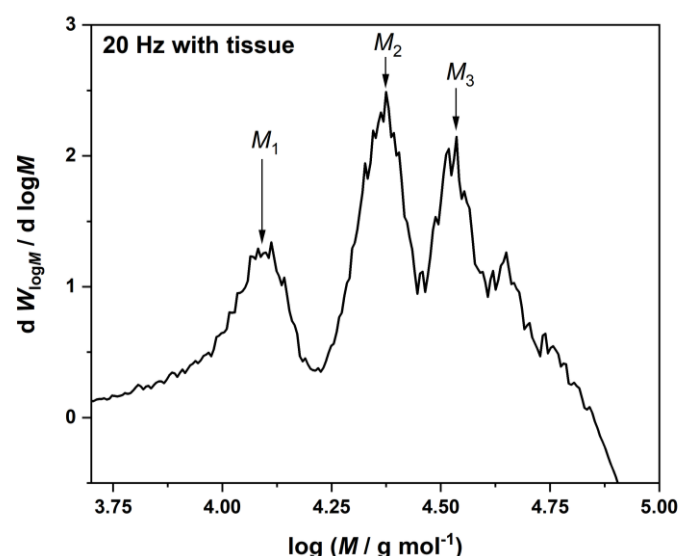


**Figure 6.9:** First derivative of SEC trace PMMA generated 800 nm pulsed laser triggered Ivocerin fragmentation ( $c = 12 \text{ mmol L}^{-1}$  in bulk MMA) with a repetition rate of 20 Hz after the laser beam penetrated through a slice of bacon, where the inflection points of the distribution are  $M_1 = 13,000 \text{ g mol}^{-1}$ ,  $M_2 = 24,000 \text{ g mol}^{-1}$  and  $M_3 = 36,000 \text{ g mol}^{-1}$ .

**Table 6.3:** Overview of molecular weight of the polymer chains  $M_i$  at the inflection points in the first derivative of the SEC generated trace at 800 nm with a repetition rate of 20 Hz, after the penetration of thin tissue and without tissue.

$\lambda / \text{nm}$	$M_1 / \text{g mol}^{-1}$	$M_2 / \text{g mol}^{-1}$	$M_3 / \text{g mol}^{-1}$
800 (tissue)	13,000	24,000	36,000
800 (no tissue)	14,000	28,000	43,000

**Table 6.4:** Overview of the propagation rate coefficients (**Eq. 3.33**) of MMA calculated for polymer chains with the assigned molecular weight  $M_i$  generated by 800 nm (red dashed) pulsed fs laser triggered Ivocerin fragmentation ( $c = 12 \text{ mmol L}^{-1}$  in bulk MMA) with a repetition rate of 20 Hz after penetration through tissue and compared to the IUPAC literature<sup>275</sup> propagation rate coefficient of MMA.

Repetition rate / Hz	$k_p(M_1) / \text{L mol}^{-1} \text{ s}^{-1}$	$k_p(M_2) / \text{L mol}^{-1} \text{ s}^{-1}$	$k_p(M_3) / \text{L mol}^{-1} \text{ s}^{-1}$	$k_p(\text{Lit.}) / \text{L mol}^{-1} \text{ s}^{-1}$
20 (with tissue)	237	218	216	267

## 6.4 Electrospray Ionization-Mass Spectrometry

The previous **Chapters 6.1** and **6.2** highlighted the ability of high intensity NIR light to trigger 2PA in Ivocerin with subsequent cleavage into primary radical species, enabling the laser controlled initiation of polymerization. Moreover, **Chapter 6.3** demonstrated that 2PP is even initiated after the incident NIR light propagated through biological tissue. As a next step, in the current chapter the generated polymer products are examined in detail via ESI-MS, followed by a comparison of the end group distribution with the one given by the Vis light fs PLP experiment in **Section 5.3**.

A stock solution of 12 mmol L<sup>-1</sup> Ivocerin in MMA was prepared and 500 μL aliquots were subsequently transferred to a capped transparent vial, allowing oxygen removal by percolation with nitrogen gas. The vial containing the solution was placed in an elevated metal block and exposed to 800 nm fs pulses from below with an energy of 650 μJ (5.5 mJ cm<sup>-2</sup>). For more experimental details refer to **Section 4.5**. Applying a chopper-controlled repetition rate of 100 Hz during an irradiation time of 30 min, the solution was exposed to 180,000 laser pulses resulting in an overall incident energy of 117 J. As the polymer growth is laser-controlled under the given condition, which was confirmed in **Chapter 6.2**, the chains grew to a size of 10 - 30 monomer units according to **Eq. 3.33**. Thus, a molecular weight of 1000 - 3000 g mol<sup>-1</sup> was achieved, well suitable for ESI-MS analysis.

Transferring the irradiated solutions from the vials to small aluminium pans enabled the solvent (MMA) to evaporate, resulting in the isolation of the generated polymer. For ESI-MS analysis, the synthesized polymer was dissolved in a mixture of THF and methanol with a volume ratio of 3:2, such that a molarity of 0.03 mg mL<sup>-1</sup> was achieved. After adding of 30 μL of a 100 μM NaTFA containing THF solution, the mixture was injected into the ESI-MS instrument. The mass spectrum was recorded in the *m/z* range of 1000 to 2000. **Figure 6.10** depicts a zoom into one unit from 1010 - 1110 *m/z*. serving as the basis for a detailed assignment of polymer species. To analyze the isotopic patterns of the generated polymers, the spectrum was simulated using Xcalibur (Thermo Fisher), assuming Gaussian-shaped peaks with a resolution of 60,000. This simulation method facilitated the identification of individual polymer species within a single repeating pattern.

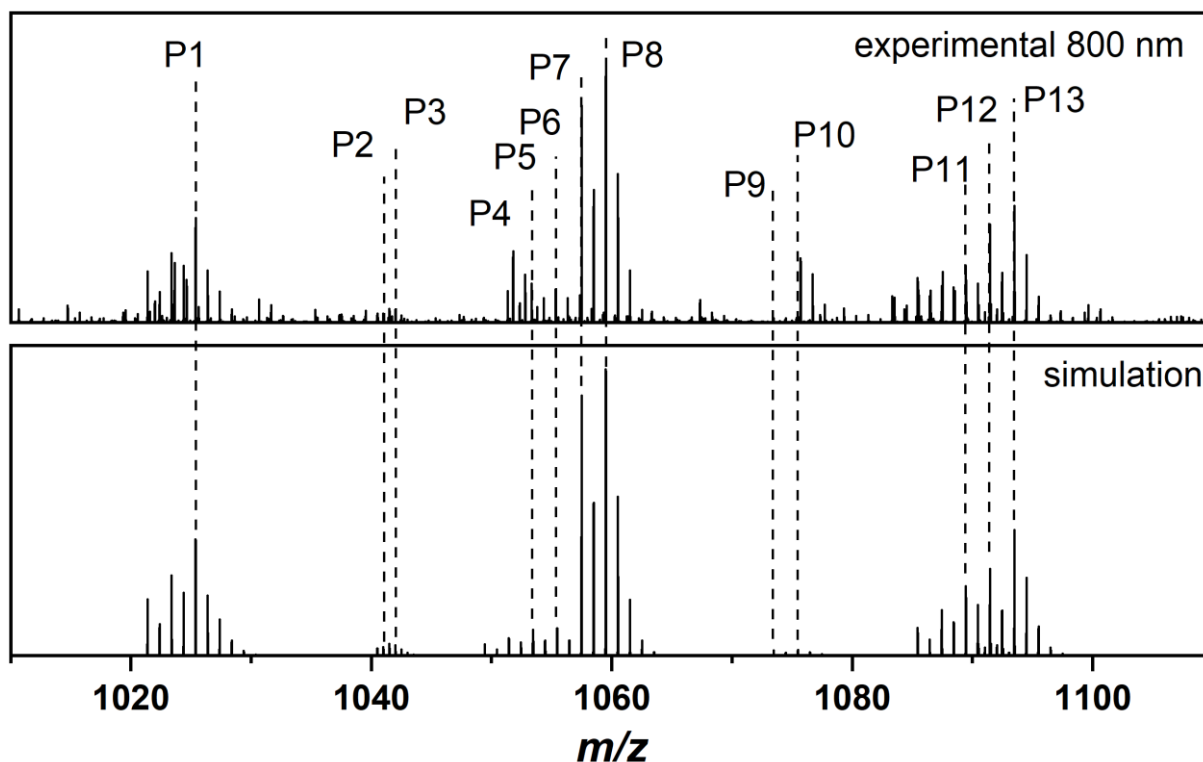


**Figure 6.10:** Comparison of an experimental ESI-MS spectrum (zoom into one repeat unit) of PMMA in THF/methanol (3:2) (top) with a simulated isotopic pattern (bottom) in the  $m/z$  range of 1010 – 1110. The experimental mass spectrum was obtained from polymers generated after 30 min irradiation of 12 mmol L<sup>-1</sup> Ivocerin in MMA with 102  $\mu\text{J cm}^{-2}$  fs laser pulses at 800 nm at a repetition rate of 100 Hz. 10  $\mu\text{L}$  of the irradiated solution was dissolved in 2 mL of a THF/methanol (3:2) solution with 100  $\mu\text{M}$  NaTFA.

Overall, 13 polymer species were identified (**Table 7.5**), including the three main species **P1**, **P7** and **P8**, **P11**- **P13** with a remarkably high abundance of 50% as well as some minor species **P4** - **P6** with 20% and **P2**, **P3**, **P9** and **P10** in traces with only 2% relative to the main species. **P1** (1025  $m/z$ ) represents a combination product of an acylgermyl fragment at one terminus and an acyl fragment at the opposite terminus of the polymer chain. The products **P7** (1057  $m/z$ ) and **P8** (1059  $m/z$ ) are one-sided acyl-terminated disproportionation species. **P11** (1089  $m/z$ ) and **P12** (1091  $m/z$ ) are characterized by the same end groups as **P7** and **P8**, but form a germlyl centred two arm polymer. A combination product with both ends terminated by an acyl group was assigned to product **P8** (1093  $m/z$ ). **P2** (1041  $m/z$ ) and **P3** (1042  $m/z$ ) are acyl-terminated disproportionation products with two Na<sup>+</sup> counter ions. The species **P4** (1053  $m/z$ ), **P5** (1055  $m/z$ ) and **P6** (1057  $m/z$ ) can be described as double-sided disproportionation products. While **P4** features terminal MMA units with a double bond at both ends, **P5** and **P6** feature one terminal MMA unit with a double bond at the  $\alpha$ - and a hydrogen at the  $\omega$ -position (**P5**) as well as two terminal MMA units with a hydrogen at both the

$\alpha$ - and  $\omega$ -position (**P6**). **P9** (1073  $m/z$ ) and **P10** (1075  $m/z$ ) are identical polymers as **P7** and **P8**, but bind  $K^+$  instead of  $Na^+$  counter ions.

The polymer species identified in the mass spectrum of PMMA generated via fs 2P PLP (**Figure 6.10**) are essentially the same as those assigned in the pattern of the fs 1P PLP, as shown in **Figure 5.9**. A comparison of the relative abundances of the species assigned in the fs 2P PLP and the fs 1P PLP is provided in **Table 6.6**. In both experiments the acyl-based species **P7** and **P8** are the most abundant. The germyl-based, two-arm disproportionation products **P4**, **P5** and **P6** occur with a slightly different abundance of 20% in the fs 2P PLP and 30% in the fs 1P PLP. Regarding the germyl-based disproportionation products with one terminal acyl group **P11** and **P12**, these species were slightly more abundant in the NIR fs PLP with 50% compared to 40% in the fs 1P PLP. A more significant difference was observed for **P1**, which showed an equivalent abundance as the main products in the 2PP, but only 40% relative abundance in the one-photon polymerization (1PP). Moreover, in contrast to the 1P-induced PLP, which produced a uniform distribution of **P1**, **P11** and **P12**, the formation of **P1** is favoured in the NIR PLP. As **P1** features both an acyl and an acylgermyl end group and **P11** and **P12** are germyl-based two arm polymers, it was assumed that the germyl fragment is preferred not to be cleaved from the acylgermyl radical.

**Table 6.5** Overview of the exact mass, resolution and relative abundance of the assigned species in the recorded and simulated spectrum of the PMMA after PLP of MMA with Ivocerin triggered by 800 nm fs pulses with a fluence of 5.5 mJ cm<sup>-2</sup> and a repetition rate of 100 Hz.

<i>Species</i>	<i>Ionization</i>	<i>(<math>m/z</math>)<sup>exp</sup> (Da)</i>	<i>(<math>m/z</math>)<sup>sim</sup> (Da)</i>	<i><math>\Delta(m/z)</math></i>	<i>X</i>
<b>P1</b>	Na <sup>+</sup>	1025.395	1025.394	0.001	1
<b>P2</b>	2 Na <sup>+</sup>	1041.009	1041.007	0.002	0.02
	2 Na <sup>+</sup>	1091.035	1091.034	0.001	0.02
<b>P3</b>	2 Na <sup>+</sup>	1042.016	1042.014	0.002	0.02
	2 Na <sup>+</sup>	1092.041	1042.040	0.001	0.02
<b>P4</b>	Na <sup>+</sup>	1053.465	1053.458	0.007	0.2
<b>P5</b>	Na <sup>+</sup>	1055.461	1055.465	0.004	0.2
<b>P6</b>	Na <sup>+</sup>	-	1135.677		0.2
<b>P7</b>	Na <sup>+</sup>	1057.500	1057.494	0.006	1
<b>P8</b>	Na <sup>+</sup>	1059.515	1059.512	0.003	1
<b>P9</b>	K <sup>+</sup>	1073.474	1073.472	0.002	0.02
<b>P10</b>	K <sup>+</sup>	1075.485	1075.487	0.002	0.02

<i>Species</i>	<i>Ionization</i>	$(m/z)^{exp}$ (Da)	$(m/z)^{sim}$ (Da)	$\Delta(m/z)$	<i>X</i>
<b>P11</b>	Na <sup>+</sup>	1089.447	1089.453	0.006	0.5
<b>P12</b>	Na <sup>+</sup>	1091.464	1091.459	0.005	0.5
<b>P13</b>	Na <sup>+</sup>	1093.499	1093.498	0.001	0.5

**Table 6.6:** Comparison of the relative abundances *X* of the assigned polymer species *P<sub>i</sub>* in the mass spectra after irradiation of 12 mmol L<sup>-1</sup> Ivocerin in MMA with 800 nm fs laser pulses under 1P conditions (5.5 mJ cm<sup>-2</sup>) and with 400 nm fs pulses under 2P conditions (102 μJ cm<sup>-2</sup>).

<i>Species</i>	<i>X (NIR fs PLP)</i>	<i>X (Vis fs PLP)</i>
P1	1	0.4
P7	1	1
P8	1	1
P4	0.2	0.3
P5	0.2	0.3
P6	0.2	0.3
P11	0.5	0.4
P12	0.5	0.4
P13	0.5	0.8

Although differing slightly, both the 2PP fs PLP and 1P fs PLPs are characterized by similar distributions of the abundances of end groups. Thus, similar channel branching of the initiator cleavage can be assumed (for more details refer to **Scheme 5.1**). An initial 800 nm pulse is proposed to cleave the C-Ge bond of Ivocerin via 2PA leading to the generation of primary acyl and acylgermyl radicals. Moreover, the observed germly centered species indicate the presence of secondary germly radicals. A cleavage of acylgermyl radicals into acyl and germly radicals is presumably caused by either thermally or photochemically. Thermal activation however, was deemed unlikely as excess energy would be required in the excited vibrational states. Given the structural similarity between mono-*para*-methoxybenzoyldiethylgermyl and mono-*para*-methoxyacyldiethylgermane, both featuring an n-π\* band,<sup>276</sup> which absorbs within the Vis range, the formation of a germly species formation as a secondary radical in a photo-induced cleavage via subsequent 2PA is relatively likely. Since radical formation usually occurs on a timescale of ps to ns, the cleavage of primary radicals into secondary radicals,

induced by fs pulses, is unlikely. Therefore, it is more likely that secondary radicals are generated by consecutive pulses. Neshchadin *et al.*<sup>277</sup> reported of radical formation from bisacylgermane occurring slightly red-shifted to the absorption maximum of bisacylgermane. Considering that Ivocerin is a *para*-substituted bisacylgermane, a radical originating from Ivocerin may also be observed red-shifted to the absorption maximum of Ivocerin (410 nm). Assuming that acylgermyl can still be excited at the edge of the absorption band using 400 nm fs laser pulses, plausible pathways of generating secondary germyl fragments are direct cleavage of the C-Ge bond of primary acylgermyl radicals via 2PA or consecutive cleavage of an acyl radical following the reaction of the acylgermyl radical with a monomer unit. Germyl fragments are biradicals characterized by high reactivity and propensity for quenching, and thus are unstable. In contrast, acylgermanes, which are more stable, may be capable of reacting with a monomer unit and initiating macromolecular growth with subsequent cleavage of the acyl fragment induced by consecutive 2PA of the acylgermyl end group.

## 6.5 Summary

In summary, this chapter presented the first detailed study of the 2PP of MMA using NIR fs laser pulse triggered Ivocerin as photoinitiator encompassing the initiator decomposition to the polymer product formation. Commencing with stationary absorption spectroscopy, the absorption behaviour of Ivocerin was screened, followed by determination of the fluence-dependent initiator conversion via recorded absorption spectra post-exposure to 800 nm fs laser pulses. SEC analysis subsequent to fs 2P PLP experiments operating at 800 nm in the Hz regime affirmed the generation of polymers and demonstrated precise laser control over the polymerization applying various laser repetition rates. As a next step, a thorough examination of the polymer products using ESI-MS provided insights into end group distribution, thus facilitating drawing conclusions of the decomposition mechanism of Ivocerin.

To verify that the excitation of Ivocerin with 800 nm fs pulses followed the 2PA mechanism, indeed, the initiator conversion was monitored via stationary UV/Vis spectroscopy. Following a sequence of irradiation experiment with a fluence ranging from 1.6 mJ cm<sup>-2</sup> to 4 mJ cm<sup>-2</sup>, the initiator concentration was determined from the absorption spectra after each step and subsequently plotted on a double logarithmic scale in dependence of the laser beam fluence. As the data point followed a linear regression with a slope of  $2.3 \pm 0.3$ , the decomposition of Ivocerin proceeded quadratically, thus evidencing 2PA of Ivocerin at 800 nm.

The 2P PLP experiments were initiated with 800 nm fs pulses with various repetition rates of 10 Hz, 20 Hz, 50 Hz and 100 Hz with subsequent analysis of the generated polymers via SEC.

An experimental technique introduced by Olaj *et al.*,<sup>87</sup> outlined in **Section 3.5**, was employed to assign multiples of the polymer molecular weight to the peaks of the first derivatives of the SEC traces. **Eq. 3.33** was utilized to determine the propagation rate coefficient  $k_p$  of the propagating polymer chains with molecular weight  $M_i$  at each repetition rate. Being consistent with the accepted literature value established by IUPAC<sup>275</sup> ( $267 \text{ mol L}^{-1} \text{ s}^{-1}$ ), the calculated coefficients unequivocally demonstrated laser control over the 2PP at 800 nm according to the PLP mechanism.

The analysis of the end group distribution of the 800 nm triggered 2PP via ESI-MS unveiled a comprehensive set of 13 polymer species dominated by acyl-based and germyl-based combination and disproportionation products. Notably, a predominance of the acyl-fragmented species was observed. Specifically, the relative abundance of germyl-fragmented products was about 20% compared to the more prevalent acyl-based species. As a plausible mechanism, a two-step initiator cleavage was proposed, comprising of the generation of an  $\alpha$ -cleavage into an acyl- and an acylgermyl radical in a first, followed by cleavage of a germyl biradical in a second step. These were identical to the previously assigned species of the 1P PLP, thus part of a pool of expected polymer products. Apart from slight differences in the relative abundances, the comparison of the 1P fs PLP and 2P fs PLP revealed matching polymer products. Consequently, a consistent initiator cleavage mechanism was assumed for both excitation mechanisms.

## 7 NIR Light-Induced Polymerization with Gold Nanorods

The previous **Section 6** shed light on the advantageous properties of NIR light by means of 2PA of the photoinitiator Ivocerin to synthesize polymers. However, as high light intensities are required to enable 2PA processes, this method is suboptimal for some applications including sensitive materials, such as organic tissue. As an alternative route to initiate polymerization using long wavelengths, an alternative method of NIR-induced polymerization will be presented in the current chapter - exploiting the plasmonic properties inherent to AuNR. Using AuNR offers an exciting and innovative approach to polymerization by converting light into thermal energy under mild conditions. This process facilitates the cleavage of thermal initiators, thus providing an alternative avenue for photo-induced polymerizations. Given that the plasmonic characteristics of AuNRs are contingent upon their geometric properties, these particles can be finely tuned to absorb light at specific wavelengths tailored to distinct applications. Theoretical<sup>39,183</sup> and experimental<sup>163</sup> reports delved into the distinctive attributes of AuNRs, exploring their exceptional heat generation capabilities and elucidating why they are exceptionally well-suited for mediating polymerization processes induced by NIR light. Summarizing the most important aspects, these reports highlight the ability of AuNR to absorb light and transfer it into a short-lived strong heat. Further, this heat is strongly localized in the interface of the AuNR and the surrounding solution combined with negligible temperature increase in the bulk medium. Since the heat transfer to the direct vicinity of the AuNR is sufficient to decompose thermal initiators for the initiation of radical polymerizations, AuNR are highly promising as photothermal converters for an alternative routine for initiating NIR light-induced polymerization under mild reaction conditions. These findings served to elucidate the rationale behind the selection of AuNRs for the present thesis.

Initially, a proof-of-principle experiment underlining the successful approach of the AuNR-mediated NIR-induced polymerization using <sup>1</sup>H-NMR spectroscopy. Knowing that the heat generated by AuNR triggers the initiation of thermal polymerization, the ability to initiate polymerization through tissue was explored. Subsequent experiments aimed at understanding the effect of reactant concentration variation on the polymerization outcome via <sup>1</sup>H-NMR spectroscopy and SEC analysis, showing that the polymerization followed the kinetics of FRP according to the Mayo equation.<sup>223,224</sup> Further, ESI-MS served to elucidate the polymer chain structure. As is known from previous studies,<sup>11,41-44</sup> absorptivity of photo-sensitive molecules and their photochemical reactivity are not congruent. Thus, it was of particular interest to examine the wavelength-dependent monomer conversion, which is directly related to the heat production by AuNR, in comparison to the absorptivity of the AuNR. Such an experiment,

a so-called action plot, was conducted using the quasi-monochromatic properties of a tunable ns laser. Having demonstrated that AuNR-mediated polymerization is accessible using both fs and ns lasers, the final subchapter demonstrates that AuNR even produce sufficient heat to initiate thermal polymerization when introducing LEDs as a more practical light source.

## 7.1 Stationary Absorption Spectroscopy

AuNRs were selected as a photothermal converter primarily for their remarkable plasmonic properties in the NIR regime. Furthermore, the citrate functionalization of these nanorods maintains good solubility in water and low cytotoxicity, compared to other surface coatings such as CTAB.<sup>45</sup> Given that the absorption characteristics of these nanorods are contingent upon their geometry, AuNR with dimensions of 55 nm x 15 nm<sup>2</sup> were specifically chosen and acquired, as they exhibit strong absorption at 800 nm. The absorption spectrum of the employed AuNR in an aqueous environment is depicted in **Figure 7.1**. The spectrum exhibits a minor peak around 500 nm, corresponding to the transverse plasmonic absorption band, and a more prominent peak around 800 nm, corresponding to the longitudinal plasmonic resonance band. The gradual increase in absorption in the IR region beyond 1100 nm can be attributed to vibrational overtones of water.<sup>281</sup> Given that plasmonic heating is initiated on a fs timescale (as elucidated in **Section 3.5.3**), these particular AuNRs are exceedingly well-suited for conducting proof-of-principle NIR-polymerization experiments, inducing plasmonic heat generation via 800 nm fs laser pulses.

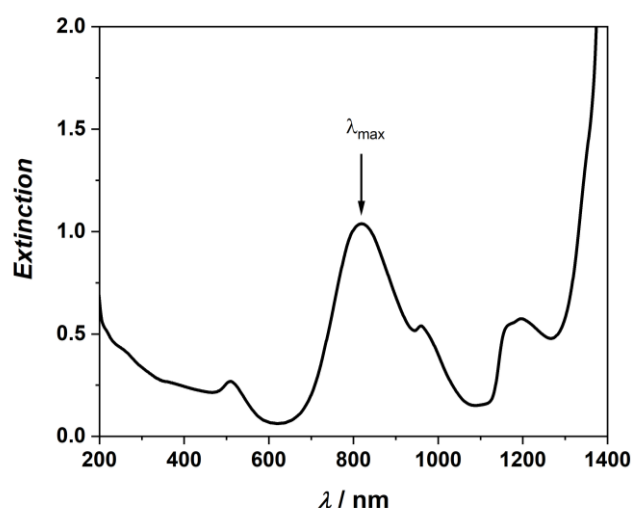


**Figure 7.1:** Extinction of the purchased solution of AuNR in water (55x15 nm, bare citrate, OD 1) in the range of 200 – 1400 nm. The stationary absorption spectrum was measured in a 1 cm cuvette. The AuNR solution shows an absorption maximum at 800 nm with an extinction of 1. Adapted with permission from ref. 183. Copyright 2022 Wiley.

## 7.2 $^1\text{H-NMR}$ Spectroscopy

Intending to initiate polymerization via NIR light-induced AuNR-mediated heat production as an initial experiment, the thermal initiator AIBN was dissolved in the water-soluble monomer DMA (containing  $9 \text{ mmol L}^{-1}$  AIBN,  $2.69 \text{ mol L}^{-1}$  DMA, and  $150 \mu\text{L}$  of AuNR dispersion). The reaction mixture was exposed to irradiation in the presence of AuNRs using  $800 \text{ nm}$  fs laser pulses ( $35 \text{ fs}$ ,  $1 \text{ kHz}$ ). It has previously been discussed that the rate of heat transfer from AuNR to the surrounding medium increases with higher pulse intensities (for more details refer to **Section 3.5.3**). Therefore, a high laser intensity of  $25 \text{ GW cm}^{-2}$  was selected to ensure rapid heat transfer enabling efficient decomposition of AIBN. When the reaction solution was irradiated within a  $1 \text{ mm}$  cuvette, a white solid precipitate quickly formed. This observation is indicative of polymer formation, as further illustrated by the cuvette containing a white solid in **Figure 10.9** in the appendix. To substantiate the assumption that the polymerization activity is indeed linked to the heat dissipation from the AuNRs, the experiment was repeated under identical conditions with only AIBN and DMA. Without AuNRs, no white solid precipitate was observed, confirming the hypothesis.

The white solid produced after irradiation could neither be separated properly from the cuvette, nor dissolved in a suitable solvent for analysis. The limited solubility of the solid polymer implies that high molecular weight polymers have indeed formed, possibly due to a relatively low number of primary radicals generated through the heating effect of the AuNR. To facilitate the solubility of the generated polymer for further analysis, a water-soluble CTA, namely 3-mercaptopropionic acid, was introduced to reduce the length of the polymer chains. Traditionally, polymers are analyzed after solvent precipitation. However, in case of DMA evaporation did not work efficiently, as the vapour pressure of DMA at ambient temperature is very low ( $65 \text{ Pa}$ ). Therefore,  $^1\text{H-NMR}$  analysis was chosen as alternative method to prove the formation of PDMA. A cuvette containing  $350 \mu\text{L}$  solution ( $9 \text{ mmol L}^{-1}$  AIBN,  $2.69 \text{ mol L}^{-1}$  DMA,  $150 \mu\text{L}$  of AuNR and  $10^{-2} \text{ mol L}^{-1}$  CTA) was exposed to  $800 \text{ nm}$  fs pulses with an intensity of  $25 \text{ GW cm}^{-2}$ . After  $30 \text{ min}$  irradiation,  $50 \mu\text{L}$  were taken from the solution and transferred to an NMR tube. The sample was topped up with  $500 \mu\text{L}$  of  $\text{D}_2\text{O}$  and measured using a Bruker Ascend  $400 \text{ MHz}$ .

**Figure 7.2** depicts the  $^1\text{H-NMR}$  spectrum of the irradiated solution (bottom row) compared to an identical solution without irradiation (top row). The upper part of **Figure 7.2** shows the  $^1\text{H-NMR}$  spectrum of pure DMA in  $\text{D}_2\text{O}$ . The doublets 'a' and 'b' with a chemical shift around  $5.7 \text{ ppm}$  and  $6.2 \text{ ppm}$ , and the triplet 'c' at  $6.75 \text{ ppm}$ , represent the protons of the double bond.

The singlet at 3 ppm is associated with the 3 protons of each methyl group. Further resonances arise between 1 – 2 ppm as well as 2.5 – 3 ppm, which are associated with the protons 'f' and 'g' of the C-C bond of the polymer backbone. As the assigned polymer peaks were consistent with literature,<sup>282</sup> this served as clear evidence for polymer formation. However, since the polymer resonance of protons 'f' overlaps with the monomer resonance at 3 ppm, these were not useful for further analysis, such as determining monomer conversion. The resonance peak of proton 'g' was well separated, making it suitable for the calculation of the monomer conversion (for further details refer to **Section 3.7**).

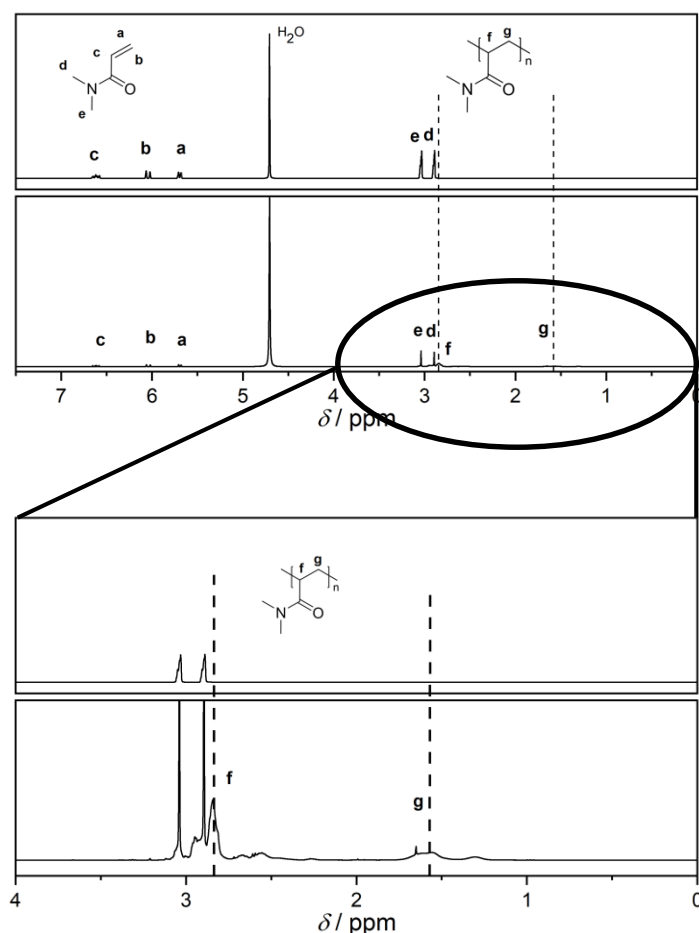


**Figure 7.2:**  $^1\text{H}$ -NMR spectrum of pure DMA dissolved in  $\text{D}_2\text{O}$  without irradiation recorded with a 400 MHz NMR spectrometer. The resonances are assigned to the protons of DMA (left);  $^1\text{H}$  NMR spectrum of a solution of DMA, AIBN, AuNR and CTA dissolved in  $\text{D}_2\text{O}$  after irradiation of 30 min (right). The resonances are assigned to the protons associated with the DMA monomer and the generated polymer.

The initial proof-of-principle experiment, followed by  $^1\text{H-NMR}$  spectroscopy analysis, successfully demonstrated that polymer chain growth can indeed be initiated by NIR light when utilizing the water-soluble monomer DMA and AIBN as a thermal initiator in the presence of AuNRs. The thermal polymerization reaction, catalyzed by the plasmonic heating effect of AuNRs, is anticipated to follow the mechanism of FRP as the heat generated radicals initiate polymer chain, followed by successively adding monomer units to the propagating polymer. Therefore, the instantaneous degree of polymerization as a function of monomer and radical concentration can be described using the Mayo equation (**Eq. 3.31**).<sup>223,224</sup> To further investigate the kinetics of the reaction and map the degree of polymerization, a study was conducted using two monomer concentrations, one high ( $6.73 \text{ mol L}^{-1}$ ) and one low ( $0.69 \text{ mol L}^{-1}$ ), and varying the irradiation time (or number of photons). The results are illustrated in **Figure 7.3**.

While the time-dependent conversion exhibits a similar trend for both concentrations, the increase in conversion differs notably between them. Both polymerizations are remarkably fast, achieving high conversions within just 5 min. In the case of the higher monomer concentration ( $6.73 \text{ mol L}^{-1}$ ), the conversion increase is extremely rapid, reaching its maximum of 65% after 15 min and then progressing more slowly. For the lower concentration ( $0.69 \text{ mol L}^{-1}$ ), the conversion increase is less pronounced and reaches its peak, close to 50%, within 45 min. According to the standard FRP kinetics (**Eq. 3.31**),<sup>223,224</sup> in a conventional thermally activated FRP, the instantaneous degree of polymerization scales directly with the monomer concentration. Considering the nearly one-order-of-magnitude difference in concentration, the significant contrast in the initial slope aligns with expectations. In the case of the low DMA concentration, the monomer conversion remains below 1% after 2 min of irradiation. In contrast, for the higher monomer concentration, the conversion already exceeds 15%, which aligns with expectations from the degree of polymerization equation.<sup>223,224</sup> This trend persists after 3 min of irradiation, with the low concentration achieving a conversion of 2.5% and the high concentration reaching 37%. For longer irradiation times, the conversions tend to converge, resulting in a difference of less than one order of magnitude. Initially, the abundance of monomer units allows for a rapid conversion. However, as the available monomer units decrease over time due to ongoing polymerization, the conversion rate naturally decreases. This deceleration continues until a plateau is reached, representing the point at which the conversion has maximized given the available reactants. Since the conversion is inherently limited by the available starting materials, it is to be expected both trends eventually converge. The observed conversion plateau may also be co-associated with a potential deactivation of the AuNR over time.

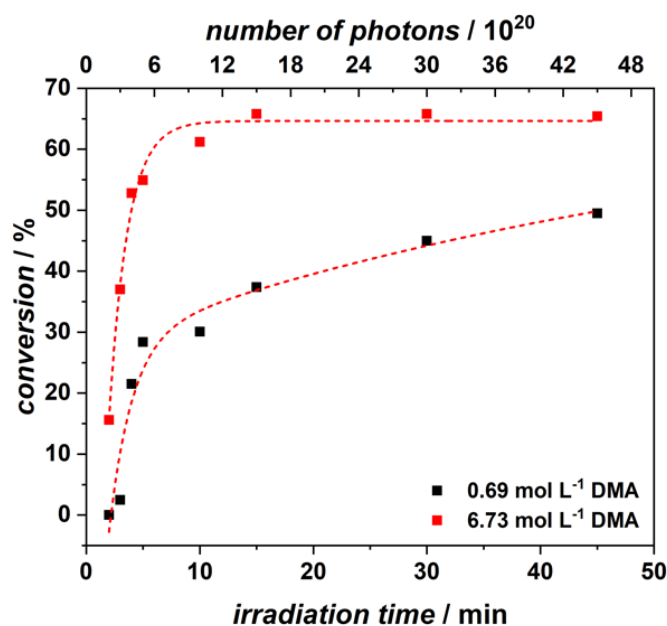


**Figure 7.3:** Monomer conversion as a function of reaction time or number of photons; (red) conversion for the highest monomer concentration ( $6.73 \text{ mol L}^{-1}$ ), (black) conversion for the lowest monomer concentration ( $0.69 \text{ mol L}^{-1}$ ). The lines are fits to guide the eye. Adapted with permission from ref. 183. Copyright 2022 Wiley.

In a follow up study the monomer conversion was mapped varying the concentration of one reactant while keeping the concentration of the other reactants constant. The concentration variation procedure is described in more detail in **Section 4.6**. Each sample was exposed to 800 nm fs pulses with a beam intensity of  $25 \text{ GW cm}^{-2}$  for 30 min. **Figure 7.4** shows that the monomer conversion of a solution of  $9 \text{ mmol L}^{-1}$  AIBN,  $50 \mu\text{L AuNR}$  and  $10^{-2} \text{ mol L}^{-1}$  CTA with gradually increasing monomer concentration from  $0.69 \text{ mol L}^{-1}$  to  $6.93 \text{ mol L}^{-1}$ . Beginning from 27% conversion for the lowest monomer concentration reaching its asymptotic limit slightly above 70%. These results confirm that AuNR mediated thermal polymerization of DMA follows FRP kinetics. The variation of the concentration of the other reactants was expected to affect the polymerization as well. Next, the effect of varying the concentration of AIBN and AuNR content on the monomer conversion was explored, while keeping the light exposure time constant at 30 min.

In line with the predictions of the Mayo equation,<sup>223,224</sup> all reactants (DMA, AIBN, AuNR) exhibit the same effect of gradual increasing the monomer conversion as their concentration was increased, as shown in **Figure 7.4 - Figure 7.6**. As the concentration of AIBN directly affects the amount of generated radicals the monomer conversion aligns with the variation of AIBN concentration. Varying the concentration of AuNR indirectly results in an increase or decrease of the radical concentration proportional to the amount of produced heat. Both increasing the AIBN, as well as the AuNR, concentration led to higher monomer conversion.

The monomer conversion of a solution containing  $0.69 \text{ mol L}^{-1}$  DMA,  $50 \text{ }\mu\text{L}$  AuNR,  $10^{-2} \text{ mol L}^{-1}$  CTA and a low AIBN concentration (ranging from  $0.17 \text{ mmol L}^{-1}$  to  $1.5 \text{ mmol L}^{-1}$ ) increases very rapidly to about 70% within 2 min and then remains nearly constant (**Figure 7.5**). This phenomenon may be attributed to an inadequate heating effect by the AuNRs, which may not activate initiator molecules effectively beyond the  $1.5 \text{ mmol L}^{-1}$  concentration range. As described previously, the elevated temperature of the local medium surrounding the AuNRs contributes to the generation of more radicals, subsequently leading to increasing monomer conversion from 32% to slightly more than 50%, as demonstrated in **Figure 7.6**. However, the higher the number of initiator molecules, the more heat is required to decompose the molecules into radicals. Thus, the concentration of AuNR defines the potential amount of radicals formed due to the limit in heat production. Although no clear conversion limit was observed within the presented range of AuNR concentration, an asymptotic conversion limit is expected to occur if further increasing the AuNR concentration.

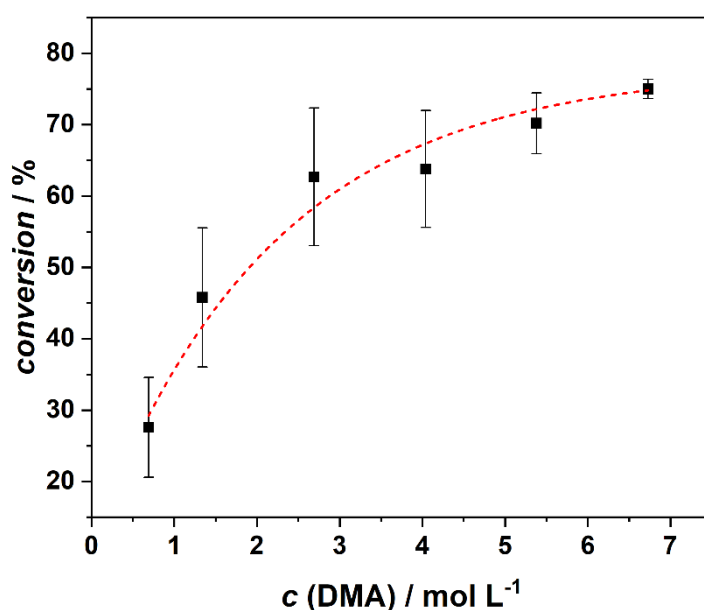


**Figure 7.4:** Monomer to polymer conversion after 30 min irradiation of solutions containing  $9 \text{ mmol L}^{-1}$  AIBN,  $50 \text{ }\mu\text{L}$  AuNR in water,  $10^{-2} \text{ mol L}^{-1}$  CTA and monomer concentrations ranging from  $0.69 - 6.73 \text{ mol L}^{-1}$  with  $800 \text{ nm}$  fs pulses with an intensity of  $25 \text{ GW cm}^{-2}$ ; the dashed line serves to guide the eye only. Adapted with permission from ref. 183. Copyright 2022 Wiley.

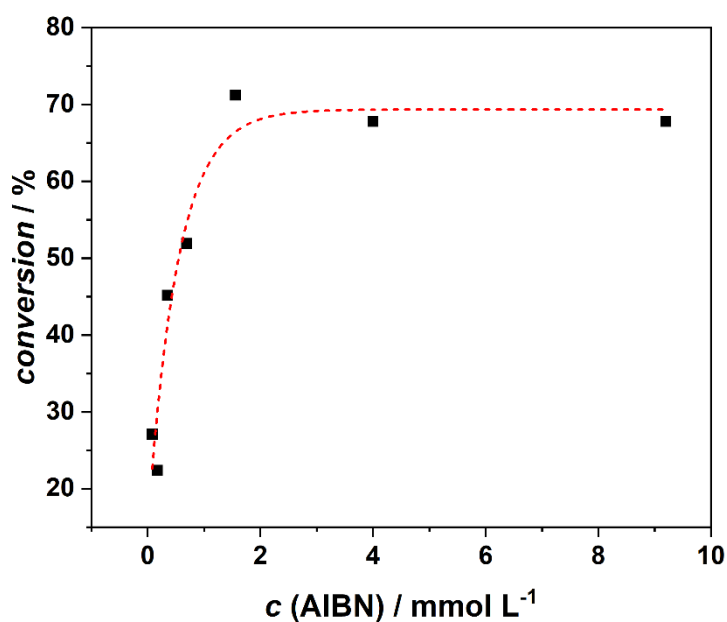


**Figure 7.5:** Monomer to polymer conversion after 30 min irradiation of solutions containing  $6.73 \text{ mol L}^{-1}$  DMA,  $50 \mu\text{L}$  AuNR,  $10^{-2} \text{ mol L}^{-1}$  CTA and varying concentration of AIBN ranging from  $0.08 - 9.2 \text{ mmol L}^{-1}$  with  $800 \text{ nm}$  fs pulses with an intensity of  $25 \text{ GW cm}^{-2}$ ; dashed line serves to guide the eye along the data points. Adapted with permission from ref. 183. Copyright 2022 Wiley.

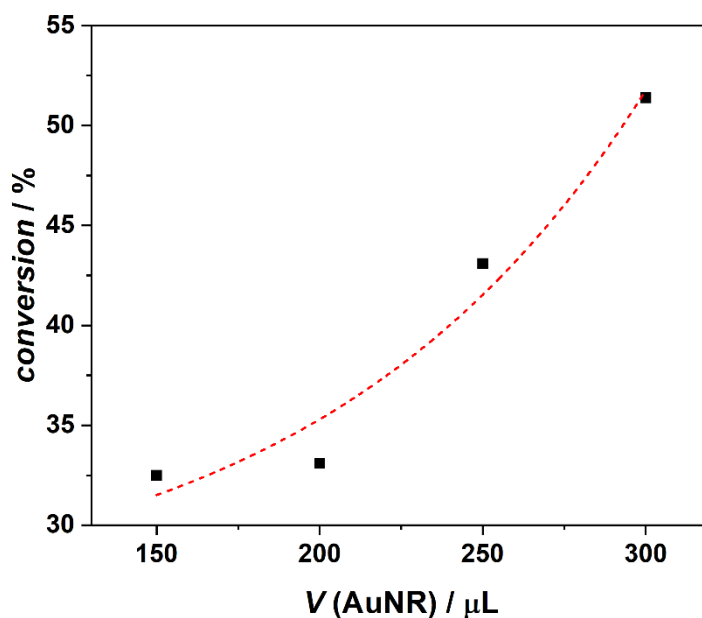


**Figure 7.6:** Monomer to polymer conversion after 30 min irradiation of solutions containing  $9 \text{ mmol L}^{-1}$  AIBN,  $0.69 \text{ mol L}^{-1}$  DMA,  $10^{-2} \text{ mol L}^{-1}$  CTA and a varying AuNR volume ranging from  $150 - 300 \mu\text{L}$  with  $800 \text{ nm}$  fs pulses with an intensity of  $25 \text{ GW cm}^{-2}$ ; the dashed line serves to guide the eye along the data points. Adapted with permission from ref. 183. Copyright 2022 Wiley.

### 7.3 Polymerization through Tissue

The combination of water solubility, low toxicity, and the ability to generate plasmonic local heat when exposed to NIR light makes AuNRs highly intriguing and promising for use in biological media. To demonstrate that the polymerization reaction in an aqueous environment can also be initiated through biological tissue, a slice of bacon was positioned between the laser and the cuvette.

The absorption spectrum of the bacon sample was recorded using a 1 mm slice of bacon and found to exhibit an OD of approximately 1 at the incident wavelength of 800 nm. Given this result, one would expect the tissue to absorb around 90% of the incident light. However, when measuring the laser intensity immediately after the laser beam passed through the slice of bacon (as shown in **Scheme 6.1**), a value of  $10 \text{ GW cm}^{-2}$  was obtained, corresponding to an absorption rate of only 60%. The discrepancy can be understood by taking into account the natural structure of bacon tissue that light strongly scatters and diffuses during penetration. In the laser experiment, the detector was placed in close proximity to the tissue, while in the spectrometer, the detector is positioned at a greater distance from the tissue. As described in **Section 3.1** the OD is defined by the logarithm of the ratio of the output intensity of the light source  $I_0$  and the incident light intensity on the detector  $I$ . Consequently, as the scattering effects of the bacon likely decrease the detected light intensity, this leads to a higher observed OD for the bacon. To assess the impact of tissue on the conversion compared to identical experiments conducted without tissue, the results were compared. **Figure 7.7** demonstrates that polymers were generated even after the laser beam propagated through tissue, underpinning the potential of AuNR to be used in biological applications. Since the tissue absorbs a significant portion of the incident light, the AuNRs were activated with less energy, resulting in reduced heat production. Consequently, the formation of radicals was reduced, providing an explanation for the observed lower conversion for each data point when tissue was present.

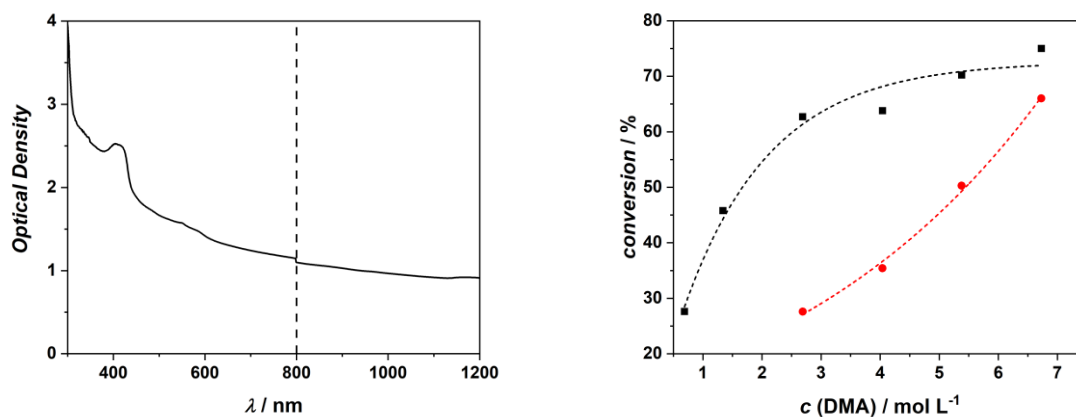


**Figure 7.7:** (left) Extinction measurement of 1 mm thick slice of bacon. The dashed line at 800 nm to highlight the irradiation wavelength. (right) Comparison of monomer to polymer conversion after 30 min irradiation of various monomer concentrations with AIBN and AuNR (black) and identically concentrated samples with a 1 mm thick slice of bacon placed in front of it, also irradiated for 30 min (red). Adapted with permission from ref. 183. Copyright 2022 Wiley.

## 7.4 Size Exclusion Chromatography

In addition to highlighting the effect of the concentration variation of each reactant on the monomer conversion (**Section 7.2**), mapping the degree of polymerization while varying parameters such as monomer concentration, AIBN concentration, and the quantity of AuNRs via SEC was undertaken. To this end, solutions were prepared with the concentration of one reactant systematically varied – while keeping the other concentrations constant. Each solution was then exposed to 800 nm fs laser pulses with an intensity of 25 GW cm<sup>-2</sup> for 30 min.

**Figure 7.8** displays the MWD alongside the number average molecular weight,  $M_n$ , as a function of the monomer concentration, spanning from 0.69 mol L<sup>-1</sup> to 6.73 mol L<sup>-1</sup> in a solution with 9 mmol L<sup>-1</sup> AIBN, 50 μL AuNR and 10<sup>-2</sup> mol L<sup>-1</sup> CTA (**Table 7.1**). Increasing the monomer concentration shifts the MWD toward higher molecular weights, consistently elevating the  $M_n$ , (from 1500 g mol<sup>-1</sup> to 5000 g mol<sup>-1</sup>). According to the Mayo equation (**Eq. 3.31**),<sup>223,224</sup> the instantaneous degree of polymerization scales with the monomer concentration, predicting higher molecular weights when increasing the monomer concentration. The observed behaviour aligns well with the expected outcomes, considering that a higher number of monomer molecules results in both increased polymer chain growth and a higher likelihood of initiation by surrounding primary radicals.

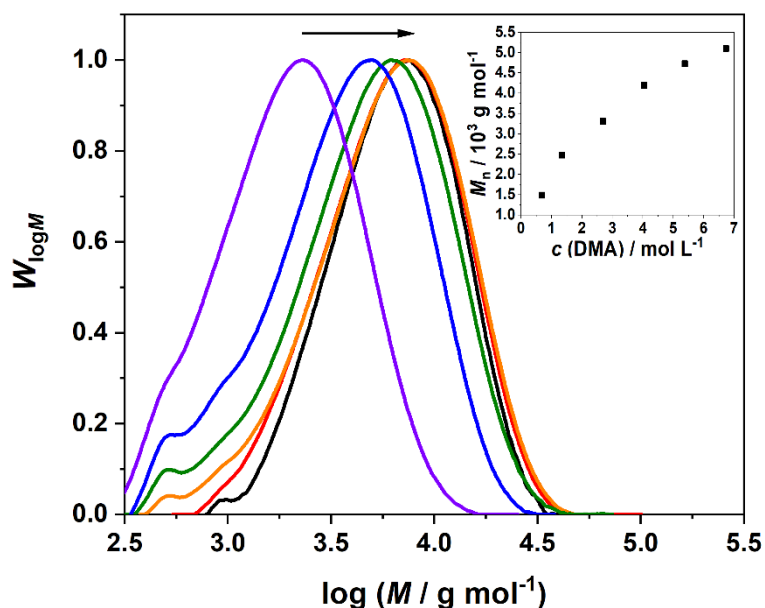


**Figure 7.8:** MWD of PDMA as a function of the monomer concentration: (black) 6.73 mol L<sup>-1</sup> DMA, (red) 5.38 mol L<sup>-1</sup>, (orange) 4.04 mol L<sup>-1</sup>, (green) 2.69 mol L<sup>-1</sup>, (blue) 1.34 mol L<sup>-1</sup>, (violet) 0.69 mol L<sup>-1</sup>. Inset: Number average molecular weight,  $M_n$ , after 30 min irradiation of solutions containing 9 mmol L<sup>-1</sup> AIBN, 50  $\mu$ L AuNR, 10<sup>-2</sup> mol L<sup>-1</sup> CTA and varying monomer concentration ranging from 0.69 – 6.73 mol L<sup>-1</sup> with 800 nm fs pulses with an intensity of 25 GW cm<sup>-2</sup>. Adapted with permission from ref. 183. Copyright 2022 Wiley.

**Table 7.1:** Overview of the  $M_n$  values, dispersity, after 30 min irradiation of solutions containing various monomer concentrations and 50  $\mu$ L AuNR, 9 mmol L<sup>-1</sup> AIBN and 10<sup>-2</sup> mol L<sup>-1</sup> CTA with 800 nm fs pulses with an intensity of 25 GW cm<sup>-2</sup>.

$c$ (DMA) / mol L <sup>-1</sup>	$M_n$ / g mol <sup>-1</sup>	Dispersity
0.69	1500	1.7
1.34	2500	2.0
2.69	3300	2.0
4.04	4200	1.9
5.38	4700	1.7
6.73	5000	1.6

It was a significant aspect to investigate the impact of the AuNR quantity in the solution, given that the initiation system fundamentally relies on their heating properties. It is critical to emphasize that no polymer formation occurs in the absence of AuNRs, as previously mentioned at the beginning of **Section 7.2**. For this experimental sequence, solutions containing 9 mmol L<sup>-1</sup> AIBN, 0.69 mol L<sup>-1</sup> DMA, 10<sup>-2</sup> mol L<sup>-1</sup> CTA and a variable volume of AuNR in the

range of 150 – 300  $\mu\text{L}$  were prepared. In contrast to the effects observed with increasing monomer concentration, an increase in the AuNR content leads to a shift in the MWD toward lower molecular weights, as illustrated in **Figure 7.9**. Furthermore,  $M_n$  (2000  $\text{g mol}^{-1}$  to 1000  $\text{g mol}^{-1}$ ) exhibits a clear decrease with increasing AuNR concentration (**Table 7.2**). This decline can be attributed to increased heating on the surrounding aqueous solution resulting from an increased AuNR quantity. With more AuNRs present, a larger fraction of initiator molecules experiences the resultant temperature increase, leading to an increase in the number of radicals formed. Consequently, the molecular weight of the polymer chains is lower due to an increased number of initiated chains per monomer units and an increased likelihood of chain termination reactions, a trend that aligns with the predictions of the Mayo equation (**Eq. 3.31**).<sup>223,224</sup>

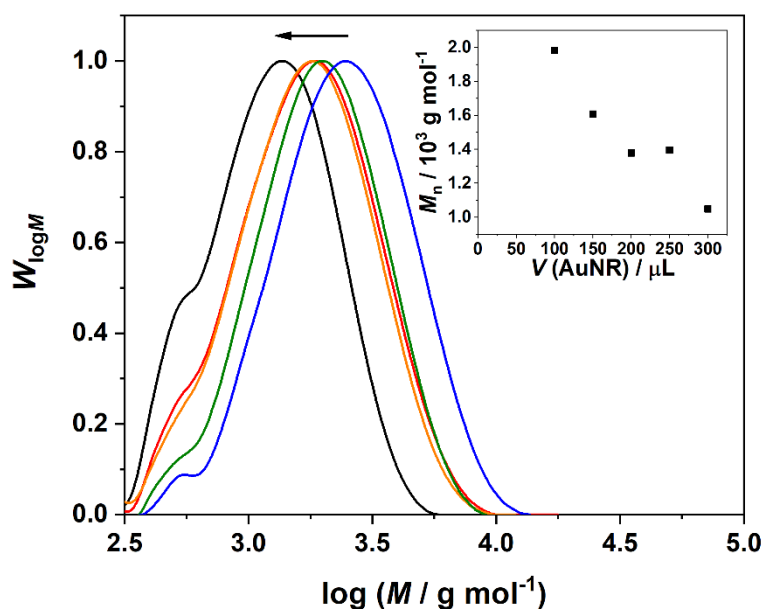


**Figure 7.9:** MWD of poly(DMA) dependent on the variation of the AuNR concentration: (black) 300  $\mu\text{L}$  AuNR, (red) 250  $\mu\text{L}$  AuNR, (orange) 200  $\mu\text{L}$  AuNR, (green) 150  $\mu\text{L}$  AuNR, (blue) 100  $\mu\text{L}$  AuNR. Inset: Number average of molecular weight,  $M_n$ , after 30 min irradiation of solutions containing 9  $\text{mmol L}^{-1}$  AIBN, 0.69  $\text{mol L}^{-1}$  DMA,  $10^{-2}$   $\text{mol L}^{-1}$  CTA and varying AuNR volume ranging from 100 -300  $\mu\text{L}$  with 800 nm fs pulses with an intensity of 25  $\text{GW cm}^{-2}$ . Adapted with permission from ref. 183. Copyright 2022 Wiley.

**Table 7.2:** Overview of the  $M_n$  values, dispersities and monomer conversion after 30 min irradiation of a solution with various AuNR concentrations and 9 mmol L<sup>-1</sup> AIBN, 6.73 mol L<sup>-1</sup> DMA and 10<sup>-2</sup> mol L<sup>-1</sup> CTA with 800 nm fs pulses with an intensity of 25 GW cm<sup>-2</sup>.

$V(\text{AuNR}) / \mu\text{L}$	$M_n / \text{g mol}^{-1}$	Dispersity
100	2000	1.4
150	1600	1.5
200	1400	1.4
250	1300	1.4
300	1000	1.4

A similar impact is observed when varying the concentration of the initiator AIBN from 0.08 mol L<sup>-1</sup> to 9.2 mol L<sup>-1</sup>, while keeping the concentration of DMA at 4.04 mol L<sup>-1</sup>, CTA at 10<sup>-2</sup> mol L<sup>-1</sup> and the volume of AuNR solution at 150  $\mu\text{L}$ . An increase in the initiator concentration leads to a higher concentration of primary radicals, akin to the effect seen with a higher AuNR content, causing a shift in the MWD toward lower molecular weights (**Figure 7.10**). However, there is a distinctive characteristic when examining the conversion in relation to AIBN concentration.

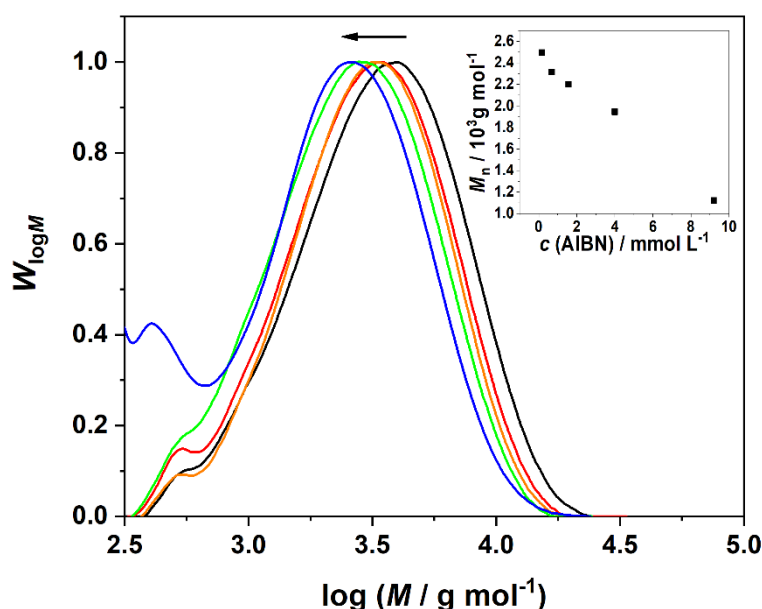


**Figure 7.10:** MWD of poly(DMA) as a function of the AIBN concentration; (black) 9.2 mmol L<sup>-1</sup> AIBN, (red) 4 mmol L<sup>-1</sup> AIBN, (orange) 1.56 mmol L<sup>-1</sup> AIBN, (green) 0.69 mmol L<sup>-1</sup> AIBN, (blue) 0.17 mmol L<sup>-1</sup> AIBN. Inset: Number average of molecular weight after 30 min irradiation of solutions containing 6.73 mol L<sup>-1</sup> DMA, 50  $\mu\text{L}$  AuNR, 10<sup>-2</sup> mol L<sup>-1</sup> CTA and varying AIBN concentration ranging from 0.08 – 9.2 mmol L<sup>-1</sup> with 800 nm fs pulses with an intensity of 25 GW cm<sup>-2</sup>. Adapted with permission from ref. 183. Copyright 2022 Wiley.

**Table 7.3:** Overview of the  $M_n$  values, dispersities, and monomer conversion after 30 irradiation of a solution with various AIBN concentrations and 50  $\mu\text{L}$  AuNR, 6.73  $\text{mol L}^{-1}$  DMA and  $10^{-2}$   $\text{mol L}^{-1}$  CTA with 800 nm fs pulses with an intensity of 25  $\text{GW cm}^{-2}$ .

$c(\text{AIBN}) / \text{mmol L}^{-1}$	$M_n / \text{g mol}^{-1}$	Dispersity
0.08	-	-
0.17	2500	1.7
0.35	-	-
0.69	2300	1.7
1.56	2200	1.6
4	1900	1.7
9.2	1100	2.4

The beginning of the current section established that the presence of AuNR is critical for polymer generation. An intriguing observation, however, is that the thermal initiator AIBN is not always mandatory; polymers can be generated even without AIBN, as depicted in **Figure 7.11**. The strong local heating effect of the AuNR appears to be sufficient to activate the spontaneous self-initiation of DMA, a phenomenon well-documented in the literature.<sup>273</sup> Although AIBN is not mandatory for the polymer reaction, it still impacts the polymerization. **Figure 7.11** compares the number average molecular weight ( $M_n$ , listed in **Table 7.4**) of polymer reactions with various monomer concentrations, both with and without AIBN. It clearly shows that  $M_n$  reaches higher values, on average 27% higher, in the absence of AIBN. This is due to the additional AIBN-derived radicals when AIBN is present. This in turn enhances the number of initiated monomer units per primary radical, and hence termination reactions. Further evidence of the significant effect of AIBN on the polymerization will be presented in the following.

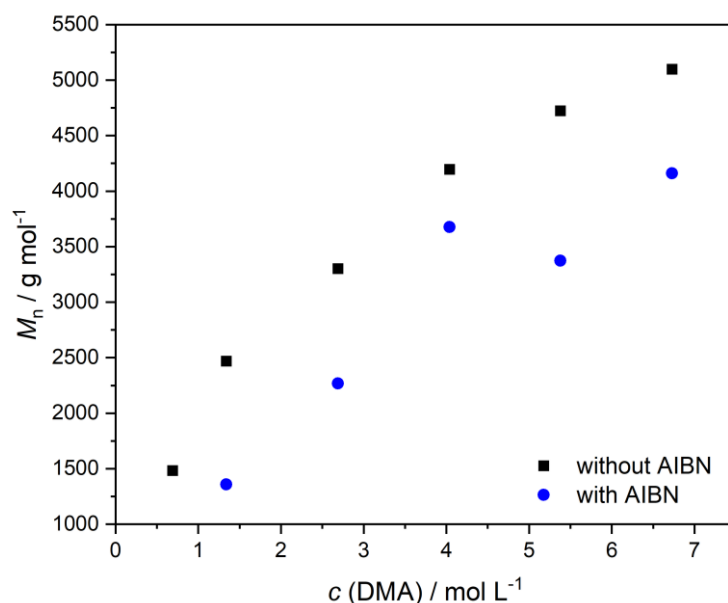


**Figure 7.11:** Comparison of the monomer concentration-dependent number average molecular weight of a solution with DMA (monomer), 50  $\mu\text{L}$  AuNR in water,  $10^{-2}$  mol L<sup>-1</sup> CTA with 9 mmol L<sup>-1</sup> AIBN (blue) and without AIBN (black) after 30 min irradiation with 25 GW cm<sup>-2</sup> fs pulses at 800 nm.

**Table 7.4:** Overview of monomer concentration-dependent  $M_n$  of a solution with DMA, 50  $\mu\text{L}$  AuNR in water,  $10^{-2}$  mol L<sup>-1</sup> CTA with 9 mmol L<sup>-1</sup> AIBN and without AIBN after 30 min irradiation with 25 GW cm<sup>-2</sup> fs pulses at 800 nm.

c (DMA) / mol L <sup>-1</sup>	0.69	1.34	2.69	4.04	5.38	6.73
$M_{n, \text{AIBN}}$ / g mol <sup>-1</sup>	-	1300	2200	3700	3400	4200
$M_{n, \text{no AIBN}}$ / g mol <sup>-1</sup>	1500	2500	3300	4200	4700	5000

The results of **Chapters 7.2** and **7.4** evidence control over monomer conversion and molecular weight of the polymers according to the predictions of the Mayo equation<sup>223,224</sup> of the degree of polymerization of a FRP. In the following subchapter, the polymer product formation will be examined using ESI-MS.

## 7.5 Electrospray Ionization Mass Spectrometry

Using AuNR as plasmonic heat generator to initiate thermal polymerization, polymers within the molecular weight range of 1000 to 3000 g mol<sup>-1</sup> were successfully obtained, making them well-suited for analysis via ESI-MS.

**Figure 7.12** displays one repeat unit within the 1000-2000 *m/z* range of a typical recorded mass spectrum. This spectrum resulted from a 30 min irradiation of a solution containing 4.04 mol L<sup>-1</sup> DMA, 9 mmol L<sup>-1</sup> AIBN, 100 μL AuNRs, and 10<sup>-2</sup> mol L<sup>-1</sup> CTA, using 800 nm fs laser pulses. The figure also includes the assigned species for clarity and underscores that the polymerization reaction is – not surprisingly given the presence of the CTA – predominantly controlled by transfer processes. Somewhat surprisingly, despite the use of AIBN as a thermal initiator, no cyanoisopropyl end groups were observed, as demonstrated by the assigned species **P1-P6** (**Figure 7.13**). As noted, this outcome is not entirely unexpected, given the presence of a chain transfer mechanism, which predominantly terminates polymer chains with thiol end groups.

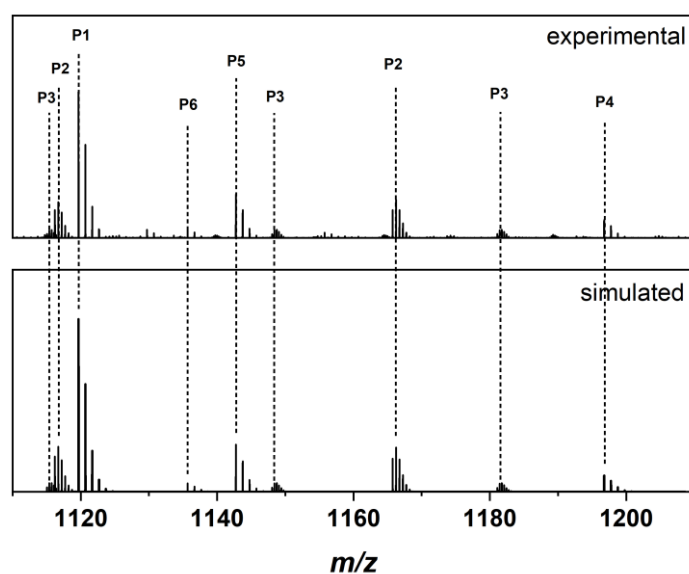


**Figure 7.12:** Zoom into the range of 1100-1210 *m/z* of ESI-MS spectrum of PDMA in THF/methanol (3:2) after 30 min irradiation of a solution of 4.04 mol L<sup>-1</sup> DMA, 9 mmol L<sup>-1</sup> AIBN, 100 μL AuNR and 10<sup>-2</sup> mol L<sup>-1</sup> CTA with 25 GW cm<sup>-2</sup> fs pulses at 800 nm (top) and assigned polymer species **P1-P6** (bottom). Adapted with permission from ref. 183. Copyright 2022 Wiley.

The detailed assignment of species within the 1100 – 1210 *m/z* range, as depicted in **Figure 7.12**, was accomplished using Xcalibur as the isotopic pattern simulation software. However, few minor peaks could not be assigned, as no matching polymer species were found. By means of the *m/z* ratio of the simulated polymer products, four primary species were successfully

assigned to the isotopic pattern in the recorded mass spectrum. For a comprehensive overview of all assigned species, refer to **Figure 7.13** and **Table 7.5**. Notably, the species **P1-P4** share the same end group composition, featuring hydrogen at the  $\alpha$ -terminus and a thiol functionalization at the  $\omega$ -terminus. Nevertheless, there is a distinction in the counter ion associated with each polymer species. The peaks near 1119  $m/z$  correspond to polymer species **P1** with a single counter ion. Furthermore, the doubly charged species **P2** and the triple charged **P3** can be identified at 1116  $m/z$  and 1166  $m/z$ , as well as at 1115  $m/z$ , 1148  $m/z$ , and 1181  $m/z$ , respectively. The species at 1196  $m/z$  can be attributed to the polymer product **P4**, which carries an  $H^+$ -counter ion. Another polymer species, **P5**, featuring both a hydrogen and a thiol-functionalized end group along with an additional water molecule, can be found at 1142  $m/z$ . Additionally, a species denoted as **P6** was assigned to a product with a peak at 1135  $m/z$ , exhibiting a structure similar to **P1** but with an oxidized sulphur atom.

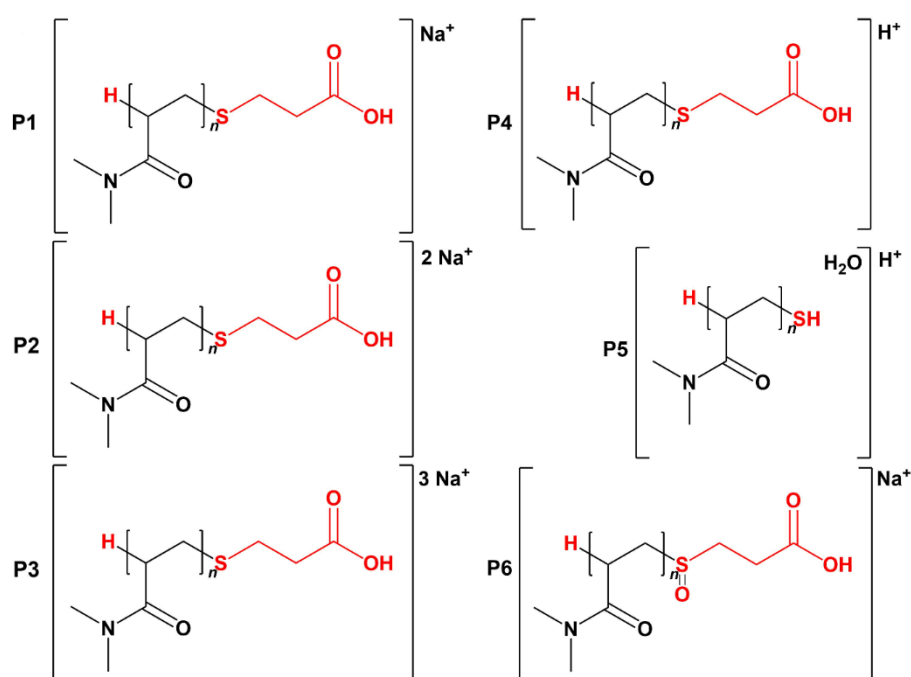


**Figure 7.13:** Assigned polymer species **P1-P6** obtained from a simulation corresponding to an experimental mass spectrum generated after 30 min irradiation of 4.04 mol L<sup>-1</sup> DMA, 9 mmol L<sup>-1</sup> AIBN, 100  $\mu$ M AuNR and 10<sup>-2</sup> mol L<sup>-1</sup> CTA with 25 GW cm<sup>-2</sup> laser pulses at 800 nm. 10  $\mu$ L of the irradiated solution were dissolved in 2 mL of a THF/methanol (3:2) solution with 100  $\mu$ M NaTFA (left). Adapted with permission from ref. 183. Copyright 2022 Wiley.

**Table 7.5:** Overview of the exact mass, resolution and relative abundance of the assigned species in the recorded and simulated mass spectrum of PDMA 30 min irradiation of 4.04 mol L<sup>-1</sup> DMA, 9 mmol L<sup>-1</sup> AIBN, 100 μL AuNR and 10<sup>-2</sup> mol L<sup>-1</sup> CTA with 25 GW cm<sup>-2</sup> laser pulses at 800 nm.

<i>Species</i>	<i>Ionization</i>	<i>(m/z)<sup>exp</sup> (Da)</i>	<i>(m/z)<sup>sim</sup> (Da)</i>	<i>Δ(m/z)</i>
<b>P1</b>	Na <sup>+</sup>	1119.681	1119.682	0.001
<b>P2</b>	2 Na <sup>+</sup>	1116.712	1116.713	0.001
	2 Na <sup>+</sup>	1166.247	1166.248	0.001
<b>P3</b>	3Na <sup>+</sup>	1115.724	1115.724	0.000
	3 Na <sup>+</sup>	1148.746	1148.747	0.001
	3 Na <sup>+</sup>	1181.769	1181.769	0.000
<b>P4</b>	H <sup>+</sup>	1196.768	1196.769	0.001
<b>P5</b>	H <sup>+</sup>	1142.757	1142.758	0.001
<b>P6</b>	Na <sup>+</sup>	1135.677	1135.677	0.000

The end group distribution of polymers products generated AuNR-mediated thermal polymerization is governed by fragments of the CTA. Although AIBN functioned as thermal initiator, no cyanoisopropyl fragments were assigned to the isotopic pattern. This observation, however, aligns with the SEC results in **Section 7.4**, highlighting the ability of polymerization of DMA thermally initiated via the heat production of the AuNR even without the presence of AIBN. As plausible explanation, the produced heat was assumed to cause spontaneous self-initiation of polymerization of the monomer, which potentially terminates by abstraction of a H-atom from the CTA. Next, the generated radical CTA initiated and terminated polymer chain growth. As the presence of AIBN decreases the molecular weight of polymers, as depicted in **Figure 7.11**, AIBN, however, obviously affects the polymerization. Conceivably, cyanoisopropyl radicals abstract H-atoms from the CTA, thus increasing the amount of CTA radicals. Further, the presence of oxygen presumably enabled the oxidation of sulphur.

## 7.6 Action Plot

In the proof-of-principle studies on the polymerization with AuNR and the subsequent analysis outlined earlier in the current chapter, an irradiation wavelength of 800 nm was used as this is close to the absorption maximum of AuNR and easily accessible due to the fundamental wavelength of the fs laser available. However, previous studies<sup>11,41-44</sup> from the Barner-Kowolik group have shown that the reactivity and the absorption curve of photoreactive molecules

are often not aligned. These studies, so-called action plots, involved the screening of the monomer to polymer conversion as a function of wavelength compared to the absorptivity of the photoinitiator. Due to their quasi-monochromatic properties, ns lasers are ideally suited for such experiments, as molecules can be excited in a wavelength-resolved manner. As the photo-induced heat generation by AuNR operates on a different mechanism than the photo-sensitive molecules investigated in previous action plots,<sup>11,41-44</sup> it was particularly interesting to conduct an action plot experiment with the AuNR and closely inspect the wavelength-dependent heat generation.

The experimental set-up employed for action plot measurements was different to that described in **Sections 7.2 - 7.5**. Here, an elevated metal block, with a central hole to place a glass vial, enabled the sample to be irradiated from below. This apparatus is comparable to the set-up described in **Sections 5 and 6**. AuNR in water were added to a solution containing DMA as and AIBN. As mentioned previously, CTA was added to the reaction solution in order to control the polymer chain length. To ensure solubility of the polymer for analysis, CTA was added in high concentration of 0.38 mol L<sup>-1</sup>. However, high CTA concentrations were found to affect the rearrangement of the AuNRs. This is because thiols have a high binding affinity to Au and act as linkers between the AuNRs.<sup>283</sup> Evidence of this phenomenon can be seen in the absorption spectrum shown in **Figure 7.14**. For comparison, an absorption curve of the reaction solution without CTA (black) and with CTA (black dashed) is shown. In the solid curve, the plasmonic absorption band is essentially identical to the AuNR solution (**Figure 7.1**), but the absorption maximum is lower due to dilution. The dotted curve, on the other hand, shows a broadening of the absorption band into the IR range, due to a two-step mechanism that links the AuNRs into chains.<sup>283</sup> In the first step, the CTA binds to the AuNR, due to the high binding affinity of gold and sulfur, serving as a linker by forming H-bridges and binding other AuNRs that are linked to the acid, resulting in a broadband absorption in the IR range.

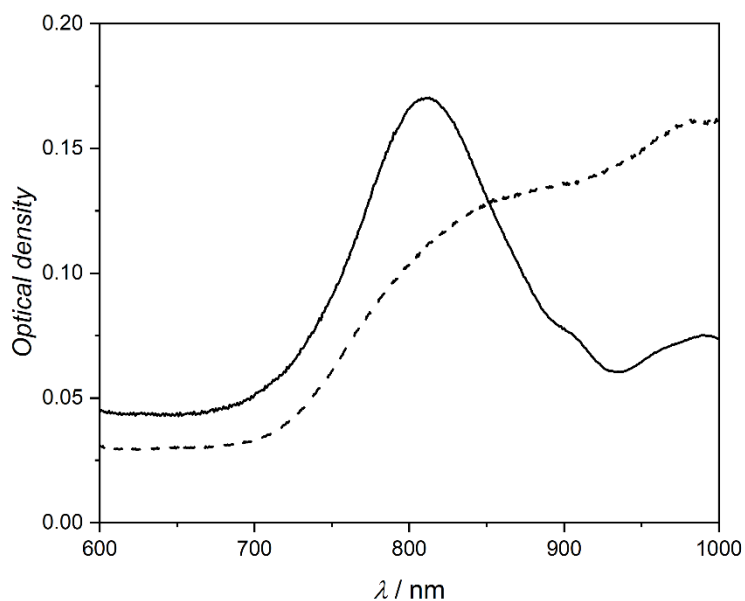


**Figure 7.14:** OD of a solution with 4.85 mol L<sup>-1</sup> DMA, 3.53 mol L<sup>-1</sup> isopropanol, 0.01 mol L<sup>-1</sup> AIBN, 75 μL AuNR in water without CTA (black) and with 10 μL (0.38 mol L<sup>-1</sup>) CTA (black dashed), corresponding to the experimental polymerization conditions, as a function of wavelength. Adapted with permission from ref. 285. Copyright 2023 Royal Society of Chemistry.

The action plot was measured in the spectral range of 620-950 nm, with measurements taken in steps of 20 nm. It is essential to maintain a constant photon number at each wavelength to ensure that the comparison between different wavelengths is meaningful. How the photon number can be adjusted is described in **Section 4.8**. Since ns laser pulses will produce different thermal conditions in the vicinity of the AuNR, compared to fs laser pulses, it was necessary to first determine suitable reaction conditions to ensure that polymerization was initiated primarily by the local heat generation. For each sample, 150 μL aliquots were taken from a stock solution of AIBN dissolved in DMA and filled up with 75 μL AuNR in water, 75 μL isopropanol and 10 μL CTA, such that each sample featured a concentration of 0.01 mol L<sup>-1</sup> AIBN, 4.85 mol L<sup>-1</sup> DMA, 3.53 mol L<sup>-1</sup> isopropanol, 0.38 mol L<sup>-1</sup> CTA and 75 μL of AuNR. Identical to the previous experiments, an initial irradiation duration of 30 min was chosen, however, which was problematic as polymer formation was observed after 30 min even without the addition of AuNR. The increased energy input of the longer pulse duration was found to be sufficient to significantly heat the reaction solution and initiate a reaction. By reducing the exposure time to 15 min, it was possible to activate polymerization only when AuNR were added. The initial experimental conditions involved an irradiation time of 15 min at 800 nm

with an energy input of 260  $\mu\text{J}$ . A simulation, similar to the one for the proof-of-principle experiment and conducted by a collaborator at the QUT,<sup>183</sup> indicated that these reaction conditions are conducive for initiating radical formation followed by polymerization.<sup>41</sup> The simulation method utilized in this study, developed by Metwally *et al.*,<sup>284</sup> focuses on the absorption of optical power by the electron gas within the AuNR, subsequently transferred to the lattice, leading to a rise in temperature. The resultant heat diffuses into the surrounding medium, influencing the temperature of the medium, an essential factor in initiating polymerization. Notably, the key difference from the previous simulation (refer to **Section 3.5.3**) is the duration of the incident laser pulses. As the pulse duration extends from the fs regime to 5 ns, the evolution of electron gas, lattice and medium temperature becomes interrelated. Unlike prior findings, where the initial temperature change in AuNR denoted the maximum temperature shift, the longer pulse duration prevents an analytical calculation of this change. Instead, a source term based on the laser fluence was employed in the diffusion equation within the NR, subsequently resolved numerically, following a methodology similar to that detailed in the report of Metwally *et al.*<sup>284</sup> The maximum temperature of the AuNR in the case of the ns irradiation is 350 K. Consequently, the local environment experiences a modest temperature increase, reaching a maximum rise of approximately 24 K. Nonetheless, considering that the thermal decomposition of AIBN commences at around 40 °C, this temperature increase should be sufficient to initiate the desired reactions. Based on these reaction conditions, a satisfactory conversion of about 30% was achieved when irradiating at 800 nm (**Figure 7.15**). These conditions were subsequently used as a reference point, facilitating the calculation of the required energy levels for further experiments (as summarized in **Table 7.6**).

**Table 7.6:** Overview of wavelength-dependent energy for the action plot.

<i>Wavelength / nm</i>	<i>Energy / <math>\mu\text{J}</math></i>
950	219
840	248
820	254
800	260
780	267
760	274
740	281
720	289
700	297
680	306

<i>Wavelength / nm</i>	<i>Energy / <math>\mu</math>J</i>
660	315
640	325
620	335

**Figure 7.15** presents the results of the action plot with the conversion measured in triplicate at each wavelength to ensure both reproducibility and to provide an error estimate (refer to **Table 7.7**). The reactivity of the system was observed within the spectral range of 620 nm and 950 nm. Surprisingly, the reactivity maximum does not align with the absorption maximum, which is observed close to 800 nm. Instead it exhibits a significant blue-shifted maximum occurring at approximately 760 nm accompanied by a substantial conversion of 37%. Notably, no polymerization was detected below 620 nm and above 950 nm. This observation is intriguing for two reasons: on the one hand, it implies that wavelengths above 950 nm do not generate sufficient heat, despite having a higher OD in this spectral region compared to the highly reactive zone (**Figure 7.14**). On the other hand, the remarkable aspect of this action plot is that it displays a blue shift concerning the absorption maximum, contrary to previous action plots that typically demonstrated red shifts.<sup>11,41-44</sup> The observed discrepancy might arise from the end-to-end stacking phenomenon, which enhances the OD, but may not necessarily contribute to light absorption that can be converted into heat, rather, it might be linked to scattering effects. As described in **Section 3.5.3**, it is well established that the properties of AuNR are geometry-dependent and that the plasmonic absorption band shifts with changes in the aspect ratio.<sup>240,246</sup> A plausible hypothesis for the deviation between reactivity and absorption is geometrical reshaping induced by cumulative heating of the AuNR. However, the action plot simulation<sup>183</sup> argues against this notion, particularly as the relatively low temperatures achieved by the AuNR practically eliminates reshaping via melting as a plausible mechanism.

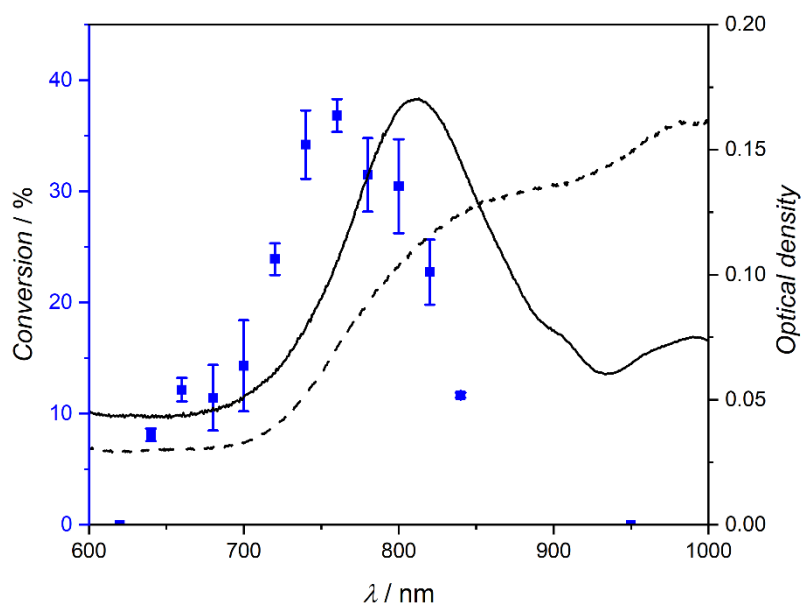


**Figure 7.15:** Conversion with error bars (blue) of a solution with 4.85 mol L<sup>-1</sup> DMA, 3.53 mol L<sup>-1</sup> isopropanol, 0.01 mol L<sup>-1</sup> AIBN, 75 μL AuNR in water and with 10 μL (0.38 mol L<sup>-1</sup>) CTA, after 15 min irradiation with a ns laser at a constant number of photons (1.61·10<sup>19</sup>) and OD of this solution without CTA (black curve) and with 10 μL (0.38 mol L<sup>-1</sup>) CTA (black dashed curve), corresponding to the experimental polymerization conditions, as a function of wavelength. Adapted with permission from ref. 285. Copyright 2023 Royal Society of Chemistry.

**Table 7.7:** Overview of the wavelength-dependent triplicate conversions and average conversion as well as the error determined by standard deviation of the action plot.

$\lambda / \text{nm}$	<i>Conversion</i> 1 / %	<i>Conversion</i> 2 / %	<i>Conversion</i> 3 / %	<i>Average</i> <i>Conversion</i> / %	<i>Error / %</i>
620	0	0	0	0	0
640	8.5	7.7		8.1	0.6
660	12.9	11.4		12.2	1.1
680	14.4	11.4	8.5	11.4	2.9
700	11.4	17.2		14.3	4.1
720	24.9	22.9	19.4	22.4	1.4
740	34.9	30.0	37.4	34.2	3.0
760	36.3	38.9	35.4	36.8	1.5
780	32.0	34.5	27.9	31.4	3.3
800	33.3	23.5	25.6	30.4	4.2

$\lambda$ / nm	Conversion 1 / %	Conversion 2 / %	Conversion 3 / %	Average Conversion / %	Error / %
820	25.2	19.5	23.5	22.7	2.9
840	11.8	11.8	11.4	11.7	0.2
950	0	0	0	0	0

To confirm that heating effects are not contributing to the blue-shifted reactivity spectrum, time-dependent UV/Vis spectroscopy was employed. An initial measurement was conducted on a reference specimen concentrated with 4.85 mol L<sup>-1</sup> DMA, 3.53 mol L<sup>-1</sup> isopropanol, 0.01 mol L<sup>-1</sup> AIBN, 0.38 mol L<sup>-1</sup> CTA and 75  $\mu$ L AuNR without irradiation and then subsequent measurements were carried out with 260  $\mu$ J ns laser pulses (0.67 J cm<sup>-2</sup>) at intervals of up to 15 min. **Figure 7.16** measured by a collaborator at QUT<sup>285</sup> confirms the absence of a blue-shift in the absorption spectrum, thereby corroborating the theoretical predictions. It is worth noting that El-Sayed<sup>242,243</sup> reported AuNR reshaping in response to both ns and fs laser irradiation. However, it is essential to highlight that their ns laser experiment involved significantly higher laser fluence (0.64 – 16.7 J cm<sup>-2</sup>). As reported by Ben-Yakar,<sup>39</sup> AuNRs begin melting at temperatures exceeding 1337 K. Given that the simulation for the fs experiment with AuNR estimated an initial temperature surpassing 1000 K (refer to **Section 3.5.3**), this provided an opportunity to demonstrate that the fs system behaves in a manner consistent with established knowledge under the specified conditions. Thus, the reaction mixture (4.85 mol L<sup>-1</sup> DMA, 3.53 mol L<sup>-1</sup> isopropanol, 0.01 mol L<sup>-1</sup> AIBN, 0.38 mol l<sup>-1</sup> CTA and 75  $\mu$ L AuNR) was monitored over time using 800 nm fs pulses with 25 GW cm<sup>-2</sup>, as given in **Section 7.2**. **Figure 7.17** presents the time-dependent UV-vis spectra, revealing a pronounced blue shift of approximately 90 nm after 10 min.

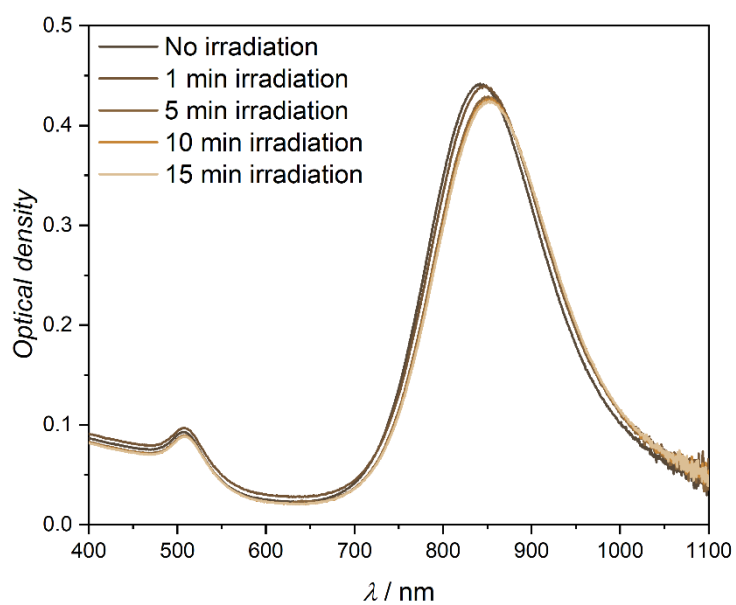


**Figure 7.16:** Absorption spectra of a solution of 4.85 mol L<sup>-1</sup> DMA, 3.53 mol L<sup>-1</sup> isopropanol, 75 μL AuNR in water. From dark to pale: Absorption spectrum of the solution immediately after preparation without irradiation, after 1 min irradiation, after 5 min irradiation, after 10 min irradiation and after 15 min irradiation with 10 ns pulses at 800 nm with 260 μJ. Adapted with permission from ref. 285. Copyright 2023 Royal Society of Chemistry.

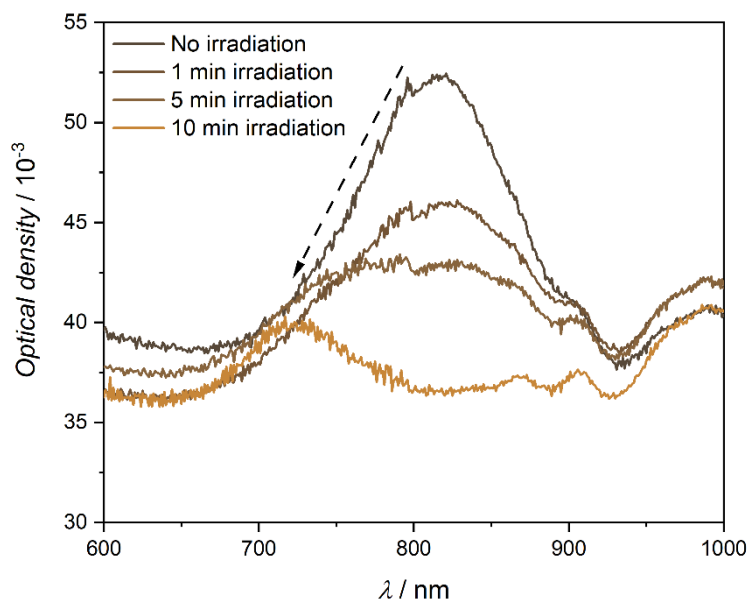


**Figure 7.17:** Absorption spectra of a solution of 4.85 mol L<sup>-1</sup> DMA, 3.53 mol L<sup>-1</sup> isopropanol, 0.01 mol L<sup>-1</sup> AIBN, 75 μL AuNR in water and 10 μL (0.38 mol L<sup>-1</sup>) 3-mercaptopropionic acid. From dark to pale: Absorption spectrum without irradiation, absorption spectrum after 1 min irradiation, absorption spectrum after 5 min irradiation, absorption spectrum after 10 min irradiation with 170 fs pulses at 800 nm with 250 μJ. The black dashed arrow indicates the blue shift of the absorption maximum during the increasing longer irradiation times. Adapted with permission from ref. 285. Copyright 2023 Royal Society of Chemistry.

Cumulative heating from consecutive ns pulses, which had initially been considered as a possible cause of the observed blue shift in reactivity, has been effectively eliminated as a contributing factor. However, there is another plausible explanation for the observed blue shift in reactivity, as detailed earlier in the current chapter. The end-to-end aggregation of AuNRs, as shown via transmission electron microscopy (TEM) in **Figure 7.18** recorded by a collaborator at QUT,<sup>285</sup> increases the light scattering intensity due to the excitation of bonding and anti-bonding modes of the stacked AuNR.<sup>286</sup> As a result, the scattering potentially dominates over absorption.<sup>161</sup> Although the aggregation of AuNRs leads to a higher OD at longer wavelengths (refer to **Figure 7.14**), it is proposed that the increase is primarily attributed to scattering effects, which dominate over absorption, but do not lead to photothermal conversion. This, in turn, would hinder monomer conversion at higher wavelengths and potentially account for the first action plot with an observed blue shift in reactivity. Deconvoluting absorption and scattering events in nanoparticles is a non-trivial exercise<sup>287</sup> and is outside the scope of this thesis.

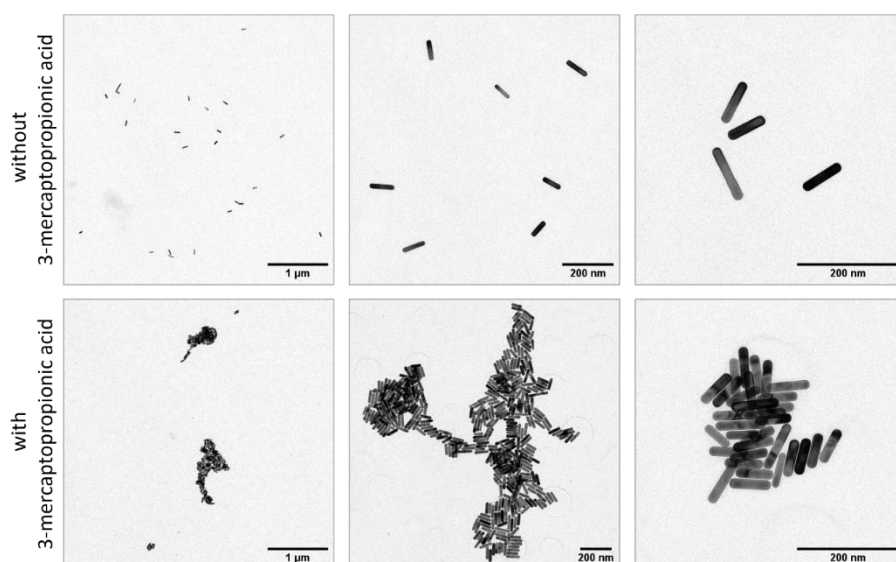


**Figure 7.18:** 3-mercaptopropionic acid (CTA) causes agglomeration of the AuNRs. The brightfield TEM images in the top row show the dispersion to individual AuNRs in the reaction solution without CTA. The AuNRs form agglomerates of random shape and number of NRs upon the addition of CTA (bottom row). Adapted with permission from ref. 285. Copyright 2023 Royal Society of Chemistry.

## 7.7 Polymerization with LEDs

**Sections 7.2 - 7.6** have effectively demonstrated that AuNR-mediated NIR-induced polymerization can be initiated using both fs and ns lasers. Moreover, these sections have explored the optimal excitation range for achieving maximum monomer conversion. Based on this knowledge, LEDs, which are no longer quasi-monochromatic, will be introduced as a more practical light source to activate plasmonic heating of AuNRs, thereby initiating thermal polymerization. The LED experiment was designed to not only provide fundamental insights, but also to showcase its practical applicability, for example, to bridge advanced research and higher education of students. It serves as an illustrative example of the conversion of light energy into heat, making it a valuable educational tool.

Given the success of previous experiments using DMA as a monomer and AIBN as a thermal initiator in conjunction with heat-generating AuNRs, these same reactants were employed preparing solutions with 2.4 mol L<sup>-1</sup> DMA, 0.01 mol L<sup>-1</sup> AIBN, 350 μL AuNR and 4.94 mol L<sup>-1</sup> isopropanol for the LED-induced polymerization experiment. Two variations of the experiment were conducted. First, the polymerization was carried out with the addition of the CTA, enabling polymer analysis using <sup>1</sup>H-NMR spectroscopy. Second, the polymerization was performed without the CTA, which facilitated better visual detection of polymer formation by the naked eye. The latter aspect is particularly valuable for educational purposes, making it suitable for school experiments, as the increased viscosity resulting from long-chain polymers

enhances their visibility. To ensure a sufficiently robust heat generation from the AuNRs, which is required to activate the thermal initiator AIBN, commercially available 10 W high-power COB LEDs with an emission area of approximately  $1 \times 1 \text{ cm}^2$ , resulting in a light intensity of  $10 \text{ W cm}^{-2}$  directly on the LED surface, were utilized. A 1 cm glass cuvette was lateral attached in direct contact to the LED minimizing divergence to ensure uniform illumination of the solution.

In line with the experiments conducted using fs and ns lasers, it was imperative to demonstrate the essential role of AuNRs in initiating polymerization when employing LEDs. Since the action plot from the ns laser experiments indicated that maximum monomer conversion occurs at approximately 760 nm, LEDs with an emission wavelength of 745 nm were selected for this purpose. Additionally, 650 nm LEDs and 590 nm LED were utilized to showcase polymerization at the edge of the absorption band and that polymerization does not occur when AuNRs are irradiated with light outside the plasmonic absorption band. This experimental sequence further emphasized the critical role of the plasmonic properties of AuNRs in the polymerization process.

Analogue to the AuNR-mediated polymerization with fs and ns laser,  $^1\text{H-NMR}$  spectroscopy served to clearly evidence the generation of polymers using LEDs, a crucial point for academic science. The upper portion of **Figure 7.19** displays the  $^1\text{H-NMR}$  spectrum of the reaction solution ( $2.4 \text{ mol L}^{-1}$  DMA,  $0.01 \text{ mol L}^{-1}$  AIBN,  $350 \mu\text{L}$  AuNR and  $4.94 \text{ mol L}^{-1}$  isopropanol) after irradiation with  $10 \text{ W cm}^{-2}$  at 745 nm in the absence of AuNRs. The spectrum exhibits the monomer peaks at 3 ppm as well as 5.7 ppm, 6.2 ppm and 6.75 ppm. However, the polymer resonances at 1.5 ppm and 3 ppm are absent. The spectrum provides clear evidence that polymer formation does not occur in the absence of AuNRs. The lower part of **Figure 7.19** presents the  $^1\text{H-NMR}$  spectrum of an identical experiment, yet with the addition of AuNRs. In contrast to the upper spectrum, the polymer associated resonances are distinctly visible, confirming the crucial role of AuNRs in polymerization. Notably, there are no monomer resonances at 5-7 ppm, indicating complete monomer conversion. Remarkably, the continuous energy input from the LEDs to the solution presumably results in more pronounced macroscopic heating of the solution compared to the fs and ns laser pulses, which is, for example, expressed by a sensible heat of the cuvette. However, as AuNRs are critical initiators of the reaction, it appears that the heating by the LEDs alone is not sufficient for initiation. Local heat generation by the AuNRs is thus essential for activating the thermal initiator.

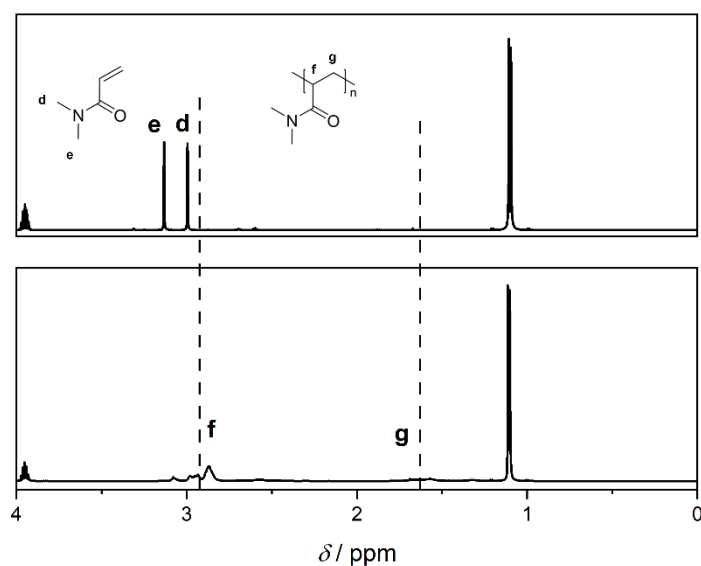


**Figure 7.19:**  $^1\text{H-NMR}$  spectrum of a solution of  $2.4 \text{ mol L}^{-1}$  DMA,  $4.94 \text{ mol L}^{-1}$  isopropanol,  $0.01 \text{ mol L}^{-1}$  AIBN, and  $350 \mu\text{L}$  AuNR in water (bottom row) and without AuNR (top row) after 10 min irradiation with two 745 nm LEDs; recorded with a 600 MHz NMR spectrometer.

As high schools usually do not have access to an  $^1\text{H-NMR}$  spectrometer, the experiment was slightly adapted. When the reaction is conducted without the CTA, successful polymerization was directly observed due to increased viscosity of the solution within the cuvette. Given that successful polymerization has already been confirmed via  $^1\text{H-NMR}$  spectroscopy using the 745 nm LEDs in the presence of AuNRs, the clearly noticeable increase in viscosity can be confidently attributed to the formation of polymers. In contrast, observing no change in viscosity, provides a qualitative indication for the absence of polymer formation.

**Figure 7.20** displays the  $^1\text{H-NMR}$  spectrum of the solution with the CTA after irradiation with 650 nm LEDs. In this spectrum, the polymer peak at 3 ppm is Vis, although it appears smaller in comparison to the spectrum in **Figure 7.19**. Furthermore, the monomer peaks at 5-7 ppm remain clearly Vis, suggesting that the monomer did not undergo complete reaction in this case. Consequently, the polymerization appears to be weaker when using the 650 nm LEDs in contrast to the 745 nm LEDs, in line with expectations since 650 nm falls at the edge of the absorption band of the AuNRs, and the action plot (refer to **Section 7.6**). This result clearly indicates a significant reduction in monomer conversion with 650 nm irradiation compared to the 745 nm LED. Therefore, it can be concluded that the 650 nm LEDs still generate sufficient local heat to initiate polymerization reactions, but this heat generation is notably lower than that achieved with the 745 nm LEDs.

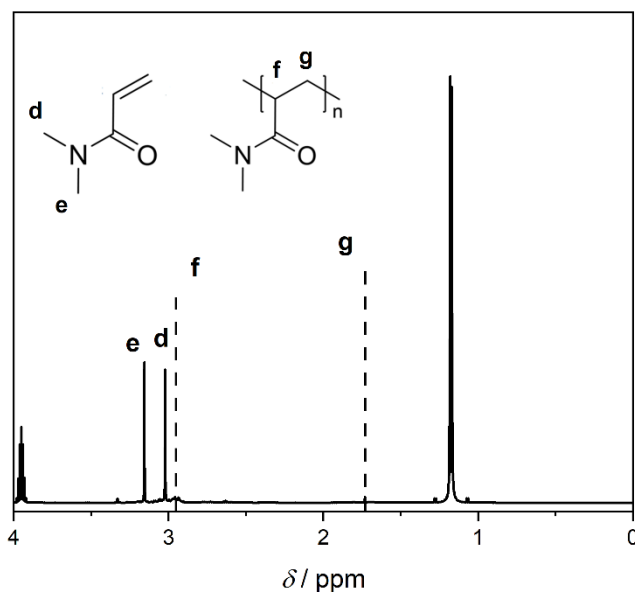


**Figure 7.20:** <sup>1</sup>H-NMR spectrum of a solution of 2.4 mol L<sup>-1</sup> DMA, 4.94 mol L<sup>-1</sup> isopropanol, 0.01 mol L<sup>-1</sup> AIBN, and 350 μL AuNR in water after 10 min irradiation with two 650 nm LEDs; recorded with a 600 MHz NMR spectrometer.

**Figure 7.21** underscores that no polymer is generated when using the 590 nm LEDs. This outcome is expected since the emission wavelength falls outside the longitudinal absorption band of the AuNRs. Consequently, the photons do not excite the plasmons of the AuNRs, preventing heat generation. Even though the solution is heated by the LEDs, the heat produced is not sufficient to initiate polymerization due to the absence of local heat from the AuNRs.

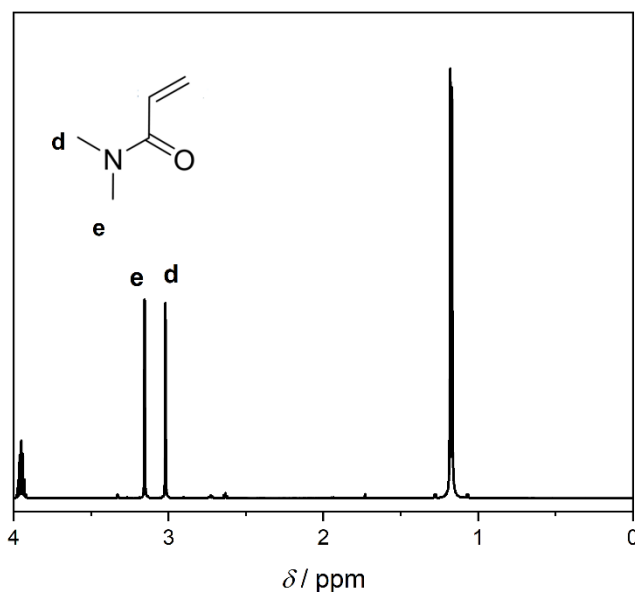


**Figure 7.21:** <sup>1</sup>H-NMR spectrum of a solution of 2.4 mol L<sup>-1</sup> DMA, 4.94 mol L<sup>-1</sup> isopropanol, 0.01 mol L<sup>-1</sup> AIBN, and 350 μL AuNR in water after 10 min irradiation with two 590 nm LEDs; recorded with a 600 MHz NMR spectrometer.

The current subchapter highlighted that AuNR-mediated thermal polymerization is accessible using LEDs as light source, thus offering a practicable approach for academic science as well as illustrative example of the conversion of light energy into heat as educational tool in high school.

## 7.8 Summary

The current chapter discussed a proof-of-principle experiment using NIR-absorbing plasmonic AuNR as photothermal converter to mediate the initiation of thermal polymerization as an alternative to NIR-induced ZPP. Theoretical and experimental publications were initially presented to establish the use of AuNR for NIR-induced polymerizations prior to evidencing polymer generation via  $^1\text{H-NMR}$  spectroscopy after exposure to 800 nm fs laser pulses. As AuNR-mediated polymerization was estimated to follow the kinetics of standard according to the prediction of the Mayo equation,<sup>223,224</sup> the degree of polymerization was mapped by varying the concentrations of both monomer and radicals using  $^1\text{H-NMR}$  Spectroscopy and SEC.

Featuring low cytotoxicity, thus being benign to tissue, paired with the high penetration depth of NIR light into tissue, makes AuNR highly promising for light intensity-sensitive application. Therefore, the generation of polymer was documented by placing a thin slice of bacon, simulating biological tissue, in front of a sample.

Previous studies have revealed that absorptivity does not automatically align with chemical reactivity. An action plot, screening the wavelength-dependent monomer conversion using a quasi-monochromatic ns laser, was applied to examine the optimum heat production of the AuNR.

A kinetic study highlights that the time-dependent monomer conversion behaves as expected, rising rapidly at short times, decelerating and eventually reaching a plateau for advanced times. As predicted by the Mayo equation,<sup>223,224</sup> the monomer conversion differs depending on the used monomer concentration. Moreover, different parameters, such as monomer concentration, initiator concentration, and AuNR concentration were varied, followed by the analysis of the MWD using SEC and conversion using  $^1\text{H-NMR}$  spectroscopy to further emphasize control over the polymerization reaction. An increase of the monomer concentration caused an elevation in the molecular weight of the generated polymers, as well as an increase in conversion. With more monomer units available, the polymer can grow to a higher chain length and a higher amount of monomer unit can be initiated to commence polymerization. In principle, increasing the initiator concentration or the AuNR concentration causes the same

result. A higher amount of initiator molecules increases the likelihood of termination reactions, which leads to shorter polymer chains and thus lower molecular weight. At the same time, more monomer units can be activated, increasing the monomer conversion. The enhanced heat production, caused by a higher AuNR amount, leads to enhanced radical formation, thus to a higher rate of termination reactions and to a higher conversion.

ESI-MS issued an isotopic pattern with the  $m/z$  ratio of the generated polymer providing valuable information of the end group distribution. Although the polymerization was transfer controlled resulting in predominantly CTA fragment end groups, the thermal initiator AIBN has a definite impact on the polymerization as it causes a decrease of the molecular weight of the polymer chains as well as an increase of the monomer-to-polymer conversion.

In addition to the use of fs lasers to initiate polymerization via the heat generated by AuNR, it was demonstrated that polymers can also be produced using ns lasers. An action plot showcasing wavelength-dependent reactivity was recorded, revealing a noteworthy blue shift concerning absorbance. The reactivity reached its peak at 760 nm, while absorbance showed its maximum at around 800 nm. This intriguing observation prompted the exploration of potential explanations. Initially, a hypothesis involving AuNR deformation due to heat-induced melting towards spherical particles was considered. However, this hypothesis was essentially ruled out via experimental control experiments and simulations. As highlighted by the absorption spectrum in **Figure 7.14**, the AuNRs are subject to end-to-end aggregation due to the CTA. This phenomenon results in an increased scattering cross section and shifting the spectrum towards longer wavelengths with scattering becoming dominant over absorption, thus suppressing polymer conversion. This promises to be a plausible explanation for the observed blue-shift. Currently, however, there is no definitive explanation for this observed phenomenon.

Furthermore, LEDs were employed to polymerize AuNR, demonstrating the versatility of different light sources and their influence on polymerization. This approach also aimed to showcase practical applications for AuNR, including their potential use in educational settings and school experiments. Similar to the action plot results, the LED experiments confirmed that monomer-to-polymer conversion is wavelength-dependent. Polymers were only generated when an excitation wavelength within the absorptive band was selected.

## 8 Conclusion

The current thesis introduces the first in-detail mechanistic study of Vis light fs PLP in the Hz and kHz regime. Shifting focus from the Vis spectral region to the NIR region, chain length controlled NIR 2PP was introduced using a fs PLP technique. As a new approach, NIR light-absorbing plasmonic AuNR were introduced as photothermal converter to mediate thermal polymerizations in water under mild reaction conditions.

**Chapter 5** demonstrated that Ivocerin decomposes linearly dependent on the excitation energy when exposed to 400 nm pulses, which is a clear indicator for a 1P mechanism. SEC analysis served to verify the successful generation of polymer and to calculate the propagation rate coefficient at various pulse frequencies, underlining the tunability of polymer chain length via the laser repetition rate.<sup>182</sup> Thus, polymerizations in the regime of 10-100 Hz are laser controlled. Further, the analysis of the polymer products highlighted the generation of acyl fragments as major and germyl fragments as minor species indicating a potential 2-step decomposition mechanism of Ivocerin based on a Ge-C bond cleavage.<sup>182</sup> Time-resolved fs spectroscopy, which allowed for the investigation of the earliest steps after photoexcitation, showed long-lived triplet states after ISC from an excited singlet state. The formation of triplet states likely represented the main relaxation channel within the observed time of 1 ns due to the absence of dominating deactivation channels. Therefore, Ivocerin potentially features a high yield of radical formation as the bond cleavage of photoinitiator usually originates from triplet states, a hypothesis which is supported by a reported photobleaching quantum yield of Ivocerin of 0.86.<sup>279</sup> Remarkably, the ISC lifetime of Ivocerin is only 9.2 ps, which is a factor of 3-5 lower than the ISC lifetime of non-substituted bisacylgermane.<sup>277</sup> As an efficient ISC is fundamental for photoinitiation,<sup>21</sup> the gained knowledge about the short lifetime of the dominating ISC helps to understand why Ivocerin is an efficient triplet photoinitiator.

In addition to the Vis light-induced fs PLP experiments, **Chapter 6** explored the accessibility of fs PLP in the Hz regime with Ivocerin as photoinitiator via two photon absorption (2PA) making use of NIR light. Milder reaction conditions due to less energy and a deeper penetration depth into tissue make NIR light advantageous over UV and Vis light, thus making it better suitable for biomedical application. Initial initiator decomposition experiments using UV/Vis spectroscopy evidenced the ability of Ivocerin to decompose under exposure of NIR light when absorbing two photons simultaneously. Underpinned by the quadratic relation of the initiator conversion and the incident beam energy, the initiator decomposition was interpreted to follow a 2PA process. Analogous to the Vis light fs PLP experiments, SEC analysis clearly showed the generation of polymer and allowed the determination of the propagation

rate coefficients for different laser repetition rates.<sup>182</sup> The consistency of the calculated propagation rate coefficient with IUPAC literature data<sup>275</sup> confirmed that the NIR light induced 2P fs PLP was laser controlled. Further, the polymer products assigned via high resolution mass spectrometry showed identical end groups as to Vis light fs PLP experiment,<sup>182</sup> involving the acyl fragment and the germyl fragment. Although slightly different to the Vis light fs PLP experiment, the end group distribution of the 2PP fs PLP experiment led to the conclusion that the initiator decomposition followed a 2 step mechanism based on the cleavage of Ge-C bonds, such as proposed for the 1PA process. The 2PP experiments reveal a potential alternative to the 1PP experiments. In particular, 2P processes are useful for applications that require high spatial precision. Moreover, **Chapter 6** demonstrates the ability of Ivocerin to initiate polymerization even after the incident laser beam penetrated through a thin slice of bacon – as an example of biological tissue – which may be a key finding for potential application in biological environments. However, it needs to be considered that 2PA processes require high light intensities, which may limit the applicability of 2PP with Ivocerin.

Using plasmonic AuNR as photothermal converter appears to be a valuable alternative to 2PP, enabling NIR light-induced polymerization without focusing of the incident light. Here, an initial proof-of-principle experiment, heating the AuNR with a fs laser, confirmed that AuNR are capable of producing sufficient heat to decompose a thermal initiator, which in turn initiates polymer chain growth. Moreover, mapping the molecular weight of the polymer chains and monomer to polymer conversion via SEC and <sup>1</sup>H-NMR spectroscopy using various concentrations of the monomer, thermal initiator and AuNR clearly showed that the polymerization reaction is controllable.<sup>183</sup> The isotopic pattern of the recorded mass spectrum was governed by end groups containing thiol fragments. As a chain transfer agent was added to decrease the molecular weight of the polymer chain enabling a proper molecular weight for mass spectrometry, it was not surprising that the assigned polymer species were dominated by the transfer agent fragment.<sup>183</sup> In a similar experiment as in **Chapter 6**, using a thin slice of bacon, highlighted that polymer can also be generated with AuNR that were exposed to 800 nm fs pulses after the laser beam propagated through tissue. A key finding was the high spatio-temporal resolution of the polymerization reaction as the produced heat by the AuNR is strongly localized dissipating only 10-20 nm from the AuNR within less than 1 ns without heating the bulk medium,<sup>39,183</sup> which is a critical aspect for sensitive applications. Although the 2PP technique allows more spatial precision due to focusing and thus smaller structures, AuNR offer several advantages over 2PP using Ivocerin, as the reaction conditions required are much milder and AuNR can be functionalized such that they can operate in aqueous environment.

Thus, AuNR are highly promising for use in polymerization of biomedical applications. Expanding the light sources from the fs laser to a ns laser and LEDs underpins the versatility of the AuNR-mediated NIR light-induced polymerization. A photochemical action plot, screening the wavelength-dependent reactivity with a quasi-monochromatic ns laser, established that the heat production can be controlled by tuning the wavelength, with a maximum in heat production blue-shifted relative to the maximum absorptivity of the reaction mixture. This intriguing observation constitutes the first known blue-shifted action plot.<sup>285</sup> The blue-shift was interpreted to originate from the presence of the transfer agent, leading to aggregation of the nanoparticles. Such aggregation broadens the absorptivity of the AuNR towards the NIR region due to an increase in aspect ratio and increases scattering effects.<sup>240,246,286</sup> Therefore, scattering may dominate over absorption in the NIR region, resulting in less heat production relative to the blue-shifted wavelength, which in turn leads to a blue-shifted reactivity maximum. Demonstrating that polymers can also be generated using LEDs as light source underlined the high versatility of AuNR and offers the chance to develop an experimental setup that would allow the demonstration of plasmonic heating in high school curricula. The major aspect of the LED-induced photothermal polymerization using AuNR is the potential for practical and low-cost application in academic research.

## 9 Outlook

In **Chapter 5**, Ivocerin was excited at 400 nm as this wavelength was close to the absorption maximum and experimentally simple to access. However, considering the insights from the previous photochemical action plot analyses,<sup>11,25,40–42,44</sup> the highest absorptivity of photosensitive molecules does not automatically align with its maximum reactivity. The first recording of an action plot using Ivocerin was conducted with a ns laser. As the variation of laser pulse durations potentially affects the excited state dynamics, future studies may include an action plot with Ivocerin in MMA using a fs laser to explore the effect of different light sources on the wavelength-dependent conversion of MMA.

Further, a systematic fs pulse triggered wavelength-dependent study on Ivocerin in MMA analyzing the end group distribution via *post-mortem* ESI-MS analysis and the earliest events after photoexcitation via transient absorption spectroscopy offers a key opportunity to further deepen the fs PLP study with Ivocerin. As a wavelength-dependent number of radicals is expected to be caused by a different relaxation behaviour, the end-group distribution may be different to the current ESI-MS results after 400 nm excitation. Varying the excitation wavelength, while keeping the reaction concentrations constant, a higher monomer conversion indicates a more efficient radical formation, potentially expressed by shorter ISC and triplet state lifetimes, which can be observed using transient absorption spectroscopy. For the sake of comparability with the current results from the 1P PLP experiments with Ivocerin, using identical concentrations, as given in **Section 5**, is recommended.

The comparison of the results of the current fs 1P PLP experiments with the results reported by Neshchadin *et al.*<sup>277</sup> indicate that the population and lifetime of triplet states does not only depend on the substitution of bisacylgermanes, but most likely also on the solvent. Therefore, it would be worthwhile expanding the wavelength-dependent fs PLP studies with Ivocerin using further monomers and solvents. As a variation of excited state relaxation lifetimes potentially affects the end-group distribution, ESI-MS would serve to identify the end-group distribution of the generated polymer products of a solution with identical concentration of Ivocerin (12 mmol L<sup>-1</sup>), however using different monomers and solvent post-exposure to fs pulses. A potential decrease of the lifetime of the earliest events, such as ISC and triplet state lifetimes can be observed using fs transient spectroscopy.

The 2P fs PLP experiments reported in **Chapter 6** have revealed that a 2P polymerization with Ivocerin as photoinitiator is controllable using fs laser pulses in the Hz regime. However,

in contrast to 1P PLP, there has been no approach to conduct the wavelength-dependent monomer conversion of MMA yet. For an in-depth understanding of the 2PP with Ivocerin, it is essential to exploit further excitation wavelengths, for example screening the reactivity in an action plot ranging from 700 – 900 nm, in a future project. Subsequently, the product formation at each single wavelength can be examined via ESI-MS to highlight potential differences in the end group distribution. Aiming to understand the product distribution in detail requires knowledge about the decomposition mechanism of the photoinitiator. Therefore, the earliest events of excited state dynamics need to be identified, using fs transient absorption spectroscopy.

Employing a fs NIR transient spectrometer as a subsequent project offers the chance to visualise the 2P transient absorption, thus enabling the observation of the first steps of 2P excited Ivocerin. Measuring 2PA transient absorption is experimentally challenging, as 2PA cross-sections ( $10^{-50}$  cm<sup>4</sup> s) are orders of magnitude smaller than 1PA extinction coefficients ( $10^2$ - $10^5$  L mol<sup>-1</sup> cm<sup>-1</sup>). Thus, the likelihood of electronic transitions via 2PA is strongly decreased compared to 1PA. As explored in **Section 3.3.2**, the likelihood of 2P-induced transitions is proportional to the intensity of the incident laser beam. Aiming to increase the probability of an electronic transition, the pump pulse was strongly focussed (in the order of magnitude of  $\mu$ m) into the sample. Usually, the pump pulse diameter is larger than the probe pulse diameter to avoid probing non-excited molecules. Otherwise, the transient response may be decreased due to a smaller amount of excited molecules being probed. However, as described, the pump pulse diameter is smaller in case of 2PA resulting in shrinking of the voxel of excited molecules, which is problematic as this setup potentially leads to a higher number of non-excited molecules. Therefore, the transient response, which is potentially decreased due to the small 2PA cross-section, may be further decreased. Carrying out future experiments with high pump pulse intensities is a feasible option in order to obtain sufficiently strong transient responses. High beam intensities, however, involve the risk of undesired nonlinear effects, such as white light generation in the cuvette or solvent. It would be valuable to conduct time-resolved fs absorption spectra measurements on well-established and strong 2P photoinitiators. In particular, selecting photoinitiators known for high 2PA coefficients, for example Rhodamine B, can function as ideal reference materials. Comparing the behaviour of Ivocerin to Rhodamine B under similar experimental conditions could help place the response of Ivocerin into context and provide insights into its photophysical and maybe photoreactive relaxation pathway under 2P conditions.

Understanding the 2P absorption behaviour of Ivocerin is fundamental to optimize the initiation reaction of 2PP. Analog to the linear extinction coefficient  $\epsilon$ , the 2P absorption coefficient  $\beta$  can be determined, providing information about the likelihood of transition after 2P excitation. However, the determination  $\beta$  is not as trivial as it is for  $\epsilon$ . Rentzepis and coworkers reported of different techniques allowing to determine  $\beta$ , such as 2P-induced fluorescence (2PIF), nonlinear transmission (NLT) and 2P transient spectroscopy.<sup>288</sup> Another technique is the so-called z-scan, first introduced by Van Stryland and coworkers,<sup>289</sup> an experimental setup to measure the nonlinear absorption or nonlinear refractive index.

In the course of the current thesis, a z-scan experiment was started to be set up conducting initial test measurements with the literature known<sup>290</sup> 2P reference dye Rhodamine B to test and optimise the setup. Optimization includes a correct adjustment of the setup, alignment of the beam path as well a well a proper detection of the transmitted beam of the photodiode. If adjusted properly, the recorded transmission curve and calculated 2PA cross-section needs to align with literature-reported data. Although this setup is relatively simple, the measurement of 2-photon absorption cross-sections is not trivial, but poses some serious challenges. Firstly, a z-scan does not measure the probability of 2PA, but also higher orders of nonlinear absorption. It is not immediately obvious to distinguish between these processes. The absorption cross-sections of 2<sup>nd</sup> order are generally very low (in the range of  $10^{-50}$  cm<sup>4</sup> s), thus nonlinear absorption can only be achieved at very high intensities. Although 3<sup>rd</sup> order absorption cross-sections are even smaller than 2<sup>nd</sup> order, such high intensities can also lead to nonlinear absorption processes of higher order. Another phenomenon that can occur at very high intensities is the so-called nonlinear saturated absorption,<sup>291,292</sup> which can distort the recorded transmission or absorption curve and thus ultimately the evaluation. Therefore, it is a challenge to adjust the amount of light incident on the photodiode so that it operates in the linear range. To identify the linear operating range of the photodiode, the output voltage of the detector was plotted against the incident intensity (**Appendix Section 10.2 Figure 10.7**).

The initial measurements involved the use of Rhodamine B to assess the functionality of the setup and ascertain whether the outcomes align with the existing literature. In this experiment, a 1 mm cuvette was employed, containing a solution of  $10^{-3}$  mol L<sup>-1</sup> Rhodamine B dissolved in ethanol. An automated 300 mm stage positioned the cuvette in the z-direction along a laser beam, which was focused through a lens to achieve a focal point of approximately 130  $\mu$ m. To provide an insight into the results, the transmission and absorption curves have been included in **Appendix Section 10.2**, accessible in **Figure 10.8**. These curves offer a visual representation of the data collected under the stipulated conditions. In the scope of a thesis

of Kim,<sup>293</sup> the experiments yielded a 2PA cross section of 86.8 GM, which differs  $\sim 62 \pm 20\%$  from the literature value<sup>290</sup> of  $140 \pm 20$  GM. Building on this initial fundament, it would be valuable to carry out further work with the z-scan and, for example, to determine the 2PA of Ivocerin in order to establish correlations with the transient absorption spectrum.

**Chapter 7** has demonstrated the feasibility of AuNR-mediated polymerization using various light sources, fs and ns laser as well as LEDs. Due to their characteristics, such as low cytotoxicity, mild reaction conditions required and controllability of the polymerization reaction, AuNR are highly promising for utilization in sensitive practical applications. Considering the localized heat production and applicability in water, AuNR are predestined for NIR light-induced polymerization in biomedical applications. Here, dental procedures, such as curing of fillings, represent a prominent example. Further, AuNR offer the potential for the targeted and strongly localized synthesis of biological macrostructure within organic tissue. For practical application, LEDs are particularly interesting, as they are easily accessible, practical to use and cheap. However, conducting an AuNR-mediated polymerization as benign and application specific as possible, requires further knowledge of how to access the optimum of wavelength-tunable heat production dependent on the light source.

As the exact cause of the blue-shift observed in the ns action plot remains unresolved, further experiments are required to delve deeper into its origin. To gain a comprehensive understanding of the behaviour and geometry of the AuNR, absorption spectra should be recorded both before and after irradiation at each measured wavelength. In addition, due to the potentially significant impact of the CTA-induced linkage effect on AuNRs, it would be advantageous to capture absorption spectra as well as TEM images before and after each irradiation, offering a more precise means of tracking the morphology of the AuNRs in solution and potentially shed light on the observed behaviour.

The heat production of AuNR strongly depends on the pulse duration of the radiation source, as shown by the simulations from a collaborator at QUT.<sup>183,285</sup> Thus, performing an action plot with identical concentrated solution as in the current thesis (refer to **Section 7.6**) also using a fs laser will be highly valuable to further explore the background of the wavelength-dependent heat production of the AuNR. Again, gathering absorption spectra and TEM images before and after each irradiation will support to comprehensively understand the observed behaviour and enable comparison to the ns laser action plot with AuNR.

As indicated in the LED experiments, the extent of monomer conversion varies depending on the wavelength of the irradiating light. Leveraging this observation, an action plot could be

generated using LEDs, enabling the comparison of reactivity to absorption at different wavelengths. Such an investigation would contribute to a deeper understanding of the polymerization process and the influence of different light sources on its outcomes. Future projects also require a wavelength-dependent end-group analysis of the generated polymers via ESI-MS post-exposure to each light source, fs and ns laser and LEDs, aiming to understand the AuNR-mediated polymerization in detail. thus, the wavelength-dependent heat production and the product formation can be correlated.

## 10 Appendix

### 10.1 Chapter 5

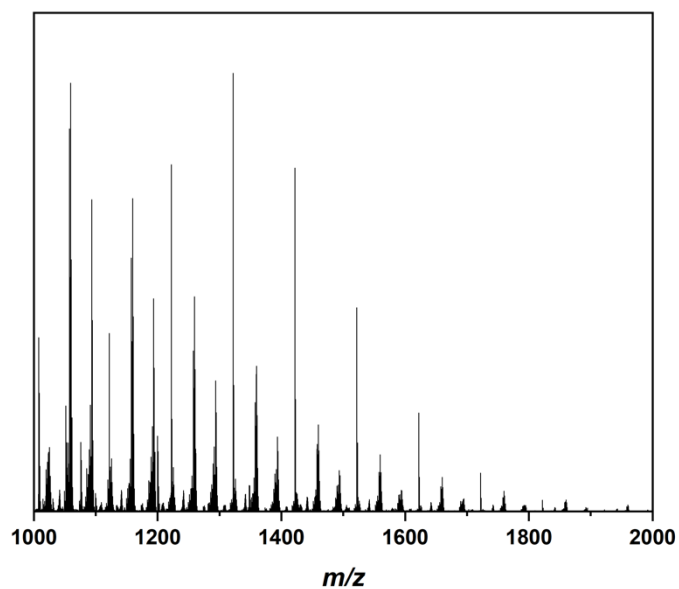


**Figure 10.1:** Experimental mass spectrum of PMMA was obtained from polymer generated after 15 min irradiation of 12 mmol L<sup>-1</sup> Ivocerin in MMA with 102  $\mu\text{J cm}^{-2}$  laser pulses at 400 nm. 10  $\mu\text{L}$  of the irradiated solution were dissolved in 2 mL of a THF/methanol (3:2) solution with 100  $\mu\text{M}$  NaTFA.

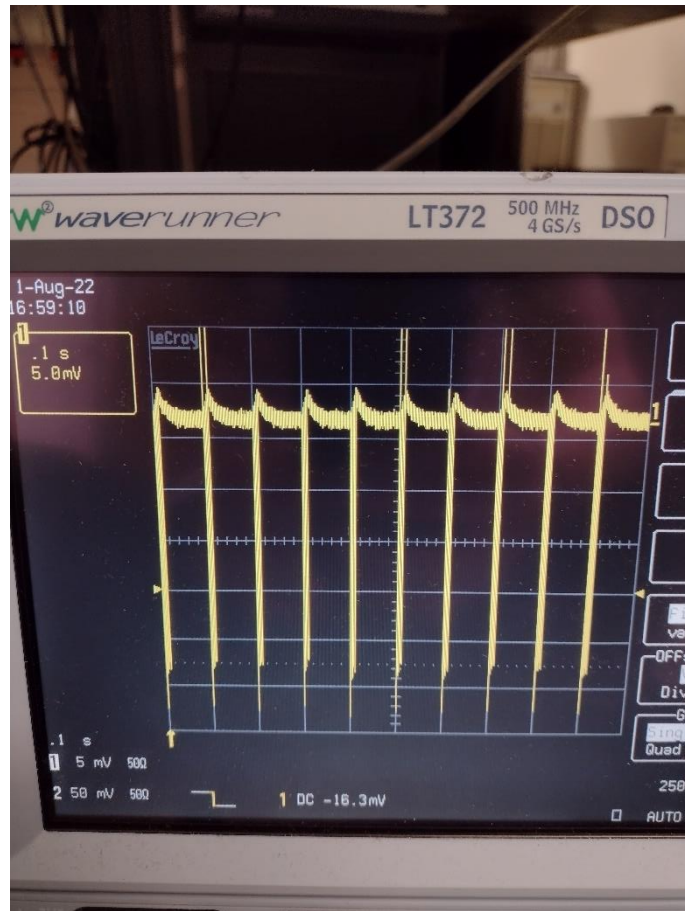


**Figure 10.2:** Oscilloscope showing the output of a photodiode that detects laser pulses with a dark time of 0.1 s between the pulses. This corresponds to a repetition rate of 10 Hz.

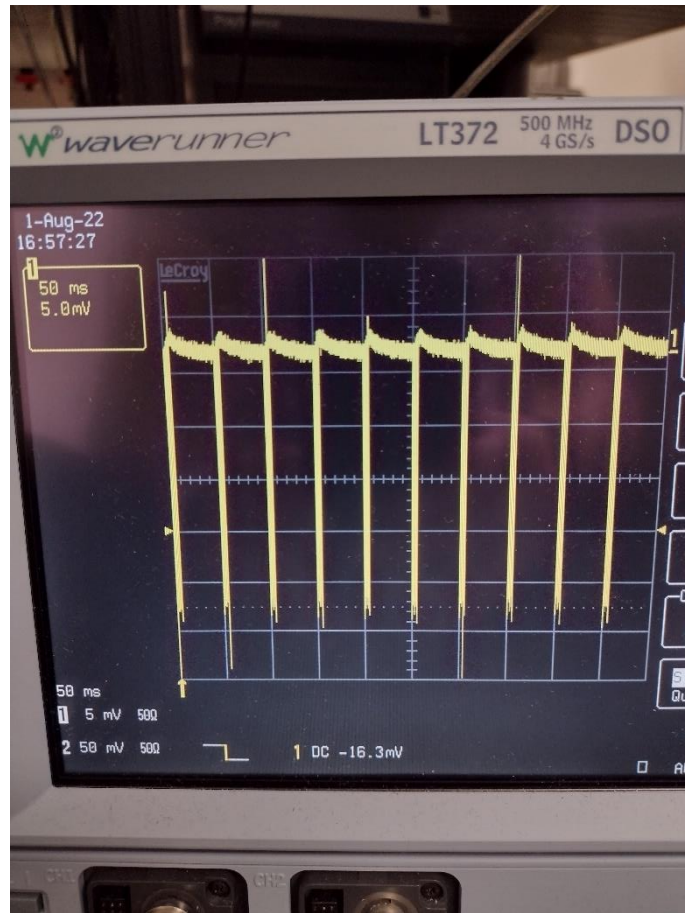


**Figure 10.3:** Oscilloscope showing the output of a photodiode that detects laser pulses with a dark time of 50 ms between the pulses. This corresponds to a repetition rate of 20 Hz.

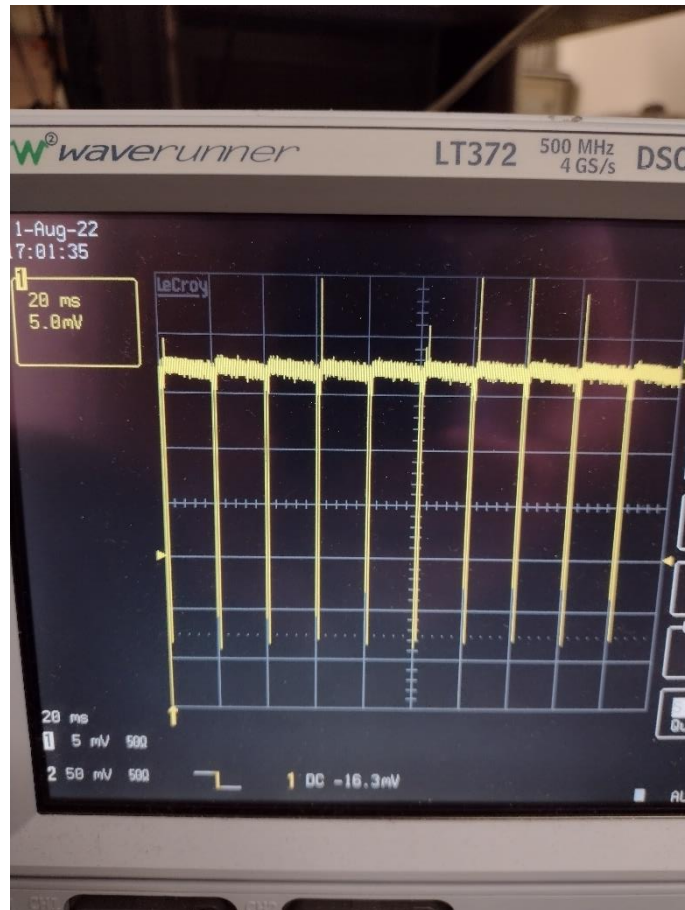


**Figure 10.4:** Oscilloscope showing the output of a photodiode that detects laser pulses with a dark time of 20 ms between the pulses. This corresponds to a repetition rate of 50 Hz.

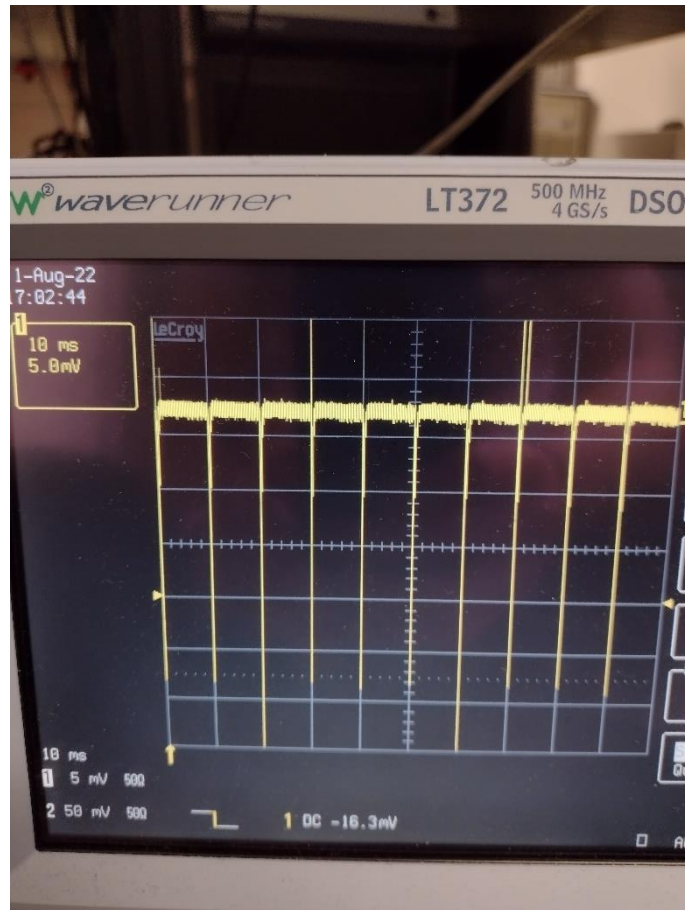


**Figure 10.5:** Oscilloscope showing the output of a photodiode that detects laser pulses with a dark time of 10 ms between the pulses. This corresponds to a repetition rate of 100 Hz.

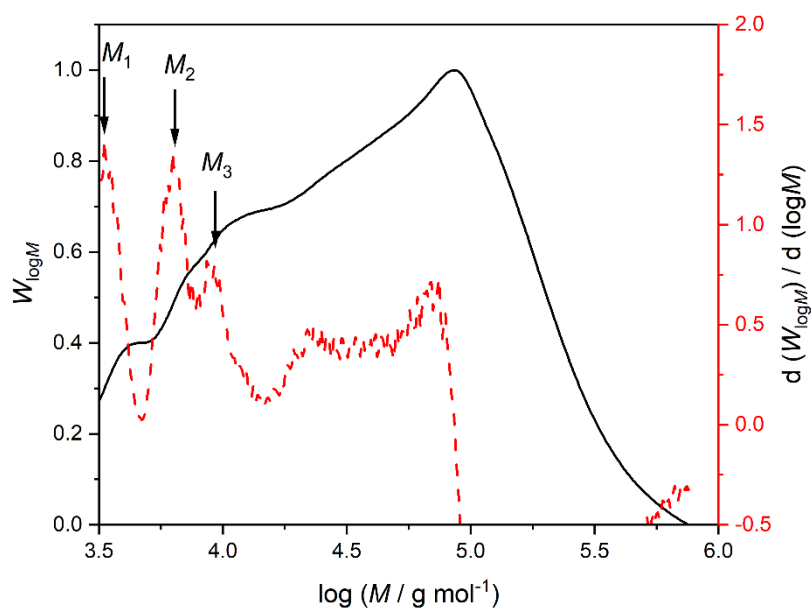


**Figure 10.6:** SEC trace (black) and first derivative of SEC trace of PMMA generated by 400 nm (red dashed) pulsed laser triggered Ivocerin fragmentation ( $c = 12 \text{ mmol L}^{-1}$  in bulk MMA) with a repetition rate of 100 Hz where the inflection points of the distribution are close to  $M_1 = 13963 \text{ g mol}^{-1}$ ,  $M_2 = 28379 \text{ g mol}^{-1}$  and  $M_3 = 42756 \text{ g mol}^{-1}$ .

10.2 Chapter 6

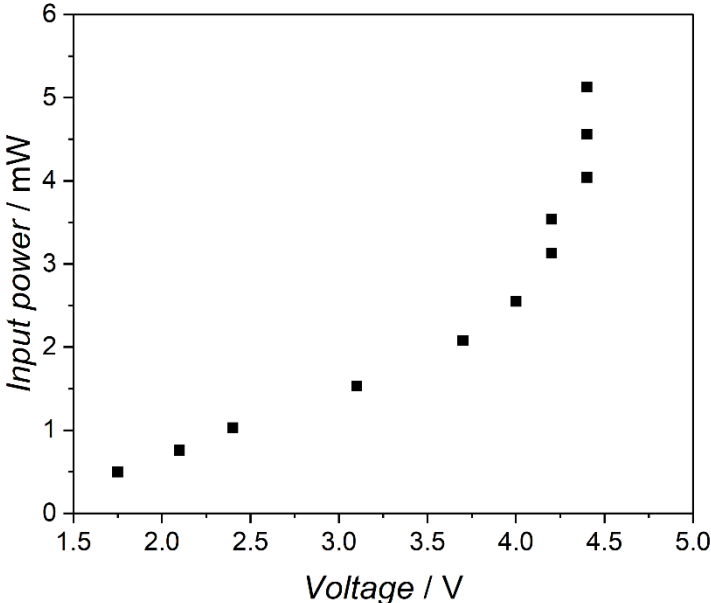


**Figure 10.7:** Incident power on the z-scan photodiode vs. output voltage generated by the incident 775 nm photons.

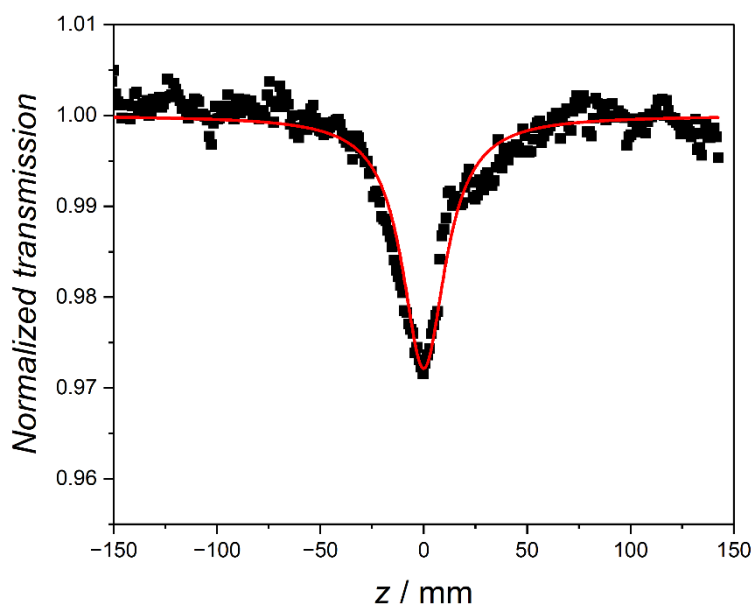


**Figure 10.8:** Normalized transmission curve of an open aperture z-scan measurement of a  $10^{-3}$  M Rhodamine in ethanol solution (black data point) with nonlinear fit-function (red).

### 10.3 Chapter 7



**Figure 10.9:** Photo of a cuvette containing precipitated PDMA forming a white solid after 30 min irradiation of a solution of  $9 \text{ mmol L}^{-1}$  AIBN,  $2.69 \text{ mol L}^{-1}$  DMA, and  $150 \mu\text{L}$  of AuNR with  $800 \text{ nm}$  fs pulses with an intensity of  $25 \text{ GW cm}^{-2}$ .

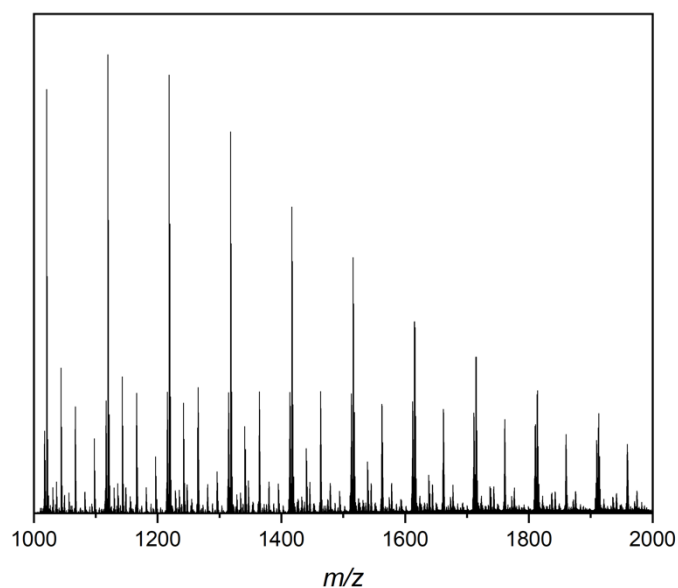


**Figure 10.10:** Full ESI-MS spectrum of PDMA in THF/methanol (3:2) after 30 min irradiation of a solution of 4.04 mol L<sup>-1</sup> DMA, 9 mmol L<sup>-1</sup> AIBN, 100  $\mu$ L AuNR and 10<sup>-2</sup> mol L<sup>-1</sup> CTA with 25 GW cm<sup>-2</sup> fs pulses at 800 nm in the range of 1000 – 2000 *m/z*.

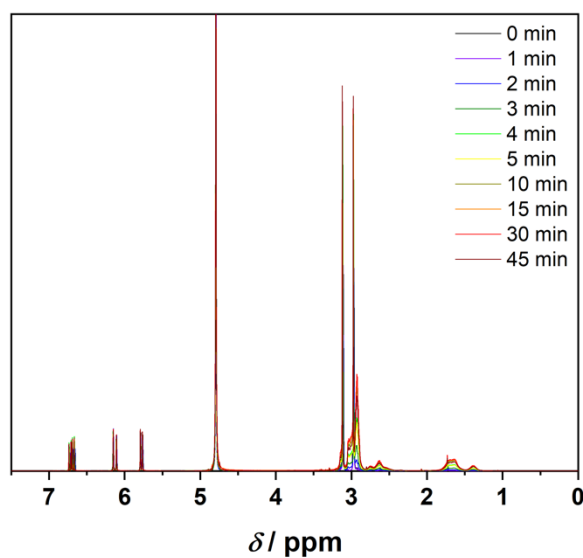


**Figure 10.11:** Superimposed <sup>1</sup>H-NMR spectra of solutions with 4.04 mol L<sup>-1</sup> DMA, 9 mmol L<sup>-1</sup> AIBN, 50  $\mu$ L AuNR and 10<sup>-2</sup> mol L<sup>-1</sup> CTA, dissolved in D<sub>2</sub>O, irradiated with 25 GW cm<sup>-2</sup> at 800 nm for various times: (black) without irradiation – 0 min, (violet) 1 min, (blue) 2 min, (dark green) 3 min, (pale green) 4 min, (yellow) 5 min, (pale orange) 10 min, (orange) 15 min, (red) 30 min, (dark red) 45 min.

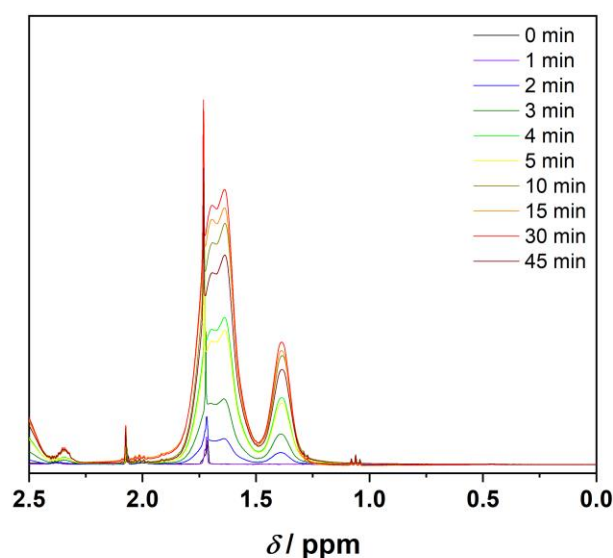


**Figure 10.12:** Superimposed <sup>1</sup>H NMR spectra of solutions with 4.04 mmol L<sup>-1</sup> DMA, 9 mmol L<sup>-1</sup> AIBN, 50 μL AuNR and 10<sup>-2</sup> mol L<sup>-1</sup> CTA, dissolved in D<sub>2</sub>O, irradiated with 25 GW cm<sup>-2</sup> at 800 nm for various times, zoomed into the regions of resonance associated with the polymer between 1 – 2 ppm: (black) without irradiation – 0 min, (violet) 1 min, (blue) 2 min, (dark green) 3 min, (pale green) 4 min, (yellow) 5 min, (pale orange) 10 min, (orange) 15 min, (red) 30 min, (dark red) 45 min.

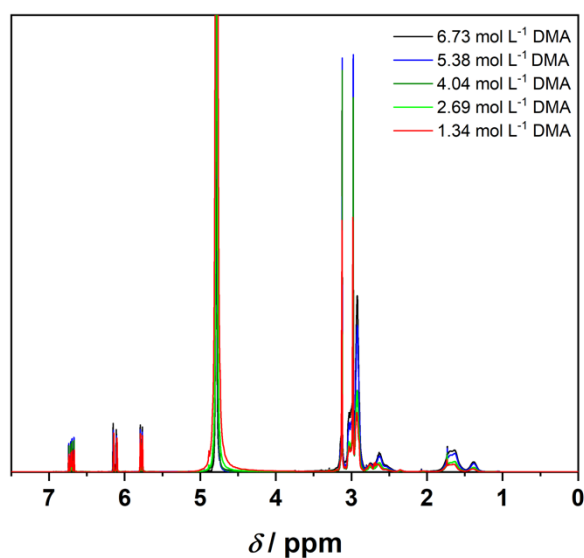


**Figure 10.13:** Superimposed <sup>1</sup>H-NMR spectra of solutions with 50 μL AuNR, 9 mmol L<sup>-1</sup> AIBN, 10<sup>-2</sup> mol L<sup>-1</sup> CTA and various monomer concentrations, irradiated with 25 GW cm<sup>-2</sup> at 800 nm for 30 min, dissolved in D<sub>2</sub>O: (black) 6.73 mol L<sup>-1</sup> DMA, (blue) 5.38 mol L<sup>-1</sup> DMA, (green) 4.04 mol L<sup>-1</sup> DMA, (yellow) 2.69 mol L<sup>-1</sup> DMA, (red) 1.34 mol L<sup>-1</sup> DMA.

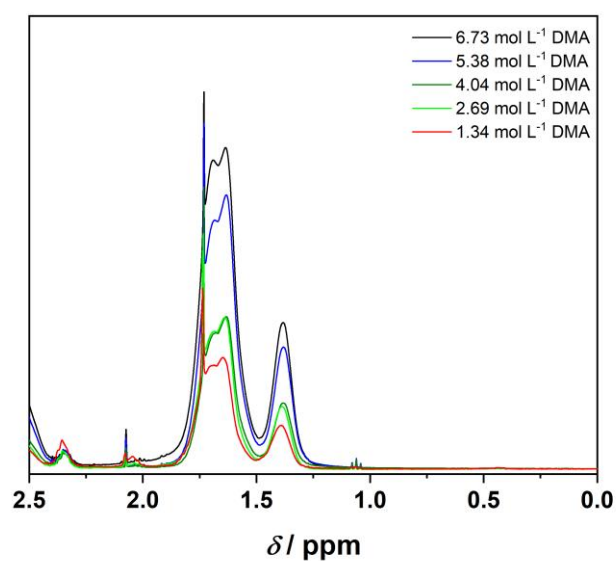


**Figure 10.14:** Superimposed <sup>1</sup>H-NMR spectra of solutions with 50  $\mu\text{L}$  AuNR, 9  $\text{mmol L}^{-1}$  AIBN,  $10^{-2}$   $\text{mol L}^{-1}$  CTA and various monomer concentrations, irradiated with  $25 \text{ GW cm}^{-2}$  at 800 nm for 30 min, dissolved in  $\text{D}_2\text{O}$ , zoomed into polymer peak between 1 – 2 ppm: (black) 6.73  $\text{mol L}^{-1}$  DMA, (blue) 5.38  $\text{mol L}^{-1}$  DMA, (green) 4.04  $\text{mol L}^{-1}$  DMA, (yellow) 2.69  $\text{mol L}^{-1}$  DMA, (red) 1.34  $\text{mol L}^{-1}$  DMA.

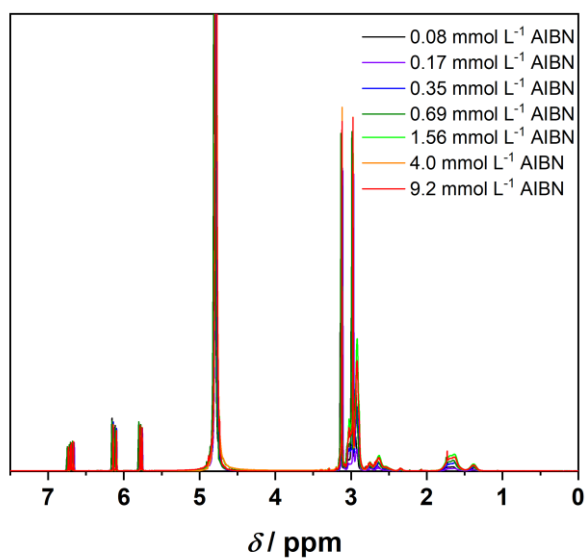


**Figure 10.15:** Superimposed <sup>1</sup>H-NMR spectra of solutions with 50  $\mu\text{L}$  AuNR, 6.73  $\text{mol L}^{-1}$  DMA,  $10^{-2}$   $\text{mol L}^{-1}$  CTA and various AIBN concentrations, irradiated with  $25 \text{ GW cm}^{-2}$  at 800 nm for 30 min, dissolved in  $\text{D}_2\text{O}$ : (black) 0.08  $\text{mol L}^{-1}$  AIBN, (violet) 0.17  $\text{mol L}^{-1}$  AIBN, (blue) 0.35  $\text{mol L}^{-1}$  AIBN, (dark green) 0.69  $\text{mol L}^{-1}$  AIBN, (yellow) 1.56  $\text{mol L}^{-1}$  AIBN, (orange) 4  $\text{mol L}^{-1}$  AIBN, (red) 9.2  $\text{mol L}^{-1}$  AIBN.

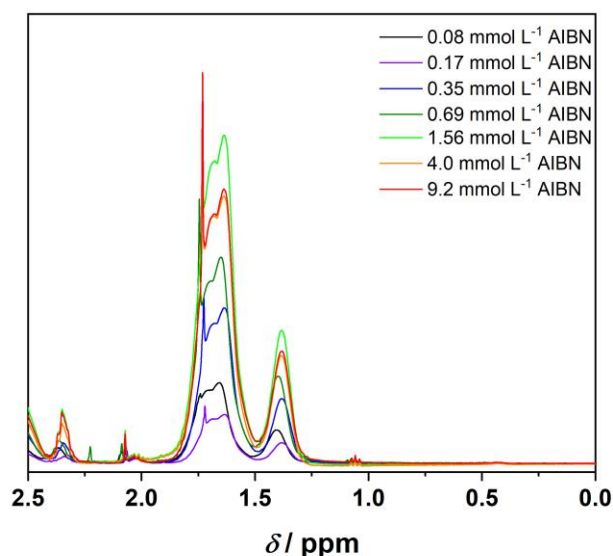


**Figure 10.16:** Superimposed  $^1\text{H-NMR}$  spectra of solutions with  $50 \mu\text{L}$  AuNR,  $6.73 \text{ mol L}^{-1}$  DMA,  $10^{-2} \text{ mol L}^{-1}$  CTA and various AIBN concentrations, irradiated with  $25 \text{ GW cm}^{-2}$  at  $800 \text{ nm}$  for  $30 \text{ min}$  dissolved in  $\text{D}_2\text{O}$ , zoomed into polymer peak between  $1 - 2 \text{ ppm}$ : (black)  $0.08 \text{ mol L}^{-1}$  AIBN, (violet)  $0.17 \text{ mol L}^{-1}$  AIBN, (blue)  $0.35 \text{ mol L}^{-1}$  AIBN, (dark green)  $0.69 \text{ mol L}^{-1}$  AIBN, (yellow)  $1.56 \text{ mol L}^{-1}$  AIBN, (orange)  $4 \text{ mol L}^{-1}$  AIBN, (red)  $9.2 \text{ mol L}^{-1}$  AIBN.

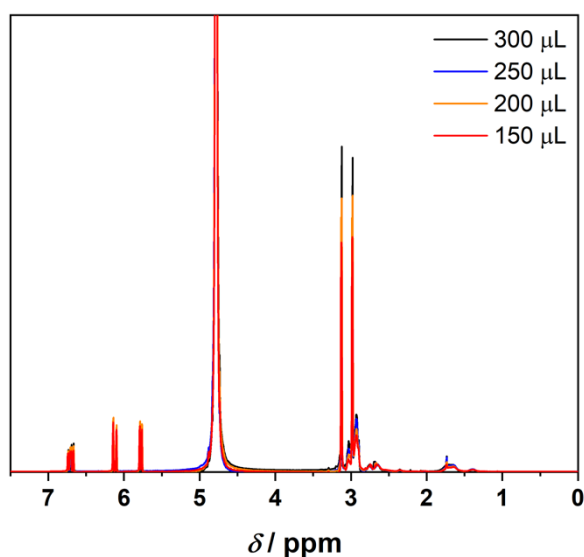


**Figure 10.17:** Superimposed  $^1\text{H-NMR}$  spectra of solutions with  $0.69 \text{ mol L}^{-1}$  DMA,  $9 \text{ mmol L}^{-1}$  AIBN  $10^{-2} \text{ mol L}^{-1}$  CTA and various AuNR concentrations, irradiated with  $25 \text{ GW cm}^{-2}$  at  $800 \text{ nm}$  for  $30 \text{ min}$ , dissolved in  $\text{D}_2\text{O}$ : (black)  $300 \mu\text{L}$  AuNR, (blue)  $250 \mu\text{L}$  AuNR, (yellow)  $200 \mu\text{L}$  AuNR, (red)  $150 \mu\text{L}$  AuNR.

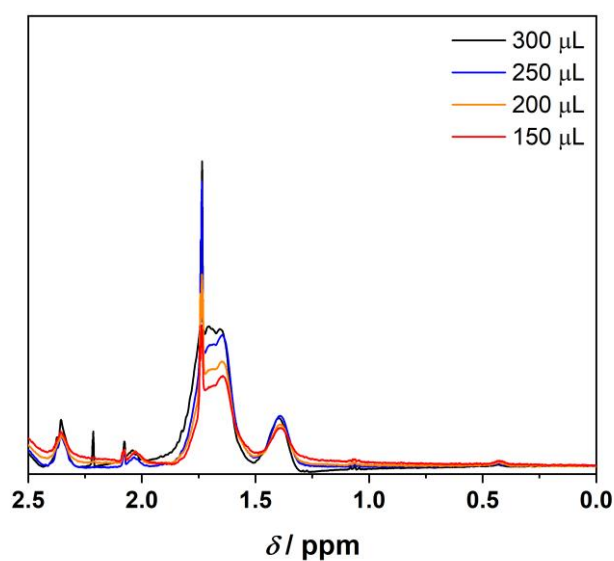


**Figure 10.18:** Superimposed <sup>1</sup>H-NMR spectra of solutions with 0.69 mol L<sup>-1</sup> DMA, 9 mmol L<sup>-1</sup> AIBN 10<sup>-2</sup> mol L<sup>-1</sup> CTA and various AuNR concentrations, irradiated with 25 GW cm<sup>-2</sup> at 800 nm for 30 min, dissolved in D<sub>2</sub>O, zoomed into polymer peak between 1 – 2 ppm: (black) 300 μL AuNR, (blue) 250 μL AuNR, (yellow) 200 μL AuNR, (red) 150 μL AuNR.

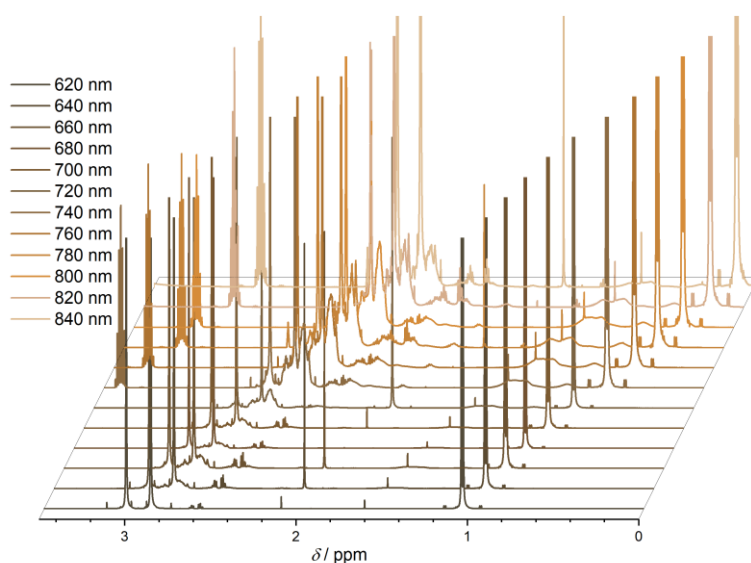


**Figure 10.19:** Stacked <sup>1</sup>H-NMR spectra of solution with 4.85 mol L<sup>-1</sup> DMA, 0.01 mol L<sup>-1</sup> AIBN, 3.53 mol L<sup>-1</sup> isopropanol, 75 μL AuNR and 10 μL (0.38 mol L<sup>-1</sup>) CTA, irradiated with 10 ns pulses for 15 min, with (from dark to pale): 335 μJ at 620 nm, 325 μJ at 640 nm, 315 μJ at 660 nm, 306 μJ at 680 nm, 297 μJ at 700 nm, 289 μJ at 720 nm, 281 μJ at 740 nm, 274 μJ at 760 nm, 267 μJ at 780 nm, 260 μJ at 800 nm, 254 μJ at 820 nm and 248 μJ at 840 nm.

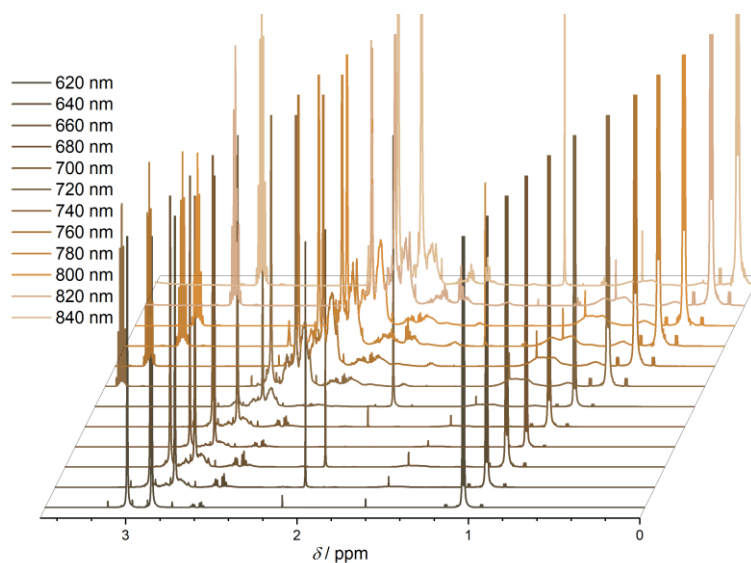


**Figure 10.20:** Stacked  $^1\text{H}$ -NMR spectra of solution with  $4.85 \text{ mol L}^{-1}$  DMA,  $0.01 \text{ mol L}^{-1}$  AIBN,  $3.53 \text{ mol L}^{-1}$  isopropanol,  $75 \mu\text{L}$  AuNR and  $10 \mu\text{L}$  ( $0.38 \text{ mol L}^{-1}$ ) CTA, irradiated with 10 ns pulses for 15 min, with (from dark to pale):  $335 \mu\text{J}$  at 620 nm,  $325 \mu\text{J}$  at 640 nm,  $315 \mu\text{J}$  at 660 nm,  $306 \mu\text{J}$  at 680 nm,  $297 \mu\text{J}$  at 700 nm,  $289 \mu\text{J}$  at 720 nm,  $281 \mu\text{J}$  at 740 nm,  $274 \mu\text{J}$  at 760 nm,  $267 \mu\text{J}$  at 780 nm,  $260 \mu\text{J}$  at 800 nm,  $254 \mu\text{J}$  at 820 nm and  $248 \mu\text{J}$  at 840 nm. Zoom into region 0-3.5 ppm.

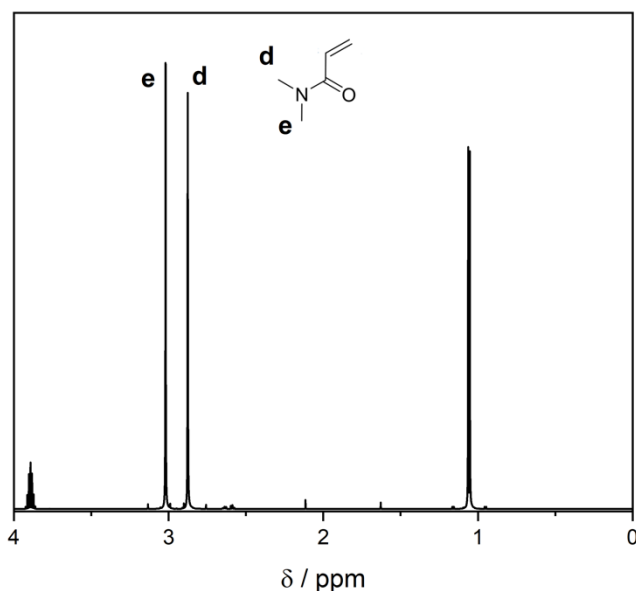


**Figure 10.21:**  $^1\text{H}$ -NMR spectra of solutions with  $4.85 \text{ mol L}^{-1}$  DMA,  $0.01 \text{ mol L}^{-1}$  AIBN,  $3.53 \text{ mol L}^{-1}$  isopropanol,  $75 \mu\text{L}$  AuNR and  $10 \mu\text{L}$  CTA, dissolved in  $\text{D}_2\text{O}$ , irradiated with 620 nm ns laser pulses with  $0.87 \text{ J cm}^{-2}$  at a repetition rate of 20 Hz for 15 min.

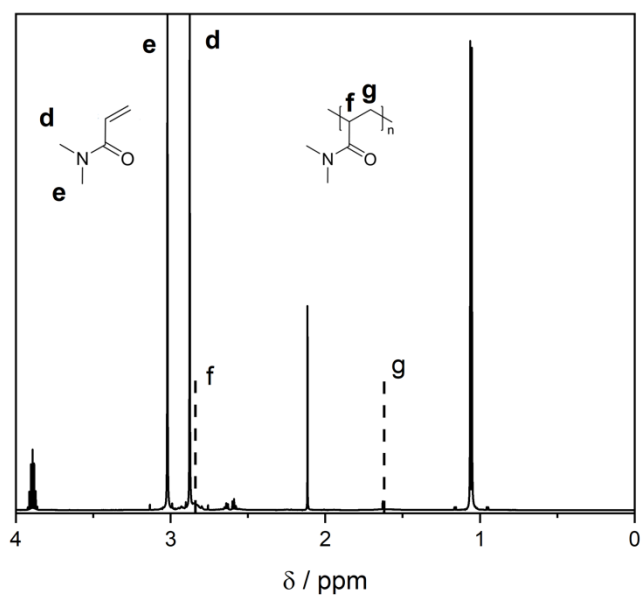


**Figure 10.22:**  $^1\text{H-NMR}$  spectra of solutions with  $4.85 \text{ mol L}^{-1}$  DMA,  $0.01 \text{ mol L}^{-1}$  AIBN,  $3.53 \text{ mol L}^{-1}$  isopropanol,  $75 \mu\text{L AuNR}$  and  $10 \mu\text{L CTA}$ , dissolved in  $\text{D}_2\text{O}$ , irradiated with  $640 \text{ nm ns}$  laser pulses with  $0.84 \text{ J cm}^{-2}$  at a repetition rate of  $20 \text{ Hz}$  for  $15 \text{ min}$ .

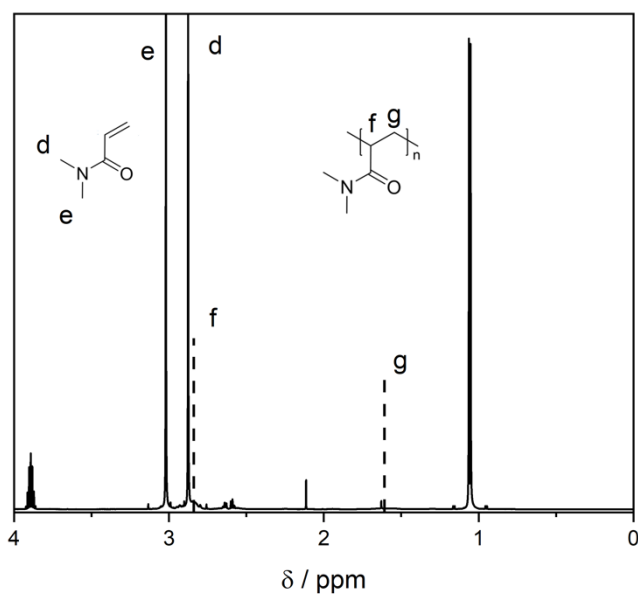


**Figure 10.23:**  $^1\text{H-NMR}$  spectra of solutions with  $4.85 \text{ mol L}^{-1}$  DMA,  $0.01 \text{ mol L}^{-1}$  AIBN,  $3.53 \text{ mol L}^{-1}$  isopropanol,  $75 \mu\text{L AuNR}$  and  $10 \mu\text{L CTA}$ , dissolved in  $\text{D}_2\text{O}$ , irradiated with  $640 \text{ nm ns}$  pulses with  $0.84 \text{ J cm}^{-2}$  at a repetition rate of  $20 \text{ Hz}$  for  $15 \text{ min}$ .

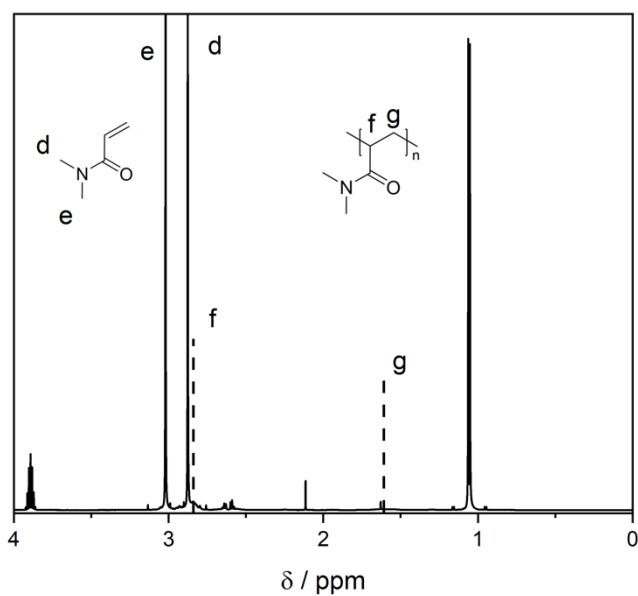


**Figure 10.24:** <sup>1</sup>H-NMR spectra of solutions with 4.85 mol L<sup>-1</sup> DMA, 0.01 mol L<sup>-1</sup> AIBN, 3.53 mol L<sup>-1</sup> isopropanol, 75  $\mu$ L AuNR and 10  $\mu$ L CTA, dissolved in D<sub>2</sub>O, irradiated with 660 nm ns pulses with 0.81 J cm<sup>-2</sup> at a repetition rate of 20 Hz for 15 min.

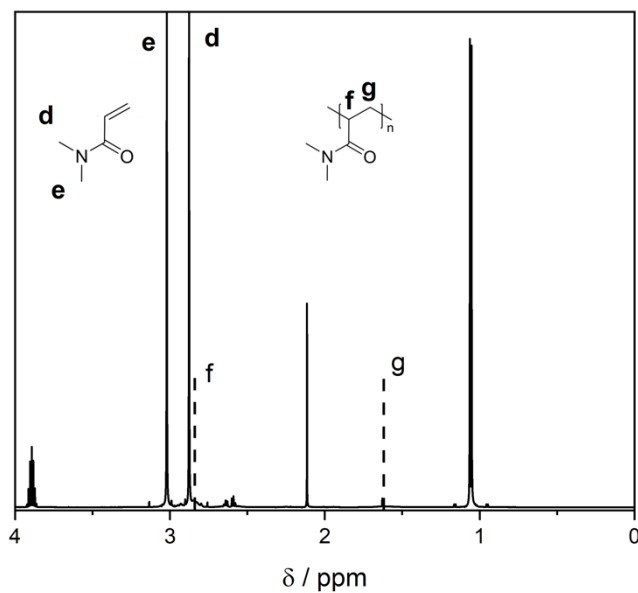


**Figure 10.25:** <sup>1</sup>H-NMR spectra of solutions with 4.85 mol L<sup>-1</sup> DMA, 0.01 mol L<sup>-1</sup> AIBN, 3.53 mol L<sup>-1</sup> isopropanol, 75  $\mu$ L AuNR and 10  $\mu$ L CTA, dissolved in D<sub>2</sub>O, irradiated with 660 nm ns pulses with 0.81 J cm<sup>-2</sup> at a repetition rate of 20 Hz for 15 min.

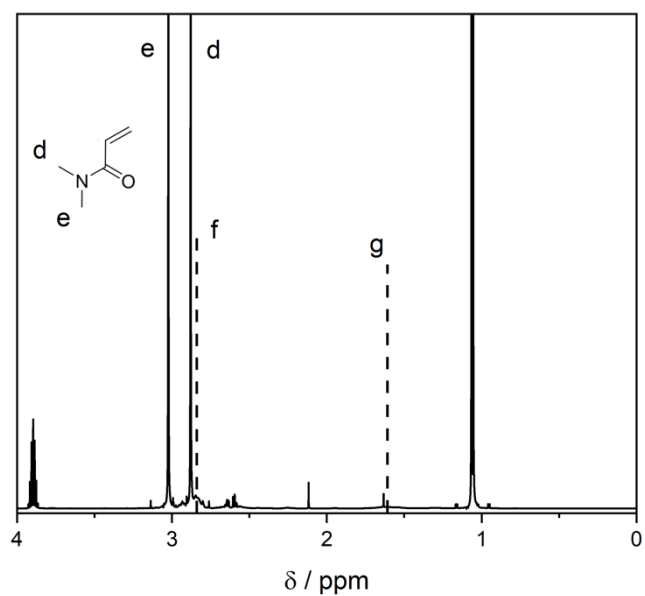


**Figure 10.26:**  $^1\text{H}$ -NMR spectra of solutions with  $4.85 \text{ mol L}^{-1}$  DMA,  $0.01 \text{ mol L}^{-1}$  AIBN,  $3.53 \text{ mol L}^{-1}$  isopropanol,  $75 \mu\text{L}$  AuNR and  $10 \mu\text{L}$  CTA, dissolved in  $\text{D}_2\text{O}$ , irradiated with  $680 \text{ nm}$  ns pulses with  $0.79 \text{ J cm}^{-2}$  at a repetition rate of  $20 \text{ Hz}$  for  $15 \text{ min}$ .

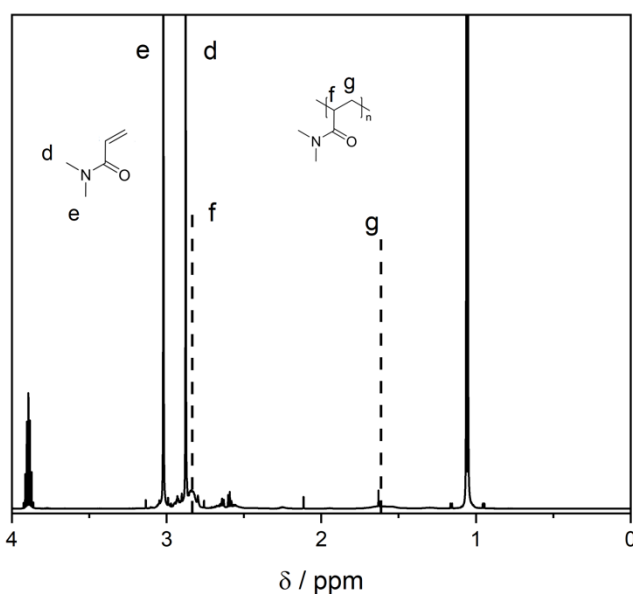


**Figure 10.27:**  $^1\text{H}$ -NMR spectra of solutions with  $4.85 \text{ mol L}^{-1}$  DMA,  $0.01 \text{ mol L}^{-1}$  AIBN,  $3.53 \text{ mol L}^{-1}$  isopropanol,  $75 \mu\text{L}$  AuNR and  $10 \mu\text{L}$  CTA, dissolved in  $\text{D}_2\text{O}$ , irradiated with  $680 \text{ nm}$  ns pulses with  $0.79 \text{ J cm}^{-2}$  at a repetition rate of  $20 \text{ Hz}$  for  $15 \text{ min}$ .

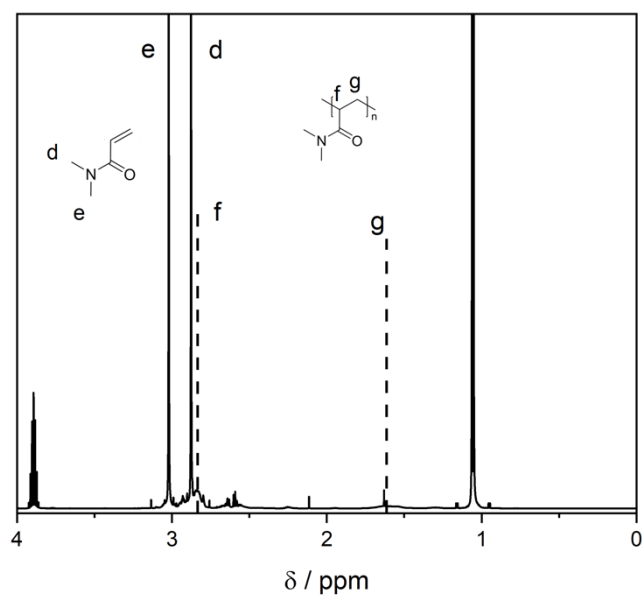


**Figure 10.28:** <sup>1</sup>H-NMR spectra of solutions with 4.85 mol L<sup>-1</sup> DMA, 0.01 mol L<sup>-1</sup> AIBN, 3.53 mol L<sup>-1</sup> isopropanol, 75  $\mu$ L AuNR and 10  $\mu$ L CTA, dissolved in D<sub>2</sub>O, irradiated with 700 nm ns pulses with 0.77 J cm<sup>-2</sup> at a repetition rate of 20 Hz for 15 min.

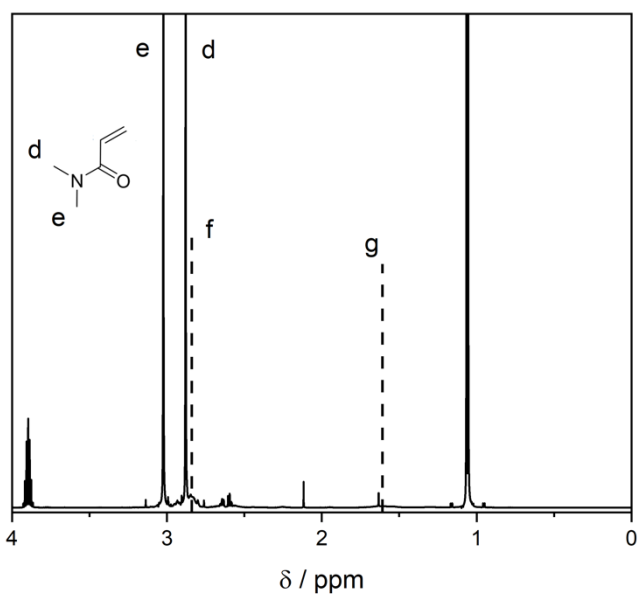


**Figure 10.29:** <sup>1</sup>H-NMR spectra of solutions with 4.85 mol L<sup>-1</sup> DMA, 0.01 mol L<sup>-1</sup> AIBN, 3.53 mol L<sup>-1</sup> isopropanol, 75  $\mu$ L AuNR and 10  $\mu$ L CTA, dissolved in D<sub>2</sub>O, irradiated with 700 nm ns pulses with 0.77 J cm<sup>-2</sup> at a repetition rate of 20 Hz for 15 min.

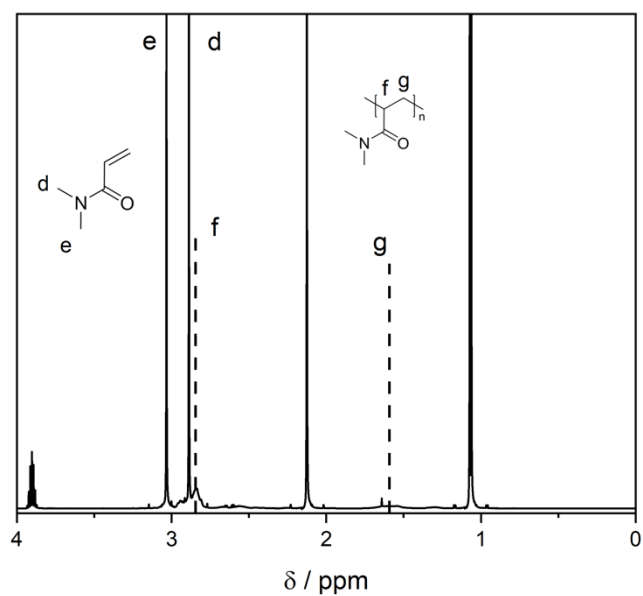


**Figure 10.30:**  $^1\text{H-NMR}$  spectra of solutions with  $4.85 \text{ mol L}^{-1}$  DMA,  $0.01 \text{ mol L}^{-1}$  AIBN,  $3.53 \text{ mol L}^{-1}$  isopropanol,  $75 \mu\text{L}$  AuNR and  $10 \mu\text{L}$  CTA, dissolved in  $\text{D}_2\text{O}$ , irradiated with  $720 \text{ nm}$  ns pulses with  $0.75 \text{ J cm}^{-2}$  at a repetition rate of  $20 \text{ Hz}$  for  $15 \text{ min}$ .

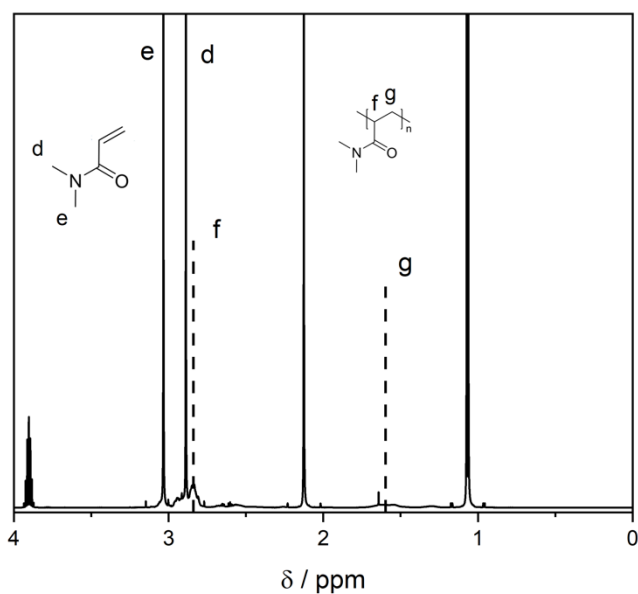


**Figure 10.31:**  $^1\text{H-NMR}$  spectra of solutions with  $4.85 \text{ mol L}^{-1}$  DMA,  $0.01 \text{ mol L}^{-1}$  AIBN,  $3.53 \text{ mol L}^{-1}$  isopropanol,  $75 \mu\text{L}$  AuNR and  $10 \mu\text{L}$  CTA, dissolved in  $\text{D}_2\text{O}$ , irradiated with  $720 \text{ nm}$  ns pulses with  $0.75 \text{ J cm}^{-2}$  at a repetition rate of  $20 \text{ Hz}$  for  $15 \text{ min}$ .

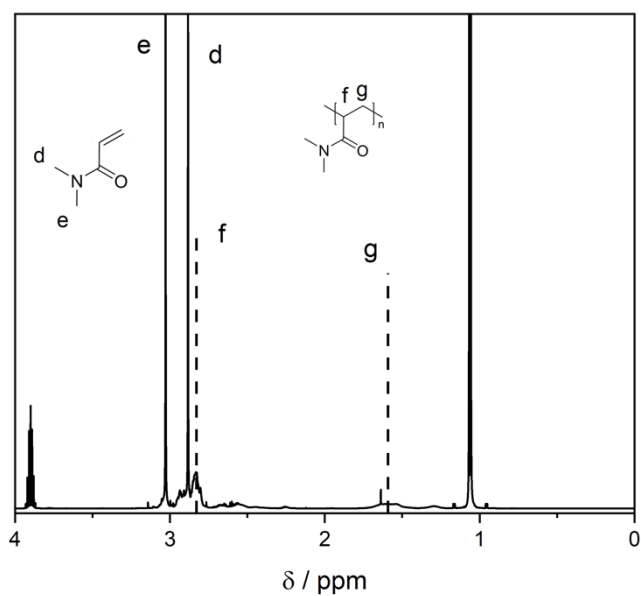


**Figure 10.32:**  $^1\text{H}$ -NMR spectra of solutions with  $4.85 \text{ mol L}^{-1}$  DMA,  $0.01 \text{ mol L}^{-1}$  AIBN,  $3.53 \text{ mol L}^{-1}$  isopropanol,  $75 \mu\text{L}$  AuNR and  $10 \mu\text{L}$  CTA, dissolved in  $\text{D}_2\text{O}$ , irradiated with  $720 \text{ nm}$  ns pulses with  $0.75 \text{ J cm}^{-2}$  at a repetition rate of  $20 \text{ Hz}$  for  $15 \text{ min}$ .

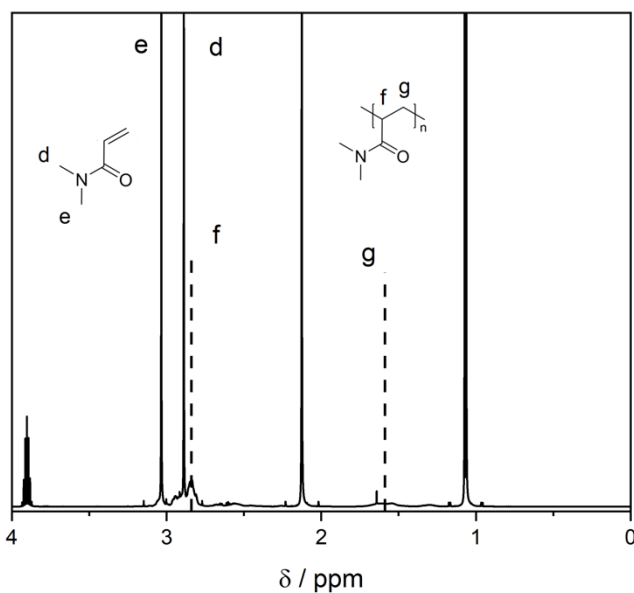


**Figure 10.33:**  $^1\text{H}$ -NMR spectra of solutions with  $4.85 \text{ mol L}^{-1}$  DMA,  $0.01 \text{ mol L}^{-1}$  AIBN,  $3.53 \text{ mol L}^{-1}$  isopropanol,  $75 \mu\text{L}$  AuNR and  $10 \mu\text{L}$  CTA, dissolved in  $\text{D}_2\text{O}$ , irradiated with  $740 \text{ nm}$  ns pulses with  $0.73 \text{ J cm}^{-2}$  at a repetition rate of  $20 \text{ Hz}$  for  $15 \text{ min}$ .

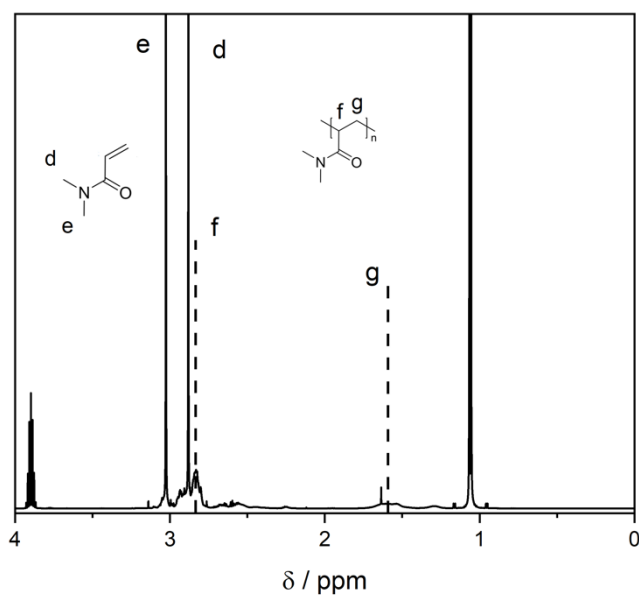


**Figure 10.34:**  $^1\text{H-NMR}$  spectra of solutions with  $4.85 \text{ mol L}^{-1}$  DMA,  $0.01 \text{ mol L}^{-1}$  AIBN,  $3.53 \text{ mol L}^{-1}$  isopropanol,  $75 \mu\text{L}$  AuNR and  $10 \mu\text{L}$  CTA, dissolved in  $\text{D}_2\text{O}$ , irradiated with  $740 \text{ nm}$  ns pulses with  $0.73 \text{ J cm}^{-2}$  at a repetition rate of  $20 \text{ Hz}$  for  $15 \text{ min}$ .

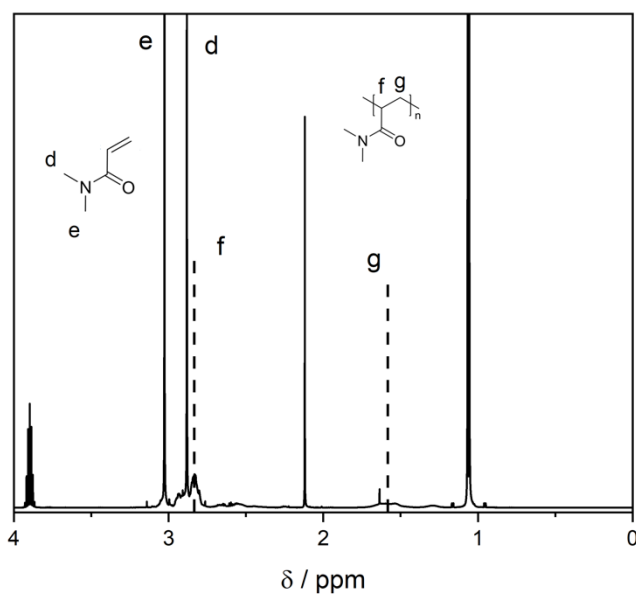


**Figure 10.35:**  $^1\text{H-NMR}$  spectra of solutions with  $4.85 \text{ mol L}^{-1}$  DMA,  $0.01 \text{ mol L}^{-1}$  AIBN,  $3.53 \text{ mol L}^{-1}$  isopropanol,  $75 \mu\text{L}$  AuNR and  $10 \mu\text{L}$  CTA, dissolved in  $\text{D}_2\text{O}$ , irradiated with  $740 \text{ nm}$  ns pulses with  $0.73 \text{ J cm}^{-2}$  at a repetition rate of  $20 \text{ Hz}$  for  $15 \text{ min}$ .

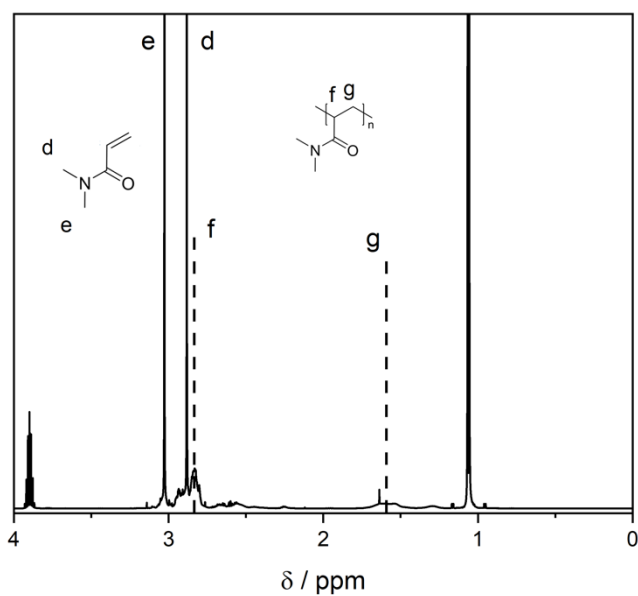


**Figure 10.36:**  $^1\text{H-NMR}$  spectra of solutions with  $4.85 \text{ mol L}^{-1}$  DMA,  $0.01 \text{ mol L}^{-1}$  AIBN,  $3.53 \text{ mol L}^{-1}$  isopropanol,  $75 \mu\text{L}$  AuNR and  $10 \mu\text{L}$  CTA, dissolved in  $\text{D}_2\text{O}$ , irradiated with  $760 \text{ nm}$  ns pulses with  $0.71 \text{ J cm}^{-2}$  at a repetition rate of  $20 \text{ Hz}$  for  $15 \text{ min}$ .

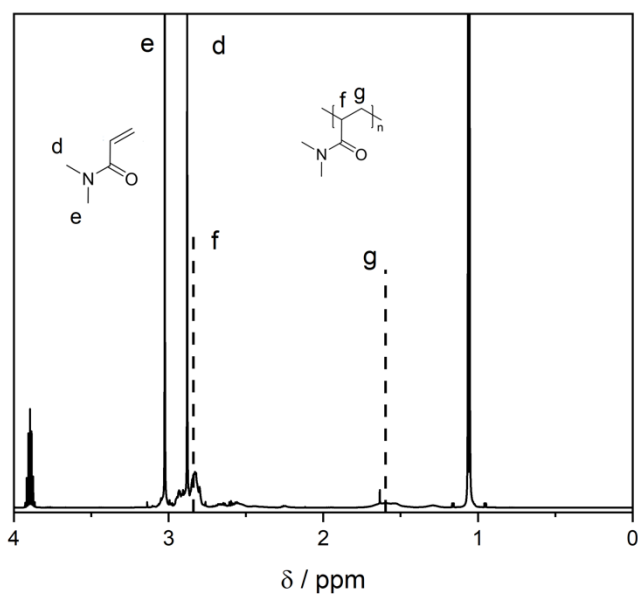


**Figure 10.37:**  $^1\text{H-NMR}$  spectra of solutions with  $4.85 \text{ mol L}^{-1}$  DMA,  $0.01 \text{ mol L}^{-1}$  AIBN,  $3.53 \text{ mol L}^{-1}$  isopropanol,  $75 \mu\text{L}$  AuNR and  $10 \mu\text{L}$  CTA, dissolved in  $\text{D}_2\text{O}$ , irradiated with  $760 \text{ nm}$  ns pulses with  $0.71 \text{ J cm}^{-2}$  at a repetition rate of  $20 \text{ Hz}$  for  $15 \text{ min}$ .

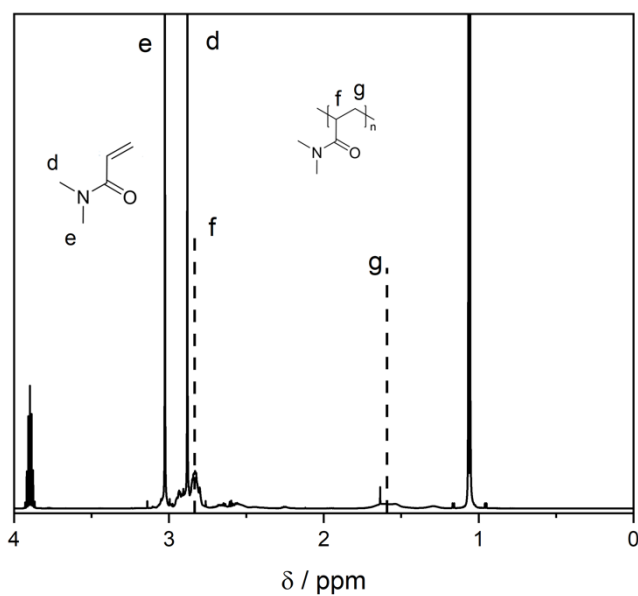


**Figure 10.38:**  $^1\text{H-NMR}$  spectra of solutions with  $4.85 \text{ mol L}^{-1}$  DMA,  $0.01 \text{ mol L}^{-1}$  AIBN,  $3.53 \text{ mol L}^{-1}$  isopropanol,  $75 \mu\text{L AuNR}$  and  $10 \mu\text{L CTA}$ , dissolved in  $\text{D}_2\text{O}$ , irradiated with  $760 \text{ nm ns}$  pulses with  $0.71 \text{ J cm}^{-2}$  at a repetition rate of  $20 \text{ Hz}$  for  $15 \text{ min}$ .

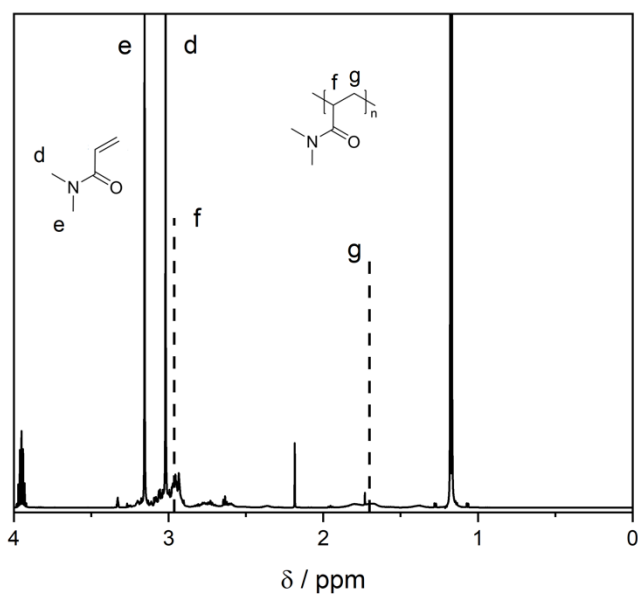


**Figure 10.39:**  $^1\text{H-NMR}$  spectra of solutions with  $4.85 \text{ mol L}^{-1}$  DMA,  $0.01 \text{ mol L}^{-1}$  AIBN,  $3.53 \text{ mol L}^{-1}$  isopropanol,  $75 \mu\text{L AuNR}$  and  $10 \mu\text{L CTA}$ , dissolved in  $\text{D}_2\text{O}$ , irradiated with  $780 \text{ nm ns}$  pulses with  $0.69 \text{ J cm}^{-2}$  at a repetition rate of  $20 \text{ Hz}$  for  $15 \text{ min}$ .

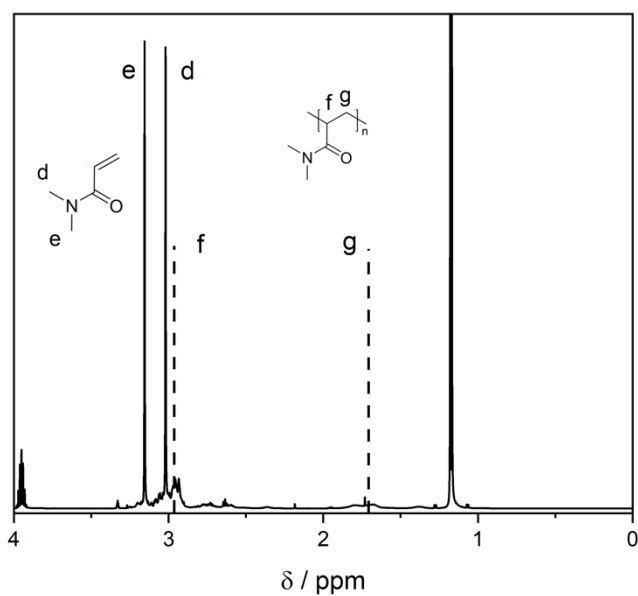


**Figure 10.40:**  $^1\text{H-NMR}$  spectra of solutions with  $4.85 \text{ mol L}^{-1}$  DMA,  $0.01 \text{ mol L}^{-1}$  AIBN,  $3.53 \text{ mol L}^{-1}$  isopropanol,  $75 \mu\text{L}$  AuNR and  $10 \mu\text{L}$  CTA, dissolved in  $\text{D}_2\text{O}$ , irradiated with  $780 \text{ nm}$  ns pulses with  $0.69 \text{ J cm}^{-2}$  at a repetition rate of  $20 \text{ Hz}$  for  $15 \text{ min}$ .

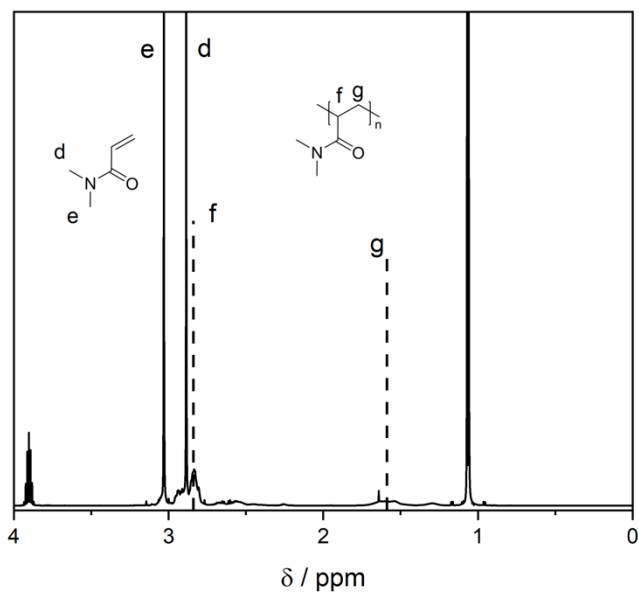


**Figure 10.41:**  $^1\text{H-NMR}$  spectra of solutions with  $4.85 \text{ mol L}^{-1}$  DMA,  $0.01 \text{ mol L}^{-1}$  AIBN,  $3.53 \text{ mol L}^{-1}$  isopropanol,  $75 \mu\text{L}$  AuNR and  $10 \mu\text{L}$  CTA, dissolved in  $\text{D}_2\text{O}$ , irradiated with  $780 \text{ nm}$  ns pulses with  $0.69 \text{ J cm}^{-2}$  at a repetition rate of  $20 \text{ Hz}$  for  $15 \text{ min}$ .

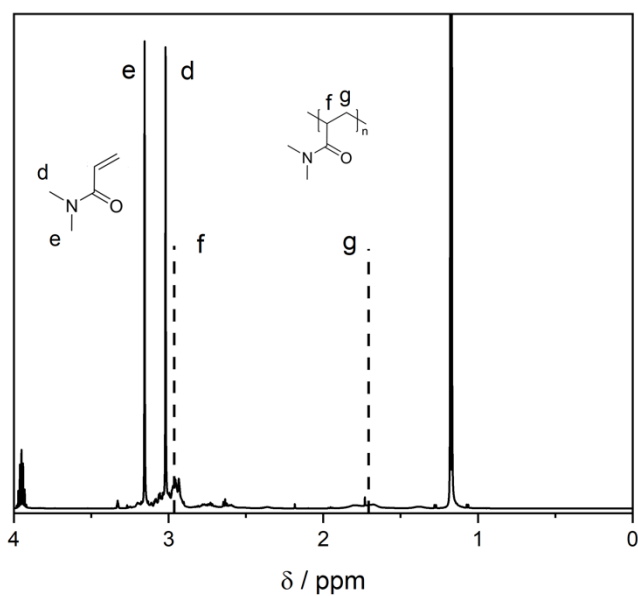


**Figure 10.42:**  $^1\text{H-NMR}$  spectra of solutions with  $4.85 \text{ mol L}^{-1}$  DMA,  $0.01 \text{ mol L}^{-1}$  AIBN,  $3.53 \text{ mol L}^{-1}$  isopropanol,  $75 \mu\text{L}$  AuNR and  $10 \mu\text{L}$  CTA, dissolved in  $\text{D}_2\text{O}$ , irradiated with  $800 \text{ nm}$  ns pulses with  $0.67 \text{ J cm}^{-2}$  at a repetition rate of  $20 \text{ Hz}$  for  $15 \text{ min}$ .

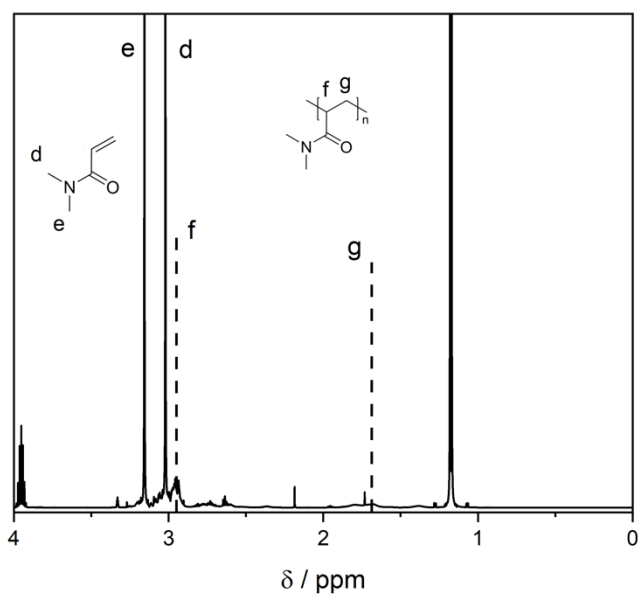


**Figure 10.43:**  $^1\text{H-NMR}$  spectra of solutions with  $4.85 \text{ mol L}^{-1}$  DMA,  $0.01 \text{ mol L}^{-1}$  AIBN,  $3.53 \text{ mol L}^{-1}$  isopropanol,  $75 \mu\text{L}$  AuNR and  $10 \mu\text{L}$  CTA, dissolved in  $\text{D}_2\text{O}$ , irradiated with  $800 \text{ nm}$  ns pulses with  $0.67 \text{ J cm}^{-2}$  at a repetition rate of  $20 \text{ Hz}$  for  $15 \text{ min}$ .

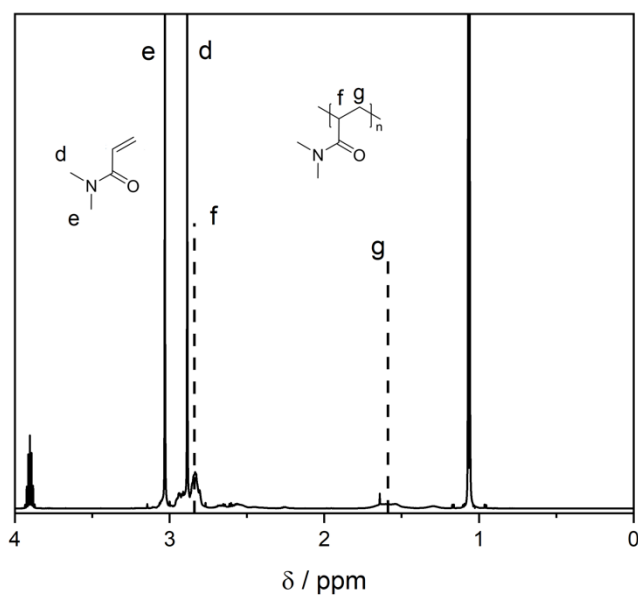


**Figure 10.44:**  $^1\text{H}$ -NMR spectra of solutions with  $4.85 \text{ mol L}^{-1}$  DMA,  $0.01 \text{ mol L}^{-1}$  AIBN,  $3.53 \text{ mol L}^{-1}$  isopropanol,  $75 \mu\text{L}$  AuNR and  $10 \mu\text{L}$  CTA, dissolved in  $\text{D}_2\text{O}$ , irradiated with  $800 \text{ nm}$  ns pulses with  $0.67 \text{ J cm}^{-2}$  at a repetition rate of  $20 \text{ Hz}$  for  $15 \text{ min}$ .

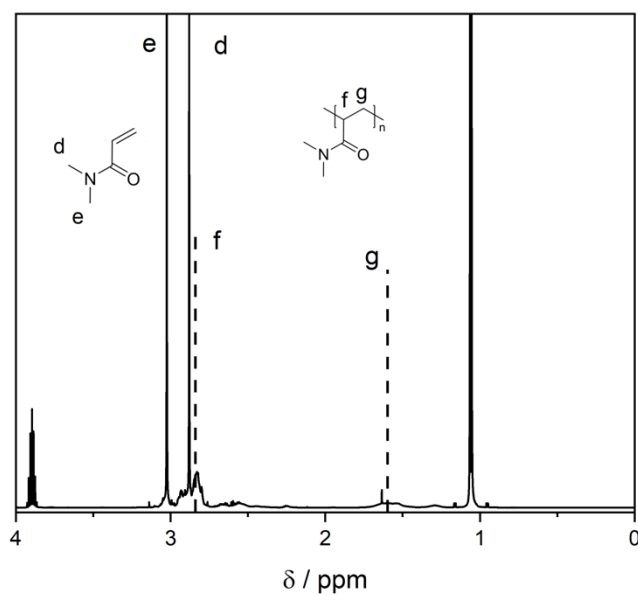


**Figure 10.45:**  $^1\text{H}$ -NMR spectra of solutions with  $4.85 \text{ mol L}^{-1}$  DMA,  $0.01 \text{ mol L}^{-1}$  AIBN,  $3.53 \text{ mol L}^{-1}$  isopropanol,  $75 \mu\text{L}$  AuNR and  $10 \mu\text{L}$  CTA, dissolved in  $\text{D}_2\text{O}$ , irradiated with  $820 \text{ nm}$  ns pulses with  $0.65 \text{ J cm}^{-2}$  at a repetition rate of  $20 \text{ Hz}$  for  $15 \text{ min}$ .

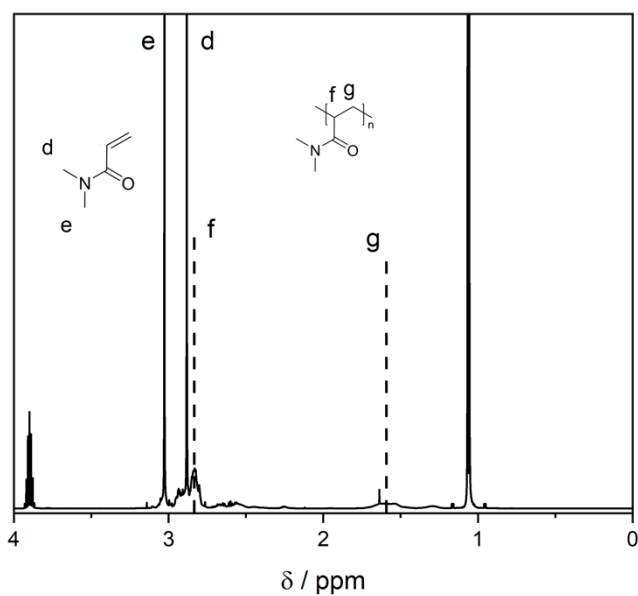


**Figure 10.46:**  $^1\text{H-NMR}$  spectra of solutions with  $4.85 \text{ mol L}^{-1}$  DMA,  $0.01 \text{ mol L}^{-1}$  AIBN,  $3.53 \text{ mol L}^{-1}$  isopropanol,  $75 \mu\text{L}$  AuNR and  $10 \mu\text{L}$  CTA, dissolved in  $\text{D}_2\text{O}$ , irradiated with  $820 \text{ nm}$  ns pulses with  $0.65 \text{ J cm}^{-2}$  at a repetition rate of  $20 \text{ Hz}$  for  $15 \text{ min}$ .

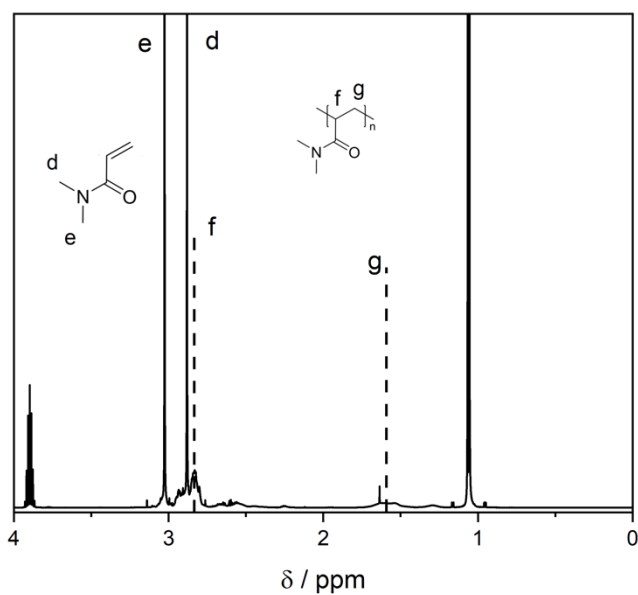


**Figure 10.47:**  $^1\text{H-NMR}$  spectra of solutions with  $4.85 \text{ mol L}^{-1}$  DMA,  $0.01 \text{ mol L}^{-1}$  AIBN,  $3.53 \text{ mol L}^{-1}$  isopropanol,  $75 \mu\text{L}$  AuNR and  $10 \mu\text{L}$  CTA, dissolved in  $\text{D}_2\text{O}$ , irradiated with  $820 \text{ nm}$  ns pulses with  $0.65 \text{ J cm}^{-2}$  at repetition rate of  $20 \text{ Hz}$  for  $15 \text{ min}$ .

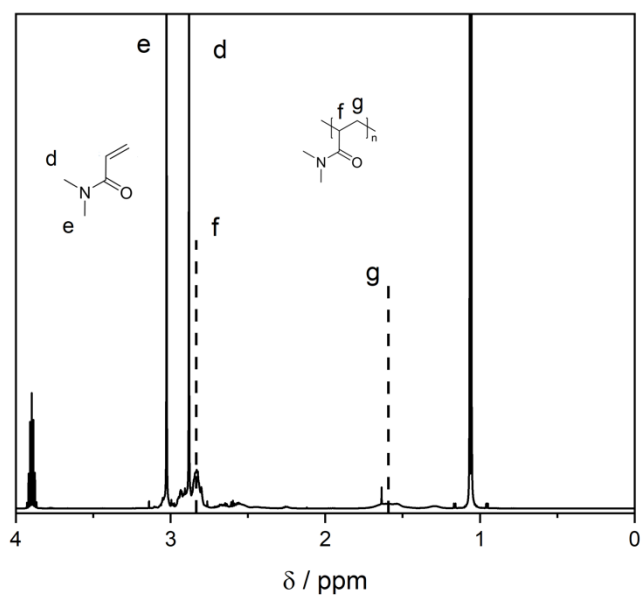


**Figure 10.48:**  $^1\text{H-NMR}$  spectra of solutions with  $4.85 \text{ mol L}^{-1}$  DMA,  $0.01 \text{ mol L}^{-1}$  AIBN,  $3.53 \text{ mol L}^{-1}$  isopropanol,  $75 \mu\text{L AuNR}$  and  $10 \mu\text{L CTA}$ , dissolved in  $\text{D}_2\text{O}$ , irradiated with  $840 \text{ nm ns}$  pulses with  $0.63 \text{ J cm}^{-2}$  at a repetition rate of  $20 \text{ Hz}$  for  $15 \text{ min}$ .

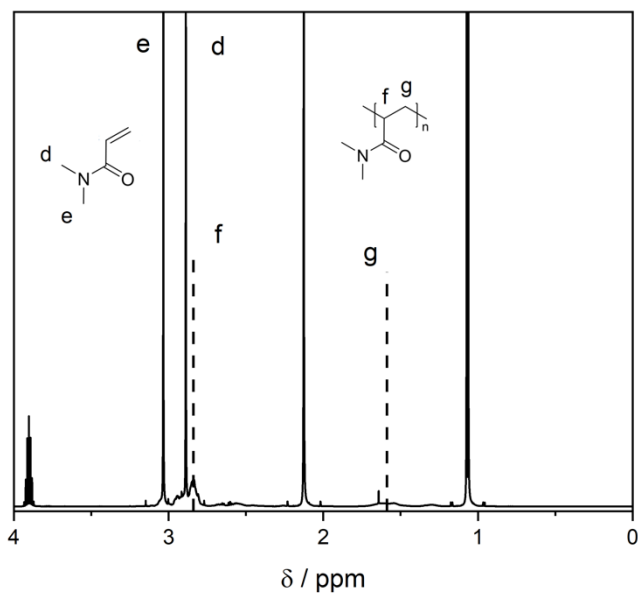


**Figure 10.49:**  $^1\text{H-NMR}$  spectra of solutions with  $4.85 \text{ mol L}^{-1}$  DMA,  $0.01 \text{ mol L}^{-1}$  AIBN,  $3.53 \text{ mol L}^{-1}$  isopropanol,  $75 \mu\text{L AuNR}$  and  $10 \mu\text{L CTA}$ , dissolved in  $\text{D}_2\text{O}$ , irradiated with  $840 \text{ nm ns}$  pulses with  $0.63 \text{ J cm}^{-2}$  at a repetition rate of  $20 \text{ Hz}$  for  $15 \text{ min}$ .

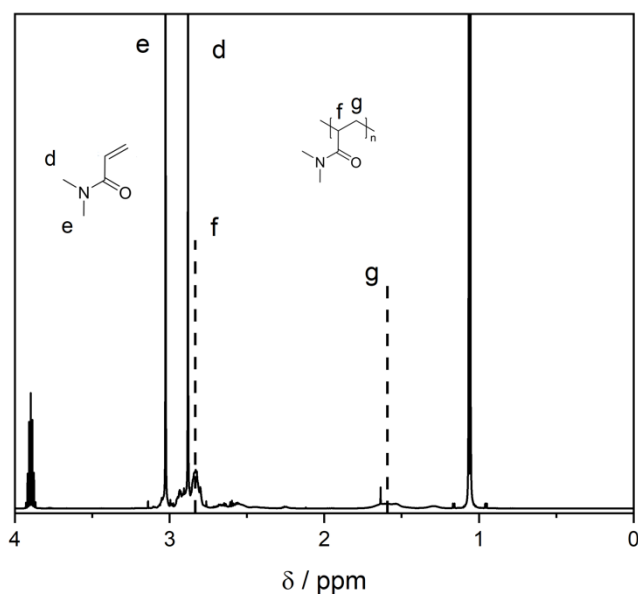


**Figure 10.50:**  $^1\text{H}$ -NMR spectra of solutions with  $4.85 \text{ mol L}^{-1}$  DMA,  $0.01 \text{ mol L}^{-1}$  AIBN,  $3.53 \text{ mol L}^{-1}$  isopropanol,  $75 \mu\text{L}$  AuNR and  $10 \mu\text{L}$  CTA, dissolved in  $\text{D}_2\text{O}$ , irradiated with  $840 \text{ nm}$  ns pulses with  $0.63 \text{ J cm}^{-2}$  at a repetition rate of  $20 \text{ Hz}$  for  $15 \text{ min}$ .

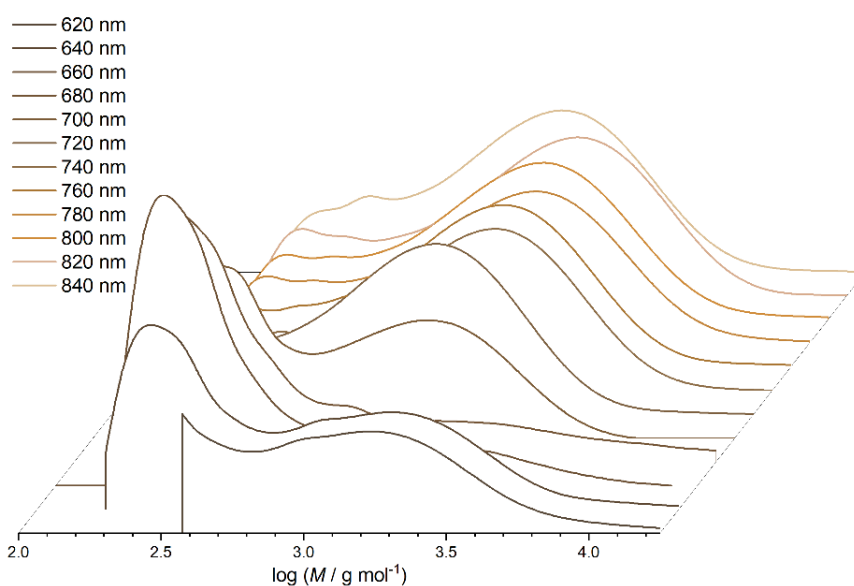


**Figure 10.51:** Stacked SEC traces of PDMA and DMA after  $15 \text{ min}$  irradiation of a solution with  $4.85 \text{ mol L}^{-1}$  DMA,  $3.53 \text{ mol L}^{-1}$  isopropanol,  $0.01 \text{ mol L}^{-1}$  AIBN,  $75 \mu\text{L}$  AuNR solution and  $10 \mu\text{L}$  3-mercaptopropionic acid with a  $10 \text{ ns}$  laser with (from dark to pale)  $335 \mu\text{J}$  at  $620 \text{ nm}$ ,  $325 \mu\text{J}$  at  $640 \text{ nm}$ ,  $315 \mu\text{J}$  at  $660 \text{ nm}$ ,  $306 \mu\text{J}$  at  $680 \text{ nm}$ ,  $297 \mu\text{J}$  at  $700 \text{ nm}$ ,  $289 \mu\text{J}$  at  $720 \text{ nm}$ ,  $281 \mu\text{J}$  at  $740 \text{ nm}$ ,  $274 \mu\text{J}$  at  $760 \text{ nm}$ ,  $267 \mu\text{J}$  at  $780 \text{ nm}$ ,  $260 \mu\text{J}$  at  $800 \text{ nm}$ ,  $254 \mu\text{J}$  at  $820 \text{ nm}$  and  $248 \mu\text{J}$  at  $840 \text{ nm}$ .

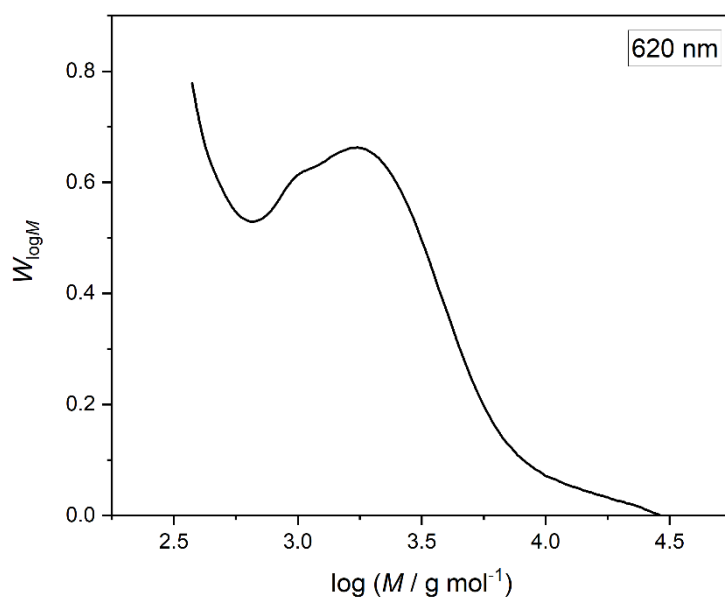


**Figure 10.52:** SEC trace of PDMA and DMA after 15 min irradiation of a solution with  $4.85 \text{ mol L}^{-1}$  DMA,  $3.53 \text{ mol L}^{-1}$  isopropanol,  $0.01 \text{ mol L}^{-1}$  AIBN,  $75 \mu\text{L}$  AuNR solution and  $10 \mu\text{L}$  3-mercaptopropionic acid with a ns laser at 620 nm.

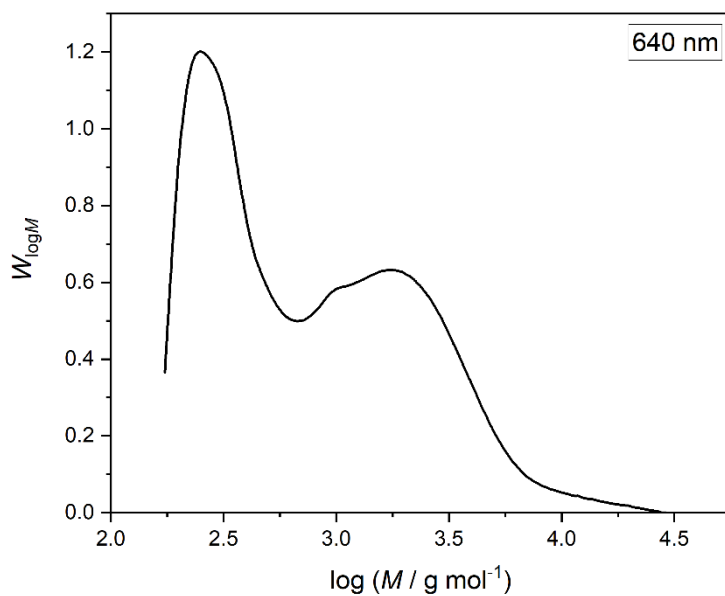


**Figure 10.53:** SEC trace of PDMA and DMA after 15 min irradiation of a solution with  $4.85 \text{ mol L}^{-1}$  DMA,  $3.53 \text{ mol L}^{-1}$  isopropanol,  $0.01 \text{ mol L}^{-1}$  AIBN,  $75 \mu\text{L}$  AuNR solution and  $10 \mu\text{L}$  3-mercaptopropionic acid with a ns laser at 640 nm.

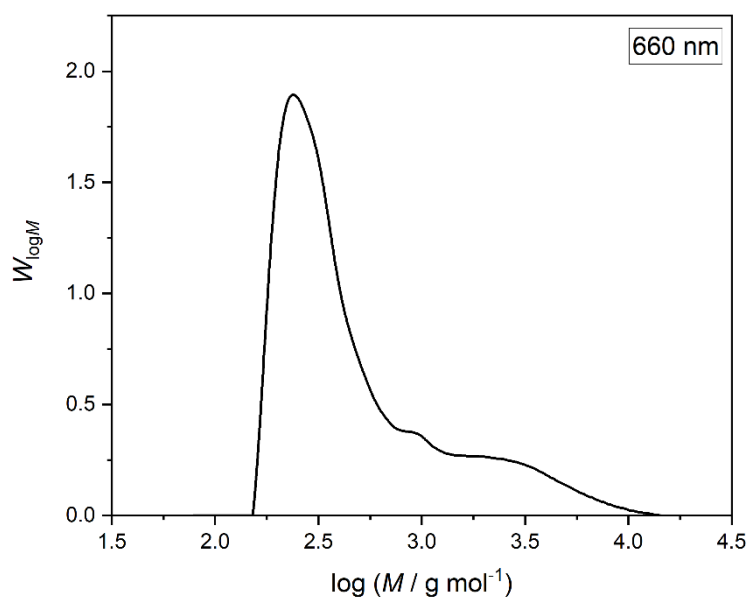


**Figure 10.54:** SEC trace of PDMA and DMA after 15 min irradiation of a solution with  $4.85 \text{ mol L}^{-1}$  DMA,  $3.53 \text{ mol L}^{-1}$  isopropanol,  $0.01 \text{ mol L}^{-1}$  AIBN,  $75 \mu\text{L}$  AuNR solution and  $10 \mu\text{L}$  3-mercaptopropionic acid with a ns laser at 660 nm.

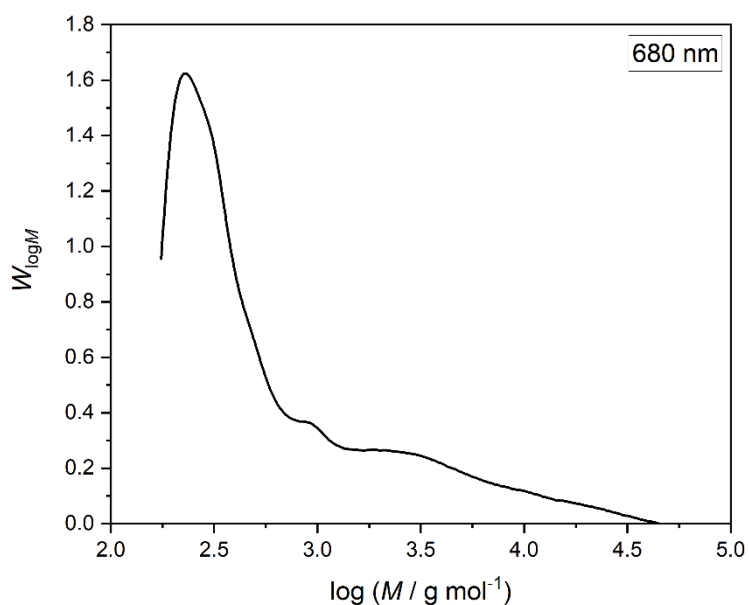


**Figure 10.55:** SEC trace of PDMA and DMA after 15 min irradiation of a solution with  $4.85 \text{ mol L}^{-1}$  DMA,  $3.53 \text{ mol L}^{-1}$  isopropanol,  $0.01 \text{ mol L}^{-1}$  AIBN,  $75 \mu\text{L}$  AuNR solution and  $10 \mu\text{L}$  3-mercaptopropionic acid with a ns laser at 680 nm.

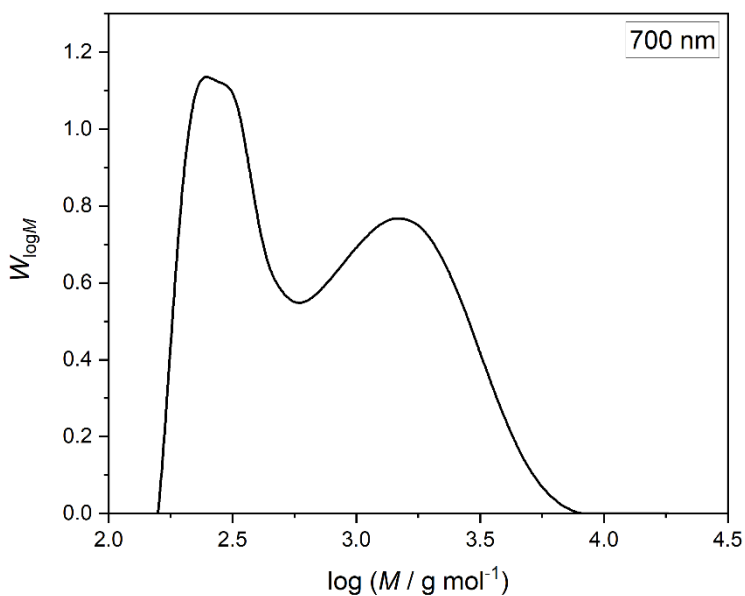


**Figure 10.56:** SEC trace of PDMA and DMA after 15 min irradiation of a solution with  $4.85 \text{ mol L}^{-1}$  DMA,  $3.53 \text{ mol L}^{-1}$  isopropanol,  $0.01 \text{ mol L}^{-1}$  AIBN,  $75 \mu\text{L}$  AuNR solution and  $10 \mu\text{L}$  3-mercaptopropionic acid with a ns laser at 700 nm.

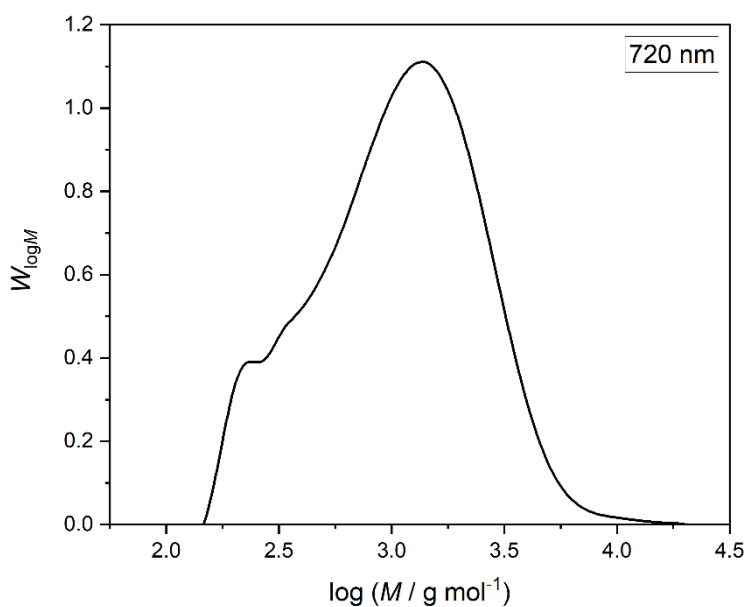


**Figure 10.57:** SEC trace of PDMA and DMA after 15 min irradiation of a solution with  $4.85 \text{ mol L}^{-1}$  DMA,  $3.53 \text{ mol L}^{-1}$  isopropanol,  $0.01 \text{ mol L}^{-1}$  AIBN,  $75 \mu\text{L}$  AuNR solution and  $10 \mu\text{L}$  3-mercaptopropionic acid with a ns laser at 720 nm.

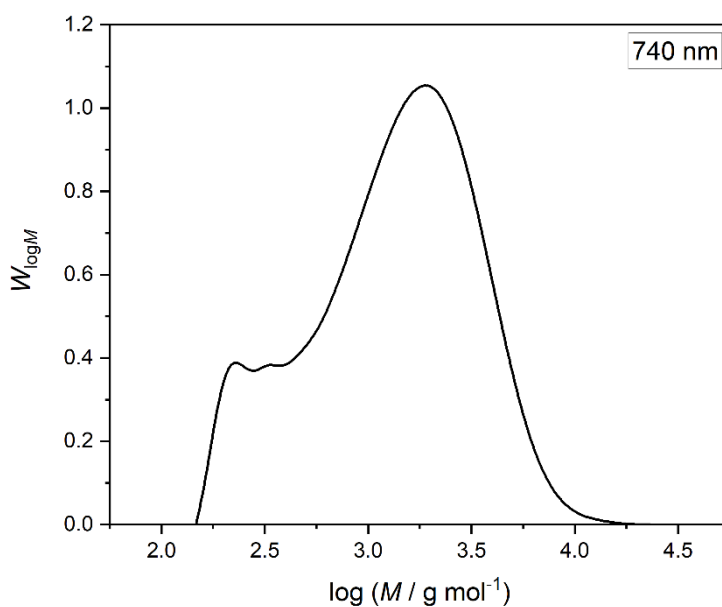


**Figure 10.58:** SEC trace of PDMA and DMA after 15 min irradiation of a solution with  $4.85 \text{ mol L}^{-1}$  DMA,  $3.53 \text{ mol L}^{-1}$  isopropanol,  $0.01 \text{ mol L}^{-1}$  AIBN,  $75 \mu\text{L}$  AuNR solution and  $10 \mu\text{L}$  3-mercaptopropionic acid with a ns laser at 740 nm.

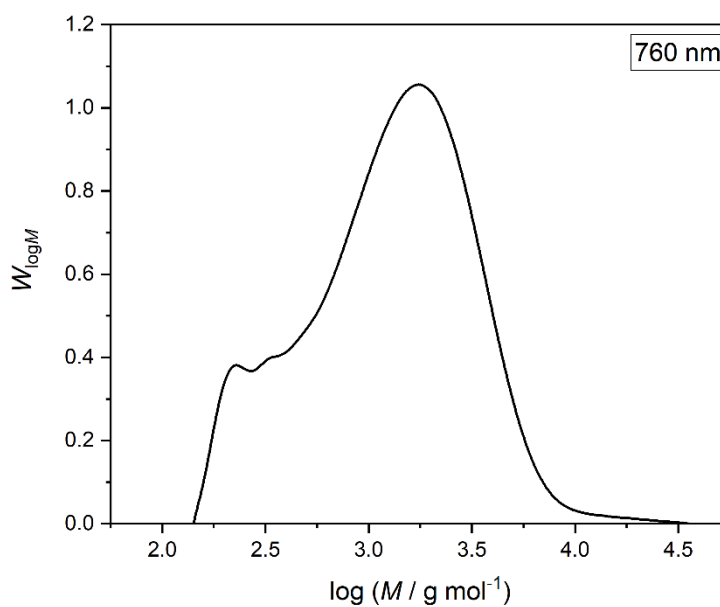


**Figure 10.59:** SEC trace of PDMA and DMA after 15 min irradiation of a solution with  $4.85 \text{ mol L}^{-1}$  DMA,  $3.53 \text{ mol L}^{-1}$  isopropanol,  $0.01 \text{ mol L}^{-1}$  AIBN,  $75 \mu\text{L}$  AuNR solution and  $10 \mu\text{L}$  3-mercaptopropionic acid with a ns laser at 760 nm.

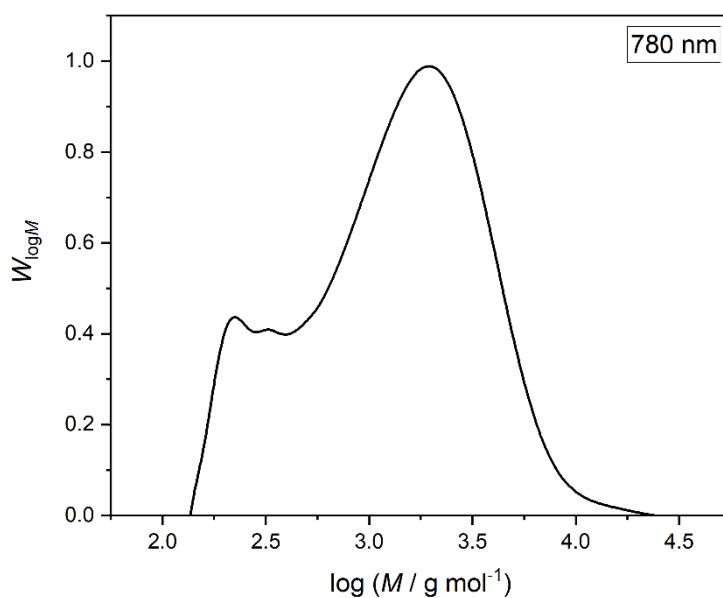


**Figure 10.60;** SEC trace of PDMA and DMA after 15 min irradiation of a solution with  $4.85 \text{ mol L}^{-1}$  DMA,  $3.53 \text{ mol L}^{-1}$  isopropanol,  $0.01 \text{ mol L}^{-1}$  AIBN,  $75 \mu\text{L}$  AuNR solution and  $10 \mu\text{L}$  3-mercaptopropionic acid with a ns laser at 780 nm.

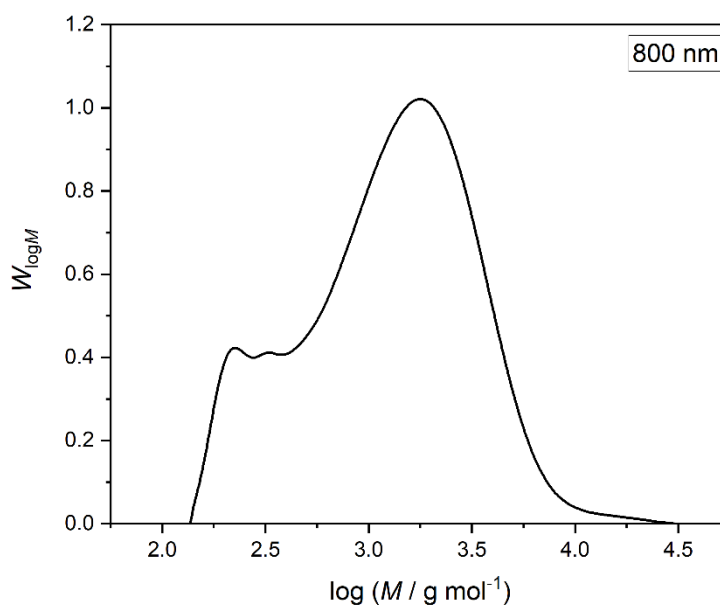


**Figure 10.61:** SEC trace of PDMA and DMA after 15 min irradiation of a solution with  $4.85 \text{ mol L}^{-1}$  DMA,  $3.53 \text{ mol L}^{-1}$  isopropanol,  $0.01 \text{ mol L}^{-1}$  AIBN,  $75 \mu\text{L}$  AuNR solution and  $10 \mu\text{L}$  3-mercaptopropionic acid with a ns laser at 800 nm.

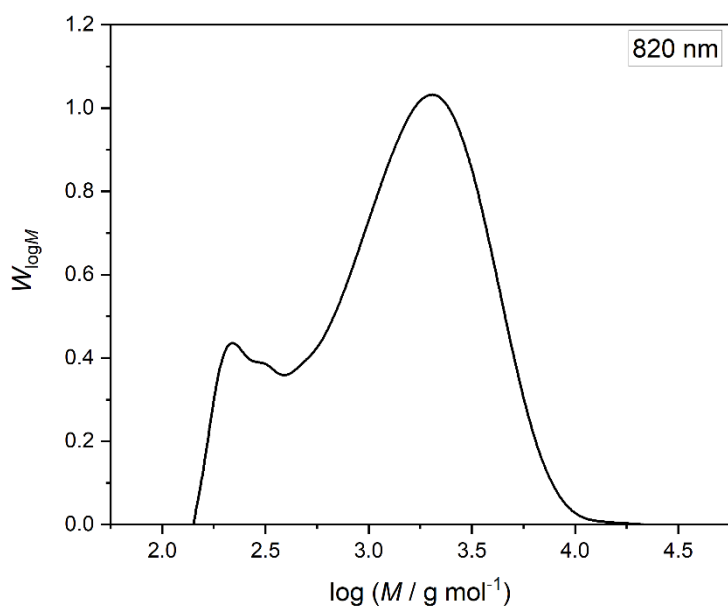


**Figure 10.62:** SEC trace of PDMA and DMA after 15 min irradiation of a solution with  $4.85 \text{ mol L}^{-1}$  DMA,  $3.53 \text{ mol L}^{-1}$  isopropanol,  $0.01 \text{ mol L}^{-1}$  AIBN,  $75 \mu\text{L}$  AuNR solution and  $10 \mu\text{L}$  3-mercaptopropionic acid with a ns laser at 820 nm.

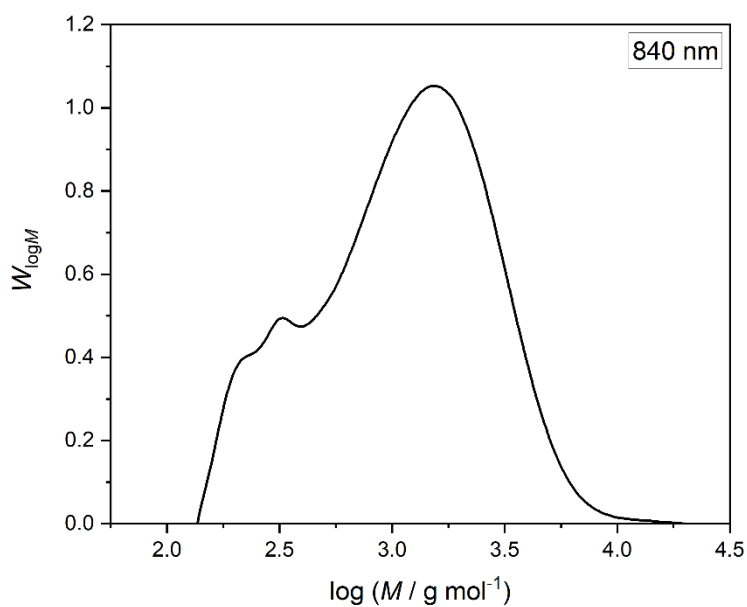


**Figure 10.63:** SEC trace of PDMA and DMA after 15 min irradiation of a solution with  $4.85 \text{ mol L}^{-1}$  DMA,  $3.53 \text{ mol L}^{-1}$  isopropanol,  $0.01 \text{ mol L}^{-1}$  AIBN,  $75 \mu\text{L}$  AuNR solution and  $10 \mu\text{L}$  3-mercaptopropionic acid with a ns laser at 840 nm.

## 11 References

- (1) Yagci, Y.; Jockusch, S.; Turro, N. J. Photoinitiated Polymerization: Advances, Challenges, and Opportunities. *Macromolecules* **2010**, *43*, 6245–6260.
- (2) Kaufmann, K. J.; Rentzepis, P. M. Picosecond spectroscopy in chemistry and biology. *Acc. Chem. Res.* **1975**, *8*, 407–412.
- (3) Zewail, A. H. Femtochemistry. *J. Phys. Chem.* **1993**, *97*, 12427–12446.
- (4) Shanmugam, S.; Xu, J.; Boyer, C. Aqueous RAFT Photopolymerization with Oxygen Tolerance. *Macromolecules* **2016**, *49*, 9345–9357.
- (5) Allegrezza, M. L.; DeMartini, Z. M.; Kloster, A. J.; Digby, Z. A.; Konkolewicz, D. Visible and sunlight driven RAFT photopolymerization accelerated by amines: kinetics and mechanism. *Polym. Chem.* **2016**, *7*, 6626–6636.
- (6) Zaquen, N.; Kadir, A. M. N. B. P. H. A.; Iasa, A.; Corrigan, N.; Junkers, T.; Zetterlund, P. B.; Boyer, C. Rapid Oxygen Tolerant Aqueous RAFT Photopolymerization in Continuous Flow Reactors. *Macromolecules* **2019**, *52*, 1609–1619.
- (7) Ishizuka, F.; Stenzel, M. H.; Zetterlund, P. B. Microcapsule synthesis via RAFT photopolymerization in vegetable Oil as a green solvent. *J. Polym. Sci. Part A: Polym. Chem.* **2018**, *56*, 831–839.
- (8) Delafresnaye, L.; Jung, K.; Boyer, C.; Barner-Kowollik, C. Two colours of light drive PET-RAFT photoligation. *Polym. Chem.* **2020**, *11*, 6453–6462.
- (9) Lueckerath, T.; Strauch, T.; Koynov, K.; Barner-Kowollik, C.; Ng, D. Y. W.; Weil, T. DNA-Polymer Conjugates by Photoinduced RAFT Polymerization. *Biomacromolecules* **2019**, *20*, 212–221.
- (10) Luo, X.; Wan, J.; Meckbach, N.; Strehmel, V.; Li, S.; Chen, Z.; Strehmel, B. A Porphyrin-Based Organic Network Comprising Sustainable Carbon Dots for Photopolymerization. *Angew. Chem. Int. Ed.* **2022**, *61*, e202208180.
- (11) Nardi, M.; Blasco, E.; Barner-Kowollik, C. Wavelength-Resolved PhotoATRP. *J. Am. Chem. Soc.* **2022**, *144*, 1094–1098.
- (12) Kütahya, C.; Wang, P.; Li, S.; Liu, S.; Li, J.; Chen, Z.; Strehmel, B. Carbon Dots as a Promising Green Photocatalyst for Free Radical and ATRP-Based Radical Photopolymerization with Blue LEDs. *Angew. Chem. Int. Ed.* **2020**, *59*, 3166–3171.
- (13) Tai, H.; Wang, W.; Vermonden, T.; Heath, F.; Hennink, W. E.; Alexander, C.; Shakesheff, K. M.; Howdle, S. M. Thermoresponsive and photocrosslinkable PEGMEMA-PPGMA-EGDMA copolymers from a one-step ATRP synthesis. *Biomacromolecules* **2009**, *10*, 822–828.
- (14) Hoogenboom, R.; Zorn, A.-M.; Keul, H.; Barner-Kowollik, C.; Moeller, M. Copolymers of 2-hydroxyethylacrylate and 2-methoxyethyl acrylate by nitroxide mediated polymerization:

kinetics, SEC-ESI-MS analysis and thermoresponsive properties. *Polym. Chem.* **2012**, *3*, 335–342.

(15) Junker, T.; Zang, L.; Wong, E. H.; Dingenouts, N.; Barner-Kowollik, C. Formation of triblock copolymers via a tandem enhanced spin capturing—nitroxide-mediated polymerization reaction sequence. *J. Polym. Sci. Part A: Polym. Chem.* **2011**, *49*, 4841–4850.

(16) Gigmes, D., Ed. *Nitroxide mediated polymerization: From fundamentals to applications in materials science* 19; R. Soc. Chem., 2016.

(17) *Visible Light-Triggered Precursor Molecules: Relating Reactivity and Ultrafast Dynamics*, 2019.

(18) Jöckle, P.; Kamm, P. W.; Lamparth, I.; Moszner, N.; Unterreiner, A.-N.; Barner-Kowollik, C. More than Expected: Overall Initiation Efficiencies of Mono-, Bis-, and Tetraacylgermane Radical Initiators. *Macromolecules* **2019**, *52*, 281–291.

(19) Jöckle, P.; Lamparth, I.; Moszner, N.; Barner-Kowollik, C.; Unterreiner, A.-N. Evidence for ultrafast formation of tribenzoylgermyl radicals originating from tetraacylgermane photoinitiators. *Polym. Chem.* **2020**, *11*, 3972–3979.

(20) Frick, E.; Ernst, H. A.; Voll, D.; Wolf, T. J. A.; Unterreiner, A.-N.; Barner-Kowollik, C. Studying the polymerization initiation efficiency of acetophenone-type initiators via PLP-ESI-MS and femtosecond spectroscopy. *Polym. Chem.* **2014**, *5*, 5053–5068.

(21) Wolf, T. J. A.; Voll, D.; Barner-Kowollik, C.; Unterreiner, A.-N. Elucidating the Early Steps in Photoinitiated Radical Polymerization via Femtosecond Pump–Probe Experiments and DFT Calculations. *Macromolecules* **2012**, *45*, 2257–2266.

(22) Kuchta, F.-D.; van Herk, A. M.; German, A. L. Propagation Kinetics of Acrylic and Methacrylic Acid in Water and Organic Solvents Studied by Pulsed-Laser Polymerization. *Macromolecules* **2000**, *33*, 3641–3649.

(23) Willemse, R. X. E.; Staal, B. B. P.; van Herk, A. M.; Pierik, S. C. J.; Klumperman, B. Application of Matrix-Assisted Laser Desorption Ionization Time-of-Flight Mass Spectrometry in Pulsed Laser Polymerization. Chain-Length-Dependent Propagation Rate Coefficients at High Molecular Weight: An Artifact Caused by Band Broadening in Size Exclusion Chromatography? *Macromolecules* **2003**, *36*, 9797–9803.

(24) Barner-Kowollik, C.; Günzler, F.; Junkers, T. Pushing the Limit: Pulsed Laser Polymerization of n -Butyl Acrylate at 500 Hz. *Macromolecules* **2008**, *41*, 8971–8973.

(25) Fast, D. E.; Lauer, A.; Menzel, J. P.; Kelterer, A.-M.; Gescheidt, G.; Barner-Kowollik, C. Wavelength-Dependent Photochemistry of Oxime Ester Photoinitiators. *Macromolecules* **2017**, *50*, 1815–1823.

- (26) del Pozo, M.; Delaney, C.; Da Pilz Cunha, M.; Debije, M. G.; Florea, L.; Schenning, A. P. H. J. Temperature-Responsive 4D Liquid Crystal Microactuators Fabricated by Direct Laser Writing by Two-Photon Polymerization. *Small Struct.* **2022**, *3*, 2100158.
- (27) Cao, C.; Qiu, Y.; Guan, L.; Wei, Z.; Yang, Z.; Zhan, L.; Zhu, D.; Ding, C.; Shen, X.; Xia, X.; *et al.* Dip-In Photoresist for Photoinhibited Two-Photon Lithography to Realize High-Precision Direct Laser Writing on Wafer. *ACS Appl. Mater. Interfaces.* **2022**, *14*, 31332–31342.
- (28) Liu, Z.-P.; Li, Y.; Xiao, Y.-F.; Li, B.-B.; Jiang, X.-F.; Qin, Y.; Feng, X.-B.; Yang, H.; Gong, Q. Direct laser writing of whispering gallery microcavities by two-photon polymerization. *Appl. Phys. Lett.* **2010**, *97*.
- (29) Cao, C.; Shen, X.; Chen, S.; He, M.; Wang, H.; Ding, C.; Zhu, D.; Dong, J.; Chen, H.; Huang, N.; *et al.* High-Precision and Rapid Direct Laser Writing Using a Liquid Two-Photon Polymerization Initiator. *ACS Appl. Mater. Interfaces.* **2023**, *15*, 30870–30879.
- (30) Izard, A. G.; Garcia, E. P.; Dixon, M.; Potma, E. O.; Baldacchini, T.; Valdevit, L. Enhanced adhesion in two-photon polymerization direct laser writing. *AIP Advances* **2020**, *10*.
- (31) Quick, A. S.; Fischer, J.; Richter, B.; Pauloehrl, T.; Trouillet, V.; Wegener, M.; Barner-Kowollik, C. Preparation of reactive three-dimensional microstructures via direct laser writing and thiol-ene chemistry. *Macromol. Rapid Commun.* **2013**, *34*, 335–340.
- (32) Blasco, E.; Müller, J.; Müller, P.; Trouillet, V.; Schön, M.; Scherer, T.; Barner-Kowollik, C.; Wegener, M. Fabrication of Conductive 3D Gold-Containing Microstructures via Direct Laser Writing. *Adv. Mater.* **2016**, *28*, 3592–3595.
- (33) Maruo, S.; Nakamura, O.; Kawata, S. Three-dimensional microfabrication with two-photon-absorbed photopolymerization. *Opt. Lett.* **1997**, *22*, 132–134.
- (34) Cumpston, B. H.; Ananthavel, S. P.; Barlow, S.; Dyer, D. L.; Ehrlich, J. E.; Erskine, L. L.; Heikal, A. A.; Kuebler, S. M.; Lee, I.-Y. S.; McCord-Maughon, D.; *et al.* Two-photon polymerization initiators for three-dimensional optical data storage and microfabrication. *Nature* **1999**, *398*, 51–54.
- (35) Zhou, X.; Hou, Y.; Lin, J. A review on the processing accuracy of two-photon polymerization. *AIP Adv.* **2015**, *5*.
- (36) Lee, K.-S.; Yang, D.-Y.; Park, S. H.; Kim, R. H. Recent developments in the use of two-photon polymerization in precise 2D and 3D microfabrications. *Polym. Adv. Technol.* **2006**, *17*, 72–82.
- (37) Qi, Y.; Bai, S.; Vogelmann, T. C.; Heisler, G. M. Penetration of UV-A, UV-B, blue, and red light into leaf tissues of pecan measured by a fiber optic microprobe system. *Ultraviolet Ground- and Space-based Measurements, Models, and Effects III*; pp 281–290.

- (38) Stolik, S.; Delgado, J. A.; Pérez, A.; Anasagasti, L. Measurement of the penetration depths of red and near infrared light in human "ex vivo" tissues. *J. Photochem. Photobiol. B* **2000**, *57*, 90–93.
- (39) Ekici, O.; Harrison, R. K.; Durr, N. J.; Eversole, D. S.; Lee, M.; Ben-Yakar, A. Thermal Analysis of Gold Nanorods Heated with Femtosecond Laser Pulses. *J. Phys. D: Appl. Phys.* **2008**, *41*, 185501.
- (40) Walden, S. L.; Carroll, J. A.; Unterreiner, A.-N.; Barner-Kowollik, C. Photochemical Action Plots Reveal the Fundamental Mismatch Between Absorptivity and Photochemical Reactivity. *Adv. Sci.* **2023**, e2306014.
- (41) Irshadeen, I. M.; Walden, S. L.; Wegener, M.; Truong, V. X.; Frisch, H.; Blinco, J. P.; Barner-Kowollik, C. Action Plots in Action: In-Depth Insights into Photochemical Reactivity. *J. Am. Chem. Soc.* **2021**, *143*, 21113–21126.
- (42) Menzel, J. P.; Noble, B. B.; Lauer, A.; Coote, M. L.; Blinco, J. P.; Barner-Kowollik, C. Wavelength Dependence of Light-Induced Cycloadditions. *J. Am. Chem. Soc.* **2017**, *139*, 15812–15820.
- (43) Kalayci, K.; Frisch, H.; Truong, V. X.; Barner-Kowollik, C. Green light triggered 2+2 cycloaddition of halochromic styrylquinoxaline-controlling photoreactivity by pH. *Nat. Commun.* **2020**, *11*, 4193.
- (44) Pelloth, J. L.; Tran, P. A.; Walther, A.; Goldmann, A. S.; Frisch, H.; Truong, V. X.; Barner-Kowollik, C. Wavelength-Selective Softening of Hydrogel Networks. *Adv. Mater.* **2021**, *33*, e2102184.
- (45) Alkilany, A. M.; Nagaria, P. K.; Hexel, C. R.; Shaw, T. J.; Murphy, C. J.; Wyatt, M. D. Cellular uptake and cytotoxicity of gold nanorods: molecular origin of cytotoxicity and surface effects. *Small* **2009**, *5*, 701–708.
- (46) Arumugam, S.; Orski, S. V.; Mbua, N. E.; McNitt, C.; Boons, G.-J.; Locklin, J.; Popik, V. V. Photo-click chemistry strategies for spatiotemporal control of metal-free ligation, labeling, and surface derivatization. *Pure Appl. Chem.* **2013**, *85*, 1499–1513.
- (47) Furuta, T. Designing Caged Compounds for Spatiotemporal Control of Cellular Chemistry. *J. Synth. Org. Chem. Jpn.* **2012**, *70*, 1164–1169.
- (48) Jia, S.; Sletten, E. M. Spatiotemporal Control of Biology: Synthetic Photochemistry Toolbox with Far-Red and Near-Infrared Light. *ACS Chem. Biol.* **2022**, *17*, 3255–3269.
- (49) Göstl, R.; Senf, A.; Hecht, S. Remote-controlling chemical reactions by light: towards chemistry with high spatio-temporal resolution. *Chem. Soc. Rev.* **2014**, *43*, 1982–1996.
- (50) Cooper, W. J.; Zika, R. G.; Petasne, R. G.; Fischer, A. M. Sunlight-Induced Photochemistry of Humic Substances in Natural Waters: Major Reactive Species. In ; pp 333–362.

- (51) Esser, P.; Pohlmann, B.; Scharf, H.-D. The Photochemical Synthesis of Fine Chemicals with Sunlight. *Angew. Chem. Int. Ed.* **1994**, *33*, 2009–2023.
- (52) Oelgemöller, M.; Jung, C.; Mattay, J. Green photochemistry: Production of fine chemicals with sunlight. *Pure Appl. Chem.* **2007**, *79*, 1939–1947.
- (53) Roth, H. D. The Beginnings of Organic Photochemistry. *Angew. Chem. Int. Ed.* **1989**, *28*, 1193–1207.
- (54) Hook, B. D. A.; Dohle, W.; Hirst, P. R.; Pickworth, M.; Berry, M. B.; Booker-Milburn, K. I. A practical flow reactor for continuous organic photochemistry. *J. Org. Chem.* **2005**, *70*, 7558–7564.
- (55) Nettekoven, M.; Püllmann, B.; Martin, R. E.; Wechsler, D. Evaluation of a flow-photochemistry platform for the synthesis of compact modules. *Tetrahedron Lett.* **2012**, *53*, 1363–1366.
- (56) Církva, V.; Hájek, M. Microwave photochemistry. Photoinitiated radical addition of tetrahydrofuran to perfluorohexylethene under microwave irradiation. *J. Photochem. Photobiol., A* **1999**, *123*, 21–23.
- (57) Fozza, A. C.; Klemberg-Sapieha, J. E.; Wertheimer, M. R. *Plasmas Process Polym.* **1999**, *4*, 183–206.
- (58) Wagner, N.; Theato, P. Light-induced wettability changes on polymer surfaces. *Polymer* **2014**, *55*, 3436–3453.
- (59) Tasdelen, M. A.; Yagci, Y. Light-induced click reactions. *Angew. Chem. Int. Ed.* **2013**, *52*, 5930–5938.
- (60) Lederhose, P.; Wüst, K. N. R.; Barner-Kowollik, C.; Blinco, J. P. Catalyst free visible light induced cycloaddition as an avenue for polymer ligation. *Chem. Commun.* **2016**, *52*, 5928–5931.
- (61) Lendlein, A.; Jiang, H.; Jünger, O.; Langer, R. Light-induced shape-memory polymers. *Nature* **2005**, *434*, 879–882.
- (62) Oehlenschlaeger, K. K.; Mueller, J. O.; Heine, N. B.; Glassner, M.; Guimard, N. K.; Delaitre, G.; Schmidt, F. G.; Barner-Kowollik, C. Light-induced modular ligation of conventional RAFT polymers. *Angew. Chem. Int. Ed.* **2013**, *52*, 762–766.
- (63) Hölz, K.; Lietard, J.; Somoza, M. M. High-Power 365 nm UV LED Mercury Arc Lamp Replacement for Photochemistry and Chemical Photolithography. *ACS Sustain. Chem. Eng.* **2017**, *5*, 828–834.
- (64) Radjagobalou, R.; Blanco, J.-F.; Petrizza, L.; Le Behec, M.; Dechy-Cabaret, O.; Lacombe, S.; Save, M.; Loubiere, K. Efficient Photooxygenation Process of Biosourced  $\alpha$ -Terpinene by

- Combining Controlled LED-Driven Flow Photochemistry and Rose Bengal-Anchored Polymer Colloids. *ACS Sustain. Chem. Eng.* **2020**, *8*, 18568–18576.
- (65) Feldmeier, C.; Bartling, H.; Riedle, E.; Gschwind, R. M. LED based NMR illumination device for mechanistic studies on photochemical reactions--versatile and simple, yet surprisingly powerful. *J. Magn. Reson.* **2013**, *232*, 39–44.
- (66) Frisch, H.; Menzel, J. P.; Bloesser, F. R.; Marschner, D. E.; Mundsinger, K.; Barner-Kowollik, C. Photochemistry in Confined Environments for Single-Chain Nanoparticle Design. *J. Am. Chem. Soc.* **2018**, *140*, 9551–9557.
- (67) Kodura, D.; Rodrigues, L. L.; Walden, S. L.; Goldmann, A. S.; Frisch, H.; Barner-Kowollik, C. Orange-Light-Induced Photochemistry Gated by pH and Confined Environments. *J. Am. Chem. Soc.* **2022**, *144*, 6343–6348.
- (68) Feist, F.; Walden, S. L.; Alves, J.; Kunz, S. V.; Micallef, A. S.; Brock, A. J.; McMurtrie, J. C.; Weil, T.; Blinco, J. P.; Barner-Kowollik, C. Wavelength-Gated Photochemical Synthesis of Phenalene Diimides. *Angew. Chem. Int. Ed.* **2021**, *60*, 10402–10408.
- (69) Coyle, E. E.; Oelgemöller, M. Micro-photochemistry: photochemistry in microstructured reactors. The new photochemistry of the future? *Photochem. Photobiol. Sci.* **2008**, *7*, 1313–1322.
- (70) Mueller, J. O.; Schmidt, F. G.; Blinco, J. P.; Barner-Kowollik, C. Visible-Light-Induced Click Chemistry. *Angew. Chem. Int. Ed.* **2015**, *54*, 10284–10288.
- (71) Rubens, M.; Latsrisaeng, P.; Junkers, T. Visible light-induced iniferter polymerization of methacrylates enhanced by continuous flow. *Polym. Chem.* **2017**, *8*, 6496–6505.
- (72) Sze, S. M.; Li, Y.; Ng, K. K. *Physics of semiconductor devices*, Fourth edition; John Wiley & Sons, Inc: Hoboken, NJ, 2021.
- (73) *Light emitting diodes*, 1995.
- (74) Jandt, K. D.; Mills, R. W. A brief history of LED photopolymerization. *Dent. Mater.* **2013**, *29*, 605–617.
- (75) Stahl, F.; Ashworth, S. H.; Jandt, K. D.; Mills, R. W. Light-emitting diode (LED) polymerisation of dental composites: flexural properties and polymerisation potential. *Biomaterials* **2000**, *21*, 1379–1385.
- (76) Uhl, A.; Mills, R. W.; Jandt, K. D. Polymerization and light-induced heat of dental composites cured with LED and halogen technology. *Biomaterials* **2003**, *24*, 1809–1820.
- (77) Jandt, K. D.; Mills, R. W.; Blackwell, G. B.; Ashworth, S. H. Depth of cure and compressive strength of dental composites cured with blue light emitting diodes (LEDs). *Dent. Mater.* **2000**, *16*, 41–47.

- (78) Konrad, W.; Fengler, C.; Putwa, S.; Barner-Kowollik, C. Protection-Group-Free Synthesis of Sequence-Defined Macromolecules via Precision  $\lambda$ -Orthogonal Photochemistry. *Angew. Chem. Int. Ed.* **2019**, *58*, 7133–7137.
- (79) Wei, H.; Lei, M.; Zhang, P.; Leng, J.; Zheng, Z.; Yu, Y. Orthogonal photochemistry-assisted printing of 3D tough and stretchable conductive hydrogels. *Nat. Commun.* **2021**, *12*, 2082.
- (80) Hildebrandt, K.; Kaupp, M.; Molle, E.; Menzel, J. P.; Blinco, J. P.; Barner-Kowollik, C. Star polymer synthesis via  $\lambda$ -orthogonal photochemistry. *Chem. Commun.* **2016**, *52*, 9426–9429.
- (81) Hildebrandt, K.; Pauloehrl, T.; Blinco, J. P.; Linkert, K.; Börner, H. G.; Barner-Kowollik, C.  $\lambda$ -Orthogonal pericyclic macromolecular photoligation. *Angew. Chem. Int. Ed.* **2015**, *54*, 2838–2843.
- (82) Hurrle, S.; Lauer, A.; Gliemann, H.; Mutlu, H.; Wöll, C.; Goldmann, A. S.; Barner-Kowollik, C. Two-in-One:  $\lambda$ -Orthogonal Photochemistry on a Radical Photoinitiating System. *Macromol. Rapid Commun.* **2017**, *38*.
- (83) Kamm, P. W.; Rodrigues, L. L.; Walden, S. L.; Blinco, J. P.; Unterreiner, A.-N.; Barner-Kowollik, C. Sequence-independent activation of photocycloadditions using two colours of light. *Chem. Sci.* **2022**, *13*, 531–535.
- (84) Lahikainen, M.; Zeng, H.; Priimagi, A. Reconfigurable photoactuator through synergistic use of photochemical and photothermal effects. *Nat. Commun.* **2018**, *9*, 4148.
- (85) Hobich, J.; Blasco, E.; Wegener, M.; Mutlu, H.; Barner-Kowollik, C. Synergistic, Orthogonal, and Antagonistic Photochemistry for Light-Induced 3D Printing. *Macromol. Chem. Phys.* **2023**, *224*, 2200318.
- (86) Mundsinger, K.; Tuten, B. T.; Wang, L.; Neubauer, K.; Kropf, C.; O'Mara, M. L.; Barner-Kowollik, C. Visible-Light-Reactive Single-Chain Nanoparticles. *Angew. Chem. Int. Ed.* **2023**, *62*, e202302995.
- (87) Olaj, O. F.; Bitai, I.; Hinkelmann, F. *Makromol. Chem.* **1987**, *188*, 1689–1702.
- (88) Gruending, T.; Voll, D.; Guilhaus, M.; Barner-Kowollik, C. A Perfect Couple: PLP/SEC/ESI-MS for the Accurate Determination of Propagation Rate Coefficients in Free Radical Polymerization. *Macromol. Chem. Phys.* **2010**, *211*, 80–90.
- (89) Jöckle, P.; Schweigert, C.; Lamparth, I.; Moszner, N.; Unterreiner, A.-N.; Barner-Kowollik, C. An In-Depth Mechanistic Investigation of the Radical Initiation Behavior of Monoacylgermanes. *Macromolecules* **2017**, *50*, 8894–8906.
- (90) Scaiano, J. C.; Lissi, E. A.; Encina, M. V. Chemistry of the biradicals produced in the Norrish Type II reaction. *Rev. Chem Intermed.* **1978**, *2*, 139–196.

- (91) Sammaljärvi, J.; Jokelainen, L.; Ikonen, J.; Siitari-Kauppi, M. Free radical polymerisation of MMA with thermal initiator in brick and Grimsel granodiorite. *Eng. Geol.* **2012**, *135-136*, 52–59.
- (92) Songsing, K.; Vatanatham, T.; Hansupalak, N. Kinetics and mechanism of grafting styrene onto natural rubber in emulsion polymerization using cumene hydroperoxide–tetraethylenepentamine as redox initiator. *Eur. Polym. J.* **2013**, *49*, 1007–1016.
- (93) Xia, J.; Matyjaszewski, K. Controlled/“Living” Radical Polymerization. Homogeneous Reverse Atom Transfer Radical Polymerization Using AIBN as the Initiator. *Macromolecules* **1997**, *30*, 7692–7696.
- (94) NORRISH, R. G. W.; PORTER, G. Chemical Reactions Produced by Very High Light Intensities. *Nature* **1949**, *164*, 658.
- (95) Gustavsson, T.; Cassara, L.; Gulbinas, V.; Gurzadyan, G.; Mialocq, J.-C.; Pommeret, S.; Sorgius, M.; van der Meulen, P. Femtosecond Spectroscopic Study of Relaxation Processes of Three Amino-Substituted Coumarin Dyes in Methanol and Dimethyl Sulfoxide. *J. Phys. Chem. A* **1998**, *102*, 4229–4245.
- (96) Lee, S.-H.; Moon, J. J.; West, J. L. Three-dimensional micropatterning of bioactive hydrogels via two-photon laser scanning photolithography for guided 3D cell migration. *Biomaterials* **2008**, *29*, 2962–2968.
- (97) Lin, Y.; Gao, C.; Gritsenko, D.; Zhou, R.; Xu, J. Soft lithography based on photolithography and two-photon polymerization. *Microfluid. Nanofluidics* **2018**, *22*.
- (98) O’Connor, N. A.; Berro, A. J.; Lancaster, J. R.; Gu, X.; Jockusch, S.; Nagai, T.; Ogata, T.; Lee, S.; Zimmerman, P.; Willson, C. G.; *et al.* Toward the Design of a Sequential Two Photon Photoacid Generator for Double Exposure Photolithography. *Chem. Mater.* **2008**, *20*, 7374–7376.
- (99) Scott, T. F.; Kowalski, B. A.; Sullivan, A. C.; Bowman, C. N.; McLeod, R. R. Two-color single-photon photoinitiation and photoinhibition for subdiffraction photolithography. *Science* **2009**, *324*, 913–917.
- (100) Hsieh, T. M.; Ng, C. W. B.; Narayanan, K.; Wan, A. C. A.; Ying, J. Y. Three-dimensional microstructured tissue scaffolds fabricated by two-photon laser scanning photolithography. *Biomaterials* **2010**, *31*, 7648–7652.
- (101) Abt, D.; Schmidt, B. V. K. J.; Pop-Georgievski, O.; Quick, A. S.; Danilov, D.; Kostina, N. Y.; Bruns, M.; Wenzel, W.; Wegener, M.; Rodriguez-Emmenegger, C.; *et al.* Designing Molecular Printboards: A Photolithographic Platform for Recodable Surfaces. *Chemistry (Weinheim an der Bergstrasse, Germany)* **2015**, *21*, 13186–13190.

- (102) Müller, P.; Müller, R.; Hammer, L.; Barner-Kowollik, C.; Wegener, M.; Blasco, E. STED-Inspired Laser Lithography Based on Photoswitchable Spirothiopyran Moieties. *Chem. Mater.* **2019**, *31*, 1966–1972.
- (103) Yang, L.; Münchinger, A.; Kadic, M.; Hahn, V.; Mayer, F.; Blasco, E.; Barner-Kowollik, C.; Wegener, M. On the Schwarzschild Effect in 3D Two-Photon Laser Lithography. *Adv. Opt. Mater.* **2019**, *7*, 1901040.
- (104) Nakayama, Y.; Miyamura, M.; Hirano, Y.; Goto, K.; Matsuda, T. Preparation of poly(ethylene glycol)-polystyrene block copolymers using photochemistry of dithiocarbamate as a reduced cell-adhesive coating material. *Biomaterials* **1999**, *20*, 963–970.
- (105) Sando, L.; Kim, M.; Colgrave, M. L.; Ramshaw, J. A. M.; Werkmeister, J. A.; Elvin, C. M. Photochemical crosslinking of soluble wool keratins produces a mechanically stable biomaterial that supports cell adhesion and proliferation. *J. Biomed. Mater. Res. Part A* **2010**, *95*, 901–911.
- (106) Abu Bakar, R.; Li, Y.; Hewitson, O. P.; Roth, P. J.; Keddie, J. L. Azide Photochemistry in Acrylic Copolymers for Ultraviolet Cross-Linkable Pressure-Sensitive Adhesives: Optimization, Debonding-on-Demand, and Chemical Modification. *ACS Appl. Mater. Interfaces.* **2022**, *14*, 30216–30227.
- (107) Swanson, M. J.; Opperman, G. W. Photochemical surface modification of polymers for improved adhesion. *J. Adh. Sci. Technol.* **1995**, *9*, 385–391.
- (108) Lin, C.-W.; Aguilar, S.; Rao, E.; Mak, W. H.; Huang, X.; He, N.; Chen, D.; Jun, D.; Curson, P. A.; McVerry, B. T.; *et al.* Direct grafting of tetraaniline via perfluorophenylazide photochemistry to create antifouling, low bio-adhesion surfaces. *Chem. Sci.* **2019**, *10*, 4445–4457.
- (109) Kilian, R. J. The Application of Photochemistry to Dental Materials. *Biomedical and Dental Applications*; pp 411–417.
- (110) Klee, J. E.; Maier, M.; Fik, C. P. Applied Photochemistry in Dental Materials: From Beginnings to State of the Art. *Dyes and chromophores in polymer science*; pp 123–138.
- (111) Lindén, L. Applied photochemistry in dental science. *J. Chem. Sci.* **1993**, *105*, 405–419.
- (112) Shimomura, H. Photochemical studies on composite resins cured by visible light. *Dent. Mater. J.* **1987**, *6*, 9–27.
- (113) Sprick, E.; Becht, J.-M.; Graff, B.; Salomon, J.-P.; Tigges, T.; Weber, C.; Lalevée, J. New hydrogen donors for amine-free photoinitiating systems in dental materials. *Dent. Mater.* **2021**, *37*, 382–390.
- (114) Bahati, D.; Bricha, M.; El Mabrouk, K. Vat Photopolymerization Additive Manufacturing Technology for Bone Tissue Engineering Applications. *Adv. Eng. Mater.* **2023**, *25*, 2200859.

- (115) Nguyen, K. T.; West, J. L. Photopolymerizable hydrogels for tissue engineering applications. *Biomaterials* **2002**, *23*, 4307–4314.
- (116) Baroli, B. Photopolymerization of biomaterials: issues and potentialities in drug delivery, tissue engineering, and cell encapsulation applications. *J. Chem. Technol. Biotechnol.* **2006**, *81*, 491–499.
- (117) Zieger, M. M.; Müller, P.; Blasco, E.; Petit, C.; Hahn, V.; Michalek, L.; Mutlu, H.; Wegener, M.; Barner-Kowollik, C. A Subtractive Photoresist Platform for Micro- and Macroscopic 3D Printed Structures. *Adv. Funct. Mater.* **2018**, *28*, 1801405.
- (118) Alabugin, A. Near-IR Photochemistry for Biology: Exploiting the Optical Window of Tissue. *Photochem. Photobiol.* **2019**, *95*, 722–732.
- (119) Kowalik, L.; Chen, J. K. Illuminating developmental biology through photochemistry. *Nat. Chem. Biol.* **2017**, *13*, 587–598.
- (120) Legrini, O.; Oliveros, E.; Braun, A. M. Photochemical processes for water treatment. *Chem. Rev.* **1993**, *93*, 671–698.
- (121) Litter, M. I. Introduction to Photochemical Advanced Oxidation Processes for Water Treatment. In *Reactions and processes*; Robertson, P. K., Bahnemann, D. W., Boule, P., Eds.; The Handbook of Environmental Chemistry; Springer-Verlag: Berlin, 2005; pp 325–366.
- (122) Cambié, D.; Bottecchia, C.; Straathof, N. J. W.; Hessel, V.; Noël, T. Applications of Continuous-Flow Photochemistry in Organic Synthesis, Material Science, and Water Treatment. *Chem. Rev.* **2016**, *116*, 10276–10341.
- (123) Kütahya, C.; Schmitz, C.; Strehmel, V.; Yagci, Y.; Strehmel, B. Near-Infrared Sensitized Photoinduced Atom-Transfer Radical Polymerization (ATRP) with a Copper(II) Catalyst Concentration in the ppm Range. *Angew. Chem. Int. Ed.* **2018**, *57*, 7898–7902.
- (124) Shanmugam, S.; Xu, J.; Boyer, C. Light-Regulated Polymerization under Near-Infrared/Far-Red Irradiation Catalyzed by Bacteriochlorophyll a. *Angew. Chem.* **2016**, *128*, 1048–1052.
- (125) Zou, X.; Zhu, J.; Zhu, Y.; Yagci, Y.; Liu, R. Photopolymerization of Macroscale Black 3D Objects Using Near-Infrared Photochemistry. *ACS Appl. Mater. Interfaces* **2020**, *12*, 58287–58294.
- (126) Lederhose, P.; Chen, Z.; Müller, R.; Blinco, J. P.; Wu, S.; Barner-Kowollik, C. Near-Infrared Photoinduced Coupling Reactions Assisted by Upconversion Nanoparticles. *Angew. Chem. Int. Ed.* **2016**, *55*, 12195–12199.
- (127) Belfield, K. D.; Ren, X.; van Stryland, E. W.; Hagan, D. J.; Dubikovskiy, V.; Miesak, E. J. Near-IR Two-Photon Photoinitiated Polymerization Using a Fluorone/Amine Initiating System. *J. Am. Chem. Soc.* **2000**, *122*, 1217–1218.

- (128) Göppert-Mayer, M. Über Elementarakte mit zwei Quantensprüngen. *Ann. Phys.* **1931**, *401*, 273–294.
- (129) Layani, M.; Wang, X.; Magdassi, S. Novel Materials for 3D Printing by Photopolymerization. *Adv. Mater.* **2018**, *30*, e1706344.
- (130) Husár, B.; Hatzenbichler, M.; Mironov, V.; Liska, R.; Stampfl, J.; Ovsianikov, A. Photopolymerization-based additive manufacturing for the development of 3D porous scaffolds. *Biomaterials for Bone Regeneration*; Elsevier, 2014; pp 149–201.
- (131) Davoudinejad, A. Vat photopolymerization methods in additive manufacturing. *Additive Manufacturing*; Elsevier, 2021; pp 159–181.
- (132) Bagheri, A.; Jin, J. Photopolymerization in 3D Printing. *ACS Appl. Polym. Mater.* **2019**, *1*, 593–611.
- (133) Zhang, J.; Xiao, P. 3D printing of photopolymers. *Polym. Chem.* **2018**, *9*, 1530–1540.
- (134) Hahn, V.; Bojanowski, N. M.; Rietz, P.; Feist, F.; Kozłowska, M.; Wenzel, W.; Blasco, E.; Bräse, S.; Barner-Kowollik, C.; Wegener, M. Challenges and Opportunities in 3D Laser Printing Based on (1 + 1)-Photon Absorption. *ACS Photonics* **2023**, *10*, 24–33.
- (135) Wu, L.; Zhao, L.; Jian, M.; Mao, Y.; Yu, M.; Guo, X. EHMP-DLP: multi-projector DLP with energy homogenization for large-size 3D printing. *RPJ* **2018**, *24*, 1500–1510.
- (136) Muldoon, K.; Song, Y.; Ahmad, Z.; Chen, X.; Chang, M.-W. High Precision 3D Printing for Micro to Nano Scale Biomedical and Electronic Devices. *Micromachines* **2022**, *13*, 642.
- (137) Quan, H.; Zhang, T.; Xu, H.; Luo, S.; Nie, J.; Zhu, X. Photo-curing 3D printing technique and its challenges. *Bioact. Mater.* **2020**, *5*, 110–115.
- (138) Pasricha, A.; Greeninger, R. Exploration of 3D printing to create zero-waste sustainable fashion notions and jewelry. *Fash Text* **2018**, *5*.
- (139) Dawood, A.; Marti Marti, B.; Sauret-Jackson, V.; Darwood, A. 3D printing in dentistry. *Br. Dent. J.* **2015**, *219*, 521–529.
- (140) Kessler, A.; Hickel, R.; Reymus, M. 3D Printing in Dentistry-State of the Art. *Oper. Dent.* **2020**, *45*, 30–40.
- (141) Prasad, S.; Kader, N. A.; Sujatha, G.; Raj, T.; Patil, S. 3D printing in dentistry. *3D Print. Med.* **2018**, *2*, 89–91.
- (142) Vasamsetty, P.; Pss, T.; Kukkala, D.; Singamshetty, M.; Gajula, S. 3D printing in dentistry – Exploring the new horizons. *Mater. Today Proc.* **2020**, *26*, 838–841.
- (143) Kalender, M.; Kilic, S. E.; Ersoy, S.; Bozkurt, Y.; Salman, S. Additive Manufacturing and 3D Printer Technology in Aerospace Industry. In *2019 9th International Conference on Recent Advances in Space Technologies (RAST)*; IEEE, 2019.

- (144) Joshi, S. C.; Sheikh, A. A. 3D printing in aerospace and its long-term sustainability. *Virtual Phys. Prototyp.* **2015**, *10*, 175–185.
- (145) Lim, C. W. J.; Le, K. Q.; Lu, Q.; Wong, C. H. An Overview of 3-D Printing in Manufacturing, Aerospace, and Automotive Industries. *IEEE Potentials* **2016**, *35*, 18–22.
- (146) Acanfora, V.; Sellitto, A.; Russo, A.; Zarrelli, M.; Riccio, A. Experimental investigation on 3D printed lightweight sandwich structures for energy absorption aerospace applications. *Aerosp. Sci. Technol.* **2023**, *137*, 108276.
- (147) Romero, P. E.; Arribas-Barríos, J.; Rodríguez-Alabanda, O.; González-Merino, R.; Guerrero-Vaca, G. Manufacture of polyurethane foam parts for automotive industry using FDM 3D printed molds. *CIRP J. Manuf. Sci. Technol.* **2021**, *32*, 396–404.
- (148) Mokbel, H.; Graff, B.; Dumur, F.; Lalevée, J. NIR Sensitizer Operating under Long Wavelength (1064 nm) for Free Radical Photopolymerization Processes. *Macromol. Rapid Commun.* **2020**, *41*, e2000289.
- (149) Dähne, S.; Resch-Genger, U.; Wolfbeis, O. S. *Near-infrared dyes for high technology applications*; NATO ASI series. Partnership sub-series 3, High technology v. 52; Kluwer: Dordrecht, Boston, 1998.
- (150) Braun, D.; Jakobi, R. Neue Initiatoren zur Polymerisationsauslösung. *Angew. Makromol. Chem.* **1982**, *105*, 217–230.
- (151) Thiele, J.; Heuser, K. Ueber Hydrazinderivate der Isobuttersäure; *Justus Liebigs Ann. Chem.* **1896**, *290*, 1–43.
- (152) Matsuoka, M. *Infrared Absorbing Dyes*; Springer International Publishing: Cham, 20.
- (153) Bonardi, A.-H.; Bonardi, F.; Morlet-Savary, F.; Dietlin, C.; Noirbent, G.; Grant, T. M.; Fouassier, J.-P.; Dumur, F.; Lessard, B. H.; Gignes, D.; *et al.* Photoinduced Thermal Polymerization Reactions. *Macromolecules* **2018**, *51*, 8808–8820.
- (154) Bonardi, A.; Bonardi, F.; Noirbent, G.; Dumur, F.; Dietlin, C.; Gignes, D.; Fouassier, J.-P.; Lalevée, J. Different NIR dye scaffolds for polymerization reactions under NIR light. *Polym. Chem.* **2019**, *10*, 6505–6514.
- (155) Schulz, G. V.; Wittig, G. Anregung von Kettenpolymerisationen durch freie Radikale. *Naturwissenschaften* **1939**, *27*, 387–388.
- (156) Henglein, A. Small-particle research: physicochemical properties of extremely small colloidal metal and semiconductor particles. *Chem. Rev.* **1989**, *89*, 1861–1873.
- (157) Alivisatos, A. P. Perspectives on the Physical Chemistry of Semiconductor Nanocrystals. *J. Phys. Chem.* **1996**, *100*, 13226–13239.
- (158) Kreibitz, U.; Vollmer, M. *Optical Properties of Metal Clusters*, 1995 edition; Springer: Berlin, 1995.

- (159) Perenboom, J.; Wyder, P.; Meier, F. Electronic properties of small metallic particles. *Phys. Rep.* **1981**, *78*, 173–292.
- (160) Hughes, A. E.; Jain, S. C. Metal colloids in ionic crystals. *Adv. Phys.* **1979**, *28*, 717–828.
- (161) Bohren, C. F.; Huffman, D. R. *Absorption and Scattering of Light by Small Particles*, 1., Auflage; Wiley-VCH: Weinheim, 2008.
- (162) Mulvaney, P. Surface Plasmon Spectroscopy of Nanosized Metal Particles. *Langmuir* **1996**, *12*, 788–800.
- (163) Nguyen, S. C.; Zhang, Q.; Manthiram, K.; Ye, X.; Lomont, J. P.; Harris, C. B.; Weller, H.; Alivisatos, A. P. Study of Heat Transfer Dynamics from Gold Nanorods to the Environment via Time-Resolved Infrared Spectroscopy. *ACS nano* **2016**, *10*, 2144–2151.
- (164) Abareshi, A.; Arshadi Pirlar, M.; Houshiar, M. Experimental and theoretical investigation of the photothermal effect in gold nanorods. *New J. Chem.* **2021**, *45*, 298–303.
- (165) Wang, X.; Li, G.; Ding, Y.; Sun, S. Understanding the photothermal effect of gold nanostars and nanorods for biomedical applications. *RSC Adv.* **2014**, *4*, 30375–30383.
- (166) Mie, G. Beiträge zur Optik trüber Medien, speziell kolloidaler Metallösungen. *Ann. Phys.* **1908**, *330*, 377–445.
- (167) Gans, R. Über die Form ultramikroskopischer Goldteilchen. *Ann. Phys.* **1912**, *342*, 881–900.
- (168) Acquista, C. Light scattering by tenuous particles: a generalization of the Rayleigh-Gans-Rocard approach. *Appl. Opt.* **1976**, *15*, 2932–2936.
- (169) Baffou, G.; Quidant, R. Thermo-plasmonics: using metallic nanostructures as nano-sources of heat. *Laser Photonics Rev.* **2013**, *7*, 171–187.
- (170) Boulais, E.; Lachaine, R.; Meunier, M. Plasma mediated off-resonance plasmonic enhanced ultrafast laser-induced nanocavitation. *Nano Lett.* **2012**, *12*, 4763–4769.
- (171) Mitamura, K.; Imae, T. Functionalization of Gold Nanorods Toward Their Applications. *Plasmonics* **2009**, *4*, 23–30.
- (172) Vigdeman, L.; Khanal, B. P.; Zubarev, E. R. Functional gold nanorods: synthesis, self-assembly, and sensing applications. *Adv. Mater.* **2012**, *24*, 4811–41, 5014.
- (173) Hwang, S.-Y.; Tao, A. R. Biofunctionalization of gold nanorods. *Pure Appl. Chem.* **2010**, *83*, 233–241.
- (174) Gui, C.; Cui, D.-X. Functionalized gold nanorods for tumor imaging and targeted therapy. *Cancer biology & medicine* **2012**, *9*, 221–233.
- (175) Oyelere, A. K.; Chen, P. C.; Huang, X.; El-Sayed, I. H.; El-Sayed, M. A. Peptide-conjugated gold nanorods for nuclear targeting. *Bioconjugate chemistry* **2007**, *18*, 1490–1497.

- (176) Huang, X.; El-Sayed, I. H.; Qian, W.; El-Sayed, M. A. Cancer cell imaging and photothermal therapy in the near-infrared region by using gold nanorods. *J. Am. Chem. Soc.* **2006**, *128*, 2115–2120.
- (177) Choi, W. I.; Sahu, A.; Kim, Y. H.; Tae, G. Photothermal cancer therapy and imaging based on gold nanorods. *Ann. Biomed. Eng.* **2012**, *40*, 534–546.
- (178) Huang, X.; El-Sayed, I. H.; El-Sayed, M. A. Applications of gold nanorods for cancer imaging and photothermal therapy. *Methods Mol. Biol.* **2010**, *624*, 343–357.
- (179) Ishtiaq, S.; Shah, K. U.; Ur-Rehman, T.; Ud-Din, F. Gold nanorods: new generation drug delivery platform. *Metal Nanoparticles for Drug Delivery and Diagnostic Applications*; Elsevier, 2020; pp 59–84.
- (180) Venkatesan, R.; Pichaimani, A.; Hari, K.; Balasubramanian, P. K.; Kulandaivel, J.; Premkumar, K. Doxorubicin conjugated gold nanorods: a sustained drug delivery carrier for improved anticancer therapy. *J. Mater. Chem. B* **2013**, *1*, 1010–1018.
- (181) Ali, H. R.; Ali, M. R. K.; Wu, Y.; Selim, S. A.; Abdelaal, H. F. M.; Nasr, E. A.; El-Sayed, M. A. Gold Nanorods as Drug Delivery Vehicles for Rifampicin Greatly Improve the Efficacy of Combating Mycobacterium tuberculosis with Good Biocompatibility with the Host Cells. *Bioconjug. Chem.* **2016**, *27*, 2486–2492.
- (182) Neidinger, P.; Voll, D.; Walden, S. L.; Unterreiner, A.-N.; Barner-Kowollik, C. Two Photon Induced Pulsed Laser Polymerization with Near Infrared Light. *ACS Macro Lett.* **2023**, *12*, 308–313.
- (183) Neidinger, P.; Davis, J.; Voll, D.; Jaatinen, E. A.; Walden, S. L.; Unterreiner, A. N.; Barner-Kowollik, C. Near Infrared Light Induced Radical Polymerization in Water. *Angew. Chem. Int. Ed.* **2022**, *61*, e202209177.
- (184) Atkins, P. W.; Friedman, R. *Molecular quantum mechanics by Peter Atkins and Ronald Friedman*, 5th ed.; Oxford, New York Oxford University Press 2011.
- (185) Franck, J.; Dymond, E. G. Elementary processes of photochemical reactions. *Trans. Faraday Soc.* **1926**, *21*, 536.
- (186) Condon, E. A Theory of Intensity Distribution in Band Systems. *Phys. Rev.* **1926**, *28*, 1182–1201.
- (187) Turro, N. J.; Ramamurthy, V.; Scaiano, J. C. *Principles of molecular photochemistry: An introduction*; University Science Books: Sausalito, op. 2009.
- (188) Atkins, P. W. *Physikalische Chemie*, 4., vollst. überarb. Aufl., 2. Nachdr; Wiley-VCH: Weinheim, 2012.
- (189) Hecht, E. *Optik*, 8. Auflage; De Gruyter Studium; De Gruyter Oldenbourg; Walter de Gruyter GmbH: Berlin, 2023.

- (190) Pechukas, P. Transition State Theory. *Annu. Rev. Phys. Chem.* **1981**, *32*, 159–177.
- (191) Truhlar, D. G.; Garrett, B. C. Variational Transition State Theory. *Annu. Rev. Phys. Chem.* **1984**, *35*, 159–189.
- (192) Jabłoński, A. Über den Mechanismus der Photolumineszenz von Farbstoffphosphoren. *Z. Physik* **1935**, *94*, 38–46.
- (193) Turro, N. J. *Modern molecular photochemistry*; University Science Books: Mill Valley, Calif, 1991.
- (194) Domcke, W.; Yarkony, D.; Köppel, H. *Conical intersections: Electronic structure, dynamics & spectroscopy*; Advanced series in physical chemistry v. 15; World Scientific: River Edge, N.J., London, 2004.
- (195) Domcke, W.; Yarkony, D.; Köppel, H. *Conical intersections: Theory, computation and experiment*; Advanced series in physical chemistry 17; World Scientific Publishing Co. Pte. Ltd: Singapore, 2012.
- (196) Matsika, S.; Krause, P. Nonadiabatic events and conical intersections. *Ann. Rev. Phys. Chem.* **2011**, *62*, 621–643.
- (197) El-Sayed, M. A. Spin—Orbit Coupling and the Radiationless Processes in Nitrogen Heterocyclics. *J. Chem. Phys.* **1963**, *38*, 2834–2838.
- (198) Spichty, M.; Turro, N. J.; Rist, G.; Birbaum, J.-L.; Dietliker, K.; Wolf, J.-P.; Gescheidt, G. Bond cleavage in the excited state of acyl phosphene oxides. *J. Photochem. Photobiol. A* **2001**, *142*, 209–213.
- (199) Frick, E.; Schweigert, C.; Noble, B. B.; Ernst, H. A.; Lauer, A.; Liang, Y.; Voll, D.; Coote, M. L.; Unterreiner, A.-N.; Barner-Kowollik, C. Toward a Quantitative Description of Radical Photoinitiator Structure–Reactivity Correlations. *Macromolecules* **2016**, *49*, 80–89.
- (200) Kasha, M. Characterization of electronic transitions in complex molecules. *Discuss. Faraday Soc.* **1950**, *9*, 14.
- (201) Lauterborn, W.; Kurz, T. *Coherent optics: Fundamentals and applications ; 73 Problems and Complete Solutions*, 2. ed.; Physics and astronomy online library; Springer: Berlin, 2003.
- (202) Sigrist, M. W. *Laser: Theorie, Typen und Anwendungen*, 8. Auflage 2018; Springer Berlin Heidelberg: Berlin, Heidelberg, 2018.
- (203) Eichler, H. J. *Laser: Bauformen, strahlführung, anwendungen*; Morgan Kaufmann: [Place of publication not identified], 2015.
- (204) Rullière, C., Ed. *Femtosecond Laser Pulses*; Springer Berlin Heidelberg: Berlin, Heidelberg, 1998.
- (205) Diels, J.-C.; Rudolph, W. *Ultrashort Laser Pulse Phenomena*, 2nd ed.; Elsevier: Burlington, 2006.

- (206) *Laserspektroskopie 2: Experimentelle Techniken*, 6. neu bearbeitete und aktualisierte Auflage; Springer Berlin Heidelberg: Berlin, Heidelberg, 2013.
- (207) Demtröder, W. *Laserspektroskopie 2: Experimentelle Techniken*, 6. neu bearbeitete und aktualisierte Auflage; Springer Berlin Heidelberg: Berlin, Heidelberg, 2013.
- (208) Zewail, A. H. Femtochemistry: Atomic-Scale Dynamics of the Chemical Bond Using Ultrafast Lasers (Nobel Lecture). *Angew. Chem. Int. Ed.* **2000**, *39*, 2586–2631.
- (209) Fritsch, K. *Modenkopplung mit hochdispersiven Spiegeln und neuen nichtlinearen Vielschicht-Beschichtungen*; Springer Fachmedien Wiesbaden: Wiesbaden, 2018.
- (210) Boyd, R. W. *Nonlinear optics*, Fourth edition; Elsevier: London, 2020.
- (211) Li, C. *Nonlinear Optics*; Springer Singapore: Singapore, 2017.
- (212) Kaiser, W.; Garrett, C. G. B. Two-Photon Excitation in Ca F<sub>2</sub> : Eu<sup>2+</sup>. *Phys. Rev. Lett.* **1961**, *7*, 229–231.
- (213) Berera, R.; van Grondelle, R.; Kennis, J. T. M. Ultrafast transient absorption spectroscopy: principles and application to photosynthetic systems. *Photosynth. Res.* **2009**, *101*, 105–118.
- (214) Monti, S.; Chiorboli, C. Transient Absorption Spectroscopy. *The Exploration of Supramolecular Systems and Nanostructures by Photochemical Techniques*; Springer, Dordrecht, 2012; pp 185–207.
- (215) Lorenc, M.; Ziolk, M.; Naskrecki, R.; Karolczak, J.; Kubicki, J.; Maciejewski, A. Artifacts in femtosecond transient absorption spectroscopy. *Appl. Phys. B* **2002**, *74*, 19–27.
- (216) Dietzek, B.; Pascher, T.; Sundström, V.; Yartsev, A. Appearance of coherent artifact signals in femtosecond transient absorption spectroscopy in dependence on detector design. *Laser Phys. Lett.* **2007**, *4*, 38–43.
- (217) Istratov, A. A.; Vyvenko, O. F. Exponential analysis in physical phenomena. *Rev. Sci. Instrum.* **1999**, *70*, 1233–1257.
- (218) Holmström, K.; Petersson, J. A review of the parameter estimation problem of fitting positive exponential sums to empirical data. *Appl. Math. Comput.* **2002**, *126*, 31–61.
- (219) Ruckebusch, C.; Sliwa, M.; Pernot, P.; Juan, A. de; Tauler, R. Comprehensive data analysis of femtosecond transient absorption spectra: A review. *J. Photochem. Photobiol. C* **2012**, *13*, 1–27.
- (220) Werner, J. *DADS algorithm, Matlab*.
- (221) Matyjaszewski, K.; Davis, T. P. *Handbook of radical polymerization*; Wiley-Interscience: Hoboken, N.J, 2010.

- (222) van Herk, A. M. Pulsed initiation polymerization as a means of obtaining propagation rate coefficients in free-radical polymerizations. II Review up to 2000. *Macromol. Theory Simul.* **2000**, *9*, 433–441.
- (223) Moad, G. *The chemistry of radical polymerization*, 2nd fully rev. ed.; Elsevier: Amsterdam, Boston, 2007.
- (224) Mayo, F. R. Chain Transfer in the Polymerization of Styrene: The Reaction of Solvents with Free Radicals 1. *J. Am. Chem. Soc.* **1943**, *65*, 2324–2329.
- (225) Barner-Kowollik, C.; Russell, G. T. Chain-length-dependent termination in radical polymerization: Subtle revolution in tackling a long-standing challenge. *Prog. Polym. Sci.* **2009**, *34*, 1211–1259.
- (226) Turro, N. J. Molecular Photochemistry. *Chem. Eng. News* **1967**, *45*, 84–96.
- (227) Huang, X.; Neretina, S.; El-Sayed, M. A. Gold nanorods: from synthesis and properties to biological and biomedical applications. *Adv. Mater.* **2009**, *21*, 4880–4910.
- (228) Chen, H.; Shao, L.; Li, Q.; Wang, J. Gold nanorods and their plasmonic properties. *Chem. Soc. Rev.* **2013**, *42*, 2679–2724.
- (229) Busbee, B. D.; Obare, S. O.; Murphy, C. J. An Improved Synthesis of High-Aspect-Ratio Gold Nanorods. *Adv. Mater.* **2003**, *15*, 414–416.
- (230) Banholzer, M. J.; Millstone, J. E.; Qin, L.; Mirkin, C. A. Rationally designed nanostructures for surface-enhanced Raman spectroscopy. *Chem. Soc. Rev.* **2008**, *37*, 885–897.
- (231) Kim, S.; Jin, J.; Kim, Y.-J.; Park, I.-Y.; Kim, Y.; Kim, S.-W. High-harmonic generation by resonant plasmon field enhancement. *Nature* **2008**, *453*, 757–760.
- (232) Giannini, V.; Fernández-Domínguez, A. I.; Heck, S. C.; Maier, S. A. Plasmonic nanoantennas: fundamentals and their use in controlling the radiative properties of nanoemitters. *Chemical reviews* **2011**, *111*, 3888–3912.
- (233) Qin, Z.; Bischof, J. C. Thermophysical and biological responses of gold nanoparticle laser heating. *Chem. Soc. Rev.* **2012**, *41*, 1191–1217.
- (234) Bohren, C. F.; Huffman, D. R. *Absorption and Scattering of Light by Small Particles*, 1st ed.; Wiley: Hoboken, 2008.
- (235) Papavassiliou, G. C. Optical properties of small inorganic and organic metal particles. *Prog. Solid State Chem.* **1979**, *12*, 185–271.
- (236) Kerker, M. *Scattering of light and other electromagnetic radiation*; Physical chemistry; Elsevier Science: New York, 2016.
- (237) Creighton, J. A.; Eadon, D. G. Ultraviolet–visible absorption spectra of the colloidal metallic elements. *J. Chem. Soc., Faraday Trans.* **1991**, *87*, 3881–3891.

- (238) Persson, B. Polarizability of small spherical metal particles: influence of the matrix environment. *Surface Science* **1993**, *281*, 153–162.
- (239) Kreibig, U.; Frangstein, C. v. The limitation of electron mean free path in small silver particles. *Z. Physik* **1969**, *224*, 307–323.
- (240) Link, S.; El-Sayed, M. A. Size and Temperature Dependence of the Plasmon Absorption of Colloidal Gold Nanoparticles. *J. Phys. Chem. B* **1999**, *103*, 4212–4217.
- (241) Ni, W.; Kou, X.; Yang, Z.; Wang, J. Tailoring longitudinal surface plasmon wavelengths, scattering and absorption cross sections of gold nanorods. *ACS nano* **2008**, *2*, 677–686.
- (242) Link, S.; Burda, C.; Nikoobakht, B.; El-Sayed, M. A. Laser-Induced Shape Changes of Colloidal Gold Nanorods Using Femtosecond and Nanosecond Laser Pulses. *J. Phys. Chem. B* **2000**, *104*, 6152–6163.
- (243) Link, S.; Burda, C.; Mohamed, M. B.; Nikoobakht, B.; El-Sayed, M. A. Laser Photothermal Melting and Fragmentation of Gold Nanorods: Energy and Laser Pulse-Width Dependence. *J. Phys. Chem. A* **1999**, *103*, 1165–1170.
- (244) Sönnichsen, C.; Franzl, T.; Wilk, T.; Plessen, G. von; Feldmann, J.; Wilson, O.; Mulvaney, P. Drastic reduction of plasmon damping in gold nanorods. *Phys. Rev. Lett.* **2002**, *88*, 77402.
- (245) Zhu, J. Shape dependent full width at half maximum of the absorption band in gold nanorods. *Phys. Lett. A* **2005**, *339*, 466–471.
- (246) Novo, C.; Gomez, D.; Perez-Juste, J.; Zhang, Z.; Petrova, H.; Reisman, M.; Mulvaney, P.; Hartland, G. V. Contributions from radiation damping and surface scattering to the linewidth of the longitudinal plasmon band of gold nanorods: a single particle study. *Phys. Chem. Chem. Phys.* **2006**, *8*, 3540–3546.
- (247) KAGANOV M. I. Relaxation between electrons and the crystalline lattice. *Sov. Phys. JETP* **1957**, *4*, 173–178.
- (248) Hohlfeld, J.; Wellershoff, S.-S.; Güdde, J.; Conrad, U.; Jähnke, V.; Matthias, E. Electron and lattice dynamics following optical excitation of metals. *Chem. Phys.* **2000**, *251*, 237–258.
- (249) COMSOL Multiphysics® v. 5.6.
- (250) Gómez-Graña, S.; Hubert, F.; Testard, F.; Guerrero-Martínez, A.; Grillo, I.; Liz-Marzán, L. M.; Spalla, O. Surfactant (bi)layers on gold nanorods. *Langmuir* **2012**, *28*, 1453–1459.
- (251) Lee, S.; Anderson, L. J. E.; Payne, C. M.; Hafner, J. H. Structural transition in the surfactant layer that surrounds gold nanorods as observed by analytical surface-enhanced Raman spectroscopy. *Langmuir* **2011**, *27*, 14748–14756.
- (252) Cheung, K. L.; Chen, H.; Chen, Q.; Wang, J.; Ho, H. P.; Wong, C. K.; Kong, S. K. CTAB-coated gold nanorods elicit allergic response through degranulation and cell death in human basophils. *Nanoscale* **2012**, *4*, 4447–4449.

- (253) Niidome, T.; Yamagata, M.; Okamoto, Y.; Akiyama, Y.; Takahashi, H.; Kawano, T.; Katayama, Y.; Niidome, Y. PEG-modified gold nanorods with a stealth character for in vivo applications. *J. Control. Release.* **2006**, *114*, 343–347.
- (254) PORATH, J. Fractionation of polypeptides and proteins on dextran gels. *Clin. Chim. Acta* **1959**, *4*, 776–778.
- (255) PORATH, J.; FLODIN, P. Gel filtration: a method for desalting and group separation. *Nature* **1959**, *183*, 1657–1659.
- (256) Mori, S.; Barth, H. G. *Size Exclusion Chromatography*; Springer Laboratory Ser; Springer International Publishing: Cham, 20.
- (257) Bloch, F. Nuclear Induction. *Phys. Rev.* **1946**, *70*, 460–474.
- (258) Purcell, E. M.; Pound, R. V.; Bloembergen, N. Nuclear Magnetic Resonance Absorption in Hydrogen Gas. *Phys. Rev.* **1946**, *70*, 986–987.
- (259) Mlynárik, V. Introduction to nuclear magnetic resonance. *Anal. Biochem.* **2017**, *529*, 4–9.
- (260) Fenn, J. B.; Mann, M.; Meng, C. K.; Wong, S. F.; Whitehouse, C. M. Electrospray ionization for mass spectrometry of large biomolecules. *Science* **1989**, *246*, 64–71.
- (261) Fenn, J. B.; Mann, M.; Meng, C. K.; Wong, S. F.; Whitehouse, C. M. Electrospray ionization-principles and practice. *Mass Spectrom. Rev.* **1990**, *9*, 37–70.
- (262) Taflin, D. C.; Ward, T. L.; Davis, E. J. Electrified droplet fission and the Rayleigh limit. *Langmuir* **1989**, *5*, 376–384.
- (263) Iribarne, J. V.; Thomson, B. A. On the evaporation of small ions from charged droplets. *J. Chem. Phys.* **1976**, *64*, 2287–2294.
- (264) Barner-Kowollik, C.; Gruending, T.; Falkenhagen, J.; Weidner, S. *Mass spectrometry in polymer chemistry*; Wiley-VCH: Weinheim, 2012.
- (265) Zubarev, R. A.; Makarov, A. Orbitrap mass spectrometry. *Anal. Chem.* **2013**, *85*, 5288–5296.
- (266) Hu, Q.; Noll, R. J.; Li, H.; Makarov, A.; Hardman, M.; Graham Cooks, R. The Orbitrap: a new mass spectrometer. *J. Mass Spectrom.* **2005**, *40*, 430–443.
- (267) Perry, R. H.; Cooks, R. G.; Noll, R. J. Orbitrap mass spectrometry: instrumentation, ion motion and applications. *Mass Spectrometry Reviews* **2008**, *27*, 661–699.
- (268) French, A. P. *An Introduction to Quantum Physics*, 1st; Routledge: Milton, 2018.
- (269) Püschmann, S. D.; Frühwirt, P.; Müller, S. M.; Wagner, S. H.; Torvisco, A.; Fischer, R. C.; Kelterer, A.-M.; Griesser, T.; Gescheidt, G.; Haas, M. Synthesis and characterization of diacylgermanes: persistent derivatives with superior photoreactivity. *Dalton Trans.* **2021**, *50*, 11965–11974.

- (270) Wagner, P. J. Chemistry of excited triplet organic carbonyl compounds. *Triplet States III*; Springer, Berlin, Heidelberg, 1976; pp 1–52.
- (271) Sidman, J. W. Electronic Transitions Due To Nonbonding Electrons Carbonyl, Aza-Aromatic, And Other Compounds. *Chem. Rev.* **1958**, *58*, 689–713.
- (272) Wei, M.-H.; Lee, C.-H.; Chang, C.-C.; Chen, W.-C. Tunable near-infrared optical properties based on poly(methyl methacrylate)–oxide waveguide materials. *J. Appl. Polym. Sci.* **2005**, *98*, 1224–1228.
- (273) Srinivasan, S.; Lee, M. W.; Grady, M. C.; Soroush, M.; Rappe, A. M. Computational evidence for self-initiation in spontaneous high-temperature polymerization of methyl methacrylate. *J. Phys. Chem. A* **2011**, *115*, 1125–1132.
- (274) Xu, Y.; Xu, Q.; Lu, J.; Xia, X.; Wang, L. Self-initiated atom transfer radical polymerization of methyl methacrylate in cyclohexanone. *Eur. Polym. J.* **2007**, *43*, 2028–2034.
- (275) Beuermann, S.; Buback, M.; Davis, T. P.; Gilbert, R. G.; Hutchinson, R. A.; Olaj, O. F.; Russell, G. T.; Schweer, J.; van Herk, A. M. Critically evaluated rate coefficients for free-radical polymerization, 2. Propagation rate coefficients for methyl methacrylate. *Macromol. Chem. Phys.* **1997**, *198*, 1545–1560.
- (276) Feuerstein, W.; Höfener, S.; Klopper, W.; Lamparth, I.; Moszner, N.; Barner-Kowollik, C.; Unterreiner, A.-N. Photophysical Properties of Benzoylgermane and para-Substituted Derivatives: Substituent Effects on Electronic Transitions. *ChemPhysChem.* **2016**, *17*, 3460–3469.
- (277) Neshchadin, D.; Rosspeintner, A.; Griesser, M.; Lang, B.; Mosquera-Vazquez, S.; Vauthy, E.; Gorelik, V.; Liska, R.; Hametner, C.; Ganster, B.; *et al.* Acylgermanes: photoinitiators and sources for Ge-centered radicals. insights into their reactivity. *J. Am. Chem. Soc.* **2013**, *135*, 17314–17321.
- (278) Gold, V. *The IUPAC Compendium of Chemical Terminology*; International Union of Pure and Applied Chemistry (IUPAC): Research Triangle Park, NC, 2019.
- (279) Frühwirt, P.; Knoechl, A.; Pillinger, M.; Müller, S. M.; Wasdin, P. T.; Fischer, R. C.; Radebner, J.; Torvisco, A.; Moszner, N.; Kelterer, A.-M.; *et al.* The Chemistry of Acylgermanes: Triacylgermenolates Represent Valuable Building Blocks for the Synthesis of a Variety of Germanium-Based Photoinitiators. *Inorg. Chem.* **2020**, *59*, 15204–15217.
- (280) Batchelor, R.; Messer, T.; Hippler, M.; Wegener, M.; Barner-Kowollik, C.; Blasco, E. Two in One: Light as a Tool for 3D Printing and Erasing at the Microscale. *Adv. Mater.* **2019**, *31*, e1904085.
- (281) Császár, A. G.; Mills, I. M. Vibrational energy levels of water. *Spectrochim. Acta Part A* **1997**, *53*, 1101–1122.

- (282) Xie, X.; Hogen-Esch, T. E. Anionic Synthesis of Narrow Molecular Weight Distribution Water-Soluble Poly(N, N -dimethylacrylamide) and Poly(N -acryloyl- N '-methylpiperazine). *Macromolecules* **1996**, *29*, 1746–1752.
- (283) Varghese, N.; Vivekchand, S.; Govindaraj, A.; Rao, C. A calorimetric investigation of the assembly of gold nanorods to form necklaces. *Chem. Phys. Lett.* **2008**, *450*, 340–344.
- (284) Metwally, K.; Mensah, S.; Baffou, G. Fluence Threshold for Photothermal Bubble Generation Using Plasmonic Nanoparticles. *J. Phys. Chem. C* **2015**, *119*, 28586–28596.
- (285) Neidinger, P.; Davis, J.; Carroll, J. A.; Kammerer, J.; Jaatinen, E.; Walden, S. L.; Unterreiner, A.-N.; Barner-Kowollik, C. Wavelength-resolved near infra-red light induced free-radical polymerization. *Polym. Chem.* **2023**, *14*, 4912–4917.
- (286) Kumar, J.; Wei, X.; Barrow, S.; Funston, A. M.; Thomas, K. G.; Mulvaney, P. Surface plasmon coupling in end-to-end linked gold nanorod dimers and trimers. *Phys. Chem. Chem. Phys.* **2013**, *15*, 4258–4264.
- (287) Shortell, M. P.; Hewins, R. A.; Fernando, J. F. S.; Walden, S. L.; Waclawik, E. R.; Jaatinen, E. A. Multi-angle fluorometer technique for the determination of absorption and scattering coefficients of subwavelength nanoparticles. *Opt. Express* **2016**, *24*, 17090–17102.
- (288) Oulianov, D.; Tomov, I.; Dvornikov, A.; Rentzepis, P. Observations on the measurement of two-photon absorption cross-section. *Opt. Commun.* **2001**, *191*, 235–243.
- (289) Sheik-Bahae, M.; Said, A. A.; Wei, T.-H.; Hagan, D. J.; van Stryland, E. W. Sensitive measurement of optical nonlinearities using a single beam. *IEEE J. Quantum Electron.* **1990**, *26*, 760–769.
- (290) Makarov, N. S.; Drobizhev, M.; Rebane, A. Two-photon absorption standards in the 550-1600 nm excitation wavelength range. *Opt. Express* **2008**, *16*, 4029–4047.
- (291) Dong, N.; Li, Y.; Zhang, S.; McEvoy, N.; Gatensby, R.; Duesberg, G. S.; Wang, J. Saturation of Two-Photon Absorption in Layered Transition Metal Dichalcogenides: Experiment and Theory. *ACS Photonics* **2018**, *5*, 1558–1565.
- (292) Kirkpatrick, S. M.; Naik, R. R.; Stone, M. O. Nonlinear Saturation and Determination of the Two-Photon Absorption Cross Section of Green Fluorescent Protein. *J. Phys. Chem. B* **2001**, *105*, 2867–2873.
- (293) Kim, J. Fallstricke bei der Bestimmung des Absorptionsquerschnitts zweiter Ordnung von Rhodamin B mit einem Z-Scan Aufbau. Vertieferarbeit, KIT, 2023.
- (294) OpenAI. (2023). ChatGPT-3.5 (May 24 version) [Large language model]. <https://chat.openai.com/chat>.

## 12 List of Publications

### Paper in reviewed journals

Neidinger, P.; Voll, D.; Walden, S. L.; Unterreiner, A.-N.; Barner-Kowollik, C. Two Photon Induced Pulsed Laser Polymerization with Near Infrared Light. *ACS macro letters* **2022**, *12*, 308–313.

Neidinger, P.; Davis, J.; Voll, D.; Jaatinen, E. A.; Walden, S. L.; Unterreiner, A. N.; Barner-Kowollik, C. Near Infrared Light Induced Radical Polymerization in Water. *Angewandte Chemie International Edition* **2022**, *61*, e202209177.

Neidinger, P.; Davis, J.; Carroll, J. A.; Kammerer, J.; Jaatinen, E.; Walden, S. L.; Unterreiner, A.-N.; Barner-Kowollik, C. Wavelength-Resolved Near Infra-red Light Induced Free-Radical Polymerization. *Polym. Chem.*, **2023**, *14*, 4912-4917.